Design of Novel Experiments and Analyses for Head and Spine Trauma Biomechanics

John Robert Humm
Marquette University

DESIGN OF NOVEL EXPERIMENTS AND ANALYSES FOR HEAD AND SPINE TRAUMA BIOMECHANICS

by

John R. Humm, M.S.

A Dissertation submitted to the Faculty of the Graduate School, Marquette University, in Partial Fulfillment of the Requirements for the Degree of Doctor of Philosophy

Milwaukee, Wisconsin

December 2020

ABSTRACT
DESIGN OF NOVEL EXPERIMENTS AND ANALYSES
FOR HEAD AND SPINE TRAUMA BIOMECHANICS

John R. Humm, M.S.

Marquette University, 2020

Previous biomechanics research studies have used both whole-body and isolated postmortem human surrogate experiments to define human injury tolerances, advance safety in injury-producing environments, and promulgate standards for the design of injury mitigating systems. Recent developments in transportation and sports-related fields have led to an increasing need to determine tolerances for combined loading (multi-axis) scenarios. This dissertation demonstrates the efficacy of the novel experimental design and head and spine trauma analysis in these modalities.

The first topic was the design of a novel experiment to examine the effect of oblique loading on the lumbar spine's tension tolerance. Isolated lumbosacral spine experiments were used to examine this injury tolerance with a custom six-degree-of-freedom spinal alignment device. The isolated experiment injury matched previous whole-body tests, and failure kinetics were obtained.

The second topic was the design of a novel experiment to measure the head and neck response to off-axis moment loading at the occipital condyle joint. A dynamic rotational system applied angular displacement centered at the OC joint in an orientation that resulted in combined flexion-extension/lateral-bending/ axial rotation of the head. Region-specific anatomic kinetics were determined using load cells and a motion capture system.

The third topic was the design of a novel experimental model to assess the accuracy of wearable sensors for concussion research. This topic aimed to design a new technique that placed a custom sensor near the head-center-of-gravity in whole-body and isolated head/head-neck PMHS. Tests were conducted to benchmark current wearable sensors in the sport and military environments. The measured head kinematics from the in-PMHS sensor serves as the gold standard for these tests.

The fourth topic was the design of a novel technique to compute three-dimensional time-varying global response kinematics of the head, spine, and pelvis in oblique frontal impacts. Collected data were combined to create three-dimensional temporal global kinematic corridors, which are needed to validate current and future finite element models of the components/subsystems, human body models, and they can also be used for benchmarking different computational models.

TABLE OF CONTENTS

LIST OF TABLES

LIST OF FIGURES

CHAPTER 1. INTRODUCTION

1.1. BACKGROUND

Previous biomechanics research studies have used both whole-body [1-4] and isolated [5-9] postmortem human surrogate (PMHS, cadavers) experiments to define human injury tolerances, advance safety in injury-producing environments, and promulgate standards for the design of injury-mitigating systems (modern vehicles, for example). Automotive and sport-related injury research has primarily focused on the human response in the sagittal [6, 10-12] (e.g., frontal car crash) or coronal [13, 14] (e.g., side car crash) plane, i.e., single planar response. Recent developments in transportation and sport-related fields have led to an increasing need to determine tolerances for combined loading (multi-axis) scenarios. Advanced measuring systems (e.g., high-speed motion capture, higher resolution CT scans, six-degree-of-freedom sensors) have increased the ability and precision to collect multi-planar biomechanical response data. They can be used effectively to determine the tolerances under combined loading; however, novel experimental designs and more in-depth analyses are necessary to achieve the goal of defining off-axis/multi-planar human tolerance. This research study demonstrates the efficacy of the novel experimental design and analysis aspects with specific reference to head and spine trauma in these modalities.

1.2. PROBLEM STATEMENT

While human tolerances are defined for transportation applications (motor vehicle, aviation, astronaut), military, and sport environments, they are primarily limited to single-planar loading. For example, the Federal Motor Vehicle Safety Standards (FMVSS)

promulgated by the National Highway Traffic Safety Administration (NHTSA) aims to reduce fatalities and highway injuries. Frontal impact standards initiated in the last century continue to focus on occupants seated in the standard position, and the impact vector remains unimodal (FMVSS-208). Likewise, side-impact standards focus on nearside occupants seated in a standard posture with little or no consideration to obliquity in loading (FMVSS-214). Similar examples apply to the FAA emergency landing pulse environment (14 CFR § 25.562). Thus, almost all research studies have focused on determining the biomechanics of injury in the planar loading mode. Recent advancements in technology and its immediate usability/adaptability have exposed limitations in applying planar loading tolerances to combined (complex) loading scenarios. Studies are needed to account for or simulate complex loading in the field of human safety. This dissertation focuses on the overall topic of quantifying the biomechanical injury variables from complex loading under different scenarios to different body regions, specifically, the head and spine. It answers the following key questions for different body regions, as presented in separate chapters.

1.3. KEY QUESTIONS

1.3.1. Key question 1:

What type of experimental design is needed to evaluate the accuracy of wearable sensors designed to monitor head impact exposure when the orientation of the vector is unknown? This is covered in chapter 2.

1.3.2. Key question 2:

What type of experimental design is needed to accurately determine the lumbar spine loads and reproduce injuries observed in oblique whole-body tests when the loads are unknown? This is covered in chapter 3.

1.3.3. Key question 3:

What type of analytical techniques are needed to determine the three-dimensional kinematic corridors in oblique impacts, and which parameter(s) best statistically support the underlying injury responses? This is covered in chapter 4.

1.3.4. Key question 4:

What type of experimental design is needed to accurately determine the atlanto-occipital joint response to dynamic rotation when the input is at an oblique angle to the mediolateral axis of the joint? This is covered in chapter 5.

1.4. APPROACH

As the primary research of this dissertation focuses on developing novel experiments and techniques for the head and spine, it uses different and unique apparatuses designed by the author to answer specific questions or problems related to the biomechanics of head and spine trauma. A summary of each device and analysis is given.

1.4.1. Chapter 2: Design of a novel experiment to evaluate wearable sensors for head exposure

To determine the accuracy of wearable sensors for head injuries, the author designed a custom alignment system and sensor mount for placing a sensor near the head center-

of-gravity, termed as topic 1 (see below for description). A rigid-arm mini-sled pendulum device is used to conduct dynamic experiments with whole-body and isolated specimens.

1.4.2. Chapter 3: Design of an experiment to induce non-planar loading to the lumbar spine

To determine the lumbar spine loads under complex loading, the author designed a custom six-degree-of-freedom spinal alignment device, termed as topic 2 (see below for description). An electro-hydraulic piston is used to conduct the experiments with a whole-body specimen and isolated lumbar spinal column.

1.4.3. Chapter 4: Techniques to analyze three-dimensional kinematics of the head and spine

1.4.3.1. Corridors

To determine the three-dimensional (3-d) global sensor and motion corridors in oblique impacts, a novel analysis of optical data from 28 cameras is developed, termed as topic 4 (see below for description). A servo-acceleration sled is used to conduct the whole - body experiments.

1.4.3.2. Injury Risk Curve

To determine the optimal injury risk curve, different components of the 3-d deflections were analyzed (uniaxial, planar, and multiplanar), and sophisticated statistical methods are used, termed as topic 4 (see below for description). Survival analysis and Brier Score Metrics are used in the analysis.

1.4.4. Chapter 5: Design of an experiment to apply complex loading to the cervical spine

To determine the occipital condyle joint responses, a custom dynamic rotational system is designed, termed as topic 3 (see below for description). The electrohydraulic linear piston device is used to conduct experiments with isolated head and neck.

In all the above experiments, the following combinations of sensors/measurement systems will be used:

- linear accelerometers
- angular rate sensors
- six-degree-of-freedom sensors
- load cells
- motion capture system
- high-speed video cameras
- Computerized Tomography (CT) machine
- portable digital x-ray
- coordinate-measuring machine (CMM)
- custom instrumentation mounts for PMHS

The first topic will be the design of a novel experimental model that can assess the accuracy of wearable sensors for concussion research. This area of research is particularly relevant given the heightened interest in concussion injuries in sport and military environments [15-17]. Wearable sensors embedded in helmets (military or football helmet), other protective equipment (mouthguards), or on the head (mastoid

patches) have been deployed in multi-institutional concussion studies to monitor head exposure [18, 19]. While the accuracy of these sensors has been examined in the laboratory using ATDs, these surrogates lack important human boundary conditions such as skin, teeth, and hair. This topic's goal will involve the design of a new technique to place a custom reference sensor near the head center-of-gravity in whole-body and isolated head/head-neck PMHS. Pre-test CT scans with a custom head alignment plate is necessary for accurate placement of the custom internal sensor. Tests using a rigid-arm pendulum with custom head support system are used to benchmark current wearable sensors in the sport and military environments. The measured head kinematics from the in-PMHS sensor serves as the gold standard for these tests.

The second topic will be designing a novel experiment to examine the effect of oblique loading on the tension (distraction) tolerance of the lumbar spine. Alternative seating concepts are currently being considered in both the automotive and aircraft industries. Many of these designs orient the occupant such that the sagittal plane is no longer parallel to the centerline of the vehicle/aircraft. In this configuration, standard frontal impacts will result in complex, oblique loading to the occupant due to the orientation of the seat with the impact vector [1, 20]. Such loading scenarios may lead to tension-type injuries at the lumbar spine. To examine this injury tolerance, isolated lumbosacral spine experiments are used with a custom six-degree-of-freedom spinal alignment device. It is used to alter the sacral-T1 alignment using an electro-hydraulic piston device. The tensile load is applied in an oblique orientation simulating forward

flexion and lateral bending of the lumbar spine. Load cell and motion-capture data are combined to determine the sacral kinetics and human injury tolerance to this mode.

The third topic will be the design of a novel experiment to measure the head and neck response to off-axis dynamic-moment loading at the occipital condyle joint (i.e., the base of the skull). The occipital condyle joint is mainly responsible for the head's nodding motion (flexion/extension). While combined injury metrics using the axial force and sagittal moment have been estimated [21-24], little research has been conducted on the effect of axial rotation on the occipital condyle bending tolerance. An isolated basilar skull/cervical spine specimen with the occipital condyle joint intact is used for this experiment. A dynamic moment system (DMS) will transfer the linear motion of the electrohydraulic piston to angular displacement centered at the occipital condyle joint. The head is rotated about the vertical axis, and the moment is applied parallel to the sagittal plane of the neck. This loading scenario will apply a torque rotated in the transverse plane from the mediolateral axis of the occipital condyle joint and result in a combined flexion-extension/lateral-bending/axial rotation of the head. Region-specific anatomic kinetics will be determined using load cells and a motion-capture system.

The fourth topic will be the design of a novel technique to compute three-dimensional time-varying global response kinematics of the head, spine, and pelvis in oblique frontal impacts. Whole-body specimens are instrumented with linear accelerometers, angular rate sensors, and motion capture targets at the head, spine, and pelvis [25]. Occupants are seated in a generic environment representative of standard automotive geometries. Collected data are combined to create three-

dimensional temporal global kinematic corridors, which are needed to validate current and future finite-element models of the components/subsystems, human body models. They can also be used for benchmarking different computational models. Statistical analyses are used to determine which parameter(s) best supports the underlying injury mechanisms and responses.

Chapter 6 gives a summary of the contributions from work performed in this dissertation include its impact on practices and standards. Peer-reviewed publications and funded grants as a result of these studies are also listed. The process used in the present dissertation can be efficaciously applied across numerous studies for advancing human safety in athletics (NFL, NCAA, etc.), aviation (FAA, NASA), military (DoD), and transportation (NHTSA) environments.

CHAPTER 2. DESIGN OF A NOVEL EXPERIMENT TO EVALUATE WEARABLE SENSORS FOR HEAD EXPOSURE

2.1. INTRODUCTION

Interest in sport-related and military environment concussions have increased within the medical community as the public has become more aware of these injuries' severity and prevalence. Biomechanical engineers have developed sensors to monitor head linear accelerations and angular accelerations/velocities during live play and training activities. The design and implementation of these sensors make it challenging to accurately measure these metrics, understand head exposure risk, and delineate concussion's underlying biomechanics.

2.1.1. Background

2.1.1.1. Concussion Background

The Center for Disease Control (CDC) has estimated that 300,000 people annually suffer sport-related mild-to-moderate traumatic brain injuries (TBI) in the United States, of which most can be classified as concussions [26]. Some estimates are much higher and indicate up to 1.6–3.8 million cases annually [27]. The 4th International Conference on Concussion in Sport describes concussion as follows:

> […] a brain injury defined by complex pathophysiological processes affecting the brain induced by biomechanical forces. Several common features that incorporate clinical, pathologic and biomechanical injury constructs that may be utilized in defining the nature of a concussive head injury include: (1) Concussion can be caused by either a direct blow to the body (head, face, neck, or

elsewhere) with an impulsive force transmitted to the head; (2) Concussions typically results in the rapid onset of short-lived impairment of neurological function that resolves spontaneously. However, in some cases, symptoms and signs may evolve over several minutes to hours; (3) Concussion may result in neuropathological changes, but the acute clinical symptoms largely reflect a functional disturbance rather than a structural injury and, as such, no abnormality is seen on standard structural neuroimaging studies; (4) Concussion results in a graded set of clinical symptoms that may or may not involve loss of consciousness. Resolution of the clinical and cognitive symptoms typically follows a sequential course. However, it is important to note that in some cases, symptoms may be prolonged [28].

Typical clinical signs of a concussion can include headache or feeling of pressure in the head, temporary loss of consciousness, confusion (feeling like 'in a fog'), amnesia surrounding the concussive event, dizziness ('seeing stars'), ringing in the ears, nausea, vomiting, slurred speech, delayed response to questions or general confusion, and fatigue. Most symptoms are resolved within 7–10 days; however, persistent problems (>10 days) have been reported in 10–15% of concussions. Typical return to play (RTP) protocols involve a graduated or stepwise progression that the athlete must complete before normal participation. The athlete must be asymptomatic at the current level (for at least 24 hours) before advancing to the next, and it takes about one week to complete the entire protocol. If the athlete becomes symptomatic, they regress to the previous level and proceed as before. A brief description of an RTP is shown in below.

Table 2.1.1.1-1: Typical Return to Play Protocol

Stage		Objective	Activity during stage
1	No activity	Recovery	Physical/cognitive rest
2	Light aerobic exercise	Increased HR	Walking, swimming, stationary cycling. No resistance training
3	Sport-specific exercise	Add movement	Light drills no head impact
4	Non-contact training drills	Exercise, coordination, and increased cognitive load	More complex drills such as passing/catching or drills involving more complicated footwork
5	Full-contact practice	Restore confidence and assess functional skills	Participate in normal training activities
6	Return to play	Normal gameplay	n/a

2.1.1.2. Brain Anatomy

The human central nervous system (CNS) is comprised of the spinal cord and brain. The brain's cerebrum has two large hemispheres separated by a deep groove that runs along the anteroposterior (rostrocaudal) direction called the longitudinal (or cerebral) fissure. The cerebrum consists of a system of ridges (gyri) and folds (sulci) leading to its characteristic appearance and is divided into five distinct lobes—frontal, parietal, temporal, occipital, and limbic.

The frontal lobe is responsible for so-called “executive functions,” which control our personality, memory, problem solving, and insight. The primary motor and premotor cortices are in the frontal lobe, and they control the body’s voluntary and involuntary movements. Broca’s area is also in the frontal lobe and is important for producing written and spoken language. The frontal lobe is often thought of as the brain's area that makes us human and separates us from other animals. The parietal

lobe's main function is to receive and process sensory information such as touch and temperature, as well as proprioception. Many of the somatosensory receptors on the skin terminate and are processed in the parietal lobe. The occipital lobe houses the visual cortex and is the visual processing center for the brain. Disruption to this area can result in blindness, even if the eyes and ocular nerves are intact. The temporal lobe helps in processing, forming, and storing visual memories, producing speech, recognizing written language, and assisting in homeostatic functions. The limbic lobe is an evolutionarily older part of the brain and governs many of our unconscious emotions and instincts. It regulates our appetite and desire and coordinates our fight-or-flight response. Just inferior cerebrum is the cerebellum (little brain), which helps refine our motor control by contributing to coordination, precision, and movement timing and plays a role in attention and regulating fear responses.

The different functions of the five lobes and cerebellum of the brain may help explain the disparate and wide-ranging symptoms of a concussion injury. An injured person may experience clinical symptoms that are physical (loss of consciousness or amnesia), behavioral (irritability), cognitive (fog-like feeling), emotional (exaggerated changes in mood), somatic (headache), sleep disturbance (insomnia), or a combination thereof, depending on the location of the injury. To better understand the many concussion symptoms, it is necessary to understand how the biomechanical forces in head injuries mechanically change the different structures and locations in the brain.

2.1.1.3. Mechanisms of Concussion

The underlying mechanisms of concussions are complex, and a summary is provided below. Briefly, head injuries typically result from dynamic loading of the head where the mechanical force duration is less than 20 milliseconds [29] (although it can be less than 200 milliseconds). Dynamic loading can be further divided into either impulsive loading, where head motion is either started or stopped without direct impact, or impact loading, where a blunt object strikes the head. Brain injuries are classified clinically as either focal or diffuse injuries [30]. Focal injuries are defined by a large lesion and comprise cortical contusions and subdural, epidural, and intracerebral hematomas. Diffuse injuries present more widespread neurological symptoms than focal injuries, and typically the lesions are not seen macroscopically. Diffuse injuries are further categorized as mild concussion (temporary disturbance of neurologic function), classical cerebral concussion (temporary loss of consciousness), and diffuse axonal injury (prolonged loss of consciousness with residual deficits). Diffuse injuries are thought to be caused by the brain's motion within the skull, and the primary risk factors are hypothesized to be linear and rotational head accelerations [31].

2.1.1.4. Head Injury Metrics

The pioneering work on head trauma metrics started with the Wayne State Injury Curve [32]. A series of 23 tests were performed on four human cadavers, divided into five different test series. The heads were instrumented with intracranial pressure transducers, and an accelerometer was mounted to the occiput. The specimens were placed on a frame that allowed them to rotate in the sagittal plane about a mediolateral

axis inferior to the feet. The forehead contacted different surfaces, and the peak acceleration and pulse-width time were measured. These tests were combined with previously collected data from isolated head drop-tests to produce a head fracture injury tolerance curve that related peak acceleration and pulse width to skull fracture. The authors observed that nearly all skull fractures result in mild concussion or unconsciousness; thus, these experiments' results could be used to infer a concussion tolerance. This was the first study to relate a measurable parameter (linear acceleration) to head injury/concussion.

Gadd [33] later expanded on Lissner's work and combined the Wayne State Curve with data from Eiband's NASA sled tests. Using a log-log plot of the two data sets, he found a linear relationship between injury and acceleration, which could be expressed as the integral of head acceleration raised to the power of 2.5. Any value over 1000 was deemed to be injurious. Gadd's work provided a standardized method to analyze head acceleration and relate it to injury.

The National Highway Traffic Safety Administration (NHTSA) later used Versace's reanalysis [34] of Gadd's work and derived the HIC or Head Injury Criterion (Equation 2.1.1.4-1), which is the current head injury metric used in the Federal Motor Vehicle Safety Standards.

$$HIC = \left\{ t_2 - t_1 \left[\frac{1}{t_2 - t_1} \int_{t_1}^{t_2} a \, dt \right]^{2.5} \right\}_{max} \qquad \textbf{\textit{Equation 2.1.1.4-1}}$$

While the relationship between linear acceleration and skull fracture (and thus concussion) was well defined, the effect of rotational acceleration was relatively unknown. Gennarelli [35] explored this relationship by comparing squirrel monkeys' responses to pure linear and pure rotational accelerations. Eleven monkeys were fitted with custom helmets. The helmets were attached to a device that induced pure translation or pure rotation of the head. At approximately the same head acceleration level, none of the animals experiencing pure translation were concussed, while all the animals in the pure rotation tests suffered concussions. On average, more than double the number of lesions was observed. These experiments were later expanded [36] and demonstrated similar results. The authors concluded that angular acceleration imparts high shear strain to the brain tissue. Due to the brain's low shear modulus, angular accelerations were more likely than linear accelerations to cause concussions.

In 2013, Takhounts [37] combined previously collected cadaver, human volunteer, and anthropomorphic test device (ATD) data. These data were entered into a brain finite-element model (FEM) to estimate the cumulative strain damage measure (CSDM) of impacts. From these measures, injury risk curves were derived and related to the angular velocity. This produced the BrIC, or Brain Injury Criterion, as shown in Equation 2.1.1.4-2., where ω_x, ω_y, and ω_z are the peak head angular velocities, and ω_{xc}, ω_{yc}, and ω_{zc} are the critical values that depend on the subject. The authors concluded that BrIC is a good supplement to the HIC for assessing head injury risk.

$$BrIC = \sqrt{\left(\frac{\omega_x}{\omega_{xC}}\right)^2 + \left(\frac{\omega_y}{\omega_{yC}}\right)^2 + \left(\frac{\omega_z}{\omega_{zC}}\right)^2} \qquad \textit{Equation 2.1.1.4-2}$$

2.1.1.5. Head Exposure

A summary of head injuries given by the U.S. Consumer Product Safety Commissions (CPSC) estimated that 446,788 sport-related injuries were treated in U.S. hospital emergency rooms. While this number is below the upper limit referenced earlier in this paper (1.6 million), McCrea [38] has estimated upwards of 50% of concussion injuries go unreported. The breakdown of the activities that produced these injuries from the US-CPSC study is shown in Figure 2.1.1.5-1. Cycling accounted for 20.7% of these injuries, followed by football (11.4%), baseball/softball (9.3%), basketball (8.4%), and water sports, which included diving, scuba diving, surfing, swimming, water polo, water skiing, and water tubing (7.0%).

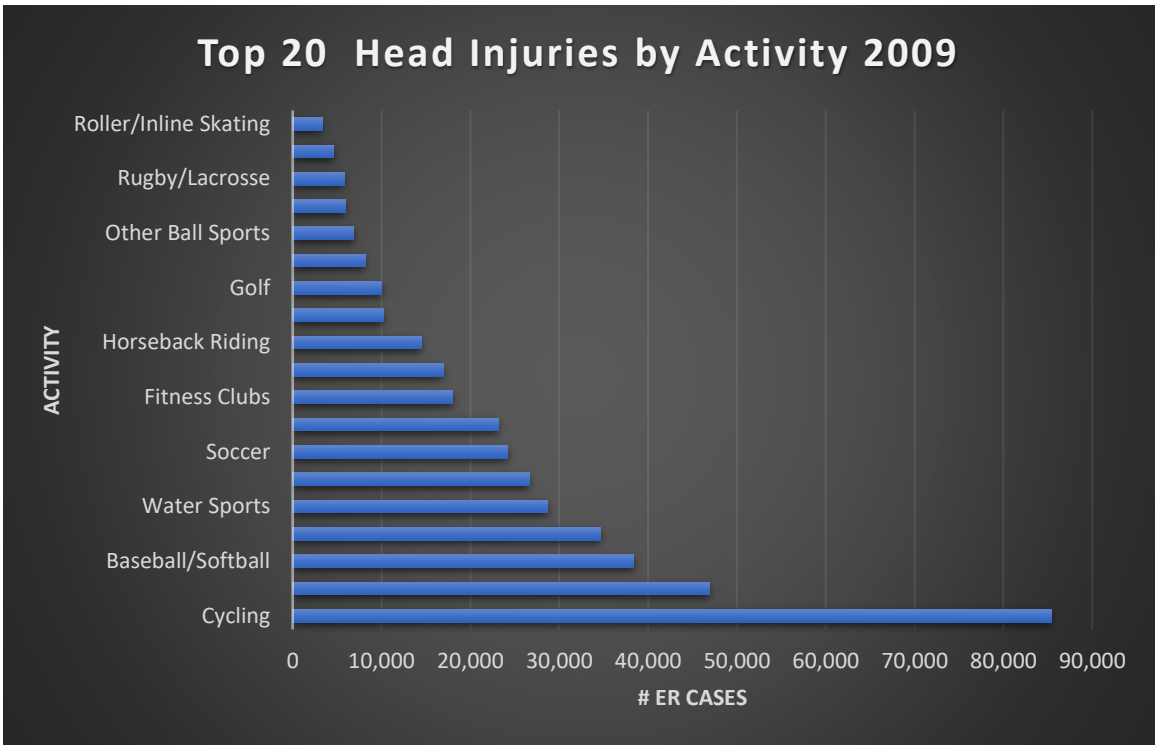

Figure 2.1.1.5-1: Number of sport-related head injuries seen in U.S. Emergency Rooms by activity in 2009

To better understand the relative risk of head injuries in high school and college football, Guskiewicz [39] sent out questionnaires about head exposure during the football season and received responses from 17,549 players. Approximately 5% of these players suffered at least one concussion, and 0.7% sustained a second injury. Players who received one concussion were three times more likely to sustain a second concussion than previously uninjured players were to receive a first. The overall rate of concussions per 1000-athlete-exposure was 1.28, with approximately 60% occurring in games and defensive backs, offensive linemen, and linebackers being the most frequently injured players. Epidemiological studies of National League Football (NFL)

players [40] have estimated that concussion occurs at a rate of 0.41 per game, or about one every other game.

2.1.1.6. Brain Modeling

While Anthropomorphic Test Devices (ATD) (crash test dummies) and the HIC have dramatically reduced head injuries in automotive accidents, to take the next step forward in delineating brain biomechanics injuries and concussion, more sophisticated surrogates/tools are necessary. With the advent of faster and cheaper processors, human body computer models are being used with greater frequency. Finite-element models (FEM) of the human allow for more detailed stress/strain analyses and a better understanding of the local forces that produce injury in trauma biomechanics. The NHTSA Simulated Injury Monitor (SIMon) is a FEM of the brain that may be used for this purpose.

The current SIMon model was constructed from the CT scans of a male individual with a head size that approximated the 50th percentile male. The model consists of 42,500 nodes and 45,975 total elements (5153 shell, 14 beam, and 40708 solid). The model's anatomic structures are the skull, cerebrum, cerebellum, brainstem, ventricles, cerebral spinal fluid (CSF) and pia arachnoid complex (PAC) layer, falx, tentorium, and parasagittal blood vessels. Figure 2.1.1.6-1 shows the SIMon model used for this study.

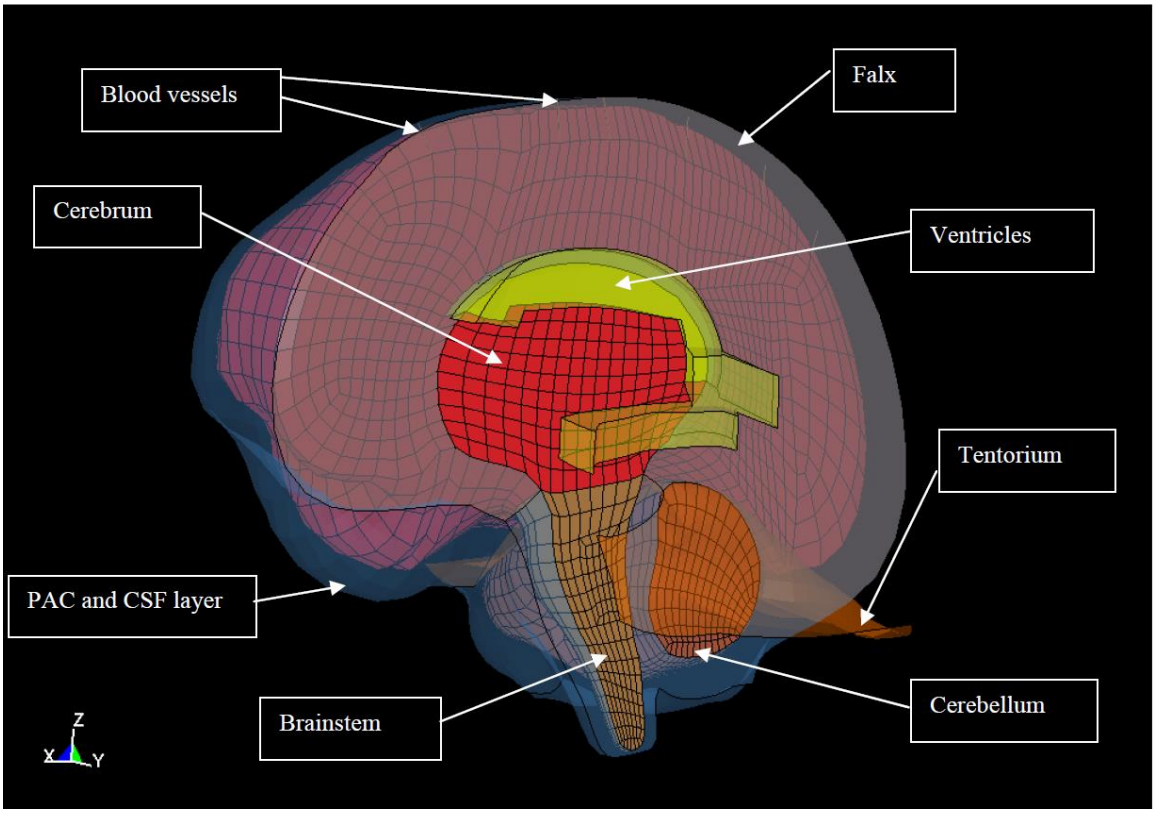

Figure 2.1.1.6-1: Components of the SIMon model, including the cerebrum, cerebellum, brainstem, blood vessels, tentorium, ventricles, falx, and PAC and CSF layer. Skull is not shown.

2.1.1.7. Previous Head Sensor Evaluation Studies

An initial evaluation of a wearable sensor designed to be fixed to the mastoid process of the athlete (xPatch) was performed using a Hybrid III ATD [41]. Results from this study demonstrated good agreement between the wearable sensor and the reference sensor at the ATD head CG. However, a study evaluating the same sensor using PMHS [42] showed that the xPatch overestimate the peak linear acceleration, and the angular acceleration data was deemed likely not usable. The errors were attributed to the skin response and highlight the need to include this important biofidelity boundary

condition. Additionally, others [43] have attempted to mimic human-like boundary conditions, including the hair, by using a wig attached to the head skin of the ATD.

2.1.2. Objectives

While the diagnosis and treatment of concussion have improved in recent years, there still exists a lack of head linear and angular acceleration data measured during concussive and sub-concussive events, as well as derived injury tolerance values. The medical community has shown increased interest in the short- and long-term risks of TBI, which has led to wearable sensor technologies that quantify exposure. These devices in order to be effective, should be unobtrusive to the user, require little maintenance, have easy data management, be scalable to a large population, and accurately measure head metrics. While ATD experiments can provide a preliminary assessment of sensor accuracy, they fail to account for biofidelity characteristics such as skin, fat, mouth, and teeth. Post-Mortem Human Surrogates (PMHS) provide more realistic test conditions for evaluating and comparing wearable head kinematic sensors. To accurately assess these sensors' efficacy, it is necessary to have a reference sensor that can measure accelerations in proximity to the PMHS head center of gravity (CG).

Because traditional methods of acquiring these accelerations cannot be used in helmeted PMHS tests, an alternative method of positioning the sensor near the head CG is required. The present study's objectives are to design an experiment that can evaluate the performance of wearable sensors that measure head kinematics using a novel instrumented PMHS model. Data from these experiments were input into a computational model of the head to determine CSDM for different brain components.

2.2. METHODS

This study was divided into three phases—two sets of PMHS tests and one set of computational runs. The first phase used a whole-body non-helmeted PMHS to test an internally mounted sensor's feasibility and accuracy. The second phase used an isolated head-neck helmeted PMHS with an internal sensor. In the third phase of this study, the data collected from the 2nd set of PMHS tests were used as input to a computational brain model.

2.2.1. Whole-Body Tests

An un-embalmed whole-body PMHS was procured and screened against hepatitis B, hepatitis C, and HIV. The approximate CG location of the head, estimated as 12 mm anterior to the auditory meatus, was marked bilaterally [44]. The specimen was thawed to the point where the neck was semi-mobile, but the brain remained mostly frozen and solid. Next, a 38 mm hole was drilled along the mediolateral (medial-lateral, M/L) axis of the head at the previously marked fiducials. A 38 mm (outer diameter) cylinder aluminum pipe was inserted through the head and secured bilaterally to the skull using an aluminum plate and bone screws. A 6DOF sensor was mounted in the center of the pipe at the midpoint of its length. A tetrahedral-style nine-accelerometer package with three angular rate sensors (NAP+3ARS) was mounted externally to the skull. The internal sensor was aligned to the Frankfurt plane using measurements of the sensor and anatomic fiducials. The external sensor was similarly aligned, and the head accelerations at the internal sensor location were computed using equations of rigid-body motion.

The internal sensor's efficacy was first verified via a series of non-helmeted, whole-body PMHS tests impacted with a 16 kg pendulum from 1 to 4 m/s. The striking end of the pendulum was a 108 mm polyurethane hemisphere. A 25 mm Ethafoam pad was placed between the impacting surface of the pendulum and the head. The specimen was placed on a rigid seat with the Frankfurt plane oriented horizontally. The head was held in position using masking tape affixed bilaterally from the top of the head to the shoulders. The center of the pendulum contacted the forehead at the mid-sagittal plane superior to the glabella. Head motion was limited to approximately 45 degrees of extension using an angled metal plate with padding to prevent the specimen's premature failure. Table 2.2.1-1 lists the conditions of the whole-body test series. A schematic of the test setup is shown in Figure 2.2.1-1.

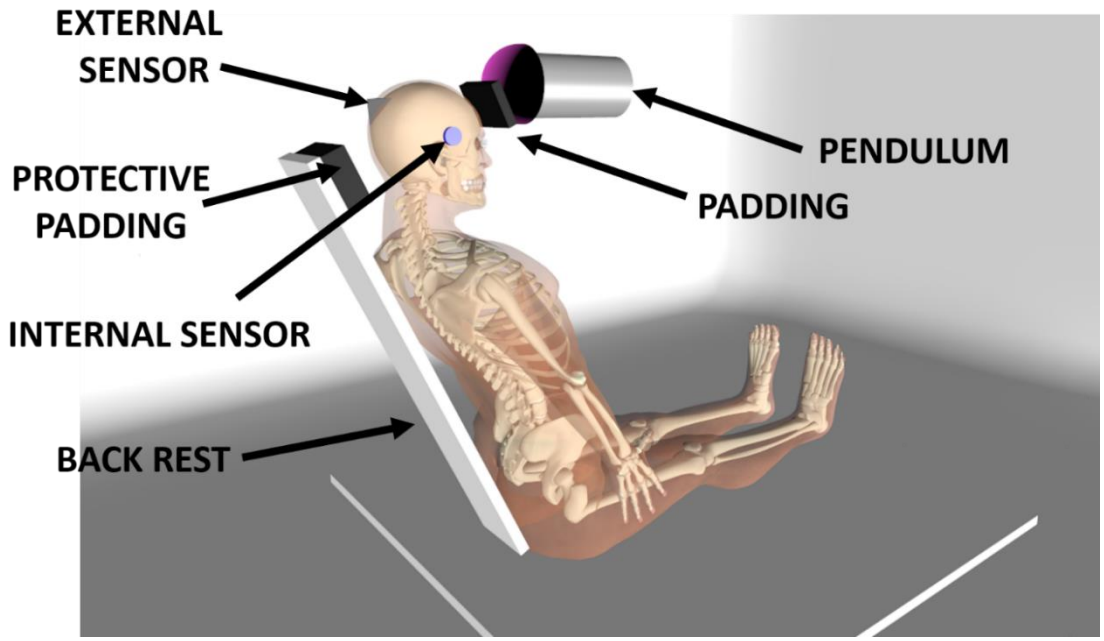

Figure 2.2.1-1: Schematic of whole-body test setup showing PMHS with external and internal sensor, backrest, and pendulum with padding

Table 2.2.1-1: Whole-body PMHS test parameters

Test ID	Impact Location	Impact Speed (m/s)
WB101	Front	1
WB102	Front	2
WB103	Front	3
WB104	Front	4

All reference data were sampled at 20 kHz according to SAE-J211 protocols. Head linear accelerations were digitally filtered at CFC1000, and head angular velocities were filtered at CFC180. A high-speed video camera set perpendicular to the specimen's sagittal plane recorded the impact at 1 kHz.

2.2.2. Isolated Tests

The instrumentation and techniques were refined using the results from the whole-body experiments. An un-embalmed PMHS, isolated from the head to T2, was procured and screened against hepatitis B, hepatitis C, and HIV. Pre-test computed tomography (CT) scans and radiographs were taken to rule out pre-existing trauma, assess specimen quality, and identify anatomic landmarks. Prior to instrumentation, an alignment fixture was attached to the superior cranium. The fixture consisted of an aluminum cylinder, terminated by a 51 mm sphere and welded on the other end perpendicular to a flat plate. The underside of the plate was fixed to the skull via an aluminum stand-off block. Pre-instrumentation CT scans of the isolated specimen with the fixture were obtained.

Three-dimensional reconstruction of the scan was used to measure the Frankfurt plane's orientation and the head's mediolateral axis relative to the alignment fixture.

The spherical end of the alignment fixture was clamped to a rigid platform mount at the base of a single-axis drill. The platform mount had a socket-type joint that allowed rotation of the sphere of the rotation fixture to align the head's M/L axis with the axis of the drill. A small pilot hole was made on the left side of the head at the approximated location of the projected head CG, and the tissue surrounding this point was removed. The M/L axis of the head was aligned with the drill axis using measurements calculated from CT scans. The drill was then used to bore a 35 mm diameter hole through the head from the left to the right side. Brain tissue was evacuated, and a 35 mm (outer diameter) plastic sleeve was inserted along the M/L axis through the head and sealed at the edges using putty. Another hole, approximately 19 mm in diameter, was made at the external occipital protuberance; the specimen was inverted, and the cranium was filled with ballistic gel. The gel was then allowed to set.

Next, a custom-made 25-millimeter-diameter by 136 mm aluminum plug, which had a machined recess at the center for mounting the 6DOF sensor, was inserted through the sleeve. The ends were secured to the head to prevent rotation of the plug. A schematic of the instrumentation and picture of the instrumented plug are shown in Figure 2.2.2-1.

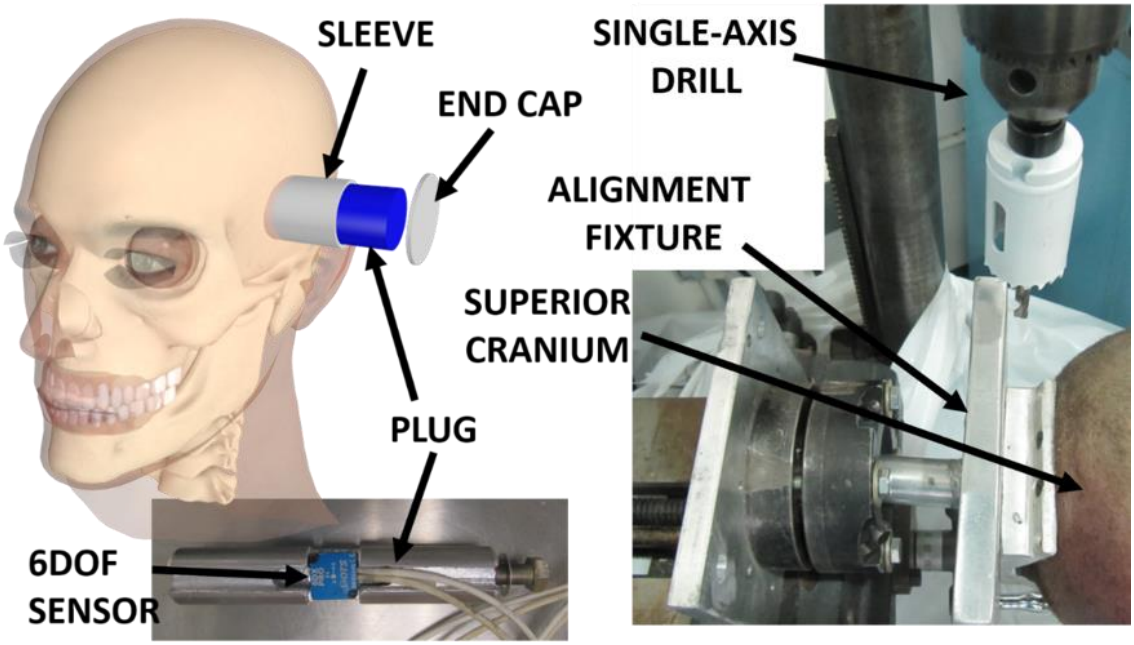

Figure 2.2.2-1: Left is a schematic of the specimen instrumentation showing the locations of the sleeve, plug, and endcap. The bottom left is a picture of the plug with a 6DOF reference sensor. Right is an image of the specimen attached to the alignment plate with a single-axis drill.

The isolated specimen mass (head with brain and neck) before instrumentation was 5.05 kg, and the instrumented mass (head with gel, sleeve, plug, reference sensor, and end caps) was 5.22 kg. The isolated subject's inferior end was potted in polymethylmethacrylate (PMMA) such that the C7-T1 joint was free. After potting, the alignment fixture was removed from the head. Another set of CTs was taken to measure the sensor's position and orientation relative to the Frankfurt plane.

The inferior end of the PMMA block was attached to a six-axis load cell fixed to the top of the mini-sled cart. The cart was attached to precision roller bearings, which could slide freely on two precision rails that were approximately 3.5 m long. The entire mini-sled sat atop a hydraulic lift table to control the pendulum impact location.

Additionally, between the six-axis load cell and cart sat a rotational plate that could adjust the specimen's axial orientation relative to the pendulum. A foam 'catch-device' was placed on the non-struck side to limit head excursion and prevent premature lower cervical spine failure. An advanced combat helmet (ACH) was mounted on the specimen using standard donning procedures adopted for PMHS testing. Each impact was delivered via a rigid-arm mini-sled pendulum device. The pendulum's striking-end consisted of a 2 kg impactor that conformed to National Operating Committee Athletic Equipment (NOCSAE) standards for helmet testing (Standard No. ND081). The total mass of the rigid arm was 19 kg. The head was supported using custom-designed pneumatic cylinders that were released prior to impact to allow the head's free motion. The test setup is shown in Figure 2.2.2-2. The specimen was impacted on the helmet at 3 m/s twice in the anteroposterior direction and once in the lateral direction (Table 2.2.2-1). A uniaxial accelerometer was fixed to the back of the rigid arm pendulum at the level of the impactor. All reference data were sampled at 20 kHz according to SAE-J211 protocols. Impact magnitude was measured using a light-velocity trap. Two high-speed video cameras, one perpendicular to the plane of impact and one approximately 45 degrees oblique to the plane, recorded the impact at 1 kHz. Pre-test radiographs were taken using a digital x-ray to ensure consistency of the specimen's intra-test initial position.

Table 2.2.2-1: Isolated head-neck PMHS test parameters

Test ID	Impact Location	Impact Speed (m/s)
ISO100	Front	3
ISO101	Front	3
ISO102	Left	3

Figure 2.2.2-2: Left is a schematic of the rigid-arm pendulum with mini-sled. Right is a picture of a helmeted surrogate on the mini sled with hydraulic support arms.

2.2.3. Brain Model

Head kinematics computed at the CG from the isolated PMHS tests were applied to the model. Brain injury risk is typically estimated using the CSDM, which is the maximum principal strain calculated as the integration of the deformation tensor rate. It predicts injury by estimating the accumulation of strain damage, which is accomplished by calculating the brain's volume fraction that exceeds a specified strain threshold or critical level. The physical significance of CSDM is that the cumulative volume of brain tissue experiencing tensile strain over this critical level is related to an injury. The best correlation to injury was determined to be CSDM-25, the point at which the brain's volume exceeds a strain threshold of 0.25. The injury risk curves associated with CSDM-25 are shown in Figure 2.2.3-1, where AIS 1 represents mild concussion with no LOC, AIS

2–3 are moderate to severe concussion typically involving LOC, and 4–5 are DAIs, which involve diffuse damage to the axons in the brain and brainstem. CSDM 10, 15, 20, and 25 for the whole brain; left and right cerebellum; left and right cerebrum; and left and right brainstem were computed.

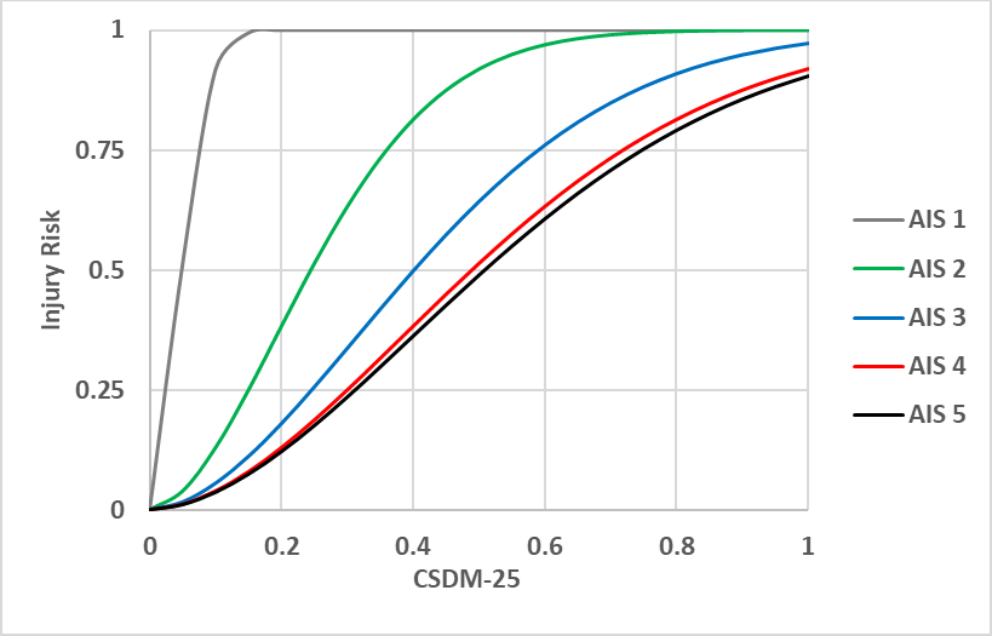

Figure 2.2.3-1: AIS 1–5 injury risk for CSDM-25

2.3. RESULTS

2.3.1. Whole-Body Tests

A comparison of internal and external sensor time-histories in the three axes for linear accelerations and angular velocities from the 4 m/s whole-body pendulum test is shown in Figures 2.3.1-1 and 2.3.1.-2.

The normalized root-mean-square error between the internal and external sensor are compared in Table 2.3.1-1. The maximum and minimum values and times of

attainment for the head kinematics in all three axes are similarly compared for the four whole-body tests in Table 2.3.1-2.

Table 2.3.1-1: Normalized root-mean-square error for the whole-body PMHS tests

	Linear Acceleration			*Angular Velocity*		
	X (%)	Y (%)	Z (%)	X (%)	Y (%)	Z (%)
1 m/s	6.5	27.4	21.7	23.3	4.5	13.3
2 m/s	1.7	13.0	7.9	12.3	1.8	6.7
3 m/s	1.6	7.0	4.2	6.2	1.1	5.3
4 m/s	2.8	6.7	2.8	2.3	0.9	5.0

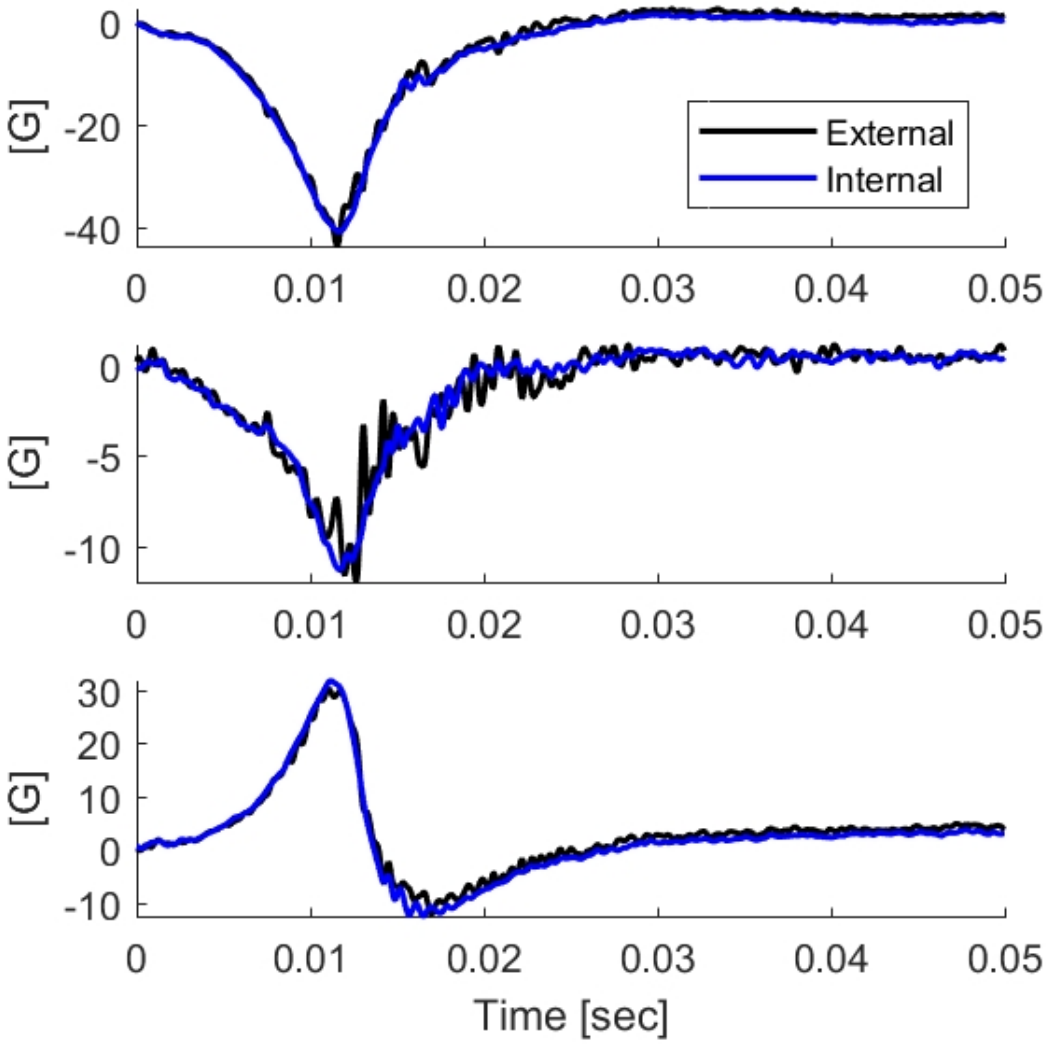

Figure 2.3.1-1: Plots of head linear accelerations for a 4 m/s whole-body pendulum test in the posteroanterior (upper), lateral (middle), and superior-inferior (lower) directions for the internal (blue) and external (black) sensors. The external sensor data were aligned to the Frankfurt plane and calculated at the internal sensor location using equations of rigid-body motion.

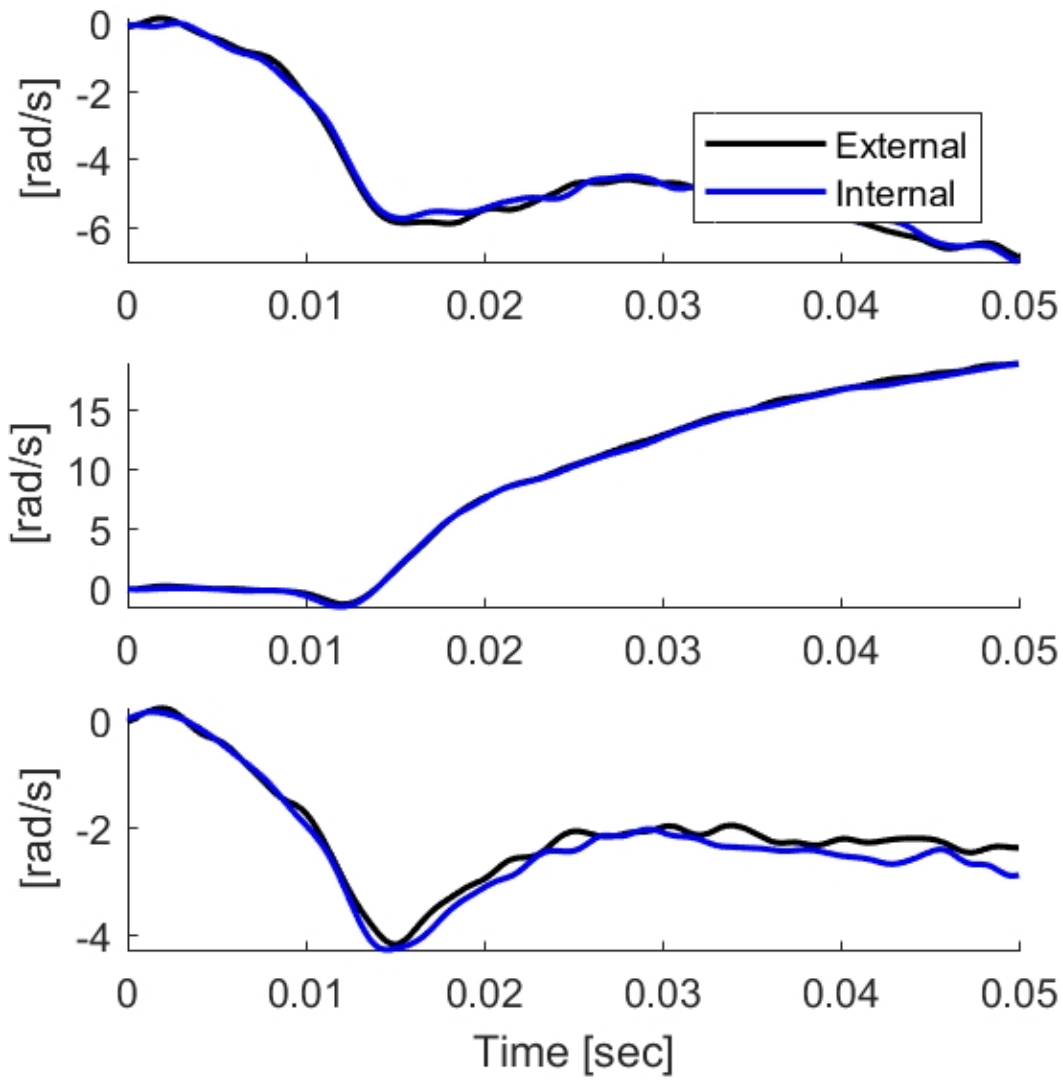

Figure 2.3.1-2: Plots of head angular velocities for a 4 m/s whole-body pendulum test about the posteroanterior (upper), lateral (middle), and superior-inferior (lower) axes for the internal (blue) and external (black) sensors. The external sensor data were aligned to the Frankfurt plane and calculated at the internal sensor location using equations of rigid-body motion.

Table 2.3.1-2: Whole-body maximum and minimum head kinematics for internal and external sensor

			1 m/s		*2 m/s*		*3 m/s*		*4 m/s*	
	Param	Units	Int	Ext	Int	Ext	Int	Ext	Int	Ext
Linear Acceleration	X	Max	g	0.3	0.0	1.5	1.4	3.4	3.4	2.5	1.3
		Time	sec	0.050	0.047	0.038	0.040	0.049	0.050	0.033	0.031
		Min	g	-3.9	-4.0	-15.6	-15.2	-37.9	-36.5	-43.8	-40.9
		Time	sec	0.024	0.023	0.016	0.016	0.015	0.014	0.012	0.012
	Y	Max	g	0.6	0.5	1.3	1.3	4.1	2.0	1.1	0.9
		Time	sec	0.047	0.044	0.015	0.014	0.020	0.024	0.028	0.033
		Min	g	-0.7	-0.6	-1.4	-1.3	-9.2	-8.6	-12.0	-11.3
		Time	sec	0.012	0.027	0.027	0.026	0.015	0.014	0.013	0.012
	Z	Max	g	1.4	0.8	2.8	2.6	15.4	15.1	30.3	31.7
		Time	sec	0.028	0.023	0.013	0.014	0.013	0.014	0.011	0.011
		Min	g	-0.9	-1.2	-1.8	-1.9	-9.2	-7.7	-12.2	-12.6
		Time	sec	0.045	0.048	0.026	0.026	0.020	0.020	0.017	0.017
Angular Velocity	X	Max	rad/s	0.1	0.2	0.7	0.7	0.0	0.0	0.1	0.0
		Time	sec	0.019	0.002	0.017	0.020	0.000	0.004	0.002	0.003
		Min	rad/s	-0.4	-0.4	-0.7	-0.6	-3.3	-3.1	-6.9	-7.0
		Time	sec	0.047	0.045	0.048	0.050	0.018	0.019	0.050	0.050
	Y	Max	rad/s	2.6	2.6	11.2	10.8	18.1	17.9	18.8	18.8
		Time	sec	0.050	0.049	0.050	0.050	0.050	0.050	0.050	0.050
		Min	rad/s	-0.1	-0.1	0.0	0.0	0.0	0.0	-1.4	-1.6
		Time	sec	0.002	0.003	0.001	0.002	0.000	0.001	0.012	0.012
	Z	Max	rad/s	0.1	0.1	0.3	0.2	0.4	0.3	0.2	0.1
		Time	sec	0.002	0.003	0.000	0.003	0.032	0.029	0.002	0.001
		Min	rad/s	-0.7	-0.8	-2.2	-2.4	-2.8	-3.0	-4.2	-4.3
		Time	sec	0.024	0.050	0.050	0.048	0.016	0.017	0.015	0.015

2.3.2. Isolated Tests

A comparison of the reference and wearable sensors linear accelerations and angular velocities for ISO101-103 are given in Figures 2.3.2-1 through 2.3.2-6. When comparing the wearable sensor to the reference sensor, linear accelerations in the primary loading axis (x-axis for 100 and 101 and y-axis for 102) demonstrate the best agreement in magnitude and curve morphology. The wearable z-axis linear acceleration—while in the plane of loading for all three tests—did not match the reference sensor in both magnitude and morphology. The out-of-plane axis (y-axis in 100 and 101 and x-axis for 102) response was less than 10% of the resultant, and, therefore, it is difficult to make relative comparisons. The wearable sensor curve morphology did not match the reference sensor about the y-axis in all three tests for the angular velocities. For the first two impacts (A/P), the reference sensor had a unimodal response, whereas the wearable sensor demonstrated a bimodal pattern. The reference sensor had a sinusoidal response for the lateral tests (ISO102), while the wearable sensor showed a unimodal pattern. While acknowledging the reduced order of magnitude in the two off-axis directions, the wearable sensor response about the x- and z-axes compared the reference sensor well.

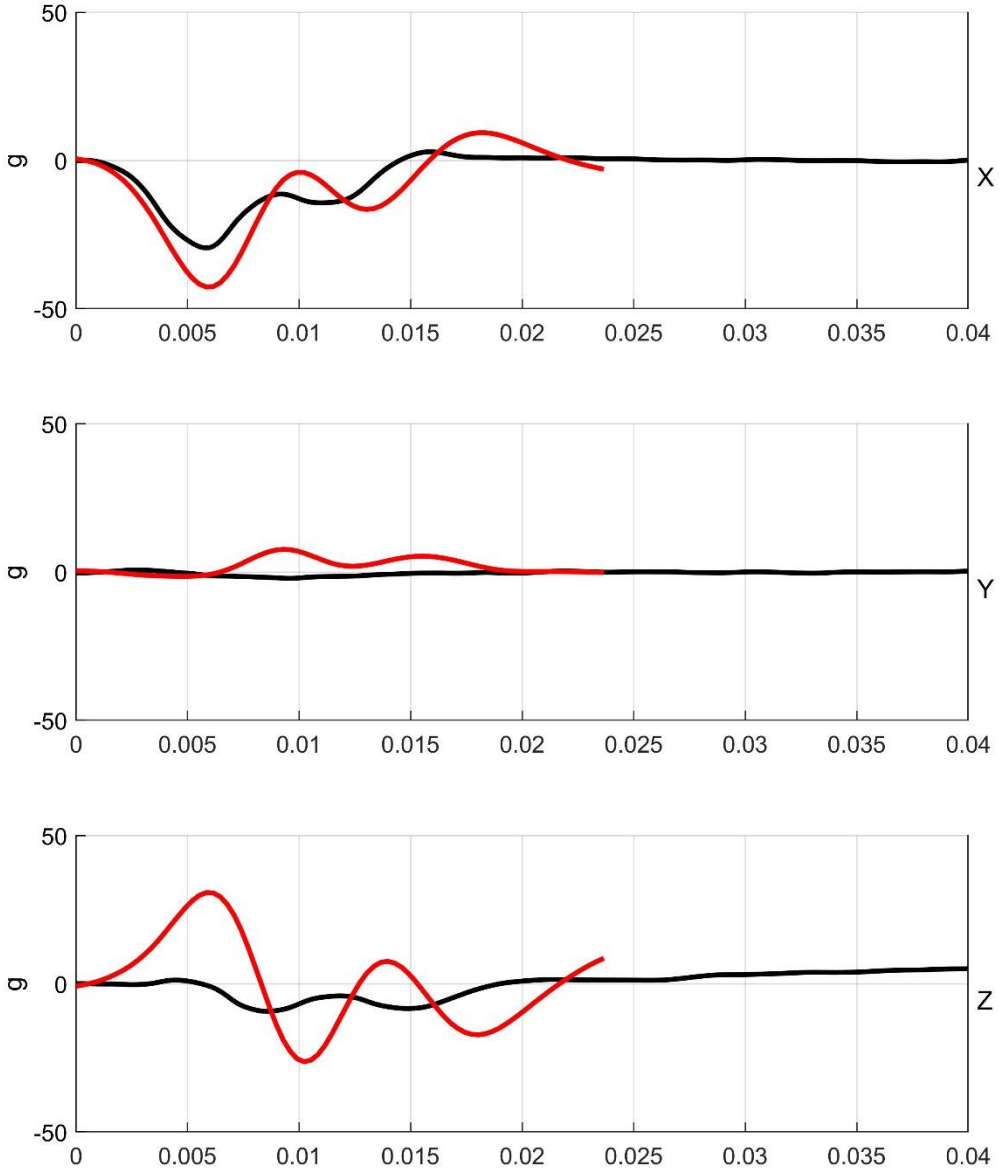

Figure 2.3.2-1: Head linear accelerations in the x (top), y (middle), and z (lower) axes comparing the reference sensor (black) to the wearable sensor (red) for isolated PMHS test ISO100 (3 m/s frontal impact).

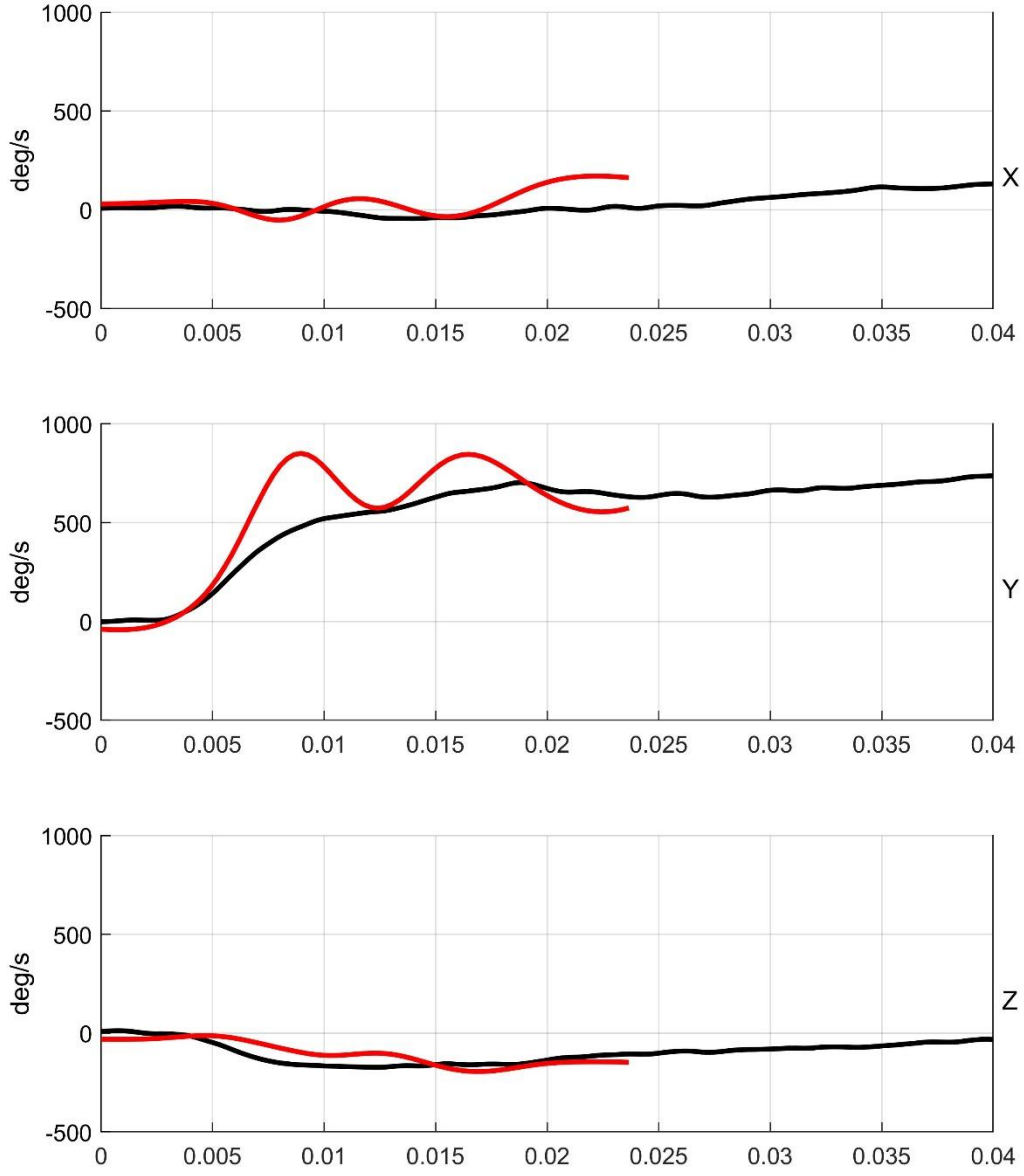

Figure 2.3.2-2: Head angular velocities in the x (top), y (middle), and z (lower) axes comparing the reference sensor (black) to the wearable sensor (red) for isolated PMHS test ISO100 (3 m/s frontal impact).

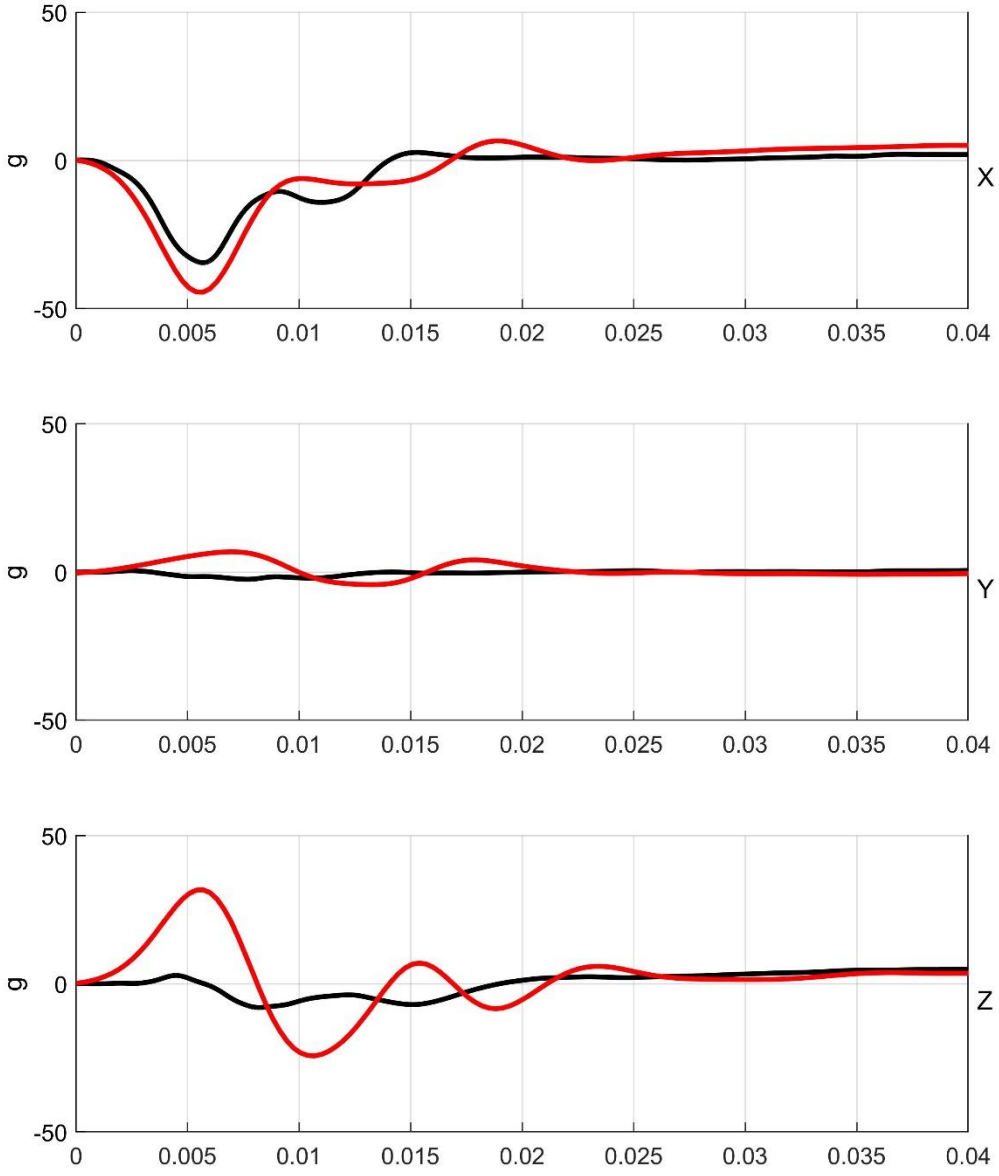

Figure 2.3.2-3: Head linear accelerations in the x (top), y (middle), and z (lower) axes comparing the reference sensor (black) to the wearable sensor (red) for isolated PMHS test ISO101 (3 m/s frontal impact).

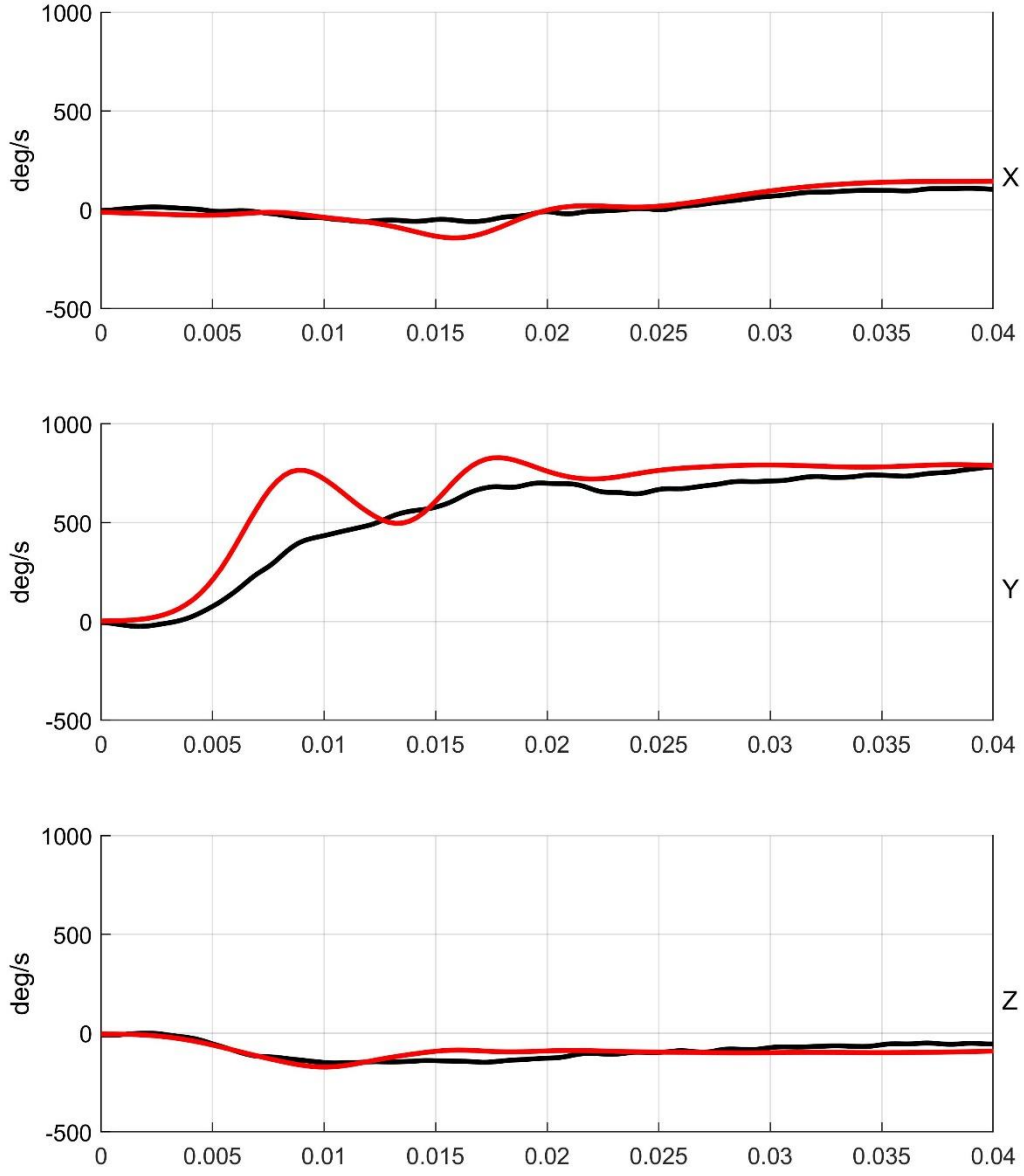

Figure 2.3.2-4: Head angular velocities in the x (top), y (middle), and z (lower) axes comparing the reference sensor (black) to the wearable sensor (red) for isolated PMHS test ISO101 (3 m/s frontal impact).

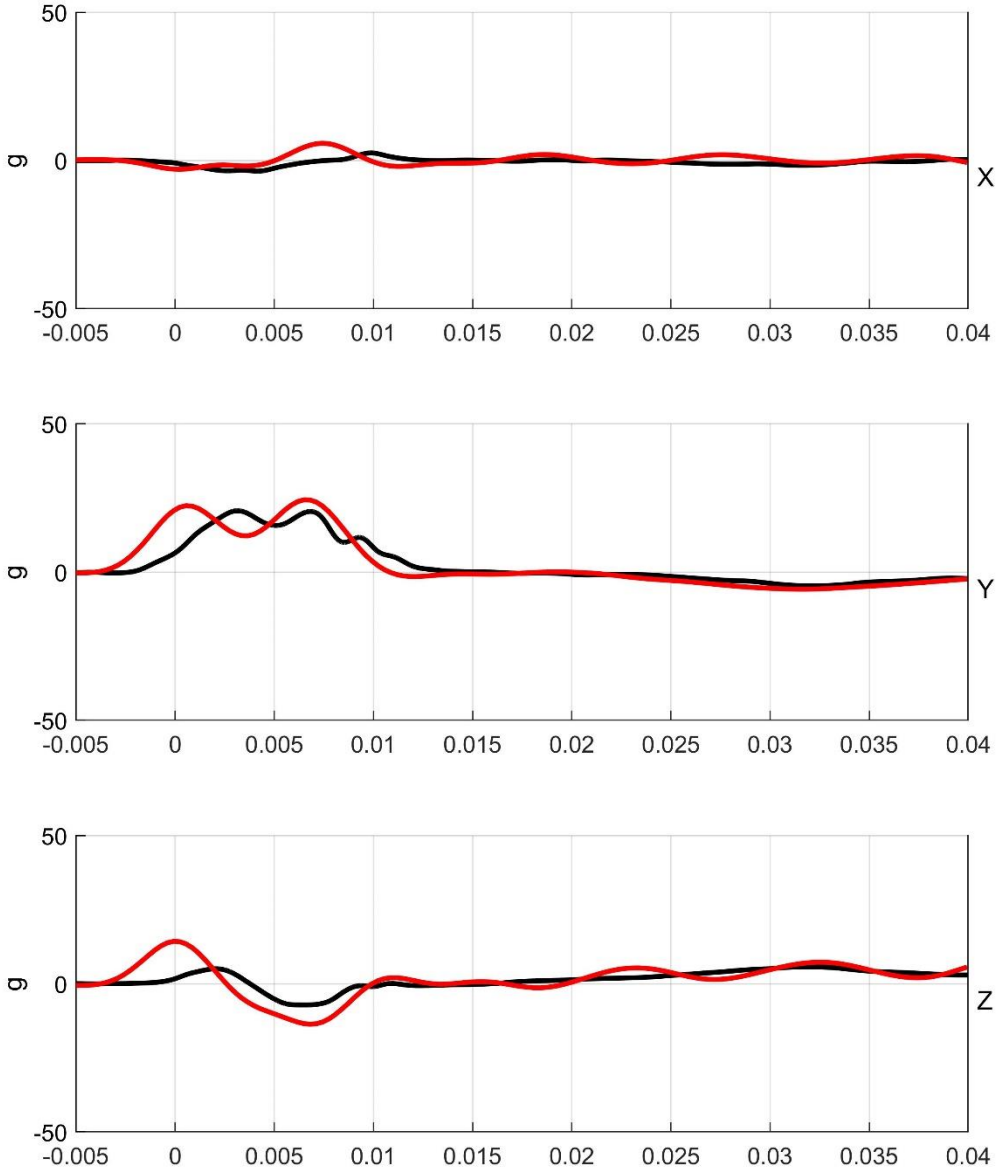

Figure 2.3.2-5: Head linear accelerations in the x (top), y (middle), and z (lower) axes comparing the reference sensor (black) to the wearable sensor (red) for isolated PMHS test ISO102 (3 m/s lateral impact).

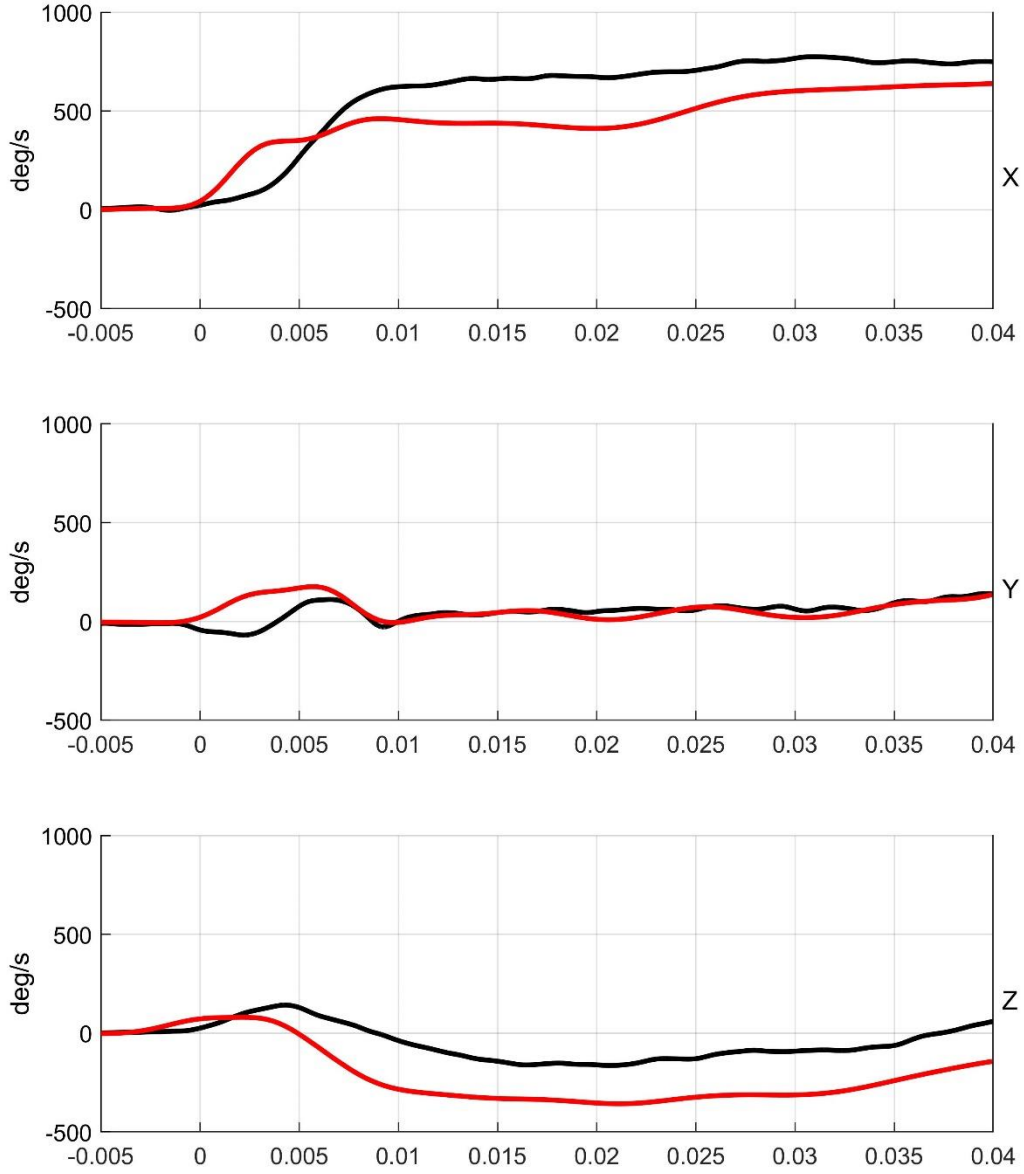

Figure 2.3.2-6: Head angular velocities in the x (top), y (middle), and z (lower) axes comparing the reference sensor (black) to the wearable sensor (red) for isolated PMHS test ISO102 (3 m/s frontal impact).

2.3.3. Computational Model

Peak CSDM 10, 15, and 20 (CSDM25 was zero for all locations and tests) are shown in Figures 2.3.3-1 through 2.3.3-3 for the three isolated tests. Individual bar charts represent the metrics for the whole brain (Tot), right and left cerebrum (CBR-R and CBR-L), right and left cerebellum (CBL-R and CBL-L), and right and left brainstem (BR-R and BR-L). For the CSDM10, the ISO100 (frontal) and ISO102 (lateral) showed nearly the same peak values for the whole brain, while ISO101 (frontal) was lower than the other two. Most of the volume exceeding CSDM10 was in the left and right cerebrum for all three tests.

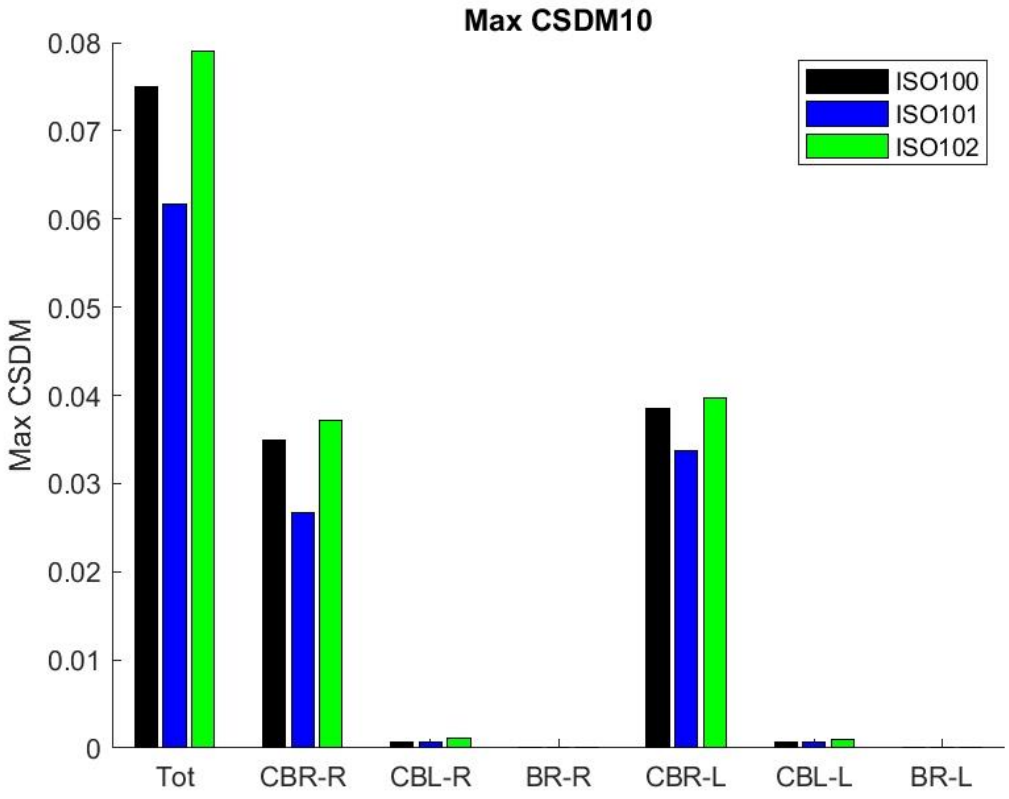

Figure 2.3.3-1: Peak CSDM10 calculated from the SIMon model of the brain for the three isolated tests. Individual bar charts are shown for the whole brain (Tot), right cerebrum (CBR-R), left cerebrum (CBR-L), right cerebellum (CBL-R), left cerebellum (CBL-L), right brainstem (BR-R), and left brainstem (BR-L). The model input was from the reference sensor. Black indicates ISO100, Blue ISO101, and green ISO102.

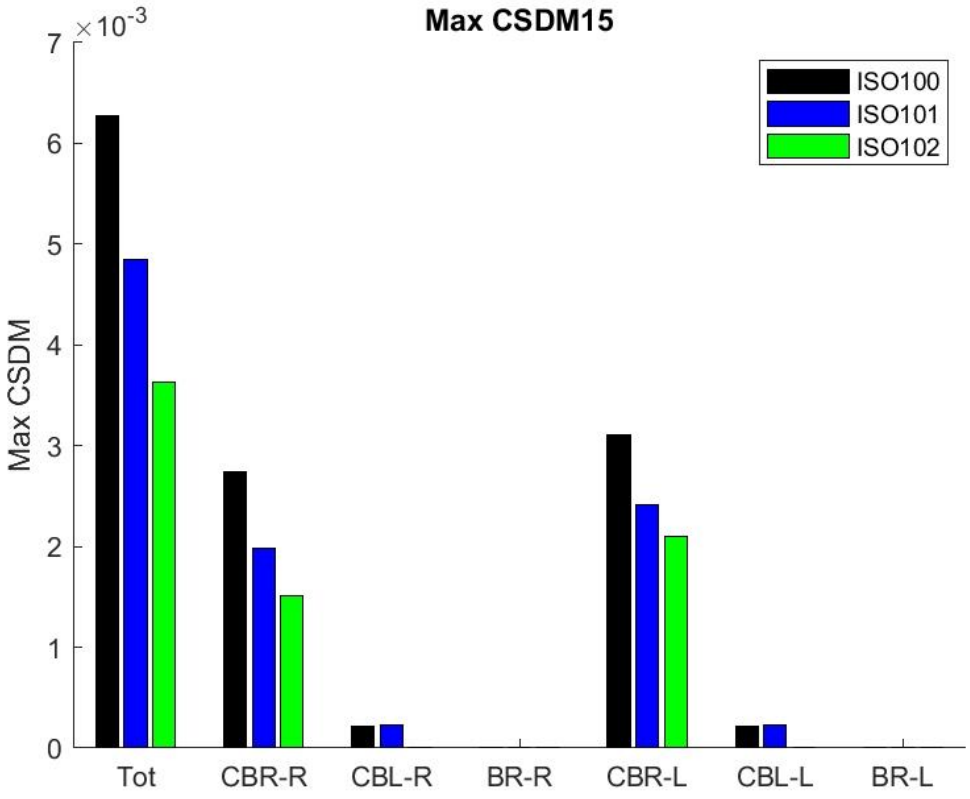

Figure 2.3.3-2: Peak CSDM15 calculated from the SIMon model of the brain for the three isolated tests. Individual bar charts are shown for the whole brain (Tot), right cerebrum (CBR-R), left cerebrum (CBR-L), right cerebellum (CBL-R), left cerebellum (CBL-L), right brainstem (BR-R), and left brainstem (BR-L). The model input was from the reference sensor. Black indicates ISO100, Blue ISO101, and green ISO102.

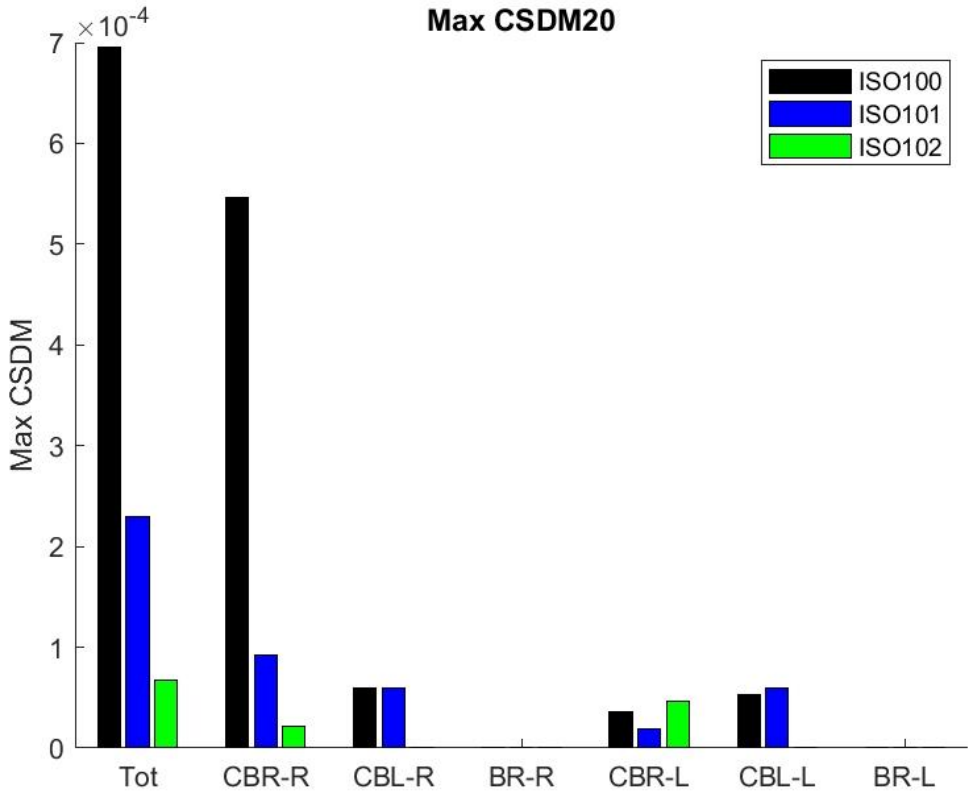

Figure 2.3.3-3: Peak CSDM20 calculated from the SIMon model of the brain for the three isolated tests. Individual bar charts are shown for the whole brain (Tot), right cerebrum (CBR-R), left cerebrum (CBR-L), right cerebellum (CBL-R), left cerebellum (CBL-L), right brainstem (BR-R), and left brainstem (BR-L). The model input was from the reference sensor. Black indicates ISO100, Blue ISO101, and green ISO102.

2.4. DISCUSSION

Head CG linear accelerations are an important metric used in estimating the risk of head fracture and brain injury. Current Federal Motor Vehicle Safety Standards (FMVSS) developed by NHTSA use the resultant head CG linear acceleration to estimate head injury risk. In ATDs, triaxial accelerometers are placed within the skull at the anatomically equivalent head CG location and can directly measure head CG linear accelerations. However, the accurate measurement of these accelerations in PMHS is significantly more challenging. Typically, sensor package(s) are mounted externally to the skull, measurements are made relating the sensor's position to anatomic fiducials, and equations of rigid-body motion are used to calculated head CG accelerations. One study used a tetrahedral-style NAP+3ARS to measure head CG accelerations in PMHS [45]. This instrumentation set was later refined with the development of a 6aw package by Kang et al. that consisted of six linear accelerometers and three angular velocity transducers [46]. While both packages have been shown to accurately calculate head CG linear acceleration, externally mounted transducers are not practical when conducting helmeted PMHS tests. Mounting these sensor packages inside the head would not be feasible due to their size. Their installation would require the removal of large sections of the cranium, thereby compromising the skull's strength and biofidelity. An ideal method for measuring head CG linear accelerations for helmeted PMHS tests is to honor the ATD head instrumentation concept but place the accelerometers at/near the head CG. This is the primary motivation/rationale for the development of the current experimental methodology.

The whole-body PMHS test series's goal was to confirm the accuracy of the internal sensor using the externally mounted nine-accelerometer package. Curve morphologies of the internal sensor essentially overlapped in all three axes for the linear accelerations and angular velocities with the calculated traces from the external sensor. Peak values and times of attainment demonstrated good agreement at tests above 1 m/s. Above 2 m/s, the normalized root mean square error was below 5% for the sagittal plane kinematics (x and linear accelerations and y angular velocity). Less agreement was observed in the off-axis directions. The head linear accelerations were computed from the external nine-accelerometer package using techniques from Padgaonkar et al. [47]. The differences in the signals between computed and directly measured head CG accelerations found in the current study have also been observed in others [3].

This study also highlighted the difficulties in placing the sensor near the head CG, as well as the need for more refined techniques and instrumentation. The internal sensor was placed by seating the specimen on a flat bench with the thorax and head supported such that the Frankfurt plane was parallel to the ground. An electric hand drill was used to bore a hole from right to left long the medial-lateral axis that was estimated from the external auditory meatuses' position. The sensor y-axis was approximately 10 degrees from the medial-lateral axis about the z-axis (right side of aluminum cylinder more forward than the left) and 5 degrees about the x-axis (right side of aluminum cylinder higher than the left). The cylinder's misalignment from the medial-lateral axis led to the lateral protrusion of the cylinder. The ends were not

parallel to the cranium's outer surface, and non-uniform external fixation of the cylinder to the skull.

Several factors make mounting a sensor inside the head near the CG difficult. First and foremost, there is no flat boney surface within the head at the location of the CG; thus, the sensor must be rigidly suspended above the cranial vault. This was accomplished in the isolated tests by fabricating an aluminum plug with recessed space in the center to accommodate the 6DOF sensor. The outer ends of the plug were tapped such that the sensor position could be aligned with the center of the head using ½" adjustment bolts lateral to the external cranium. Two aluminum plates were attached to the skull—one on either side of the head—using bone screws, and the plug was rigidly fixed to the skull using the ½" adjustment bolts. The plug's position was carefully selected to coincide with the mediolateral axis of the head near the head CG as measured from the auditory meatus. Pre-instrumentation CT scans were used to select a place within the head that was near the head CG but did not interfere with the dorsum sellae of the sphenoid bone. A 35 mm diameter cylindrical model was created and placed within a three-dimensional model of the head using 3DSlicer (slicer.org). The cylinder was placed as close as possible to the approximate head CG location, and the center of cylinder ends was marked on the left and right side of the skull on the model. Measurements were taken of the alignment plate so that these points could be transcribed to the head.

Another issue when placing a sensor in the head is replacing the internal contents of the cranium cavity. In the isolated tests, once the hole was drilled through

the skull's M/L axis and before inserting the aluminum plug, the contents of the skull were emptied, as the post-mortem consistency of the brain does not resemble *in situ* characteristics. The ballistic gel was used as a surrogate for the brain. To fill the cranial space, the specimen was inverted (head down, neck up), and a small hole was drilled at the base of the skull. A 35 mm diameter plastic sleeve was inserted through the head's M/L axis to keep the gel from flowing out of the holes on the lateral sides of the head. The gel was then poured and allowed to set overnight. This technique minimized air pockets and maintained an open space for the aluminum plug and sensor placement.

The use of the gel paralleled previous head injury studies in automotive and military literature [48], as replacing the intracranial contents with this simulant removes air from the cranium—as air is normally present in PMHS specimens—rendering improved handling of the specimen while maintaining the skull's structural integrity. Pre-test instrumented CT scans were used to verify that the gel filled the interior cranium (except for the volume inside the plastic sleeve). These processes render the specimen preparation more in line with the normal brain-skull medium. Because of the lack of air gaps within the cranium, any brain motion that might occur due to external loads—inertial or contact—is eliminated, rendering the experimental preparation a better-controlled test condition.

Accurate placement of the plastic sleeve and aluminum plug insert along a M/L axis was an important instrumentation goal. This was controlled by carefully measuring the pre-instrumentation CTs and transcribing these orientations to the fixture at the base of the single-axis drill, thereby aligning it with the head's M/L axis. The technique

was successful, as the anteroposterior and superoinferior deviations of the sensor axes were less than 2 degrees. Significant deviations of the plug from the M/L axis would make it harder to control the sensor's placement to its target position. The head sensor's final position was within 1 mm of the center of the head and within 3 mm of the targeted sagittal plane position. Additionally, the plug's misalignment with the M/L axis may cause protrusion of the aluminum end plates that fix the plug to the skull. In a severe case, this could also lead to asymmetry in the sagittal plane and affect the head's response.

The largest difference in alignment occurred about the M/L axis. It should be noted that this was not due to the error in aligning the drill but rather a rotation of the plug inside the plastic sleeve about the M/L axis prior to fixing the plug to the skull with the aluminum endplates. It should also be noted that the sensor data is aligned mathematically to the anatomic reference frame using the rotation matrix calculated from the instrumentation CT scan. Deviation of the sensor coordinate system from the anatomic system can be corrected regardless of the offset; however, from a signal perspective, the rotation misalignment about the M/L axis does not affect the measured head kinematics quality. Thus, this difference in the M/L axis should be expected. More importantly, it is not an issue if the above points are addressed during the analysis conducted in the postprocessing phase of the experimentally gathered data.

There are other points to consider before fully evaluating helmet and head-based wearable sensors. One issue is the resonant frequency of the head, head and helmet, and reference sensor. While the resonant frequency of the head/skull has been

reported in the literature (approximately 900 Hz) [49], there was no indication that the head impacts in the current study caused the head to resonate as the frequency response of the NAP in the whole-body test and the internal sensor in the internal test were well below 900 Hz. Additional characterizations of the head response to increasing loading rates are necessary, and this is a topic of future research.

It should be noted that the CG location of a PMHS head is not known *a priori*, as the experimental model included an intact head-neck complex. Determination of the head mass properties requires disarticulation at the level of the occipital condyles, which compromises the integrity of the specimen. The estimation of the CG was made with respect to the auditory meatus. It should be noted that variations exist in the contours of the periphery of the head and the internal structures. Additional tests are needed to refine the estimation technique.

The head kinematic data obtained using novel experimental techniques were shown to be adaptable to a computational model, enabling extraction of regional and component brain injury metrics. As the Simon model has been used extensively in automotive crashworthiness, the present experimental outputs were used to exercise this model. Metrics including CSDM10, CSDM15, CSDM20, and CSDM25 were below injury thresholds, which is not surprising given the magnitude of impact and the helmeted test condition. CSDM25 values were zero for all brain locations and tests. In animal models, this metric has been shown to correlate with DAI [37]. CSDM10 may be more appropriate for this test condition as it has been shown to correlate with injury in helmeted athletes [50]. In these experiments, CSDM10 magnitudes were still well below

injury thresholds.

The CT-based techniques described in this study provide a detailed methodology for researchers to adopt regarding inserting a 6DOF sensor in an intracranial cavity. This type of instrumentation is needed to evaluate wearable sensors in the military and athletic environments and the automotive field, where the impact location is uncertain (i.e., rollovers, pedestrian impact). Additionally, non-standard positions in future automotive seating environments may need this type of experimental approach to properly validate human body models for evaluating crashworthiness and advancing safety in automated vehicles.

2.5. SUMMARY

- Wearable sensors are actively being used to quantify head exposure in sport and military environments.
- Studies to quantify the accuracy of these sensors have been conducted using ATD but lack important biofidelic boundary conditions.
- PMHS tests are critical in evaluating the efficacy of any wearable helmet- or head-mounted sensor.
- PMHS head kinematics are typically calculated using sensors fixed to the cranium, palate, or ear canal, locations which may interfere with and cannot be used to assess accuracy of the wearable sensors.
- Recognizing the need to accurately measure head kinematics to predict brain injuries in sport and military situations wherein PPE is used, a novel experimental

design was developed to instrument the PMHS head with the sensors within the cranium.

- The internal sensor position was carefully controlled by using a pre-test CT scan to accurately place the sensor near the head CG along the mediolateral axis.
- The CT-based instrumentation technique demonstrated its value to future experimentalists, as the CG kinematics from the internal sensor matched well with the computed CG kinematics from externally placed sensors commonly used as the standard in impact biomechanics tests.
- Data from the reference sensor were used as input to an NHTSA-developed computational model of the brain to compute regional brain injury metrics (CSDM).
- Controlled tests with a PMHS-helmet system proved the effectiveness of the novel experimental design
- Tests are being conducted in our laboratory to evaluate wearable sensors' accuracy that measure head exposure for sport and military applications.

CHAPTER 3. DESIGN OF AN EXPERIMENT TO INDUCE NON-PLANAR LOADING TO THE LUMBAR SPINE

3.1. INTRODUCTION

3.1.1. Background

Historically, the Federal Aviation Administration (FAA) has regulated aircraft emergency landings by requiring seat and restraint systems to protect occupants due to vertical and longitudinal crash forces. Occupant protection standards in the Title 14 Code of Federal Regulations parts 25.562 and 25 have decreased fatality rates in lower commercial airline environments and increased survivability from airplane crashes [51]. The number of fatalities per million flight hours between 1983 and 2000 was less than 0.1 per year, with a crash survival rate of 96% for airline occupants [52].

The aviation industry is changing the traditional side-by-side parallel row seating configuration currently in most commercial airlines. Alternate seat positioning includes mounting the seat at an angle relative to the centerline of the aircraft. Obliquity allows airlines to optimize space and more efficiently add passenger seating room and increase comfort. The FAA-regulated standards were originally designed to protect occupants in seats mounted in forward (aligned with the aircraft centerline, ± 18°) and aft (rotated 180°, ± 18°, about the aircraft centerline) positions [51]. The introduction of newer seats/seating configurations installed from 18 through 45 degrees from the centerline of the aircraft presents unique challenges because occupant kinematics, loading, and potential for injury in emergency landing scenarios differ from the traditional pure forward- or aft-facing seats.

As a result, the FAA designed a research program simulating the aviation environment to examine the potential for injuries to the human body from lateral impacts and to establish new safety standards for side-facing seats. The goal is to provide the same level of protection for side-facing seats as is achieved for the current forward- or aft-facing seats. Early results are available [53-55]. Human neck tension force, lateral neck moment, and leg rotation injury criteria for side-facing seats have been developed based on these studies [56].

The FAA has initiated a similar program to examine occupant loading and injury in obliquely oriented seats to understand the mechanism of injury to different body regions and develop human tolerances under the multi-axis loading condition induced due to obliquity. Many previous studies have been conducted using PMHS in pure lateral and oblique side impacts [13, 57-64]. However, they are primarily applicable to automotive environments and relatively lower changes in velocities (ΔV) than the FAA-regulated pulse [51].

3.1.2. Objectives

The present exploratory study's objectives were to conduct oblique-impact sled tests using whole-body Post Mortem Human Surrogates (PMHS) with a focus on the aviation application and (V and describe injuries/patterns injury mechanisms and associated kinematic measures of different body regions. Another objective is to design an isolated PMHS experimental model that replicates the injuries observed in the whole-body tests.

3.2. METHODS

3.2.1. Whole-Body Sled Tests

3.2.1.1. PMHS Procurement and Preparation

The local Institutional Review Board approved the test protocol, and the study was conducted in a hospital environment using standard precautions for handling blood-borne pathogens. The population for this study was designed to represent adult 50th-percentile males. Two embalmed PMHS were procured and screened to rule out hepatitis B, hepatitis C, and HIV. Pre-test CT scans and radiographs were taken to rule out pre-existing trauma, assess specimen quality, and identify anatomic landmarks and musculoskeletal components. Bone mineral density was obtained from CT scans [65, 66]. The specimens were dressed in tight-fitting leotards, gloves were used on the hands, and masks covered the heads and facial features.

3.2.1.2. PMHS Instrumentation

The PMHS were instrumented with:

- Head→ Tetrahedral nine-accelerometer package with three angular rate sensors (t-NAP+3ARS)
- T1→ Six-degree-of-freedom (6DOF) sensor (triaxial linear accelerations and triaxial angular velocities)
- T6→ 6DOF sensor
- T12→ 6DOF sensor
- Sacrum→ 6DOF sensor

All sensor data were sampled at 20 kHz according to SAE-J211 standards [67].

Sets of at least three non-collinear retroreflective markers were fixed at the same anatomic positions as the 6DOF sensors to obtain kinematic data. Sensor and marker instrumentation is shown in Figure 3.2.1.2-1.

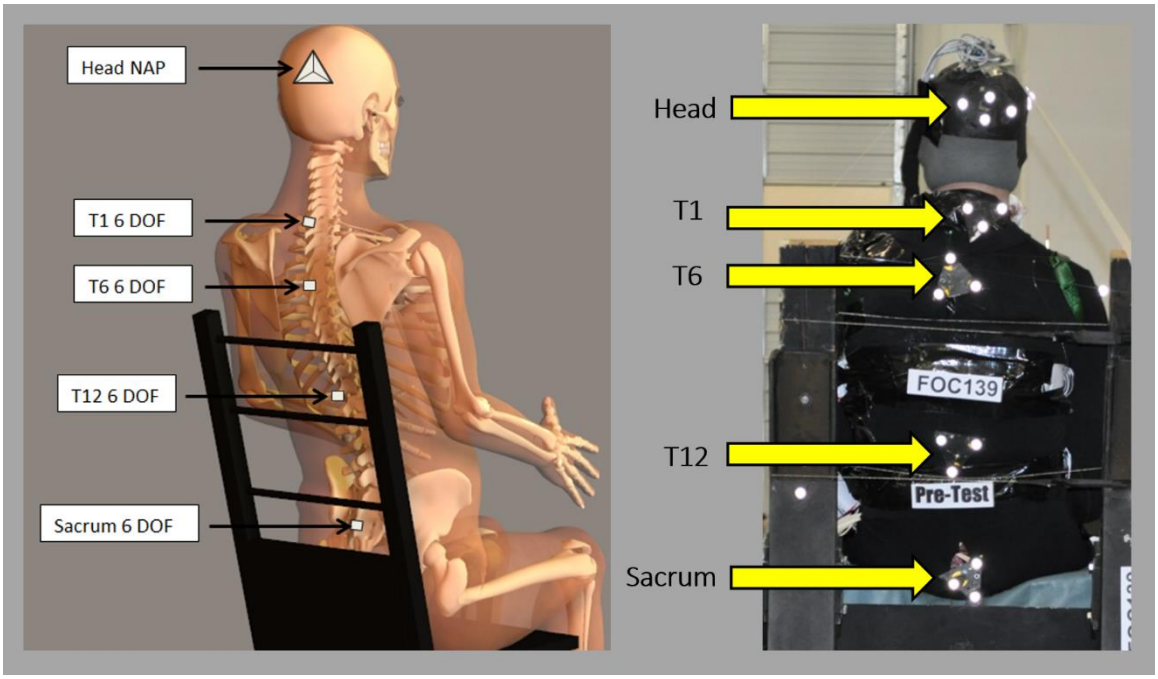

Figure 3.2.1.2-1: Left is a schematic of the sensor instrumentation on the head, spine, and sacrum. Right shows a pre-test picture of the marker plates at the same anatomic locations.

3.2.1.3. Boundary Conditions

A buck was fabricated to replicate the boundary conditions from previous FAA Civil Aerospace Medical Institute (CAMI) ATD sled tests. The buck was designed to represent a generic obliquely mounted seat in the aviation environment and was based on a survey of seat manufacturers conducted by CAMI. The oblique seat was fixed to a sled and oriented with the seat centerline at 45 degrees to the primary load vector such that the loading was aligned with the right anterolateral aspect of the occupant. This condition represented a worst-case scenario—torso flail associated with poor retention

of the shoulder belt (or no shoulder belt) while the pelvis and lower extremities are restrained by the surrounding component(s) of the oblique seat. The tests used two lap belts to restrain the pelvis: the first, a body-centered belt similar to the side-facing seats' lap belt, and the second, a more standard frontal lap belt used in commercial aircraft. Additional belts were used to restrain the femurs and tibiae and minimize pelvic axial rotation and lower extremity motion. Figure 3.2.1.3-1 shows the dual lap belt anchors' locations and path of the belts on the occupant. The femur and foot restraints are also shown.

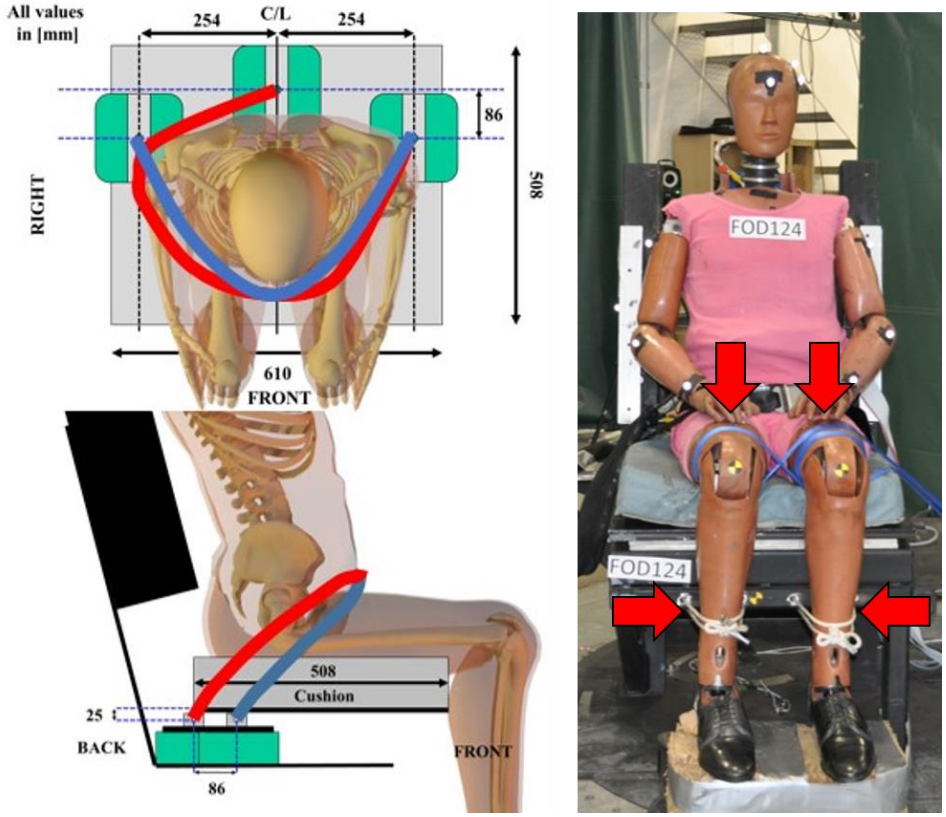

Figure 3.2.1.3-1: Left shows a schematic of the path of the double lap belt restraint. The red belt is the body-center belt while the blue is the standard frontal lap belt in an aircraft environment. Right is a pre-test picture of an ATD positioned on the sled and highlighting the lower-extremity restraints.

3.2.1.4. Sled Instrumentation

A uniaxial accelerometer was mounted to the base of the sled to determine the change in velocity (ΔV). Triaxial load cells were placed at the three belt anchor locations. Load cell locations are shown in Figure 3.2.1.4-1.

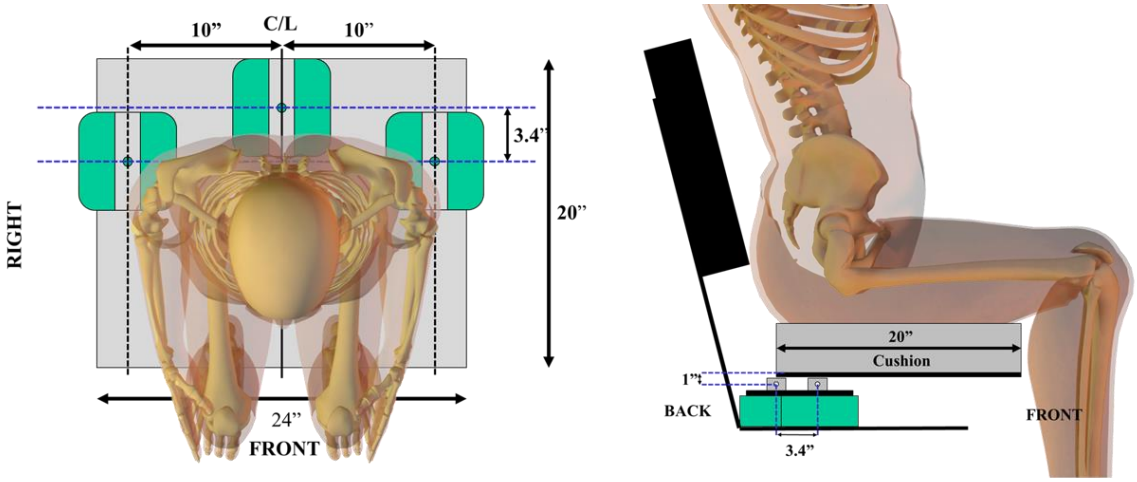

Figure 3.2.1.4-1: Left is an overhead schematic of the seat showing the seat belt load cells' locations. Right is a lateral view.

3.2.1.5. Sled Pulse

Sled acceleration was applied to the base of the buck via a servo acceleration sled (Seattle Safety, Seattle, WA) and recorded by a uniaxial linear accelerometer. Two pulses were used for the current study. The first test's change in velocity targeted the FAA emergency landing dynamic condition for horizontal impact [51] and was 13.7 m/s. The input of the second test was scaled in magnitude by 61% and was 8.3 m/s. Figure 3.2.1.5-1 shows both pulses.

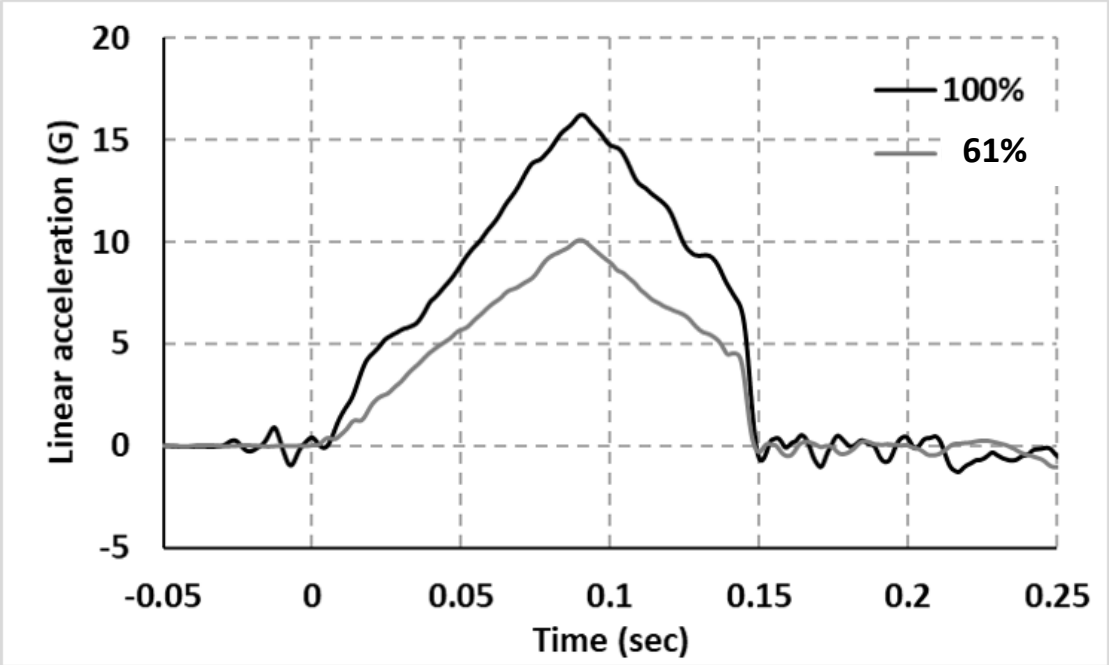

Figure 3.2.1.5-1: Input pulse for the 1st (100%) and 2nd (61%) PMHS tests

3.2.1.6. Test Matrix

Table 3.2.1.6-1: Sequential Test Matrix

Test ID	Orientation	Pulse	Spec ID
FOC104	45-degee right-side impact	High	HS679
FOC117	45-degee right-side impact	Low	HS676

3.2.1.7. Pre-Test Posture

The specimens were placed with the mid-sagittal plane of the pelvis on the centerline of the seat. Feet were placed on supporting blocks so that the ankle joint was in neutral alignment and there were 90 degrees of flexion at the hip and knee joints. Femurs and tibias were oriented parallel to the mid-sagittal plane. The head was positioned with the Frankfurt plane oriented horizontally with no axial rotation.

3.2.1.8. Data Collection

Analog data was collected with a data-acquisition system (DTS, Seal Beach, CA) at 20 kHz as per SAEJ211 (Dec. 2014). Occupant motion was captured with a 27-camera motion-capture system (Vicon, Oxford, UK) at 1000 Hz. The coordinate systems were consistent with SAE J211 (2014) and are described in Section 3.2.1.11.1. The high-speed video was collected at 1000 fps from 3 cameras (IDT, Pasadena, CA). Standard photographs were taken of PMHS instrumentation and pre-and post-test positions on the sled.

3.2.1.9. PMHS Post-Test Evaluations

Standard and functional radiographs and CT images were obtained to identify injuries. A forensic pathologist conducted a detailed autopsy and documented the pathology of each specimen.

3.2.1.10. Data Processing

3.2.1.10.1. CT Scan/CMM Measurements

The three-dimensional position of the markers and anatomic fiducials were determined using 3D-Slicer images derived from CT scans and CMM data of the specimens. For the head, the relationship between the anatomic points and markers were determined from CMM measurements. The left and right superior auditory meatus and the inferior margin of the left and right orbit were digitized, along with the tetrahedral NAP boundaries. The projected center-of-gravity of the head on the left and right lateral aspect of the cranium were also digitized after the event.

Pre-test CT scans were taken prior to mounting the sensors and markers on the PMHS; thus, the markers' positions on the sacrum and at T12 were estimated from the

instrumentation photos. To define the anatomic coordinate system at T12, four points were collected on the vertebra's superior and inferior surfaces at the ventral and dorsal locations in the mid-sagittal plane and right- and left-most lateral points on the transverse plane. Points on the superior aspect of the left and right inferior surface of the vertebral notch were also identified.

Four points were collected at the sacrum on the superior surface of the vertebra at the ventral and dorsal locations in the mid-sagittal plane and right- and left-most lateral points on the transverse plane. Points on the superior aspect of the left and right inferior vertebral notch were also identified. The centers of the retroreflective targets at both T12 and the sacrum were estimated from instrumentation photos and measurements obtained from the mounts and marker plates.

3.2.1.11. Anatomic, Seat, and Marker Transformation Matrices

Transformation matrices for each sensor and marker group relative to the local anatomic coordinates were determined by:

1. calculating the local anatomic coordinate system from CT or CMM points,
2. calculating the 4 X 4 local anatomic to global (CT/CMM space) transformation matrix,
3. calculating the local sensor coordinate system from CT/CMM points,
4. calculating the 4 X 4 local sensor to global (CT/CMM space) transformation matrix,
5. calculating the local marker coordinate system from CT/CMM points,
6. calculating the 4 X 4 local marker to global (CT/CMM space) transformation matrix,
7. multiplying 2 and 4 (inverted) to determine the anatomic-to-sensor transformation matrix, and

8. multiplying 2 and 6 (inverted) to determine the anatomic-to-marker transformation matrix.

Details are given in the following sections.

3.2.1.11.1. Coordinate Systems

3.2.1.11.1.1. Head local coordinate system

The head coordinate system was defined by taking midpoints of the left and right orbit and the left and right auditory meatus. A reference vector was created by subtracting the mid-orbit point from the mid-auditory point. The +y axis was determined by subtracting the right auditory meatus point from the left, the +z by crossing the reference vector with the +y axis, and the +x axis by crossing the +z axis with the +y axis. The head anatomic system's origin was calculated by averaging the projected left and right center-of-gravity points on the cranium.

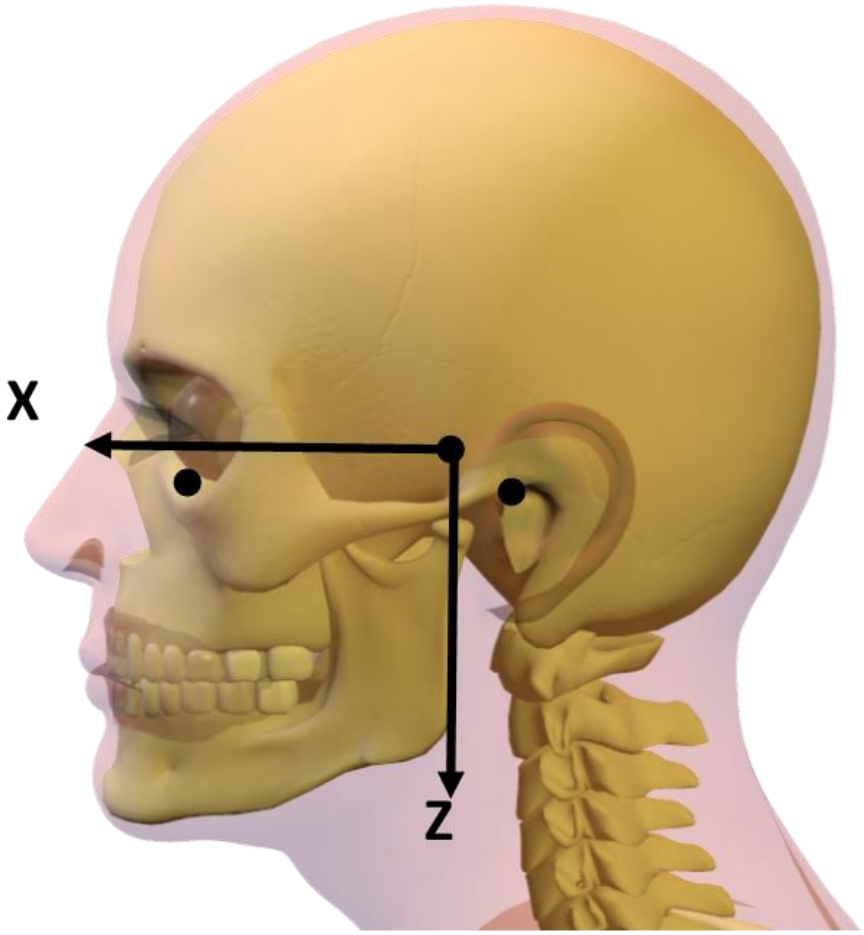

Figure 3.2.1.11.1.1-1: Head coordinate system with the origin at the center-of-gravity. The x-y plane is parallel to the Frankfurt plane. The +z-axis runs superior to inferior and is perpendicular to the x-y plane.

3.2.1.11.1.2. Spine local coordinate system (T12)

The center of the superior endplate was determined by averaging the four points on that surface. The inferior endplate center was likewise calculated. A reference vector was created by subtracting the inferior endplate center point from the superior endplate center point. The +y axis was determined by subtracting the right vertebral notch point from the left vertebral notch point, the +x axis by crossing the +y axis with the reference vector +z axis by crossing the +x axis with the +y axis. The origin of the spine coordinate system was defined as the average of the superior and inferior endplate center points.

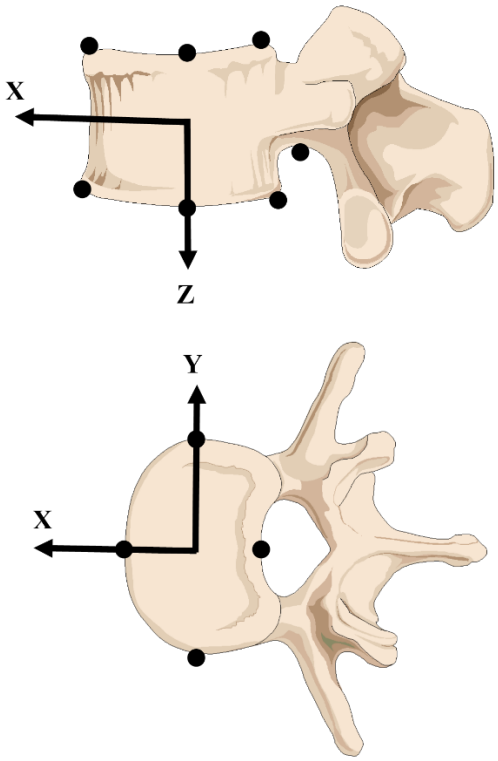

Figure 3.2.1.11.1.2-1: Spine coordinate system with the origin at the center of the vertebral body

3.2.1.11.1.3. Spine local coordinate system (T1 and T6)

A marker-based coordinate system was used for T1 and T6. The origin was the average of the three markers, and the initial orientation was set to be coincident with the seat coordinate system.

3.2.1.11.1.4. Sacral local coordinate system

A reference line was determined by subtracting the anterior point on the sacral body's superior surface from the posterior point. The +y axis was calculated by subtracting the superior aspect of the right articular process from the left. The +z axis was determined by calculating the cross product of the reference line and the +y axis. The +x axis was the cross product of the +z and +y axes. The origin is the average of the anterior, posterior, left, and right points on the sacral body.

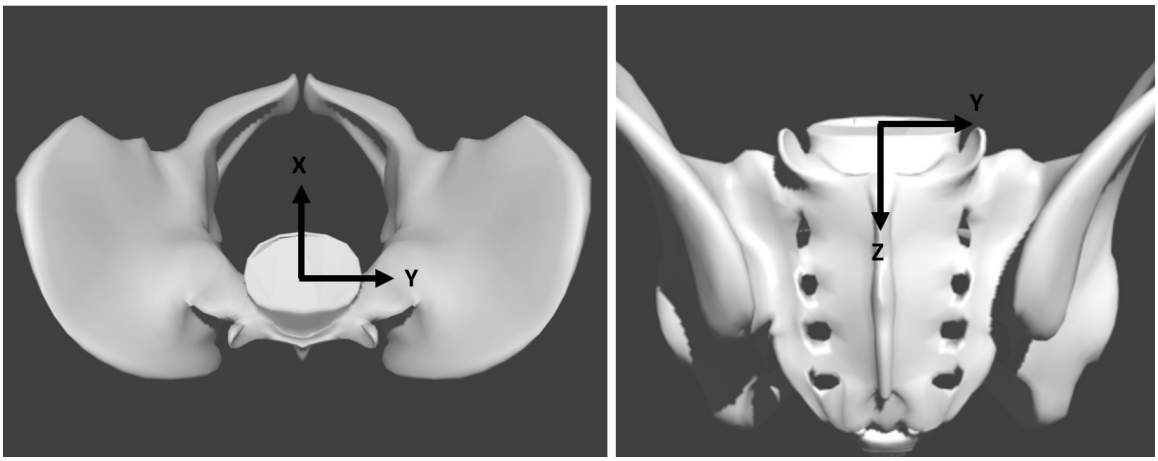

Figure 3.2.1.11.1.4-1: Sacral local coordinate system

3.2.1.11.1.5. Seat local coordinate system

The seat coordinate system origin is on the cushion's top surface at the center of the rear edge. The X-Y plane is the cushion's top surface with the +x axis forward and -y-axis to the right. The +z axis is perpendicular to the seat cushion and pointed downwards.

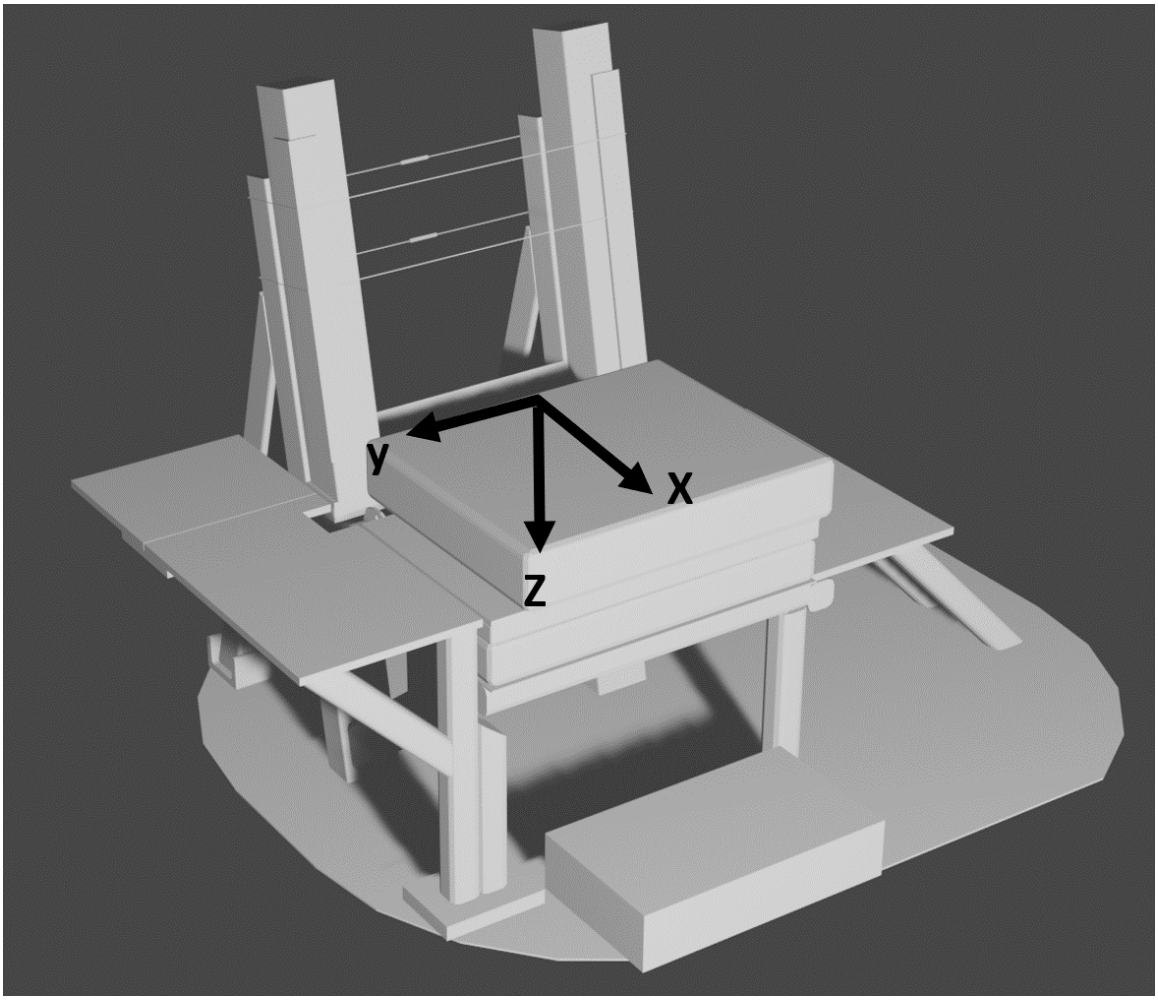

Figure 3.2.1.11.1.5-1: Seat local coordinate system

3.2.1.11.1.6. Motion-capture local coordinate system

The motion-capture local coordinate system's origin and orientation were defined by the placement of the L-frame marker wand during camera calibration. The frame was

placed with the origin near the reaction mass of the servo-brake such that the XY plane was parallel to the ground with the +X axis pointed down the track. The +Z axis was pointed upwards. Figure 3.2.1.11.1.6-1 shows the position of the wand and orientation of the motion-capture coordinate system.

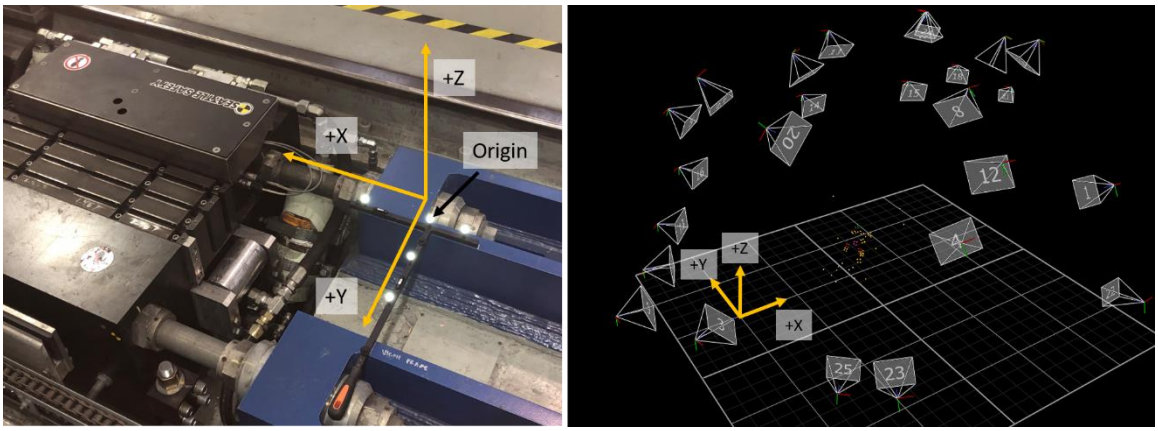

Figure 3.2.1.11.1.6-1: Motion-capture coordinate system with a picture of the L-frame wand placed at the base of the reaction mass of the servo-brake mechanism is shown on the left. The reconstructed volume showing the origin and orientation of the coordinate system and camera positions and the occupant's pre-test position is shown on the right.

3.2.1.11.2. Anatomic Local Coordinate System Time-History Calculation

Two sets of identical local-marker coordinate systems were defined at each anatomic coordinate system. The first was calculated using the marker centers' digitized coordinates from the pretest CT scan or CMM measurements. The second was determined at each time point from the measured three-dimensional marker trajectories.

3.2.1.11.2.1. Marker-to-Anatomic-Transformation Matrix

Using the anatomic rotation matrix ($R_{Anat/CT}$) and the marker sensor rotation matrix ($R_{Marker/CT}$), the transformation matrix relating the marker to the anatomic coordinate system was calculated using Equation 3.2.1.11.2.1-1.

$$[R]_{Anat/Marker} = [R]_{Anat/CT} * [R]_{CT/Marker} \qquad \textit{Equation 3.2.1.11.2.1-1}$$

where:

$$[R]_{CT/Marker} = [R]_{Marker/CT}{}^{-1} \qquad \textit{Equation 3.2.1.11.2.1-2}$$

Each rotation matrix is a 4 X 4 matrix and generically defined as:

$$[R]_{A/B} = \begin{bmatrix} i_a \cdot i_b & i_a \cdot j_b & i_a \cdot k_b & \mathrm{d_x} \\ j_a \cdot i_b & j_a \cdot j_b & j_a \cdot k_b & \mathrm{d_y} \\ k_a \cdot i_b & k_a \cdot j_b & k_a \cdot k_b & \mathrm{d_z} \\ 0 & 0 & 0 & 1 \end{bmatrix} \qquad \textit{Equation 3.2.1.11.2.1-3}$$

where:

- i_a, j_b, and k_a are the unit vectors of XYZ system in A,
- i_b, j_b, and k_b are the unit vectors of XYZ system in B, and
- d_x, d_y, and d_z are the coordinates of the B origin in the A reference.

3.2.1.11.2.2. Motion-Capture Local Anatomic Calculations

At each anatomic location, the markers' three-dimensional positions were related to the anatomic coordinate systems using the methods described in Section 3.2.1.11.1. The

two marker-based coordinate systems were used to compute the anatomical origin and orientation at each time-step in the motion-capture coordinate system.

A 4 x 4 rotation matrix (shown below) that relates the local (anatomic) coordinate system (LCS) to the motion-capture coordinate system (MCCS) was calculated for the head, T1, T6, T12, and sacrum.

$$\begin{bmatrix} r_{11} & r_{12} & r_{13} & d_x \\ r_{21} & r_{22} & r_{23} & d_y \\ r_{31} & r_{32} & r_{33} & d_z \\ 0 & 0 & 0 & 1 \end{bmatrix}_{MCCS/LCS}$$

Equation 3.2.1.11.2.2-1

where:

- r_{11}, r_{12}, and r_{13} are the MCCS x unit vector in the LCS,
- r_{21}, r_{22}, and r_{23} are the MCCS y unit vector in the LCS,
- r_{31}, r_{32}, and r_{33} are the MCCS z unit vector in the LCS, and
- d_x, d_y, and d_z are the position of the local origin in the MCCS.

$$\begin{Bmatrix} X \\ Y \\ Z \end{Bmatrix}_{MCCS} = \begin{bmatrix} r_{11} & r_{12} & r_{13} \\ r_{21} & r_{22} & r_{23} \\ r_{31} & r_{32} & r_{33} \end{bmatrix}_{MCCS/LCS} \begin{Bmatrix} x' \\ y' \\ z' \end{Bmatrix}_{LCS} + \begin{Bmatrix} d_x \\ d_y \\ d_z \end{Bmatrix}$$

Equation 3.2.1.11.2.2-2

3.2.1.11.3. Calculation of Anatomic Kinematics in Seat Coordinate System

Head, T1, T8, T12, and sacrum anatomic three-dimensional displacements and orientations relative to the seat coordinate system were determined using Equation 3.2.1.11.3-1.

$$[R]_{Seat/Anat\ LCS} = [R]_{Seat/MCCS} * [R]_{MCCS/Anat\ LCS} \qquad \textit{Equation 3.2.1.11.3-1}$$

where:

- $[R]_{Seat/Anat\ LCS}$ is the Head, T1, T6, T12, or pelvis local-coordinate-system orientation and position in the seat coordinate system;
- $[R]_{Seat/MCCS}$ is the inverse of $[R]_{MCCS/Seat}$ where $[R]_{MCCS/Seat}$ is the seat orientation and position in the motion-capture coordinate system; and
- $[R]_{MCCS/Anat\ LCS}$ is the Head, T1, T6, T12, or pelvis local-coordinate-system orientation and position in the motion-capture coordinate system.

3.2.2. Isolated Sled Tests

3.2.2.1. Test Details

The boundary conditions of the isolated sled test were similar to the whole-body test described above, including:

- seat cushion
- restraints
- instrumentation
- data acquisition
- data processing
- injury assessment

A PMHS was isolated from the superior surface of the T11 vertebral body to the distal femurs. Viscera were removed, and the abdominal skin was reattached using sutures. The distal femurs were wrapped in flexible bandages. Polymethylmethacrylate (PMMA) encased the superior end of the specimen such that the T12-L1 disc was free. A six-axis load cell was attached to the top surface of the PMMA, and, above this, metal plates

were secured to simulate torso mass. A triaxial linear accelerometer was fixed to the anterior surface of the PMMA. Retroreflective targets were attached to the posterior, left, and right sides of the PMMA. A 6DOF sensor—integrating 3 axes of linear acceleration and three angular velocities—was attached to the dorsal sacrum, as well as a retroreflective target plate. A schematic of the test setup is shown in Figure 3.2.2.1-1.

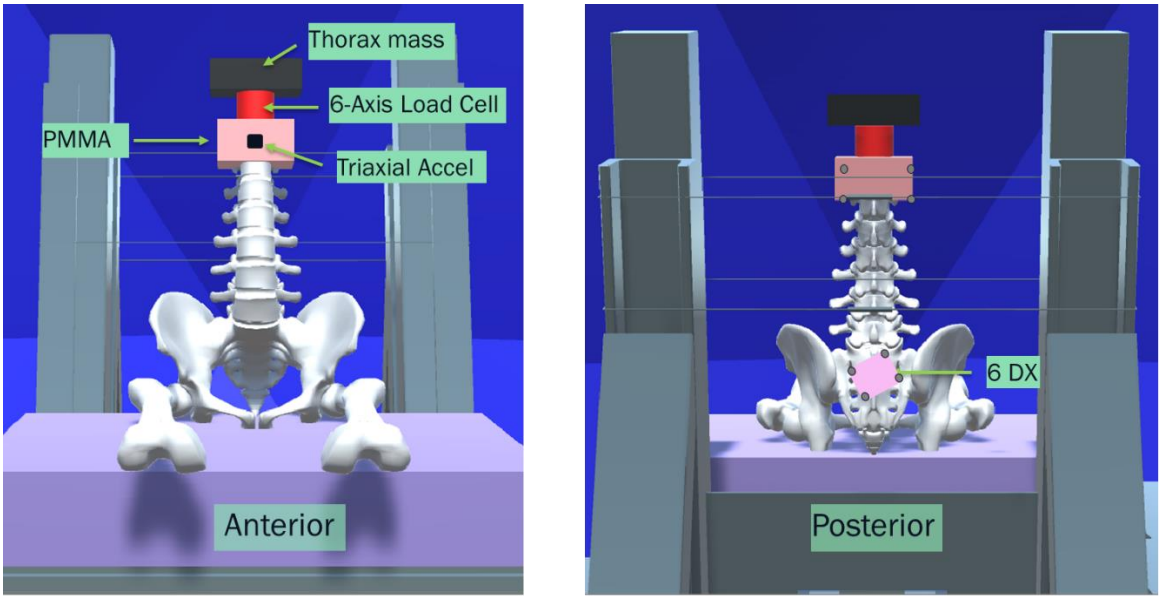

Figure 3.2.2.1-1: Anterior (left) and posterior (right) schematic of an isolated PMHS sled test showing the T12 PMMA, 6-axis load cell, thorax replacement mass, 6DX sensors, and motion-capture targets.

Tests were conducted using pulses scaled in magnitude from the FAA Emergency Landing Condition at 30% and 61% and are shown in Figure 3.2.2.1-2.

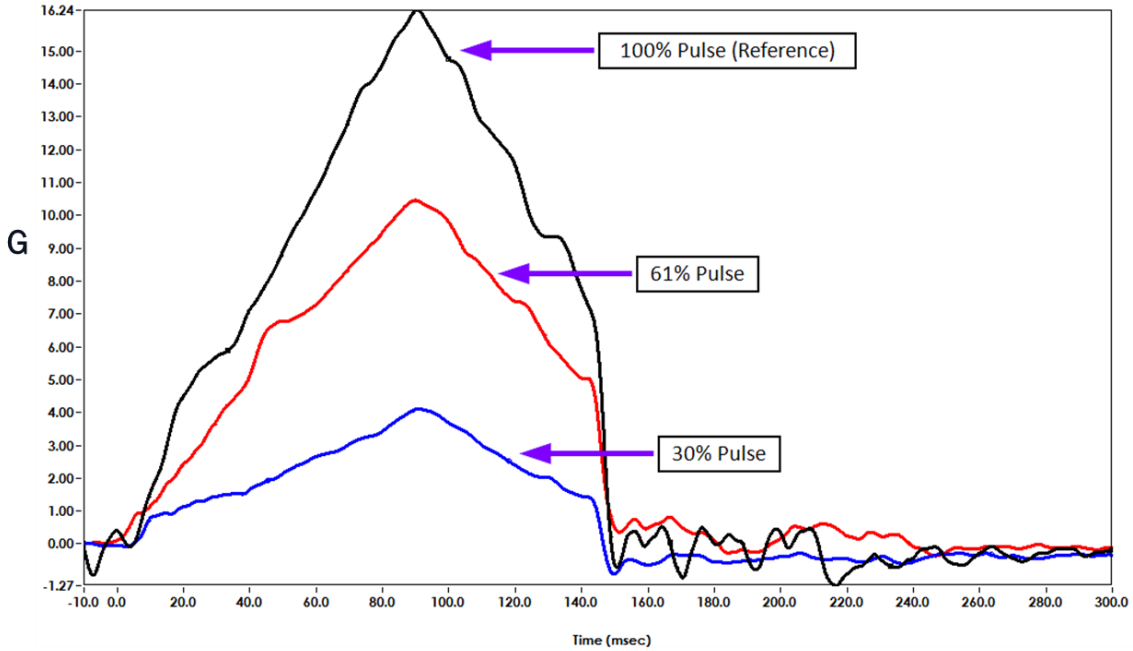

Figure 3.2.2.1-2: Pulses scaled in magnitude at 30% (blue) and 61% (red) used for isolated PMHS sled tests and shown in comparison to the reference FAA Emergency Landing Condition Pulse (100% magnitude, black).

3.2.2.2. Test Matrix

The isolated PMHS sled test matrix is shown below.

Table 3.2.2.2-1: Isolated Sled Test Matrix

Test ID	Input Pulse	Thorax Mass	Lap Belts
FILSC102	30%	4 kg	Frontal and body-centered
FILSC103	30%	8 kg	Frontal and body-centered
FILSC104	30%	10 kg	Frontal and body-centered
FILSC106	61%	4 kg	Frontal and body-centered
FILSC107	61%	8 kg	Frontal and body-centered

3.2.3. Isolated Piston Tests

3.2.3.1. Specimen Preparation

An isolated T11 to sacrum specimen was procured. The inferior end of the specimen was potted in polymethyl-methacrylate (PMMA) such that the L5-S1 disc is free and the

superior endplate of L3 is level in the sagittal plane. The superior end of the spine will be fixed in PMMA so that the T12-L1 disc is free. Six-axis load cells were mounted proximal to the superior PMMA and distal to the inferior PMMA. Sets of three non-collinear retroreflective targets were placed into the anterior vertebral body at L1–L5. Additionally, three targets were mounted on the anterior surface of the inferior and superior PMMA. A set of CT scans were obtained following PMHS instrumentation.

3.2.3.2. Test Device

A six-degree-of-freedom spinal positioning device (SPD) was fabricated to orient the posture of isolated PMHS spines relative to the uniaxial translation of the electro-hydraulic piston. It consists of a separate translation and rotation fixtures. From bottom to top, it consists of the following elements: (1) an x-y table to adjust the fore/aft and lateral position of the spine (translation), (2) a vertical lift platform to adjust the height of the spine (translation), and (3) a triaxial rotational device consisting of two vertically stacked rotational platforms with orthogonally mounted shafts and pillow blocks to rotate the lower spine in the coronal and sagittal planes (rotation). The rotational platforms can be adjusted as a unit about the vertical axes to change the specimen's position in the transverse plane. Figure 3.2.3.2-1 and Figure 3.2.3.2-2 show the two components of the SPD (3DOF translation and 3DOF rotation).

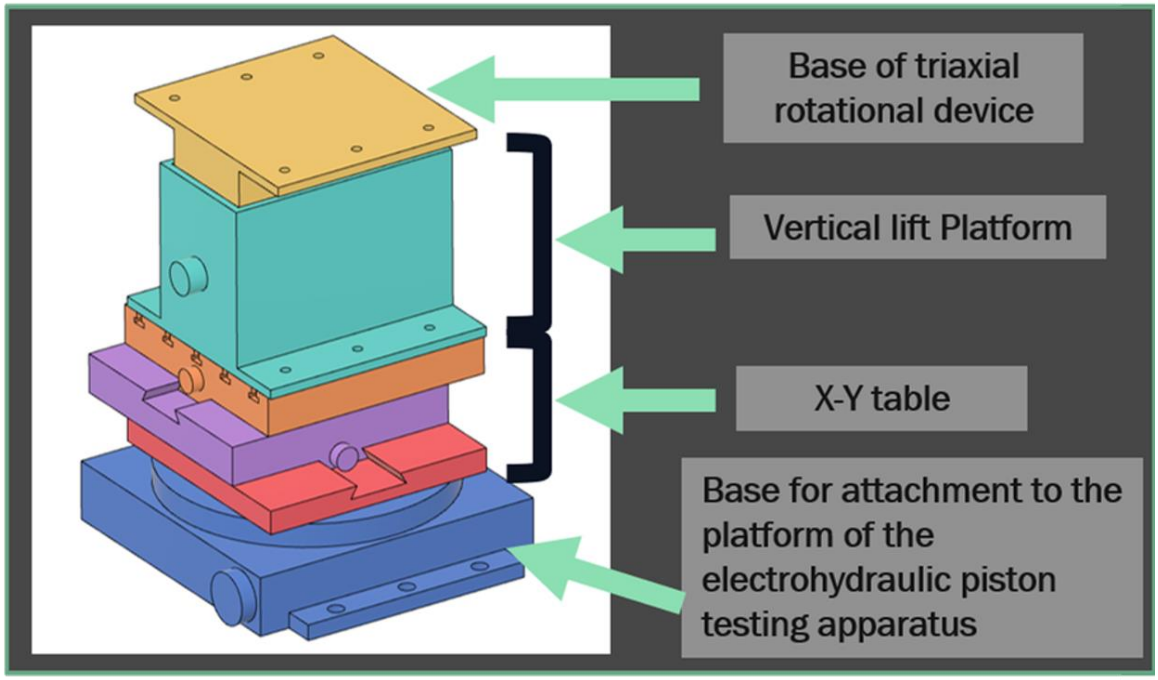

Figure 3.2.3.2-1: Schematic of the translation fixture component of the SPD. From bottom to top, it consists of a platform for mounting to the base of the electrohydraulic piston, an x-y table for A/P and lateral translation, and a vertical lift platform for superior-inferior translation. The bottom of the rotational device is attached to the top of the vertical lift platform.

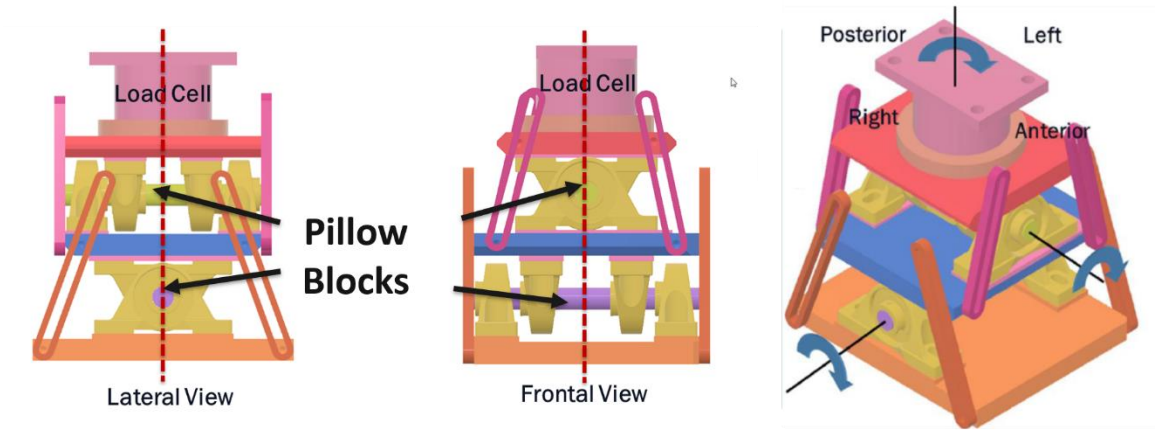

Figure 3.2.3.2-2: Schematic of the rotation fixture component of the SPD. Left and middle are a front and lateral view of the rotation showing the orthogonally mounted pillow blocks. Right is an oblique view.

3.2.3.3. Test Posture and Rate

The pre-test posture of the isolated PMHS is shown in Figure 3.2.3.3-1. The sacral angle was 5 degrees in the sagittal plane and 15 degrees in the coronal plane. The electro-hydraulic piston was programmed to distract the spine at 1 m/s.

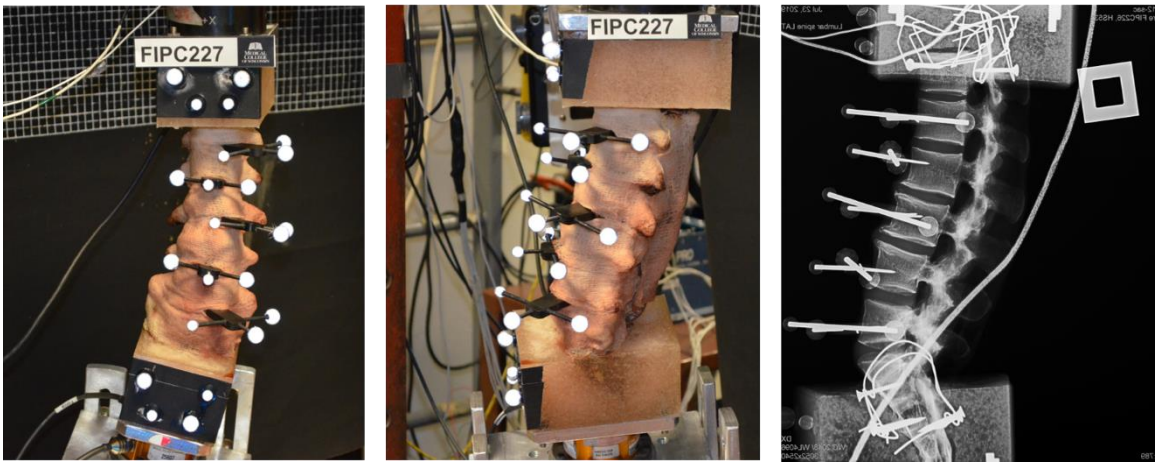

Figure 3.2.3.3-1: Left is a pre-test picture of the isolated spine from the front. The middle is a lateral picture, and on the right is a lateral x-ray.

3.2.3.4. Data Capture and Processing

Kinematic data of the spine targets were obtained using a six-camera motion-capture system at 1 kHz. Sensor data, including the six-axis load cell and piston displacement, were sampled at 20 kHz. Anatomic kinematics at each spinal level was determined using the methods described in the whole-body section. Forces and moments were calculated at the L5-S1 level using the following equation:

$$\frac{dH}{dt} = r_{L5Disc} \times F_{S1LC} + M_{S1LC} \qquad \textit{Equation 3.2.3.4.-1}$$

3.3. RESULTS

3.3.1. Whole-Body Sled Tests

3.3.1.1. Specimen demographics

Table 3.3.1.1-1 shows the specimen demographics.

Table 3.3.1.1-1: Whole-Body Specimen Demographics

Test ID	HS number	Age (years)	Stature (cm)	Mass (kg)
FOC104	679	62	172	79
FOC117	676	64	182	69

3.3.1.2. Injury Information

Injury information for the whole-body sled tests are shown in Table 3.3.1.2-1, and a post-test image of the L5-S1 injury is shown in Figure 3.3.1.2-1.

Table 3.3.1.2-1: Whole-body specimen sled tests injuries

Anatomic Region	FOC104	FOC117
Spine	C5-C6 Transection L5-S1 Transection	None
Ribcage	Rib Fractures Right: 8, 10-12 Left: 9-12	None
Pelvis	Left Pelvic Ala linear fracture	None
Extremities	None	None

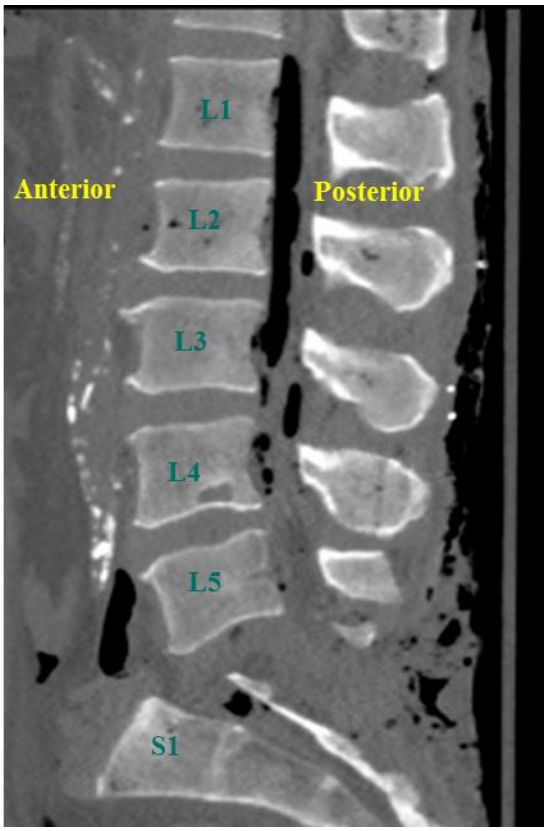

Figure 3.3.1.2-1: Post-test CT showing the L5-S1 injury (transection) for FOC104

3.3.1.3. Kinematics

The whole-body three-dimensional kinematics of the head, spine, and pelvis for the failure test are shown in Figures 3.3.1.3-1 to 3.3.1.3-3 and non-failure in Figures 3.3.1.3-4 to 3.3.1.3-6. The failure results highlight the occupant's response in all three planes, with nearly the same head excursion in the forward and lateral directions with the largest excursion in the vertical direction (~1100 mm).

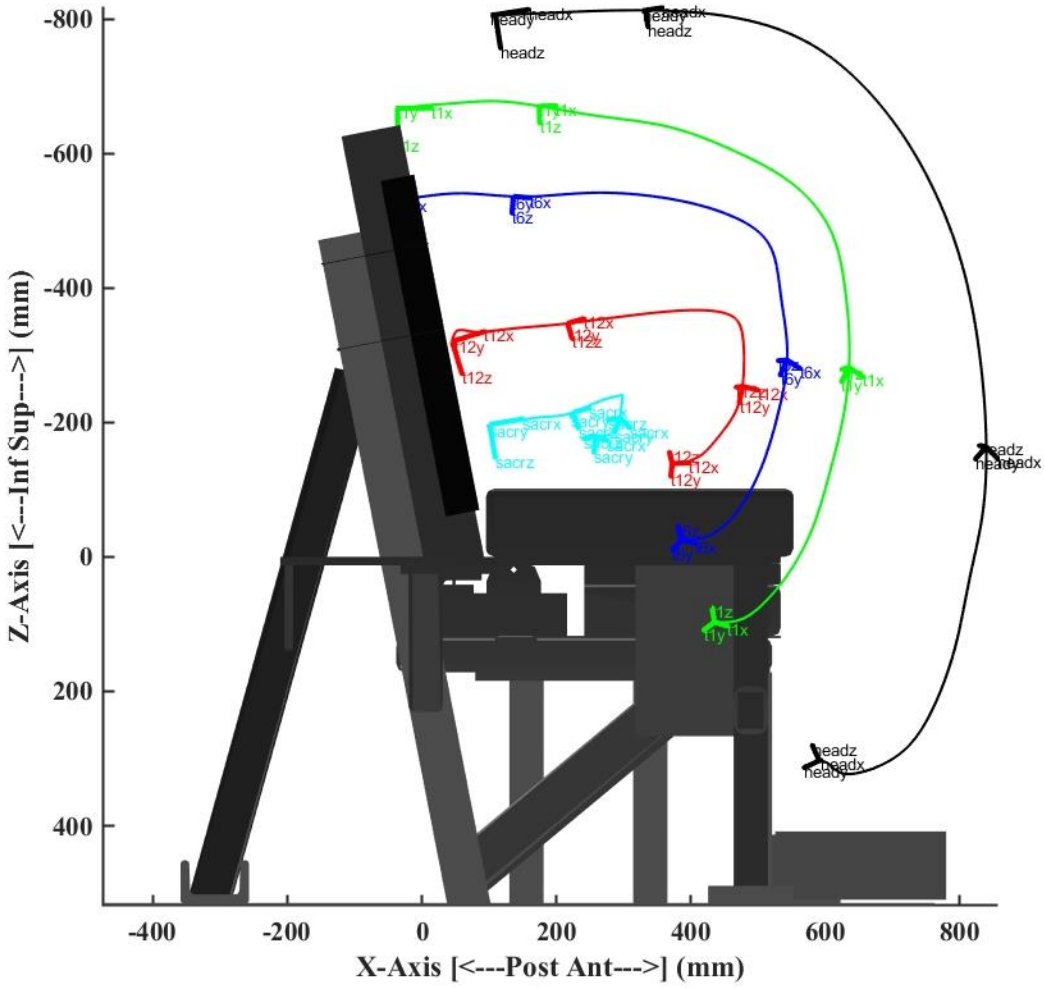

Figure 3.3.1.3-1: Lateral view of the head, T1, T6, T12, and sacrum kinematics relative to the seat for the failure test. Unit vectors show the orientation of each anatomic location at 0, 100, 200, and 300 milliseconds.

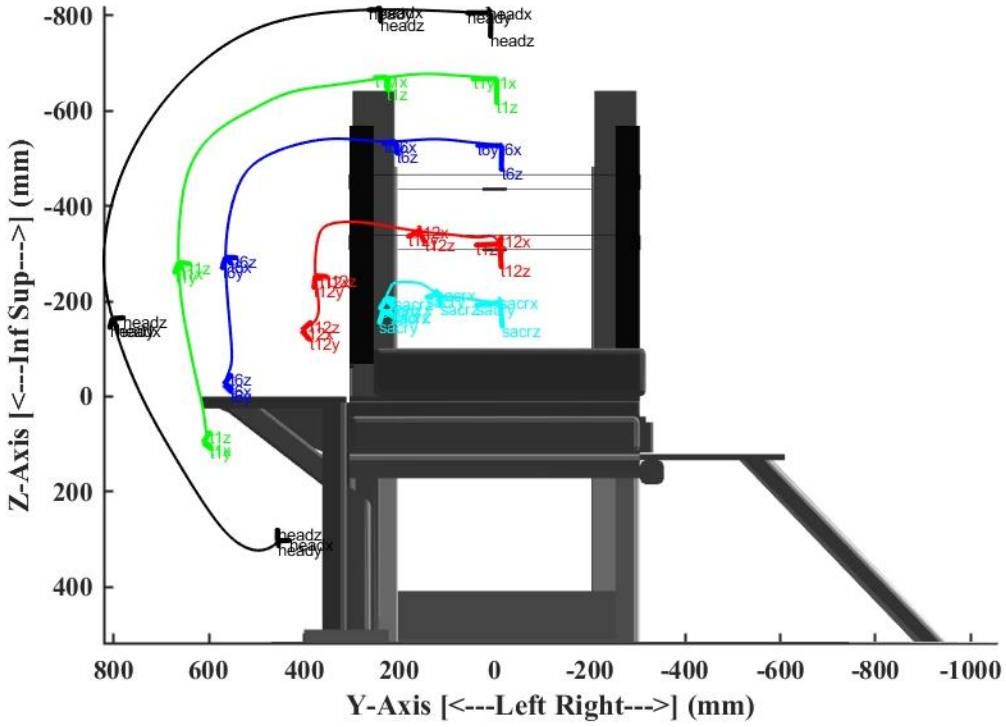

Figure 3.3.1.3-2: Front view of the head, T1, T6, T12, and sacrum kinematics relative to the seat for the failure test. Unit vectors show the orientation of each anatomic location at 0, 100, 200, and 300 milliseconds.

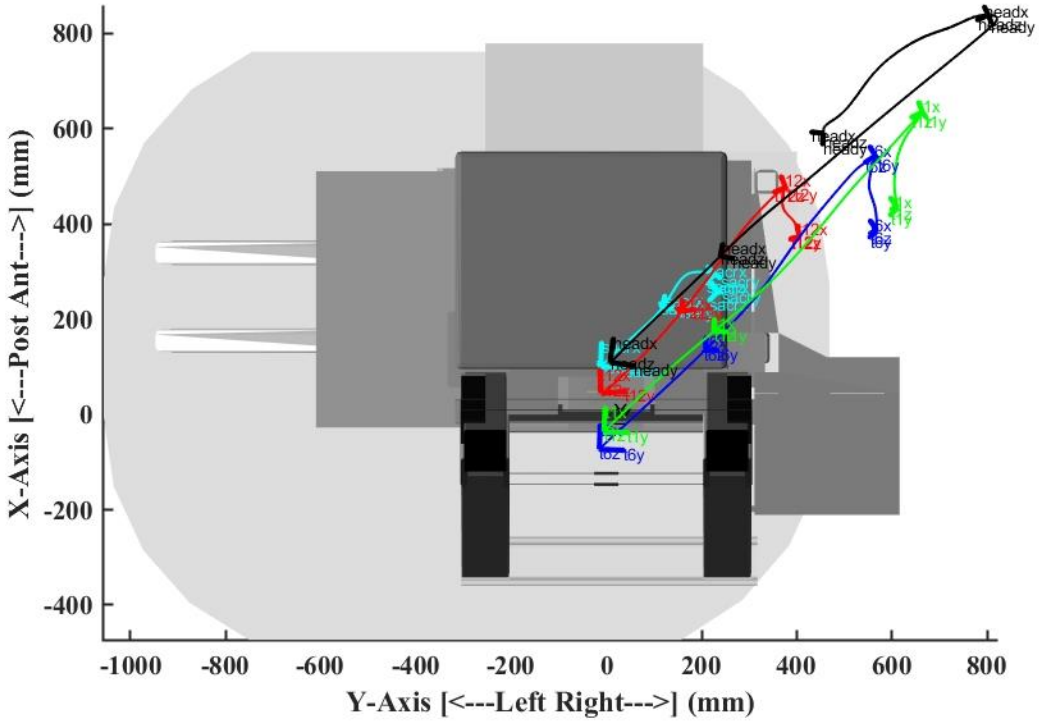

Figure 3.3.1.3-3: Overhead view of the head, T1, T6, T12, and sacrum kinematics relative to the seat for the failure test. Unit vectors show the orientation of each anatomic location at 0, 100, 200, and 300 milliseconds.

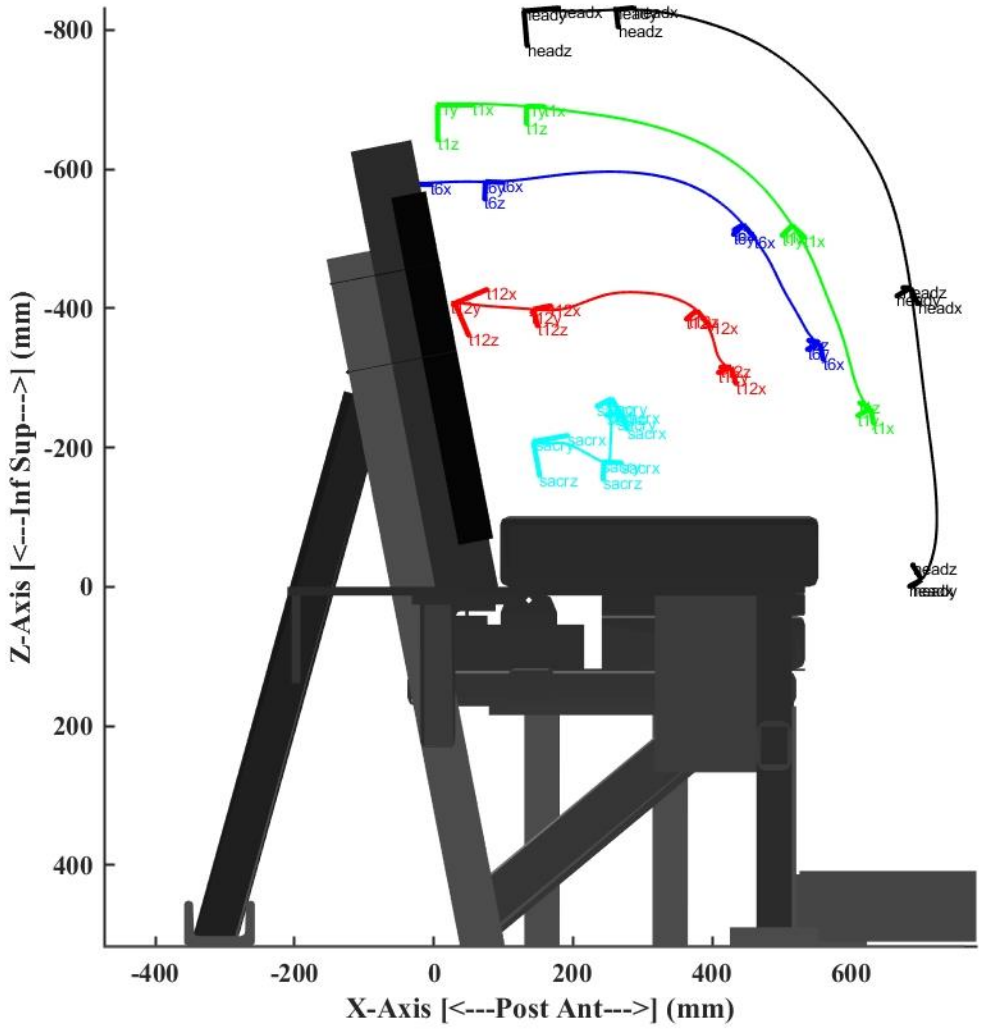

Figure 3.3.1.3-4: Lateral view of the head, T1, T6, T12, and sacrum kinematics relative to the seat for the non-failure test. Unit vectors show the orientation of each anatomic location at 0, 100, 200, and 300 milliseconds.

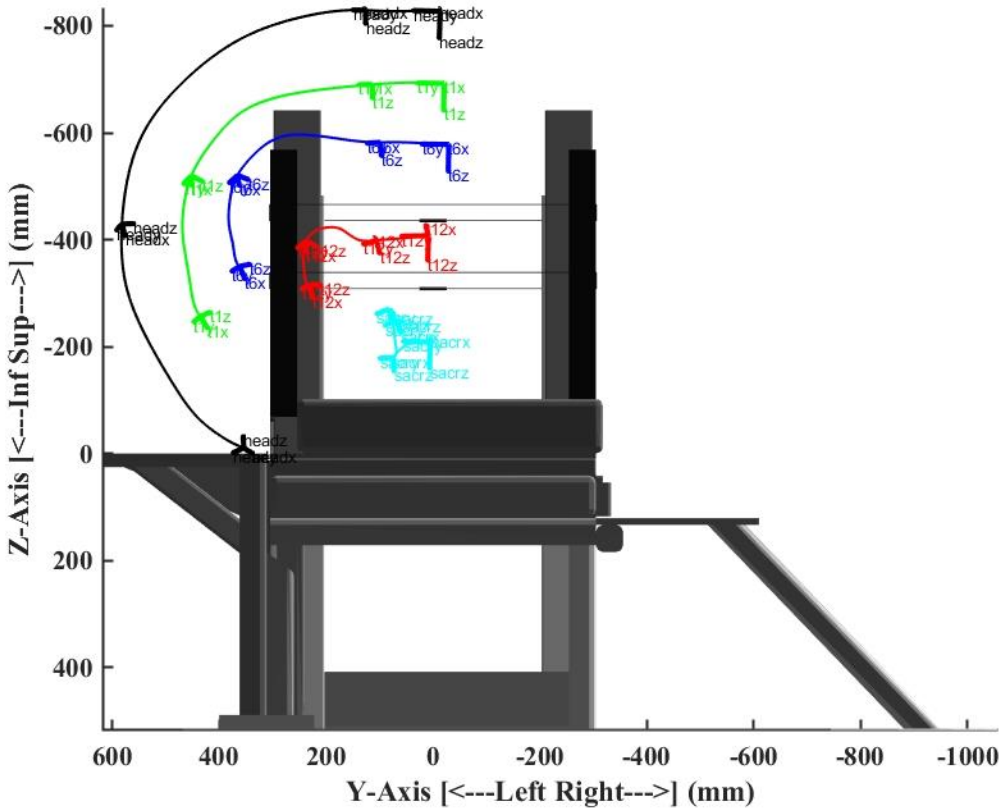

Figure 3.3.1.3-5: Front view of the head, T1, T6, T12, and sacrum kinematics relative to the seat for the non-failure test. Unit vectors show the orientation of each anatomic location at 0, 100, 200, and 300 milliseconds

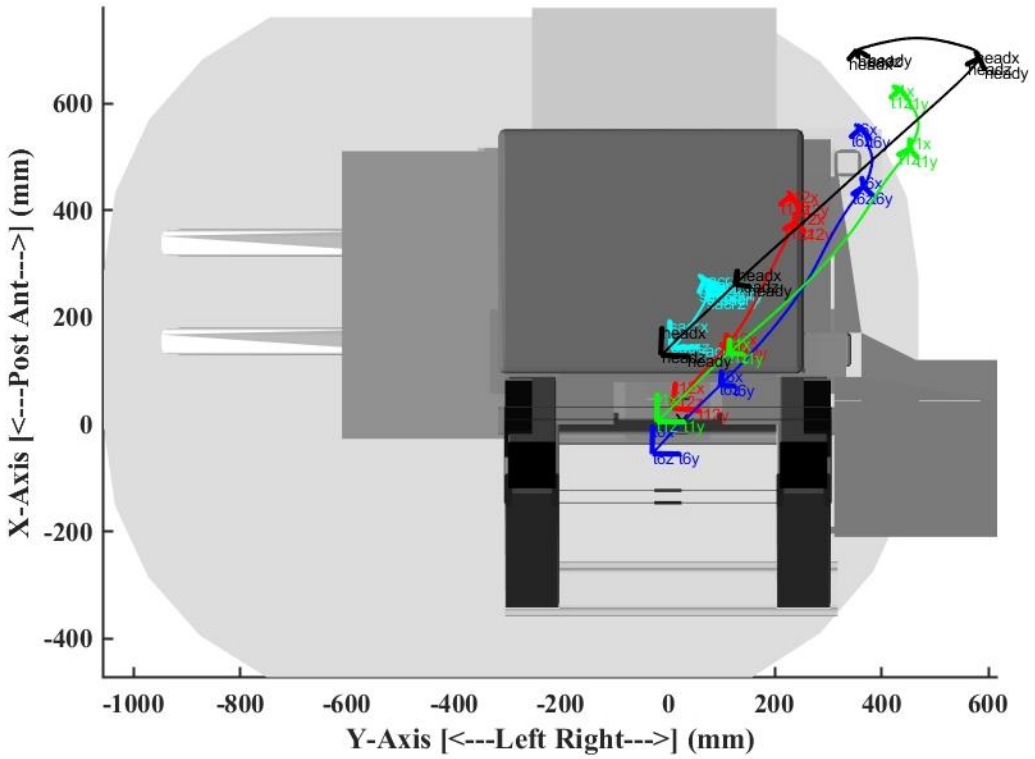

Figure 3.3.1.3-6: Overhead view of the head, T1, T6, T12, and sacrum kinematics relative to the seat for the non-failure test. Unit vectors show the orientation of each anatomic location at 0, 100, 200, and 300 milliseconds.

As expected, the distance between the sacrum and T12 remained constant in the lower-speed test and is consistent with no injury. In contrast, the higher speed test demonstrated a considerably increased distance between the two anatomic regions and a markedly different relative motion, which indicated injury and was confirmed by the post-test CT images. The relative kinematics were further explored to determine the

posture and rate of loading at the time of injury. The three-dimensional anatomic kinematics of T12 and the sacrum relative to the seat are shown in Figures 3.3.1.3-7-3.3.1.3-9 for failure (black) and non-failure (blue) tests.

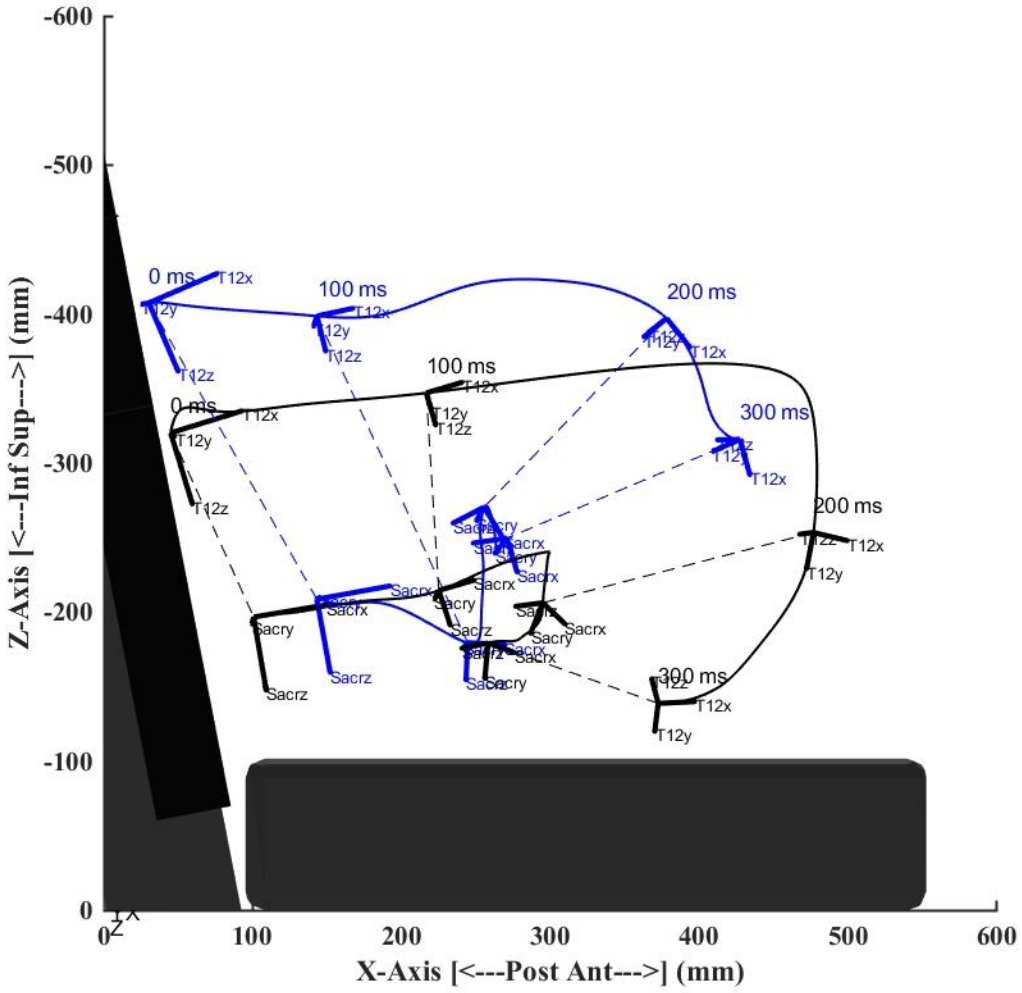

Figure 3.3.1.3-7: Lateral view of the sacral and T12 kinematics for failure (black) and non-failure (blue) test. Unit vectors show the orientation of each anatomic location at 0, 100, 200, and 300 milliseconds.

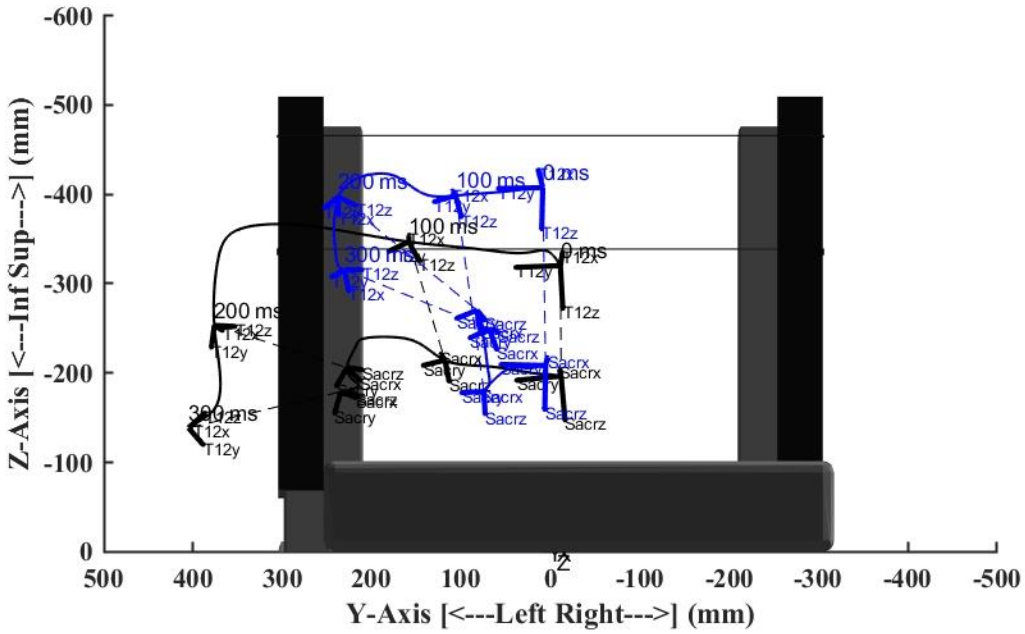

Figure 3.3.1.3-8: Front view of the sacral and T12 kinematics for failure (black) and non-failure (blue) test. Unit vectors show the orientation of each anatomic location at 0, 100, 200, and 300 milliseconds.

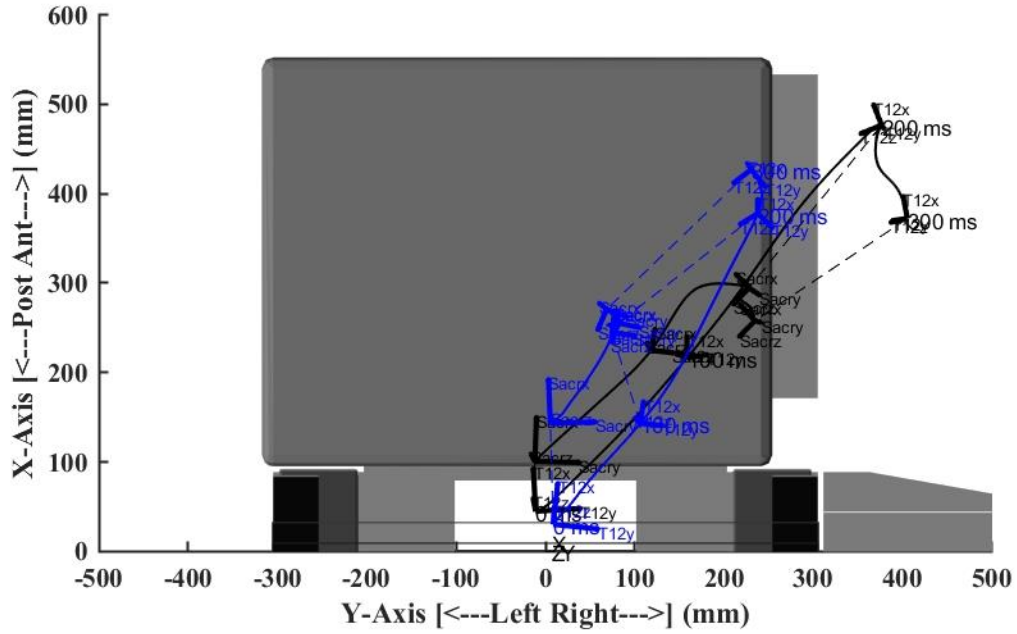

Figure 3.3.1.3-9: Overhead view of the sacral and T12 kinematics for failure (black) and non-failure (blue) test. Unit vectors show the orientation of each anatomic location at 0, 100, 200, and 300 milliseconds.

Figure 3.3.1.3-10 shows the time-history plots of the distance between the sacrum origin to the T12 origin and represents the lumbar length (blue is non-failure, and black is the failure test). The change in lumbar spine length is shown in Figure 3.3.1.3-11. In the non-injury plot, the overall length (distraction) changes by ~ 15 mm, whereas the failure run demonstrates a change of over 100 mm. The increase in overall length is attributed to the L5-S1 distraction-transection injury observed in the failure test. In the non-failure test, the total distraction peaked at 15 mm, and using this non-injury

magnitude, the failure test kinematics was evaluated on a temporal basis, and the L5-S1 injury was inferred at approximately 25 mm of distraction. This occurred at approximately 125 msec. A detailed plot of the lumbar spine kinematics from 105 to 145 msec is shown in Figure 3.3.1.3-12. The linear acceleration data from the T12 vertebrae shows higher frequency and magnitude just after 120 msec as further evidence of the time of failure. A similar appears in the sacrum linear acceleration data around 116 msec. Figure 3.3.1.3-13 shows the kinematics of T12 relative to the sacrum. A distinct change in kinematics is observed at 100 msec, where the relative forward motion of T12 to the sacrum stops and undergoes tensile loading. Examining the distraction time-history profile between 100 and 125 msec (Figure 3.3.1.3-14), the loading rate was estimated to be 1 m/s. Similarly, a computation of the average orientation of T12 relative to the sacrum between 100 and 125 msec yields a posture where the endplates of the sacrum and T12 are parallel in the midsagittal plane and 10 degrees of bending in the coronal plane. This posture and loading rate was used in the design of the isolated PMHS experimental model.

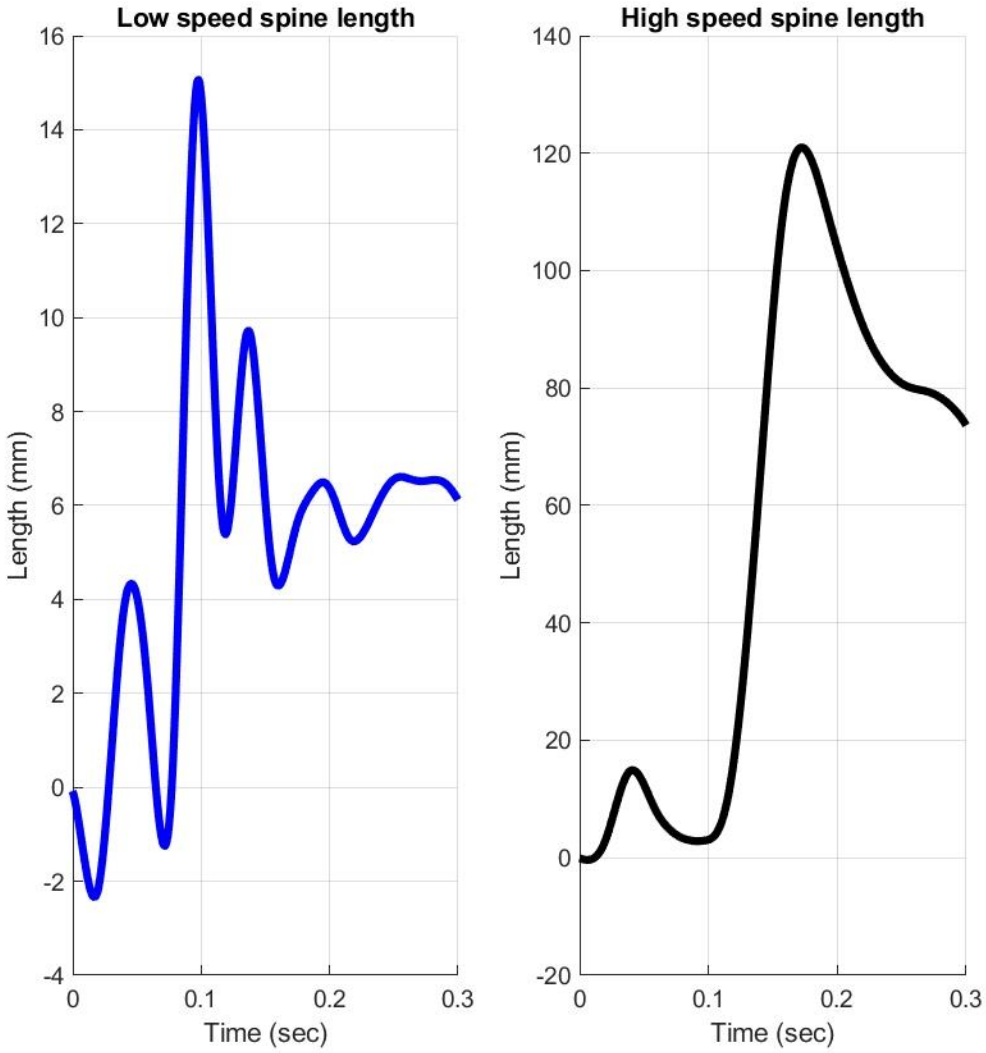

Figure 3.3.1.3-10: T12–Sacrum distance for the non-failure (blue, left) and failure (black, right) tests.

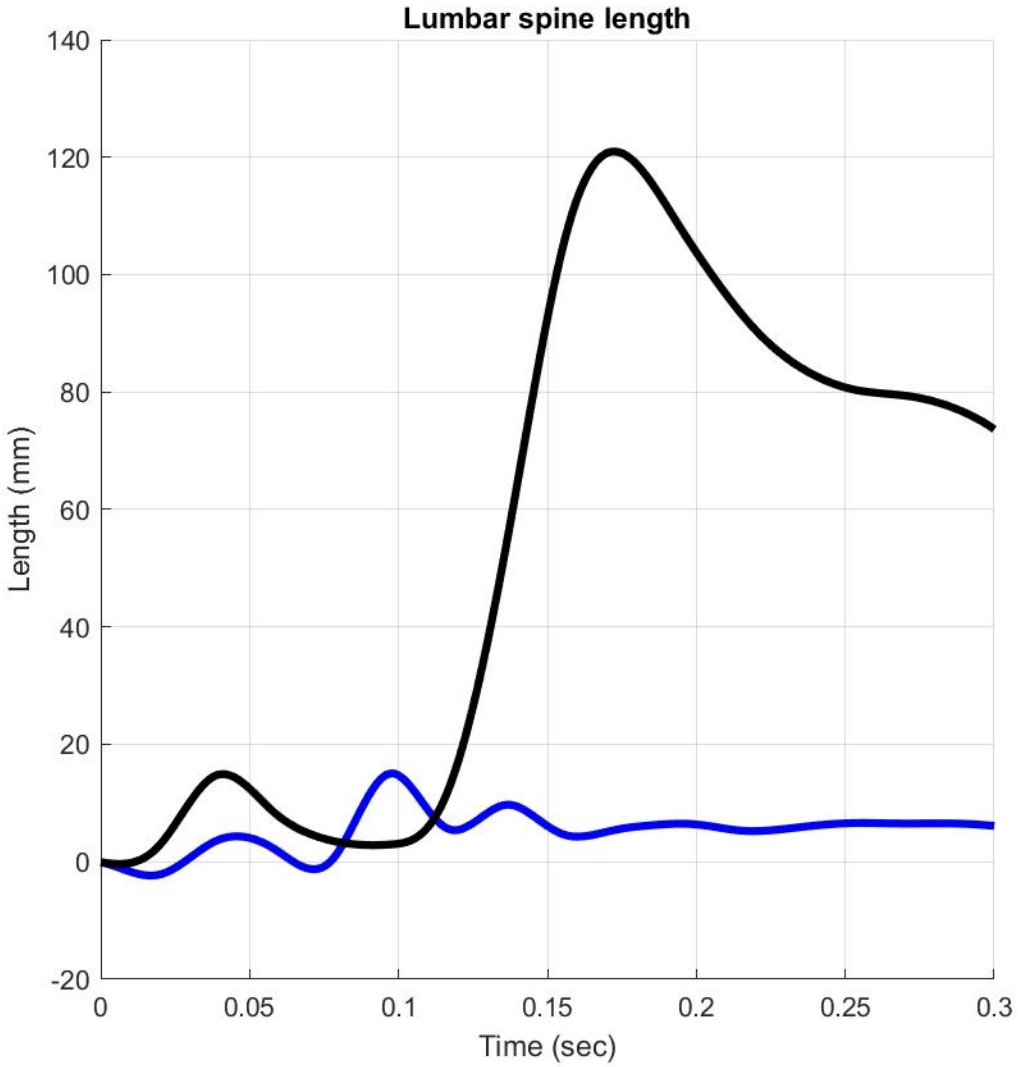

Figure 3.3.1.3-11: Change in the lumbar spine length for non-failure (blue) and failure (black).

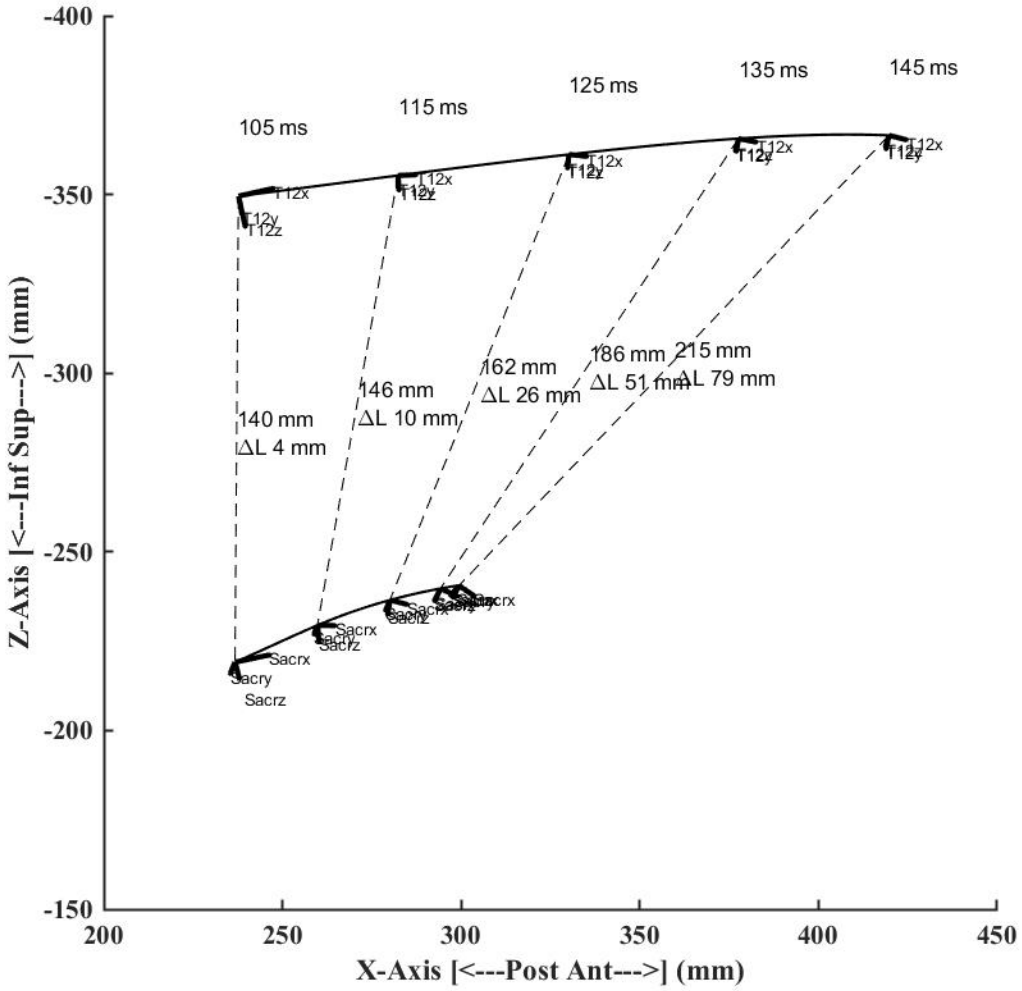

Figure 3.3.1.3-12: Lateral view of the T12 and sacrum kinematics from 100 to 140 milliseconds for the failure test. The dotted line represents the length from the sacrum origin to the T12 origin with the corresponding length and change in length (ΔL).

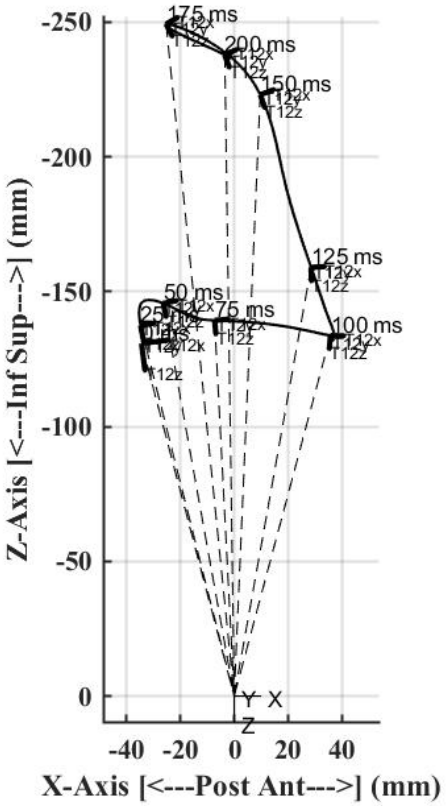

Figure 3.3.1.3-13: Lateral view of the T12 kinematics in sacrum local coordinate system from 0 to 175 msec.

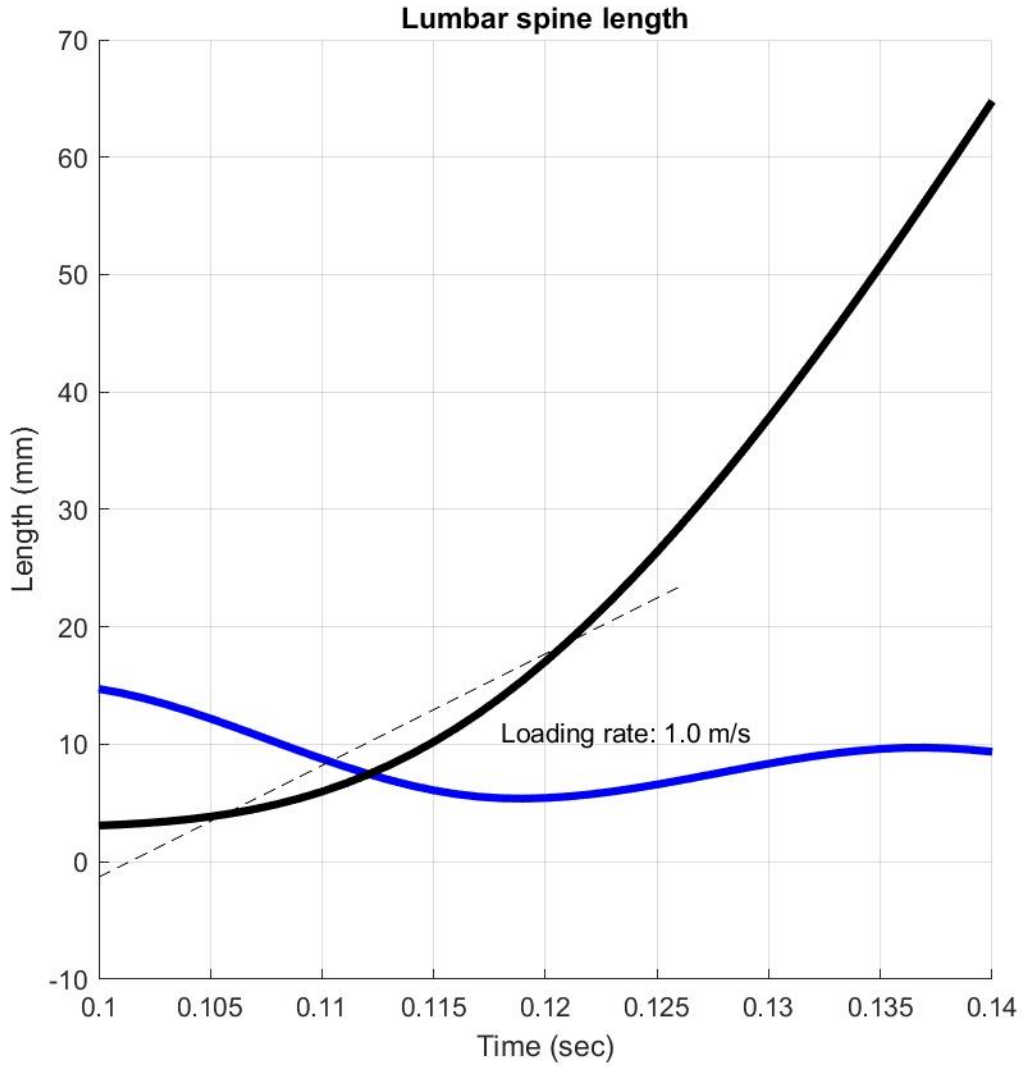

Figure 3.3.1.3-14: Closeup of the lumbar spine length of failure (black) and non-failure (blue). The dashed line shows the linear regression between 100 and 125 msec and the calculated slope of 1.0 m/s

3.3.2. Isolated Sled Test

3.3.2.1. Kinematics

The 4, 8, and 10 kg thorax mass tests at the 30% pulse had similar T12–sacrum distance time-histories in magnitude and curve morphologies. This response is shown in Figure 3.3.2.1-1. Figures 3.3.2.1-2 through 3.3.2.1-4 show a comparison of the three-dimensional kinematics of the 61% pulse isolated and whole-body experiments. The 4 kg thorax mass test demonstrated similar sacral kinematics to the whole-body test with a reduced excursion at T12. In contrast, a failure was observed in the 8 kg thorax mass test, which resulted in considerably different T12 kinematics. The 10 kg thorax mass test was not conducted at this velocity due to the injury during the preceding 8 kg test.

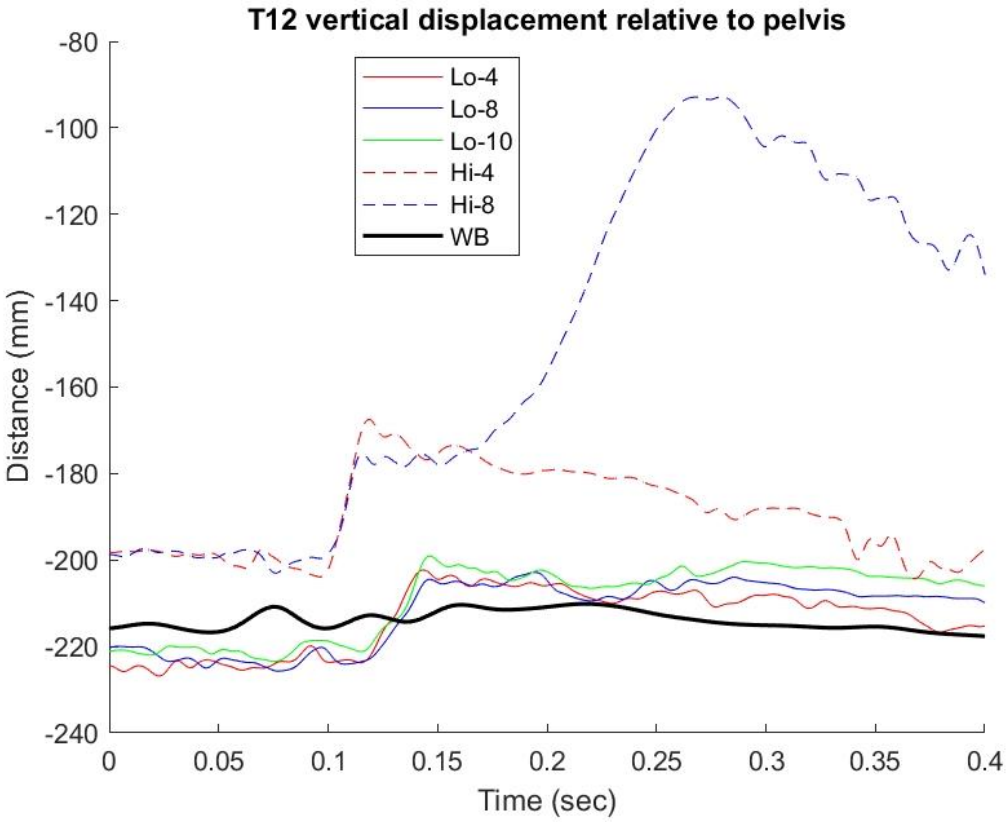

Figure 3.3.2.1-1: Distance between the T12 and sacrum for the 4, 8, and 10 kg 30% pulse tests (solid red, blue, and green lines, respectively), 4 and 8 kg 61% pulse (dashed red and blue, respectively), and whole-body 61% pulse (solid black)

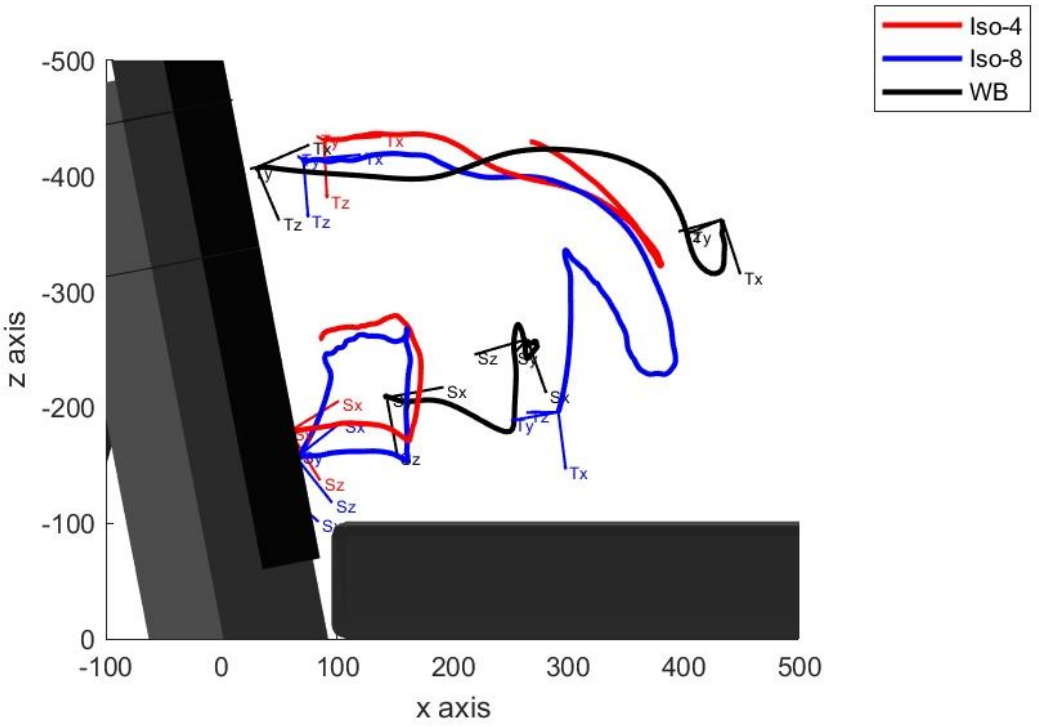

Figure 3.3.2.1-2: Lateral view of the 61% pulse T12 and sacrum kinematics relative to the seat for the isolated 4 kg thorax mass (red), isolated 8 kg thorax mass (blue), and whole-body test (black)

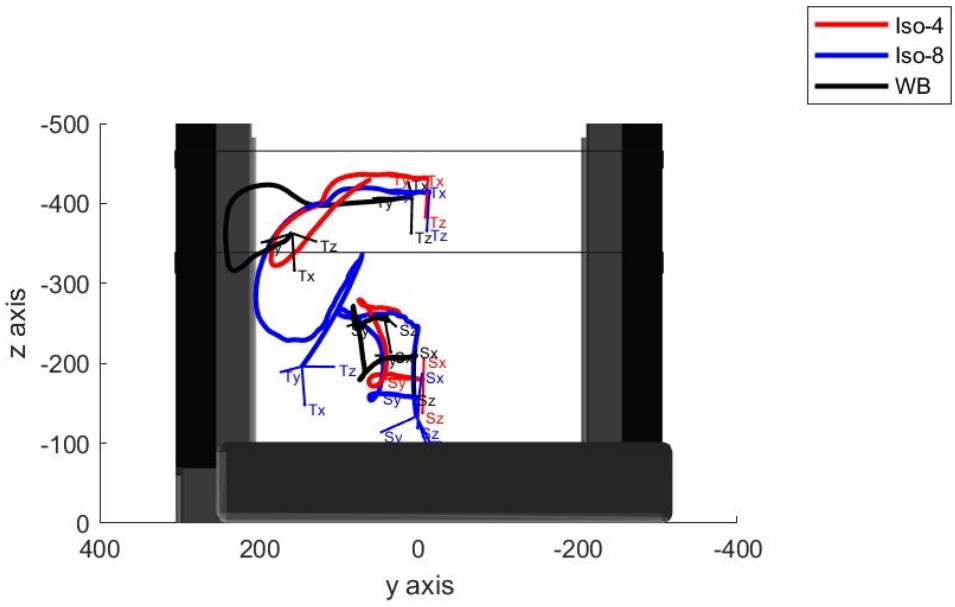

Figure 3.3.2.1-3: Front view of the 61% pulse T12 and sacrum kinematics relative to the seat for the isolated 4 kg thorax mass (red), isolated 8 kg thorax mass (blue), and whole-body test (black)

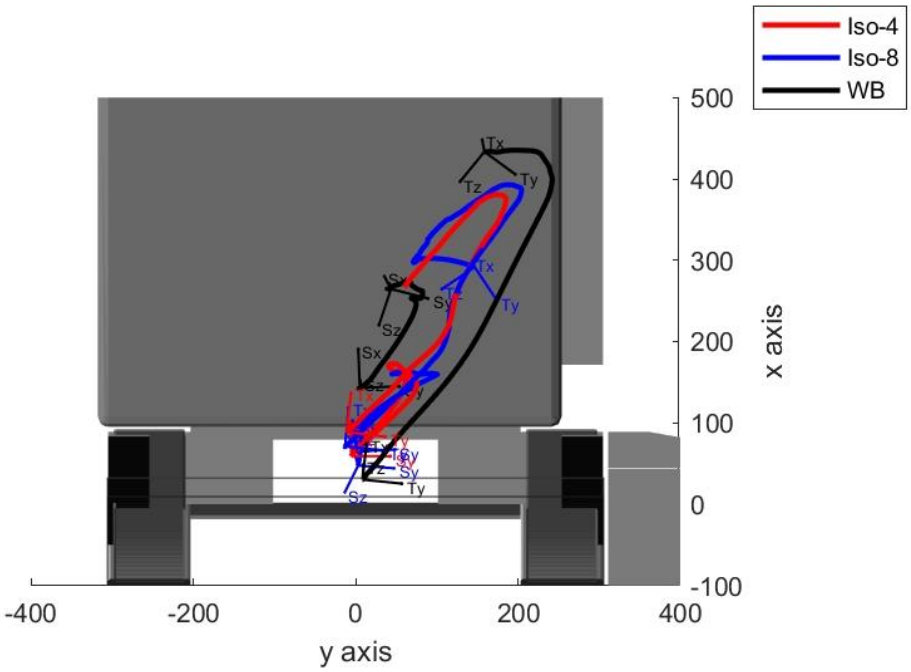

Figure 3.3.2.1-4: Overhead view of the 61% pulse T12 and sacrum kinematics relative to the seat for the isolated 4 kg thorax mass (red), isolated 8 kg thorax mass (blue), and whole-body test (black)

3.3.2.2. Kinetics

Table 3.3.2.2-1 shows the peak T12 axial force (Fz), coronal moment (Mx), and sagittal moment (My) for the 4, 8, and 10 kg thorax replacement mass at the 30 and 61% pulses.

As expected, the peak loads increased with increasing mass. A similar trend was observed for the higher severity pulse except for the last test's sagittal moment and was attributed to the mid-column failure seen during this test.

Table 3.3.2.2-1: Peak axial loads from isolated PMHS sled tests

Test ID	Input Pulse	Thorax Mass (kg)	Peak Fz (N)	Peak Mx (Nm)	Peak My (Nm)
FILSC102	30%	4	218	-5.4	23.2
FILSC103	30%	8	387	-12.0	28.5
FILSC104	30%	10	506	-15.0	37.4
FILSC106	61%	4	604	-10.5	50.3
FILSC107	61%	8	1,165	-14.4	45.8

3.3.2.3. Injuries

Figure 3.3.2.3-1 shows the post-test images from the CT scan after the 8 kg thorax mass 61% pulse. Injuries occurred at the L2-L3 level, disc rupture, and ligament tears.

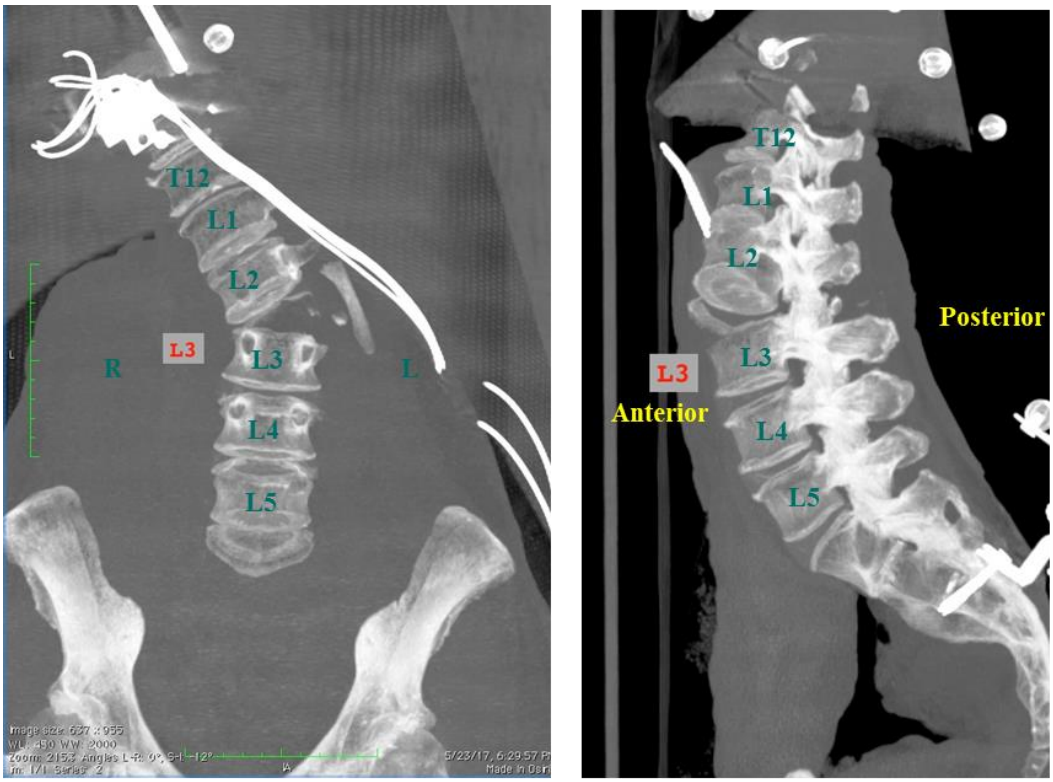

Figure 3.3.2.3-1: Post-test images showing the injury at the L2-L3 level after the 8 kg thorax mass 60% pulse test. Left shows the frontal view, and right shows a lateral view

3.3.3. Isolated Piston Test

3.3.3.1. PMHS Data

Figures 3.3.3.1-1 and 3.3.3.1-2 show the calculated anatomic loads at S1. Peak tension force was 3.1 kN while the off-axis loads (x and y) were less than 500 N. the peak coronal moment was 52 Nm, and the sagittal moment was 33 Nm.

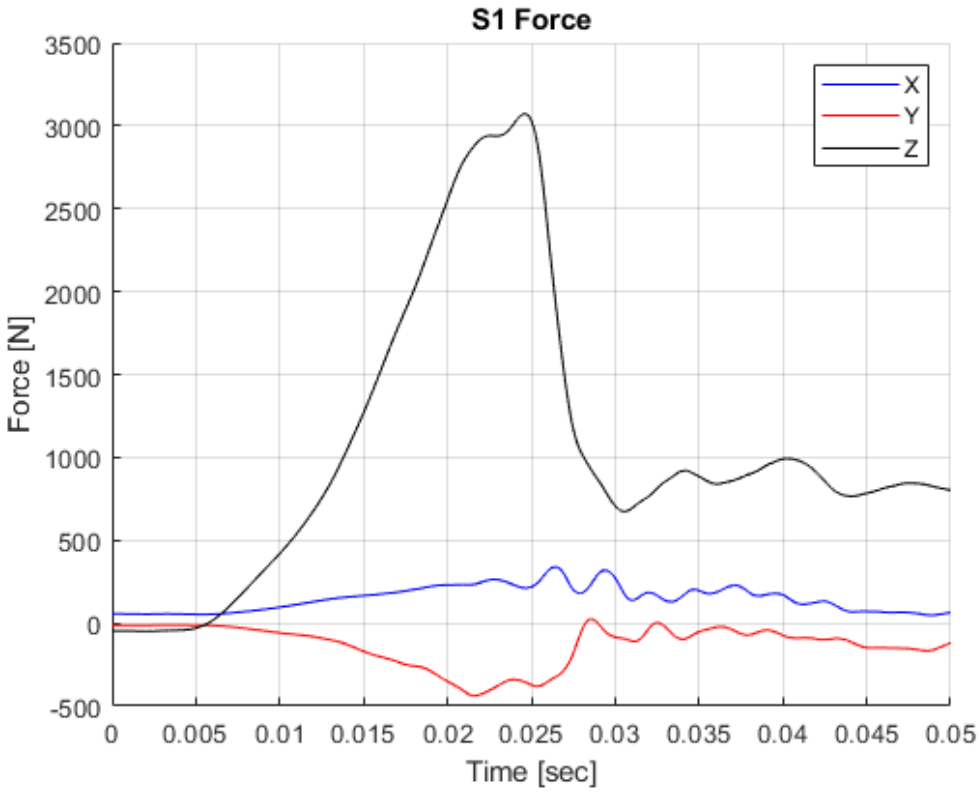

Figure 3.3.3.1-1: S1 forces in the X (A/P), Y (lateral), and Z (axial) directions

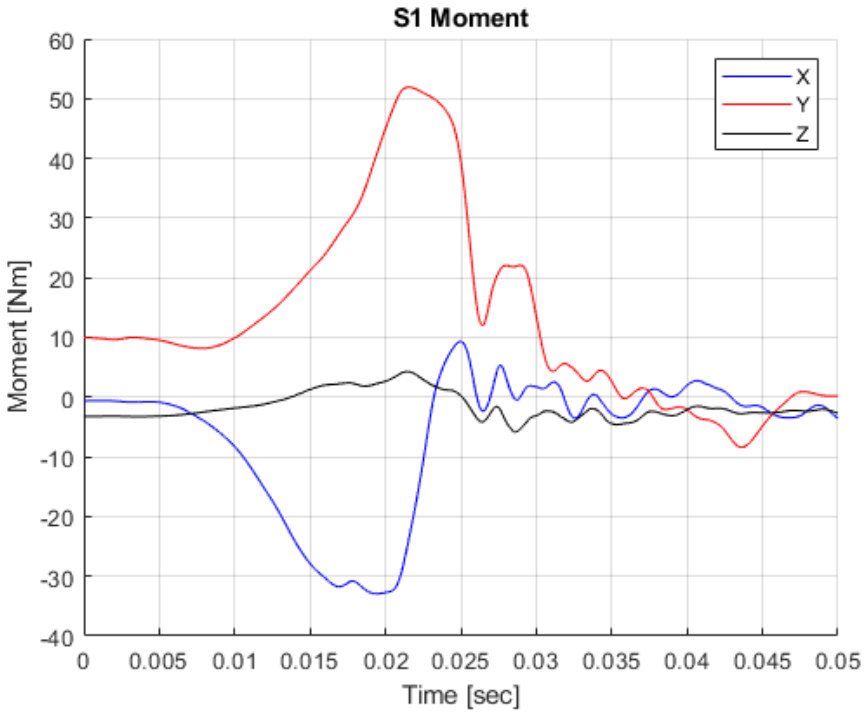

Figure 3.3.3.1-2: S1 moments about the X (A/P), Y (lateral), and Z (axial) directions

3.3.3.2. Injuries

Post-test images showed disruption of the posterior elements of the L5-S1 joint, similar to the whole-body test.

Figure 3.3.3.2-1: Injury to the L5-S1 joint from the isolated PMHS test

3.4. DISCUSSION

Dynamic test requirements for commercial aircraft were regulated for all newly built aircraft delivered after October 2009 [51]. These standards were designed to protect occupants from emergency landing events, which typically occur during takeoff or

landing phases of flights and represent likely cabin loads during a survivable crash scenario. Until recently, little research had been conducted to explore new safety standards for obliquely oriented seats in the aviation environment. As indicated in the introduction section, although research and Federal Motor Vehicle Safety Standards exist for frontal and lateral impact crashworthiness, their applications are limited to aircraft environments [68, 69].

A fundamental difference between aircraft and automobile crashes is that, in the former environment, there is a requirement to evacuate the cabin following a crash event. Occupants in an automobile crash decide to extricate themselves depending on injury severity and status of the vehicle/scene or stay within the vehicle until emergency medical service personnel arrive. The movement of the occupant is discouraged to prevent the possibility of further injury. In contrast, in an airline crash, occupants must be able to escape the cabin within 90 seconds with little to no assistance from first responders due to the high likelihood and sudden propagation of fires [51]. Thus, the likelihood of a 'survivable crash' is lower for aircraft than a motor vehicle. Injury to the lower extremities or loss of consciousness—while not immediately fatal—may be detrimental during cabin evacuation for an injured or adjacent occupant. The survivability in a motor vehicle crash does not generally depend on injuries to the other occupants. In an airplane crash event, uninjured occupants may be at a greater risk of severe injury or death if an impaired fellow occupant delays evacuation.

In automotive environments, oblique injuries are caused by the intruding door or striking vehicle. Injury biomechanics research efforts in oblique side impacts have

typically mimicked this boundary condition by impacting PMHS with padded or rigid load wall using sled equipment or a pendulum device. They have primarily focused on injuries to the thorax, abdomen, and pelvic body regions. Recent reviews are available [70, 71]. This type of loading mode is uncommon in aviation environments. However, occupant loading in far-side crashes is generally longer in duration than near-side and, hence, more similar to an aircraft emergency pulse, albeit at a lower ΔV. Additionally, the side console in the automobile and lack of structures in the passenger space allow occupant kinematics to develop, resembling oblique-facing occupants in aircraft.

The whole-body tests' goal was to determine the injuries to occupants in obliquely mounted seats in the aircraft environment. The PMHS test at the FAA emergency landing condition pulse (100%) demonstrated transection injury at L5-S1. Due to the limitations of the whole-body PMHS experimental model, the failure loads were not measurable. Therefore, the next step was to design an experimental model that produced the same type of injury as seen in the whole-body test while simultaneously measuring the failure loads. Because the whole-body test was conducted in a sled environment, the first step was to use the same restraint conditions and loading device with an isolated PMHS model wherein a load cell could determine the anatomic failure loads. The isolated PMHS sled test incorporated an intact femur-pelvis-lumbar spine to mimic the interaction between the seat cushion and belt restraints with the whole-body sled test. This experimental design's advantage was that the same sled pulse could be used in an isolated setting. The thorax mass in the whole-body was replaced with a fixed mass attached to the T12 load cell's superior end. The lumbar spine's effective

mass in the whole-body was unknown; thus, three different mass magnitudes were examined—4, 8, and 10 kg. It should be noted that this mass does not represent the mass of the lower torso of the human but rather an estimate of the potential effective mass during the acceleration pulse.

The experimental design consisted of applying pulses of different severities, as results from the whole-body tests predicted injury at the 100% pulse and no-injury at the 61% pulse. The intent of the isolated PMHS sled model was to determine the loads at increasing pulse severities from the no-injury whole-body condition (61%) in an incremental manner up to failure. The 30% pulse was selected as the starting point to investigate the role of mass on the loads at a lower severity wherein injuries were not expected and maintain the specimen's integrity. At the 30% pulse, all three thorax end conditions resulted in similar morphologies of the loads, and no injuries were observed. As expected, loads increased with increasing thorax mass. The 61% pulse was selected as the next incremental pulse as it matched the no-injury whole-body test condition. The intent was to compare the isolated PMHS sled test's kinematics to the whole-body test to select the appropriate thorax mass boundary condition. During this series, the lumbar spine's mid-column failure was observed for the 8 kg thorax mass condition. As shown in Figure 3.4-1, the isolated PMHS sled tests experimental model produced an injury that did not match the whole-body test in the location of injury and pulse severity. The mechanism of injury in the isolated sled test experimental model did not match the distraction type injury at the L5-S1 level in the whole-body test and can likely be attributed to the difference in the mass recruitment effect. In the whole-body test,

the thorax's effective mass increases as a function of time during the event as more mass is recruited from inferior to superior segments. This is reflected in the kinematics, where the pelvis coupled by the lap belts is the first anatomic region to be displaced by the accelerating seat. The head is the last body region to accelerate and is the most distal to the pelvis. The end effect of the fixed thorax mass in the isolated PMHS sled test likely caused the mid-column injury and was more representative of a fixed end condition for a beam, where higher bending stresses are predicted in the middle of the column.

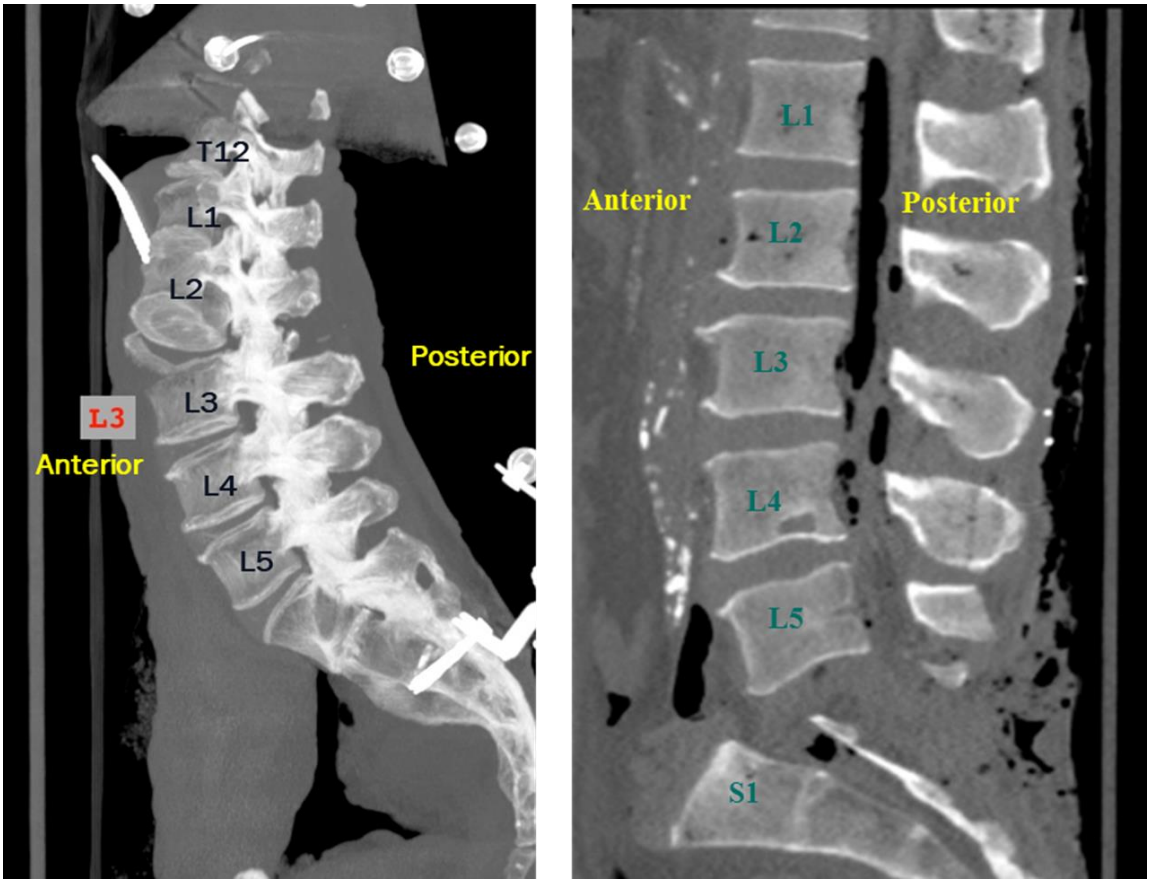

Figure 3.4-1: Comparison of injuries observed in the isolated sled test PMHS (left) and whole-body (right) sled tests

The goal of the isolated PMHS sled test experimental model was to measure the anatomic loads during the event and reproduce the injuries seen in the whole-body tests. This experimental model could potentially be used by keeping the lower abdomen's internal structures intact to support the spine. The lack of soft tissue may have contributed to the mid-column failure. As the isolated sled test experimental model did not replicate the failure test's kinematics and injury mechanism, a new design was necessary. This led to the development of an isolated piston test wherein the PMHS posture and loading condition could be more controlled.

Because an electro-hydraulic piston was used as a loading device, the loading rate calculated in the whole-body tests at the time of failure was used as the input. The relative position of T12 to the sacrum played a role in the injury mechanism of the whole-body test, which was quantified by determining the flexion and lateral bending angulations at the estimated time of failure. This information was also included in the isolated experimental model and necessitated designing a new device that could replicate this complex posture. These features could not be controlled in the isolated sled PMHS test.

To accommodate the sacrum's complex posture relative to T1 determined from the whole-body test, a six-degree-of-freedom control (integrating three linear and three angular axes) was necessary and resulted in the design of the Spinal Positioning Device. This device controlled the posture at the inferior (sacrum) end, while the superior (T12) end was fixed to the piston. The whole-body sled test boundary conditions were such that the pelvis was relatively fixed by the seatbelts, while the torso (T12 end) kinematics

were uncontrolled (flailing). In the isolated piston test experimental design, this was achieved by angulating the inferior end (pelvis) to the fixed superior end (T12) that was attached to the piston such that the relative orientation between the two anatomic regions was the same as in the whole-body test. Angular control was achieved using two vertically stacked plates with orthogonally mounted pillow blocks. This permitted independent rotation in the sagittal and coronal planes. The x-y table and vertical lift platform accommodated the linear translation necessary to achieve this posture while controlling the spine's axial preload. A loading rate of 1 m/s, determined from the whole-body failure test's kinematics, was used as input to the isolated PMHS experimental model.

The isolated piston test produced an injury at the L5-S1 joint (Figure 3.4-2) similar to the injury seen in the whole-body test while simultaneously measuring the failure loads. Thus, this model successfully reproduced the isolated experiment's goals and, with further testing, can be used to derive a lumbar spine injury criterion under this loading scenario. These tests are currently being conducted in our laboratory to develop injury risk curves.

Figure 3.4-2: Comparison of injuries observed in the isolated piston PMHS experiment (left) and whole-body (right) sled tests

3.5. SUMMARY

- Whole-body tests produced injury at the L5-S1 level at the 100% pulse and no injury at the 61% pulse.
- The kinematics of the whole-body failure tests was such that the loading rate at the time of injury was approximately 1 m/s.
- At the time of failure in the whole-body test, the lumbar spine posture was associated with combined flexion and lateral bending.
- To determine the loads associated with failure, an isolated PMHS experimental model was necessary.

- An isolated PMHS sled test experimental design was pursued that replicated an obliquely seated occupant in an aircraft environment in terms of seat geometry, belt restraint, and acceleration pulse.
- The isolated femur-pelvis-lumbar spine fixed thorax mass sled test experimental design was not effective in replicating the whole-body injury, requiring an improved design.
- An isolated PMHS piston test experimental model was pursued to match the spine's loading rate and relative posture from the whole-body test.
- A novel spinal positioning device was developed to allow 6 degrees of freedom on the distal end to control the posture while the superior end was fixed at the piston at the loading rate observed in the whole-body failure test.
- The isolated PMHS piston test with the SPD experimental design successfully replicated the injury mechanism and location seen in the whole-body tests while measuring the failure kinetics.
- This experimental design can be used for any isolated spine experiment (cervical, thoracic, lumbar spine) to study its response to complex loading and develop injury criteria.
- Work is currently being conducted in our laboratory using this experimental design to determine the lumbar injury criteria under tension and bending for the FAA.

CHAPTER 4. TECHNIQUES TO ANALYZE THREE-DIMENSIONAL KINEMATICS OF THE HEAD AND SPINE

4.1. INTRODUCTION

4.1.1. Background

Experiments using Post Mortem Human Surrogate (PMHS) tests are needed for crashworthiness studies to assess and improve human safety in the automotive, military, and other environments. Experiments using biological surrogates (intact PMHS, for example) have been the basis for promulgations of automotive regulations such as the Federal Motor Vehicle Safety Standards used in the US and the United Nations Economic Commission for Europe used in European countries and other nations (ECE-R94, 1995; FMVSS-214, 2008). The US military and the Federal Aviation Administration have separate requirements for advancing safety in that field (DeWeese, Moorcroft, & Pellettiere, 2015). Anthropomorphic Test Devices (ATDs) are used to assess vehicles' crashworthiness and/or its components. The injury assessment reference values or risk curves are obtained from PMHS results (Mertz & Irwin, 2015). Matched-pair tests with inputs matching the PMHS condition are used to test the ATDs, and the presence or absence of injury outcome from the PMHS tests coupled with the mechanical metrics from the ATD tests are generally used to specify human tolerance. This method requires that the ATD accurately mimics human subjects' response, which is accomplished by developing response corridors from a group of PMHS tests and ensuring that the ATD response falls within the established corridors.

The National Highway Traffic Safety Administration (NHTSA) has supported female-specific human surrogates' development to protect this population. The upgraded New Car Assessment Program (NCAP) includes a 5th-percentile female anthropomorphic test device (ATD) in front- and side-impact tests. Work continues to expand the population of ATDs that are more biofidelic and have enhanced injury assessment capabilities. For frontal impacts, the Test Device for Human Occupant Restraint 5th-percentile female (THOR-05F) ATD is being developed. Human body computer models have also been developed for the 5th-female population, including the Global Human Body Model Consortium model. These surrogates will provide researchers and automobile manufacturers with additional tools to reduce injuries to females in the automotive environment.

As with ATDs, whole-body and component-based human body models need corridors, as their prevalence has been increasing in recent years. The corridors can be used to validate the model. For the corridors to be effective, they should be constructed to allow the modeler to use them without assuming the experimental details such as the location of the sensor and other intricacies inherent in complex PMHS experiments. For example, the accelerometer sensor's placement location on the spine vertebra does not generally coincide with the chosen anatomical origin of the bone. In order to validate human body models against experimental sensor data, it is critical to match the location and orientation of the local anatomic axes between the model and experiment. These details are not easily obtained and often a source of error generally unknown to a modeler. Thus, there is a need to express the corridors via a

uniform or global coordinate system. The rationale for expressing the corridors from sensor signals in a global coordinate system is to make the sensor data portable and easy to implement for human body model validation. This study aims to determine the sensor-based corridors in a global coordinate system termed Global Corridors for Sensor Data.

Global coordinates for motion data are also important for the validation of computational models. A planar loading scenario is a straightforward process; however, in a non-planar loading scenario, the translational motions are coupled in at least two planes and given a group of kinematic responses, while motions along each axis at every time-step will have its own variance. Traditionally motion corridors have been considered independently because most studies have focused on planar loading (frontal or side impact) where occupants were restrained and seated in a standard (or uniform) posture. In these analyses, the corridors are determined by the mean response surrounded by a confidence interval scaled from the standard deviation and are often sufficient to characterize the motion for biofidelity assessments. This approach may not be appropriate for non-planar loadings—where the motion to the occupant occurs in all three planes—which are expected to increase in frequency as non-standard seating positions become the norm. In non-planar loading scenarios, the effect of all three components and their grouped variance (x, y, and z combined) should be included for the development of corridors. Further, it is also important to characterize the mean orientation (rotations about the three planes) of each anatomic region when considering overall biofidelity. In other words, injury prediction depends not only on

the component being biofidelic (e.g., head) but also on the component being in the right place at the right time and in the right orientation (e.g., aspect of head contacting vehicle interior). This requires a novel analysis methodology that has not been used in impact biomechanics and is another objective of the current study, termed as Global Corridors for Motion Data.

Another effect of non-standard seating posture is multiplanar thorax loading during a dynamic event. While new generations of ATDs and computational models can measure three-dimensional thorax deflection, the relative injury risk of these three components and their interrelationship needs to be evaluated. Risk curves for each metric (A/P or "x" deflection, transverse plane or "x-y" deflection, sagittal plane or "x-z deflection, and multiplanar or "x-y-z" deflection) can be developed using survival analysis. However, it is important to determine which components of rib deflection best describe the optimal risk curve. The second objective of the current study is termed non-planar thorax injury risk curves.

4.1.2. Objectives

4.1.2.1. Global Corridors

Therefore, the first two objectives of the present study are to develop Global Corridors for Sensor and Motion Data for the small-female occupants. These data can help develop computational human body models, i.e., simulations for future parametric studies.

4.1.2.2. Non-Planar Thorax Injury Risk Curve

The third objective of the current study is to develop small female injury risk curves for sternum deflection in oblique impacts for the A/P, sagittal plane, transverse plane, and multiplanar deflections and determine the optimal risk curve using survival analysis.

4.2. METHODS

4.2.1. Global Corridors

4.2.1.1. PMHS Procurement and Preparation

This study's population was designed to represent healthy, adult, small females using the criteria shown in Table 4.2.1.1-1.

Table 4.2.1.1-1: Inclusion Criteria

Parameter	Range
Gender	Female
Age (years)	35 to 85
Height (cm)	146 to 162
Mass (kg)	38.5 to 54.5
QCT BMD (mg/cc)	>80

Select PMHS parameters were relaxed to expand the PMHS inventory in the following order:

- age
- mass
- height

All PMHS were screened for blood-borne pathogens (HIV, Hepatitis B and C, and syphilis). Additionally, PMHS with pre-existing injuries to the thorax (>3 rib fractures), hip replacement(s), and severe degeneration to the spine or thorax were excluded.

A total of 16 PMHS were used for this study. Eight PMHS were tested in each of the near- and far-side configurations. In both configurations, five PMHS were tested at the high-speed pulse, and three were tested at the low-speed pulse.

4.2.1.2. PMHS Instrumentation

As shown in Figure 4.2.1.2-1, the PMHS were instrumented with:

- Head→ Tetrahedral-nine-accelerometer package with three angular rate sensors (t-NAP+3ARS)
- T1→ Six-degree-of-freedom (6DOF) sensor (integrating triaxial linear accelerations and triaxial angular velocities)
- T8→ 6DOF sensor
- L2→ 6DOF sensor
- Sacrum→ 6DOF sensor

Figure 4.2.1.2-1: Schematic of instrumentation locations

As shown in Figures 4.2.1.2-2 and 4.2.1.2-3, optical markers (each consisting of four retroreflective targets) were placed at:

- dorsal head,
- spine (T1, T8, L2),
- sacrum,
- dorsal shoulders (bilaterally),
- frontal rib 4 (bilaterally),
- frontal rib 7 (bilaterally), and
- sternum.

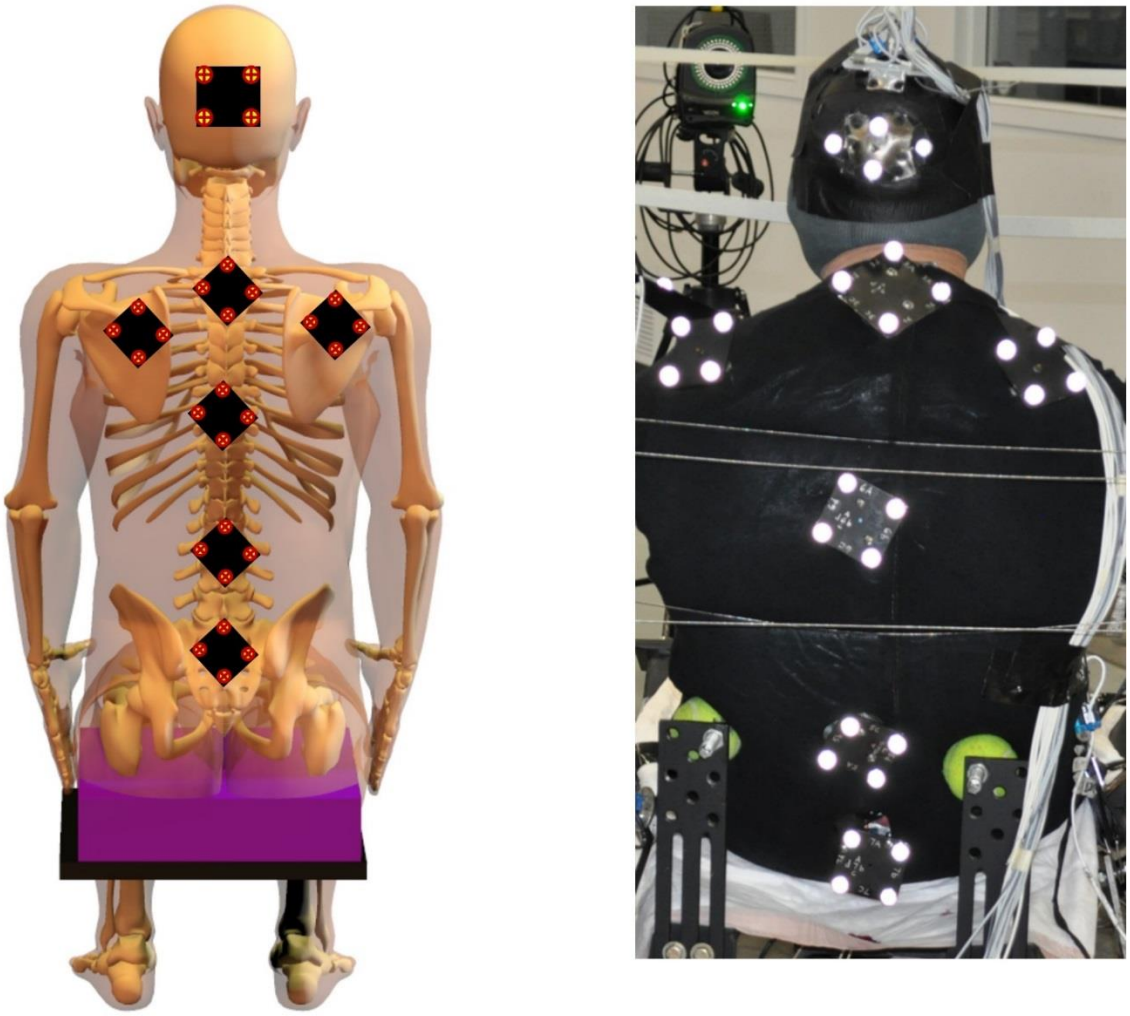

Figure 4.2.1.2-2: Left is schematic of dorsally placed markers at head, spine, sacrum, and shoulders. Right is a pre-test picture of a PMHS showing the markers at the same anatomic locations

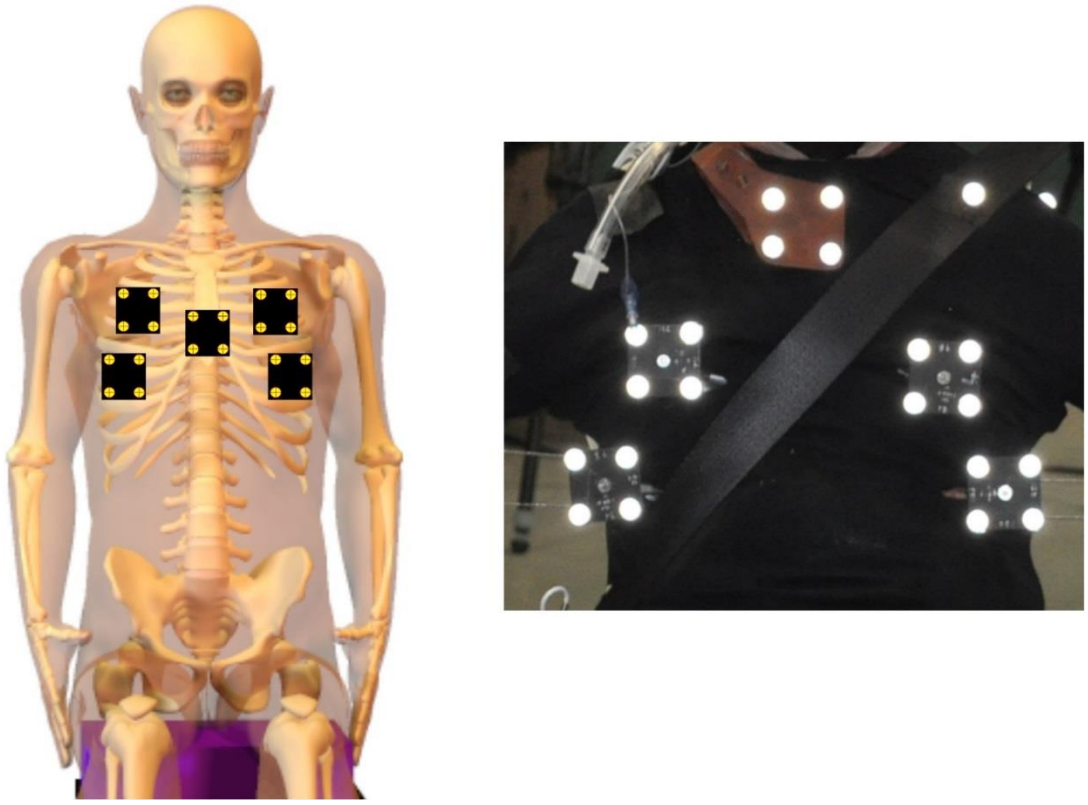

Figure 4.2.1.2-3: Left is schematic of ventrally placed markers at the ribs and sternum. Right is a pre-test picture of a PMHS showing the same anatomic locations

4.2.1.3. Boundary Conditions

A generic buck approximating the dimensions of a mid-sized sedan driver's seat—similar to those used in previous PMHS studies—was constructed [72]. The seat pan was flat with lateral wedges, and there were rigid restraints to stabilize the tibias and feet. An open-back-style torso support was used to permit direct line-of-sight to the optical markers placed on the dorsal aspect of the PMHS's head, spine, and sacrum. Two thin steel cables were routed horizontally across the dorsal aspect of the PMHS at the upper and lower thorax to support the pre-test position of the occupant. These support wires were connected between the two lateral posts and attached to inertial blocks released

with the onset of sled acceleration. This release mechanism was used to relieve the cable tension during the event and minimize potential interference with specimen instrumentation. The fore/aft and vertical positions of these cables were adjustable and placed to achieve the prescribed posture.

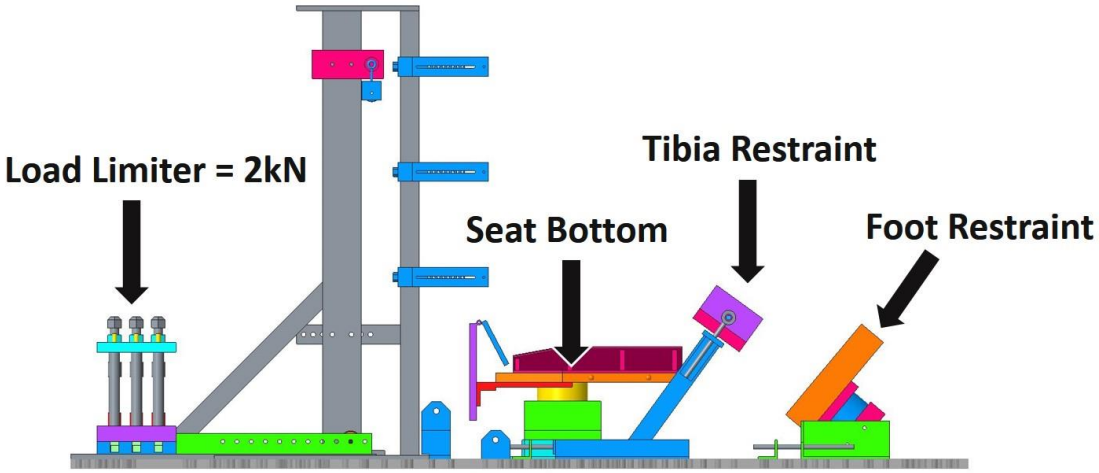

Figure 4.2.1.3-1: Lateral view of Standard Frontal Buck

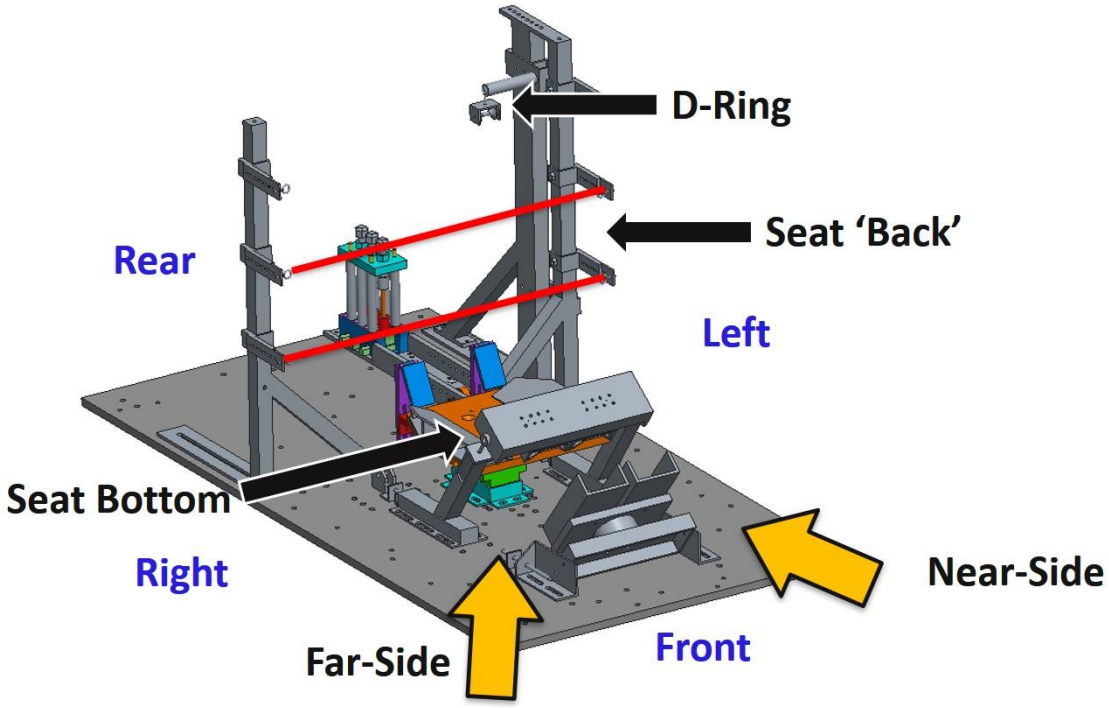

Figure 4.2.1.3-2: Oblique view of Standard Frontal Buck

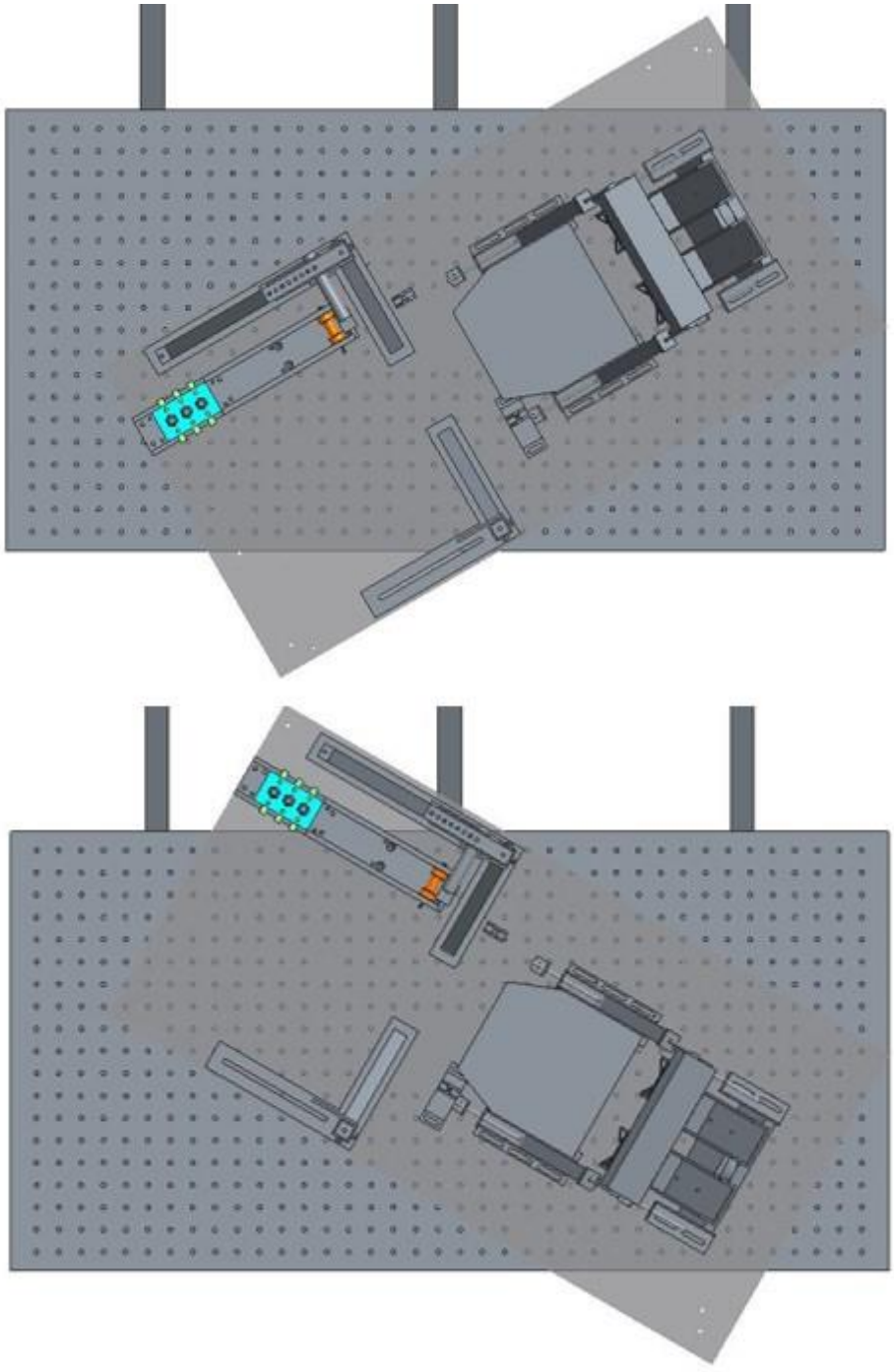

Figure 4.2.1.3-3: Alignment of buck on the sled in far- (top) and near-side (bottom) driver frontal impacts

A custom load-limiting device was used to limit the force to 2 kN. The seat-belt load-limiter controlled the shoulder belt force's magnitude by applying a frictional force via three pistons to brake pad material fixed onto a steel bar. The shoulder belt was connected to the steel bar, and the frictional force was adjusted to achieve the 2 kN limit by compressing a series of Belleville (disc) spring washers placed around the shaft of the piston.

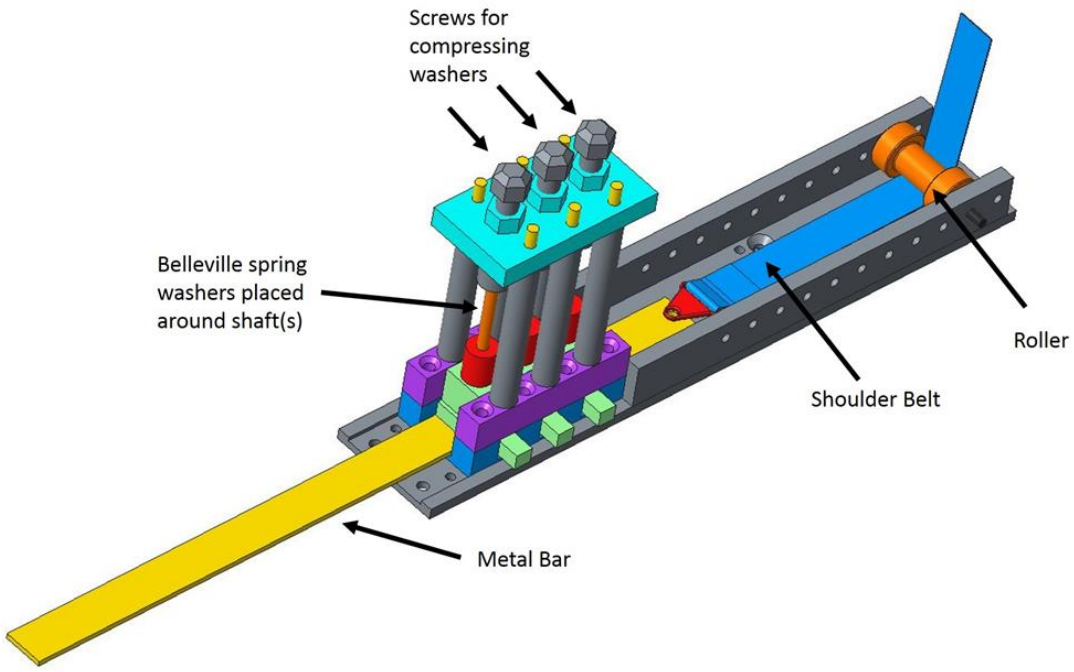

Figure 4.2.1.3-4: Schematic of a custom load-limiter system with shoulder belt attached to a metal bar. Three pistons compress a block of aluminum onto brake pad material welded to the metal bar. This exerts a frictional force on the brake pad, which acts as a load limiter to the shoulder belt.

4.2.1.4. Sled Instrumentation

The buck was instrumented with:

- Seat→ Six-axis load cell (triaxial force and triaxial moment) and triaxial linear accelerometer

- Knee restraint→ Two (2) six-axis load cells (triaxial force and triaxial moment) and triaxial linear accelerometer
- Foot→ Six-axis load cell (triaxial force and triaxial moment) and triaxial linear accelerometer
- Lap belt→ Two uniaxial load cells
- Shoulder belt→ Two uniaxial load cells

The sled was instrumented with a uniaxial accelerometer.

4.2.1.5. Sled Pulse

Sled acceleration was applied to the base of the buck via a servo acceleration sled (Seattle Safety, Seattle, WA) and recorded by a uniaxial linear accelerometer. Two pulses were used for the current study and were representative of a generic frontal crash pulse.

4.2.1.5.1. High-Speed Pulse

A 30 km/h, 9 g trapezoidal pulse shown in Figure 4.2.1.5.1-1 was used for ten specimens and designed as injury threshold tests.

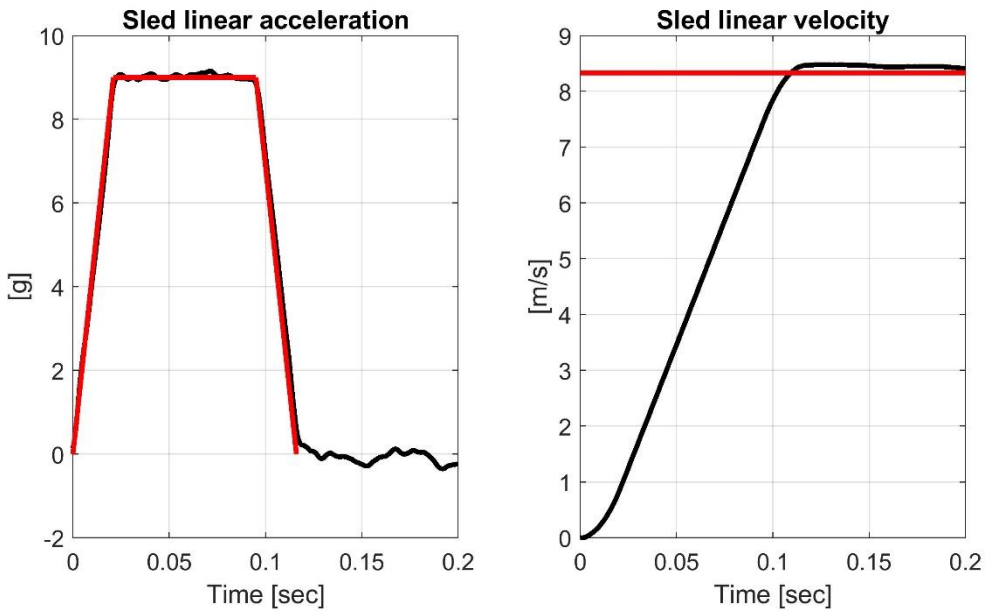

Figure 4.2.1.5.1-1: led acceleration on the left and velocity on the right for high-speed pulse

4.2.1.5.2. Low-speed pulse

A 15 km/h, 4.5 g trapezoidal pulse shown in Figure 4.2.1.5.2-1 was used for six specimens and designed as a non-injury threshold.

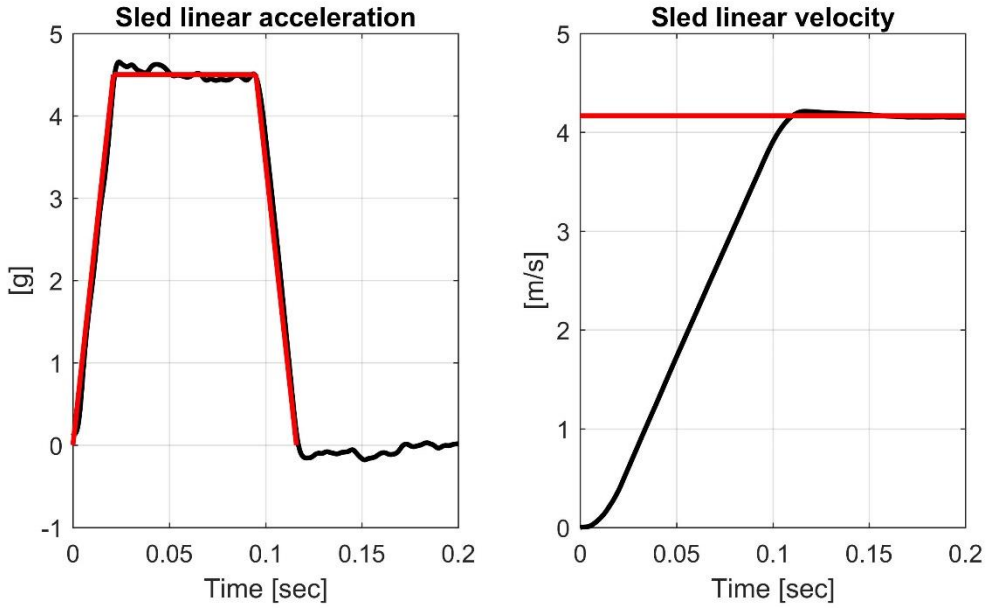

Figure 4.2.1.5.2-1: Sled acceleration on the left and velocity on the right for low-speed pulse

4.2.1.6. Test Matrix

The test matrix for the oblique small-female sled test series is shown in Table 4.2.1.6-1.

Table 4.2.1.6-1: Sequential Test Matrix

Test ID	Orientation	Pulse	Spec ID
NSFSC0120	Far-side	High	HS790
NSFSC0121	Far-side	High	HS905
NSFSC0122	Near-side	High	HS794
NSFSC0123	Near-side	High	HS802
NSFSC0124	Near-side	High	HS921
NSFSC0125	Far-side	High	HS913
NSFSC0126	Far-side	High	HS947
NSFSC0127	Near-side	High	HS903
NSFSC0128	Near-side	High	HS959
NSFSC0129	Far-side	High	HS957
NSFSC0130	Near-side	Low	HS970
NSFSC0132	Near-side	Low	HS979
NSFSC0134	Near-side	Low	HS1001
NSFSC0136	Far-side	Low	HS958
NSFSC0138	Far-side	Low	HS1009
NSFSC0140	Far-side	Low	HS1011

4.2.1.7. PMHS Positioning

Each specimen was seated in the generic buck seat and restrained at the thorax and pelvis with a three-point belt (international twill 13342 6-8% elongation, AEC Narrow Fabrics, Asheboro, NC) attached to a custom mechanism (described in Section 4.2.1.3) that limited the shoulder belt force to 2 kN. The shoulder belt was routed such that its horizontal angle from the shoulder was 25 degrees and 55 degrees in the coronal plane at the sternum. Lap and shoulder belt preloads, measured with a standard belt tensioning device (Tension Measurement Inc., Arvada, CO), was approximately 25 N. Knees and feet were placed in contact with rigid, angled restraints to minimize fore/aft

pelvis motion. Feet were secured to the restraint using straps wrapped around the ankles. Angled plates were fixed to the lateral edges of the seat pan to abate lateral pelvis excursion.

The pelvis was positioned such that the greater trochanter was within 5 mm of the 50th-percentile H-Point location. Femurs and tibias were angled 13 ± 1 degree and 32 ± 5 degrees from the horizontal plane. The torso was reclined 10 ± 1 degrees from vertical, as measured from the line connecting T3 and L1's spinous processes. The torso was held in position using two thin steel cables at the upper and lower dorsal thoracic spine. The head was positioned with the Frankfurt plane parallel to the ground and with no axial rotation. It was held in place with strips of masking tape. The torso cables and head support were inertially released during the initial acceleration of the sled. The buck was positioned 30 degrees clockwise (near-side) or counterclockwise (far-side) relative to the acceleration vector to simulate a driver's seat oblique frontal impact.

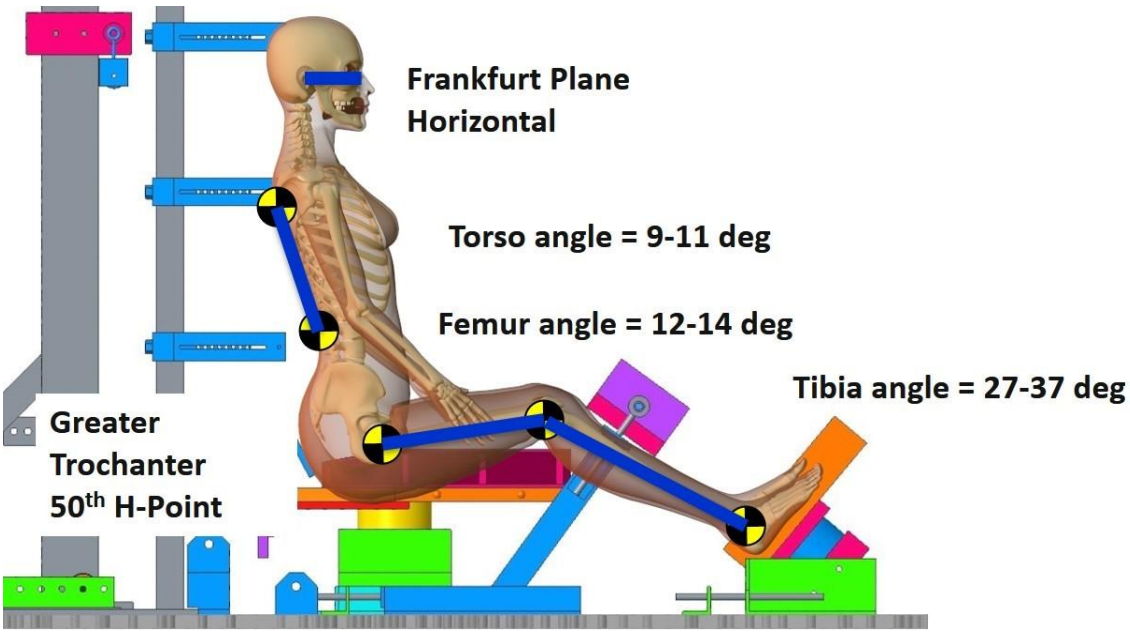

Figure 4.2.1.7-1: Schematic of occupant pre-test measurements in standard-impact buck

4.2.1.8. Data Collection

Analog data was collected with a data-acquisition system (DTS, Seal Beach, CA) at 20 kHz as per SAEJ211 (Dec. 2014). Occupant motion was captured with a 27-camera motion-capture system (Vicon, Oxford, UK) at 1000 Hz. The coordinate systems were consistent with SAE J211 (2014) and are described in Section 4.2.1.9.2.1. Standard photographs were taken of PMHS instrumentation and pre- and post-test positions on the sled.

4.2.1.9. Data Processing

4.2.1.9.1. Pre-test CT Scan Measurements

The markers' three-dimensional position, anatomic fiducials, and analog instrumentation were determined using 3D-Slicer derived from pre-test instrumented CT scans of the specimens. For the head, the Frankfurt plane was defined by the left and right superior auditory meatus, and the inferior margin of the left and right orbit were digitized, along with the boundaries of the tetrahedral NAP. The projected center-

of-gravity of the head on the left and right lateral aspect of the cranium were also digitized after the event.

For the spine, four points were collected on the vertebra's superior point at the ventral and dorsal locations in the mid-sagittal plane and right- and left-most lateral points on the transverse plane. Points on the superior aspect of the left and right inferior vertebral notch were also identified. At the pelvis, points on the left and right posterior superior iliac spine (PSIS) and left and right anterior superior iliac spine (ASIS) were collected. For the spine and pelvis, points on the posterior surface of the 6DOF sensor were selected. At the shoulders, the angulus acromialis, angulus inferior, and trigonum spina scapulae were digitized. Two points were digitized on the anterior portion of the sternum at the rib 4 joint and at the xiphoid process for the sternum. Finally, the anterior surface of the rib mount was collected for the ribs. The centers of the retroreflective targets were obtained at all anatomic locations.

4.2.1.9.2. Anatomic, Seat, Sensor, and Marker, Transformation Matrices

Transformation matrices for each sensor and marker group relative to the local anatomic coordinate were determined by:

1. calculating the local anatomic coordinate system from CT points,
2. calculating the 4 X 4 local-anatomic-to-global (CT space) transformation matrix,
3. calculating the local sensor coordinate system from CT points,
4. calculating the 4 X 4 local-sensor-to-global (CT space) transformation matrix,
5. calculating the local marker coordinate system from CT points,
6. calculating the 4 X 4 local-marker-to-global (CT space) transformation matrix,

7. multiplying 2 and 4 (inverted) to determine the anatomic to sensor transformation matrix, and
8. multiplying 2 and 6 (inverted) to determine the anatomic-to-marker transformation matrix.

Details are given in the following sections.

4.2.1.9.2.1. Coordinate Systems

4.2.1.9.2.1.1. Head local coordinate system

The head coordinate system was defined by taking midpoints of the left and right orbit and the left and right auditory meatus. A reference vector was created by subtracting the mid-orbit point from the mid-auditory point. The +y axis was determined by subtracting the right auditory meatus point from the left, the +z by crossing the reference vector with the +y axis, and the +x axis by crossing the +z axis with the +y axis. The origin of the head anatomic system was calculated by averaging the projected left and right center-of-gravity points on the cranium.

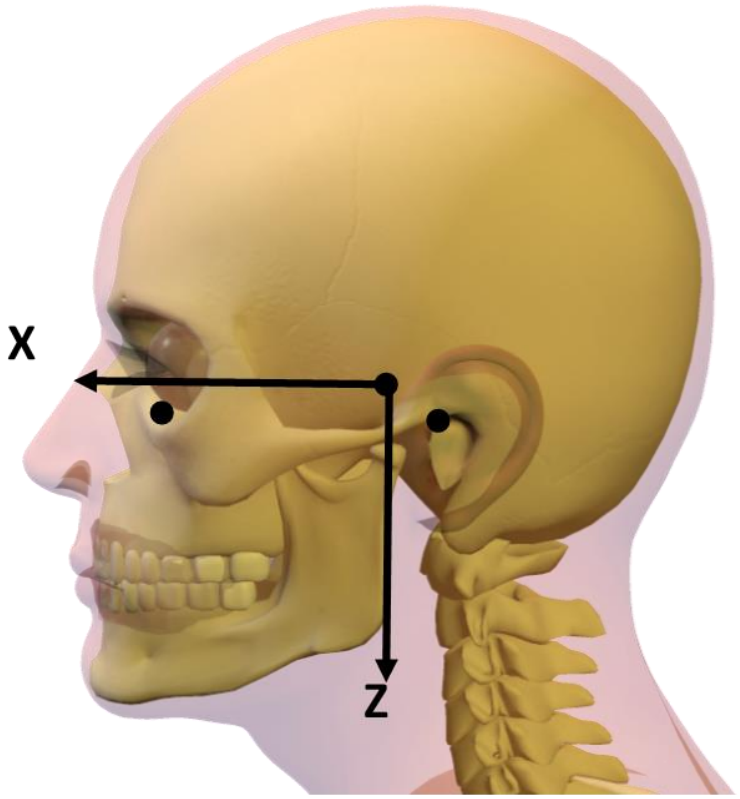

Figure 4.2.1.9.2.1.1-1: Head coordinate system with the origin at the center-of-gravity. The x-y plane is parallel to the Frankfurt plane. The +z-axis runs superior to inferior and is perpendicular to the x-y plane.

4.2.1.9.2.1.2. Spine local coordinate system

The center of the superior endplate was determined by averaging the four points on that surface. The inferior endplate center was likewise calculated. A reference vector was created by subtracting the inferior endplate center point from the superior endplate center point. The +y axis was determined by subtracting the right vertebral notch point from the left vertebral notch point, the +x axis by crossing the +y axis with the reference vector +z axis by crossing the +x axis with the +y axis. The spine coordinate system's origin was defined as the average of the superior and inferior endplate center points.

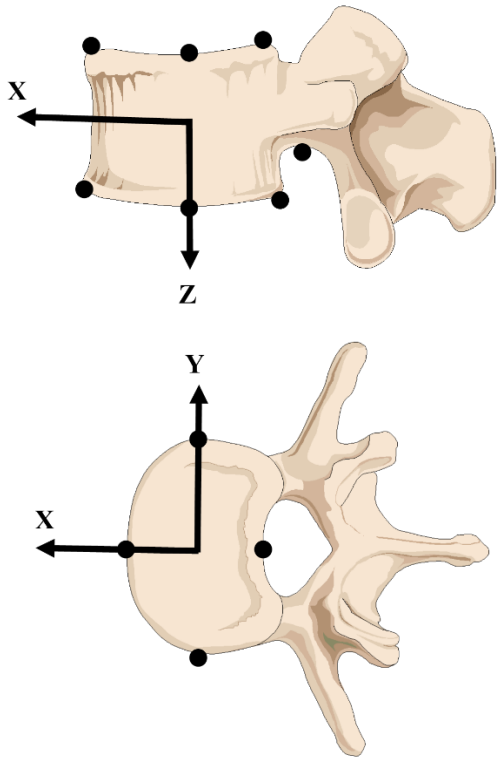

Figure 4.2.1.9.2.1.2-1: Spine coordinate system with the origin at the center of the vertebral body

4.2.1.9.2.1.3. Pelvis local coordinate system

The midpoints between the left and right ASIS and left and right PSIS were first calculated. A reference line was determined by subtracting the ASIS midpoint from the PSIS midpoint. The +y axis was determined by subtracting the right ASIS from the left ASIS, the +z axis by crossing the reference line with the +y axis, and the +x axis by crossing the +y axis with the +z axis. The origin of the pelvis was the PSIS midpoint.

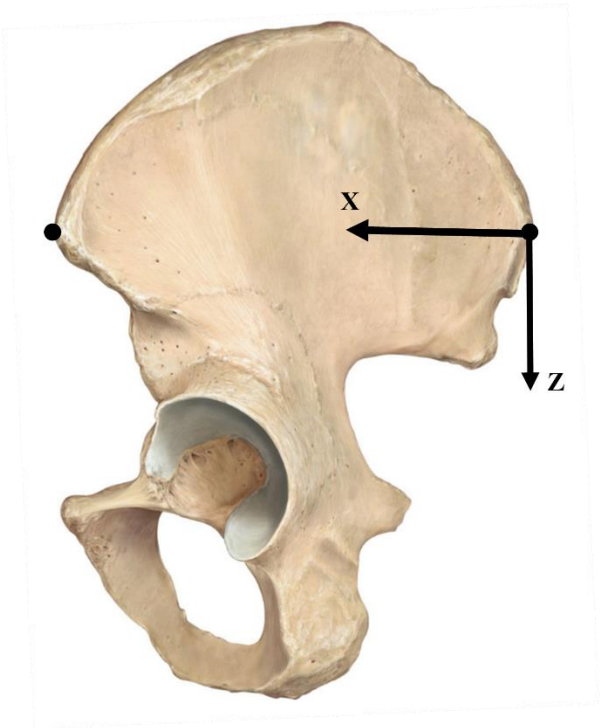

Figure 4.2.1.9.2.1.3-1: Pelvis coordinate system with the origin at the center of the left and right PSIS

4.2.1.9.2.1.4. Sternum local coordinate system

The midpoint between the left and right rib 4 at the synovial joint between the costal cartilage and the sternum body was calculated. A reference line was determined by

subtracting the xiphoid process's location from the midpoint of rib 4. The +y axis was determined by subtracting the point of right rib 4 from that of left rib 4, the +x axis by crossing the +y axis with the reference line, and the +z by crossing the +x axis with the +y axis. The origin of the pelvis was the rib 4 midpoint.

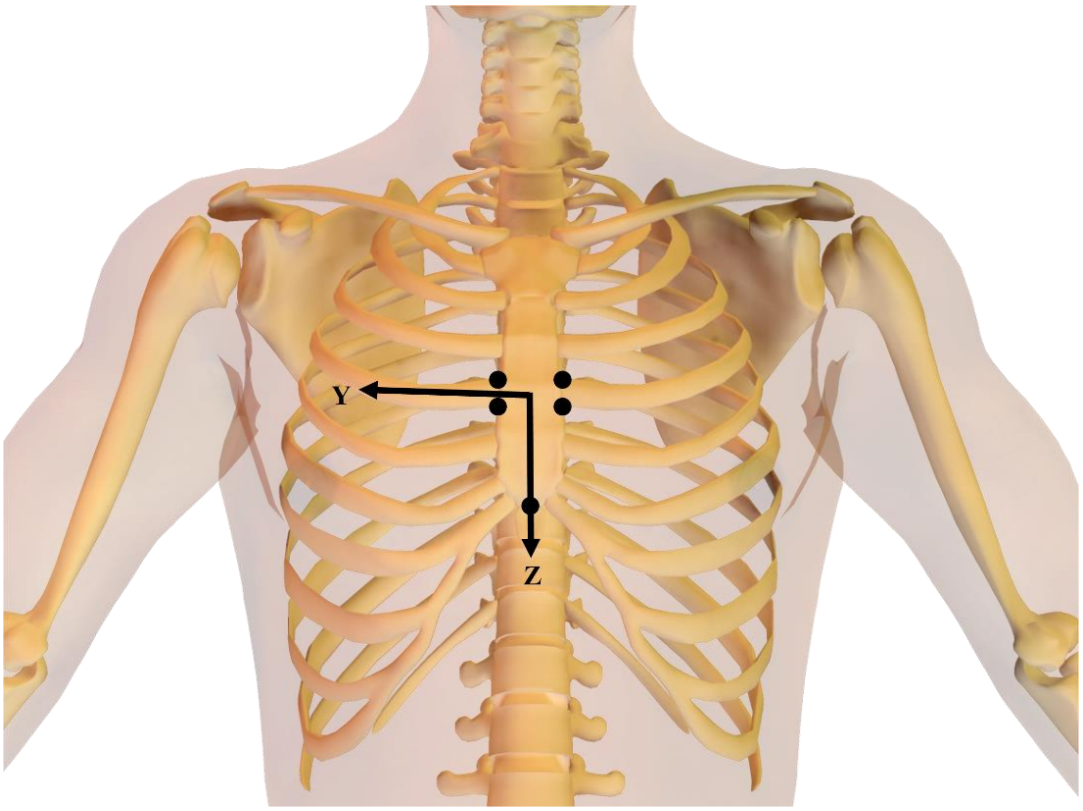

Figure 4.2.1.9.2.1.4-1: Sternum coordinate system with the origin at the center of the left and right rib 4-sternum joints

4.2.1.9.2.1.5. Rib local coordinate system

The rib coordinate system was determined by using points on the boundaries of the mount plate fixed laterally to the costochondral joint. Four points were used: the superolateral (SL), inferolateral (IL), superomedial (SM), and inferomedial (IM). The

medial and lateral midpoints were calculated separately, averaging the SM and IM (medial midpoint) and the IL and IM (lateral midpoint). Similarly, superior and inferior midpoints were determined by averaging the SM and SL (superior midpoint) and IM and IL (inferior midpoint). A reference line was calculated by subtracting the superior midpoint from the inferior midpoint. Next, the +y axis was determined for the left ribs by subtracting the medial midpoint from the lateral midpoint. The +y axis was determined for the right ribs by subtracting the lateral midpoint from the medial midpoint. For both sides, the +x axis was determined by crossing the +y axis with the reference line and the +z axis by crossing the +x axis with the +y axis. The rib coordinate system's origin was the average of the SM, SL, IM, and IL points.

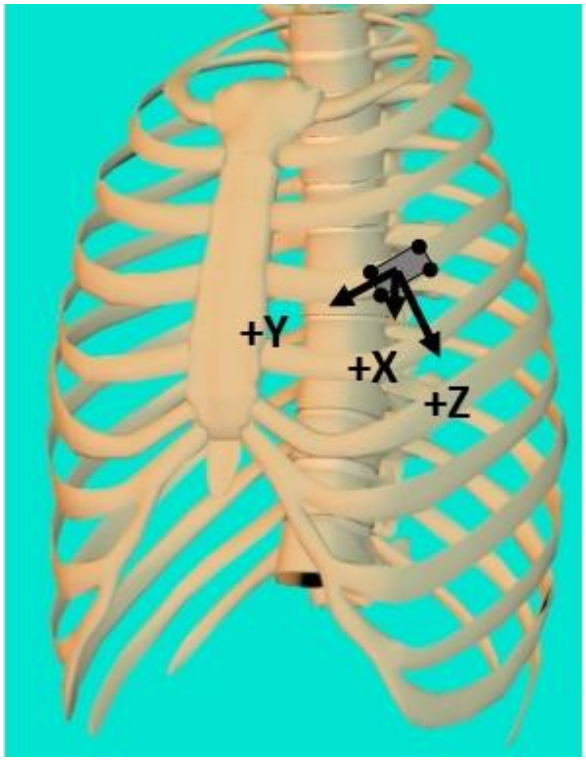

Figure 4.2.1.9.2.1.5-1: Rib (left rib 4) coordinate system with the origin at the center of the rib mount

4.2.1.9.2.1.6. Seat local coordinate system

Front and rear midpoints were calculated using points on the front left and right and rear left and right of the seat. A reference line was constructed by subtracting the right rear point on the seat from the left rear point. The +x axis was determined by subtracting the front midpoint from the rear midpoint, the +z axis by crossing the +x axis with the reference line, and the +y axis by crossing the +z axis with the +x axis. The seat coordinate system's origin is on the centerline of the seat at the 50% percentile h-point location.

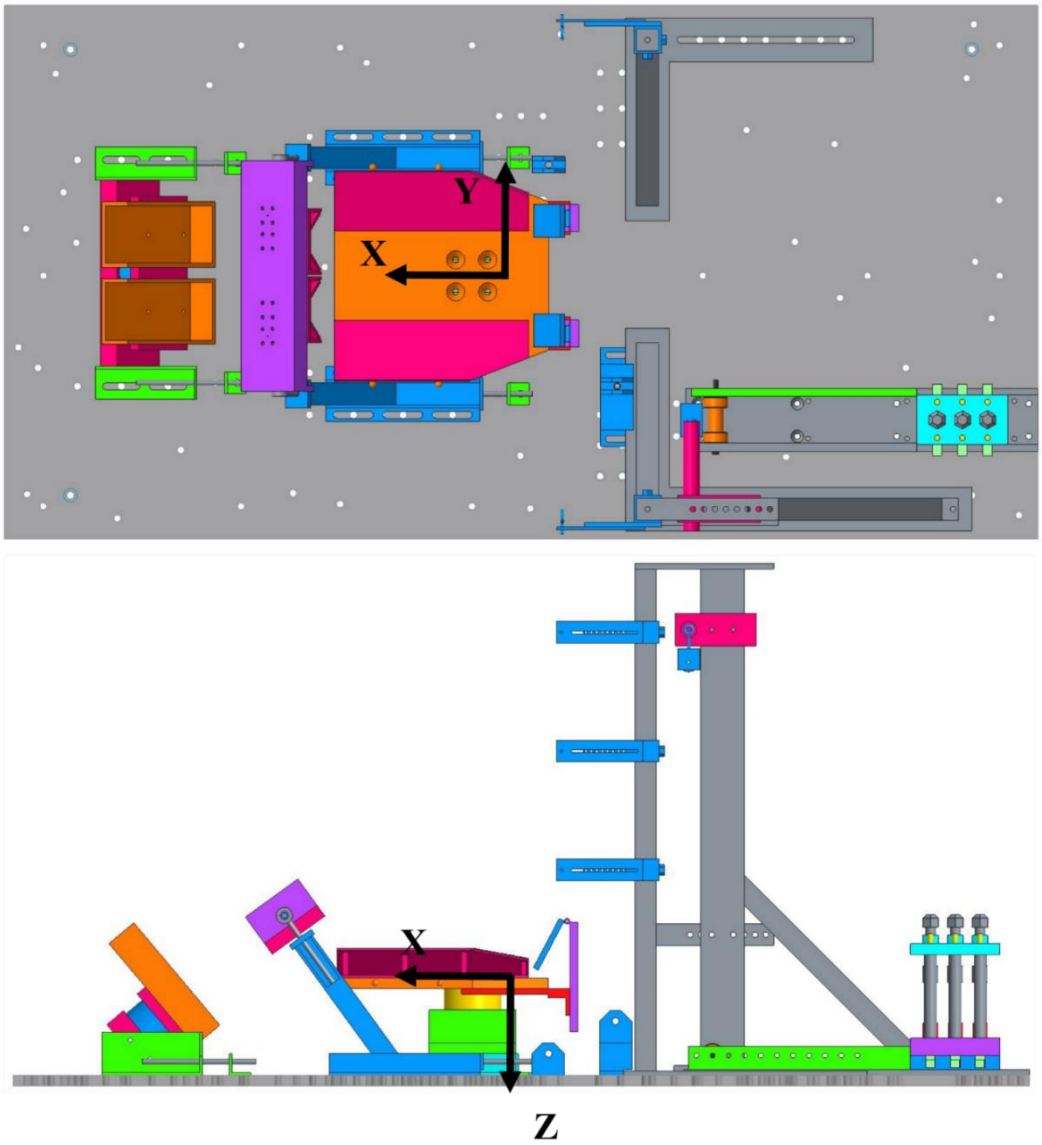

Figure 4.2.1.9.2.1.6-1: Seat coordinate system with the origin at the 50th-percentile h-point location along the centerline of the seat.

4.2.1.9.2.1.7. Motion-capture local coordinate system

The origin and orientation of the motion capture local coordinate system was defined by the L-frame marker wand placement during camera calibration. The frame was placed with the origin near the reaction mass of the servo-brake such that the XY plane was parallel to the ground with the +X axis pointed down the track. The +Z axis was pointed

upwards. Figure 4.2.1.9.2.1.7-1 shows the position of the wand and orientation of the motion-capture coordinate system.

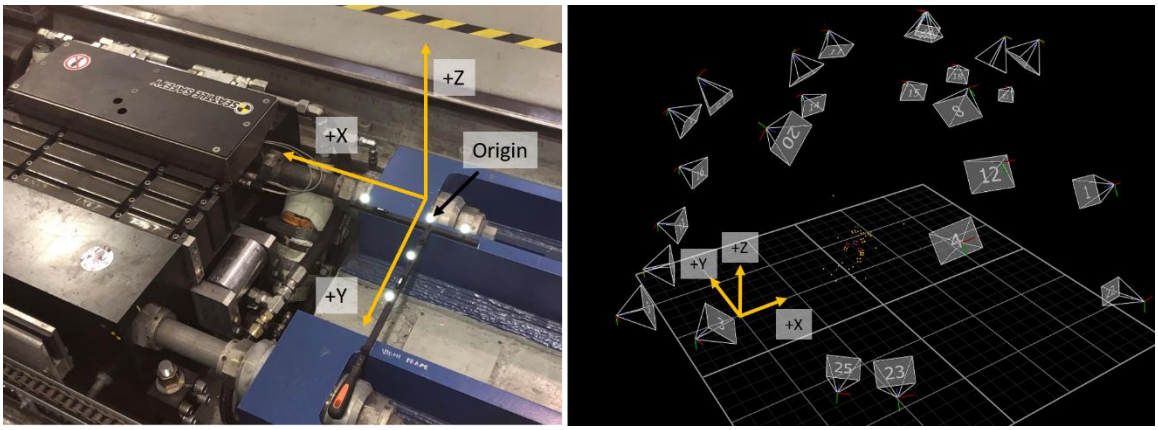

Figure 4.2.1.9.2.1.7-1: Motion capture coordinate system with a picture of the L-frame wand placed at the base of the reaction mass of the servo-brake mechanism is shown on the left. The reconstructed volume showing the origin and orientation of the coordinate system, camera positions, and pre-test position of the occupant is shown on the right.

4.2.1.9.2.1.8. CT local coordinate system

The orientation of the CT coordinate system was determined at the time of the scan. The +Z axis was coincident with the long axis of the scanner table in the inferior-to-superior direction. The +X axis was left to right, and the +Y axis was posterior to superior. The origin was determined after the scan and set to the center of the reconstructed volume.

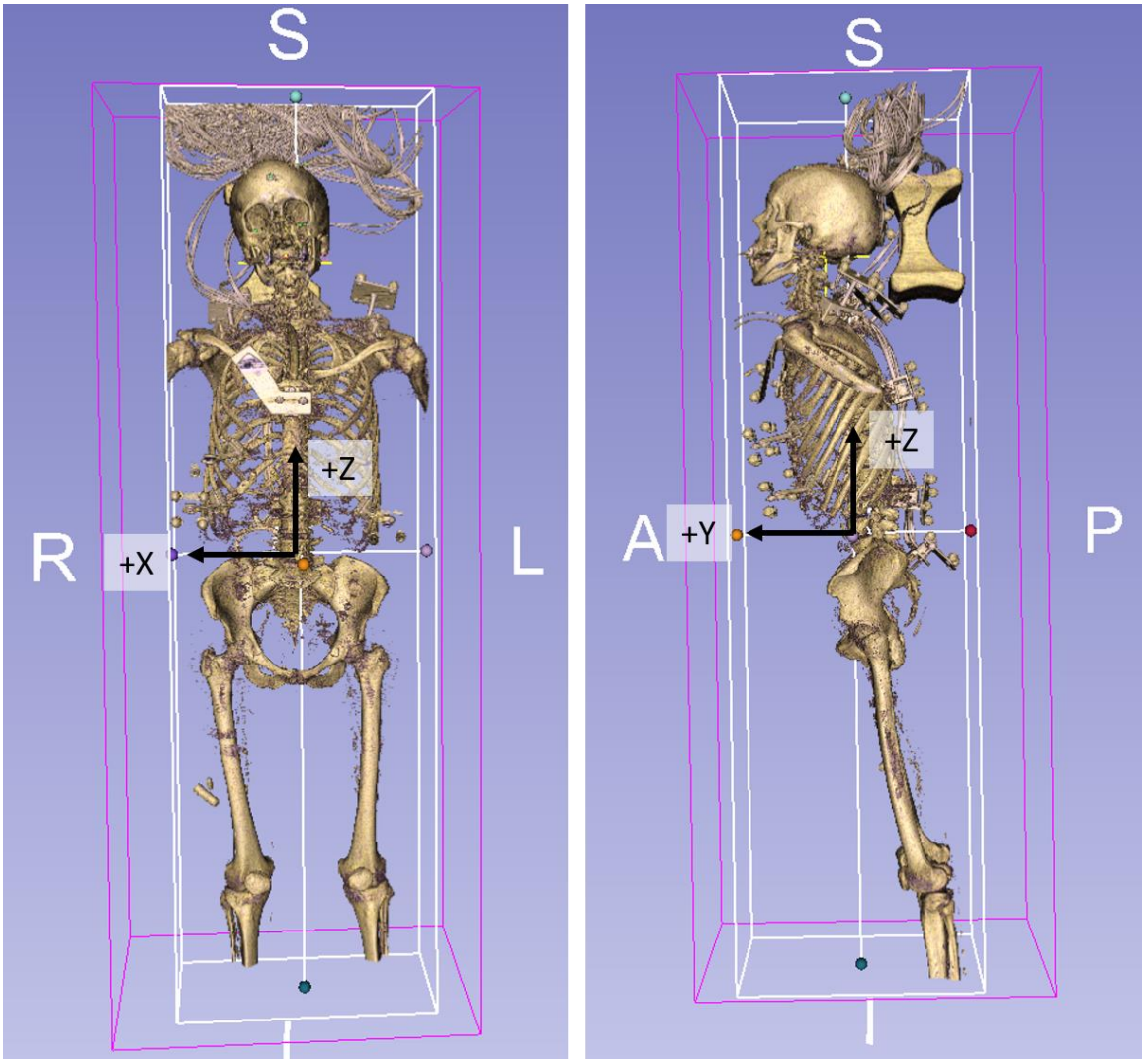

Figure 4.2.1.9.2.1.8-1: CT coordinate system showing a coronal view of the reconstructed volume on left and sagittal on right

4.2.1.9.2.2. Sensor Local-Coordinate-System Calculation

4.2.1.9.2.2.1. Head (t-NAP+3ARS)

Four points were digitized on each of the three faces of the t-NAP: three points on the surface of the face and one on the origin accelerometer. The three surface points were used to define a plane, and the accelerometer point combined with the DAS polarity information was used to determine the local sensor axes. Figure 4.2.1.9.2.2.1-1 shows

the points digitized on the t-NAP, the sensor origin's location, and the normal vectors to the x/y/z faces.

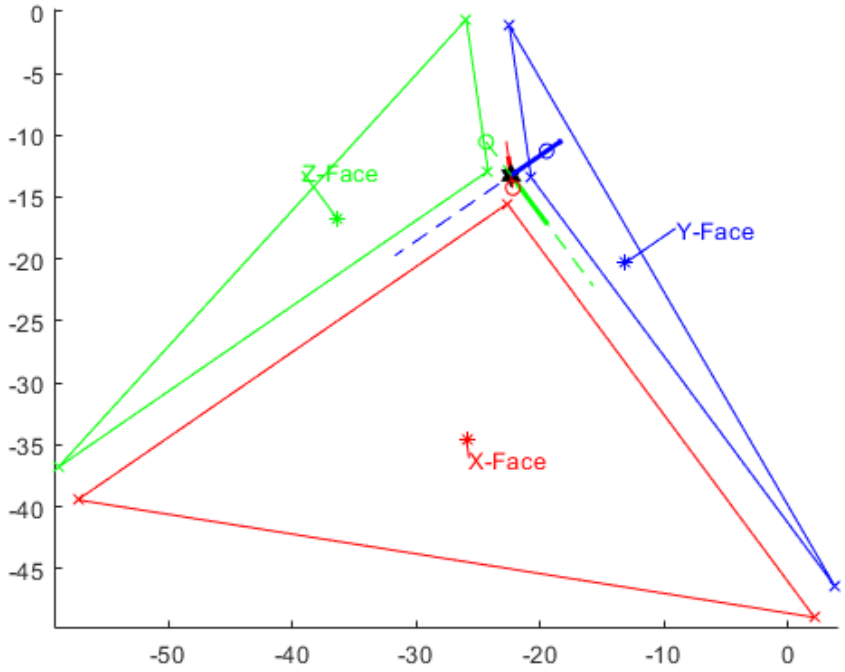

Figure 4.2.1.9.2.2.1-1: The X, Y, and Z faces of t-NAP with the sensor's origin shown at the apex. Outward normal to faces are shown at the center of the triangle. The orientation of local sensor axes is shown in solid colors at the origin.

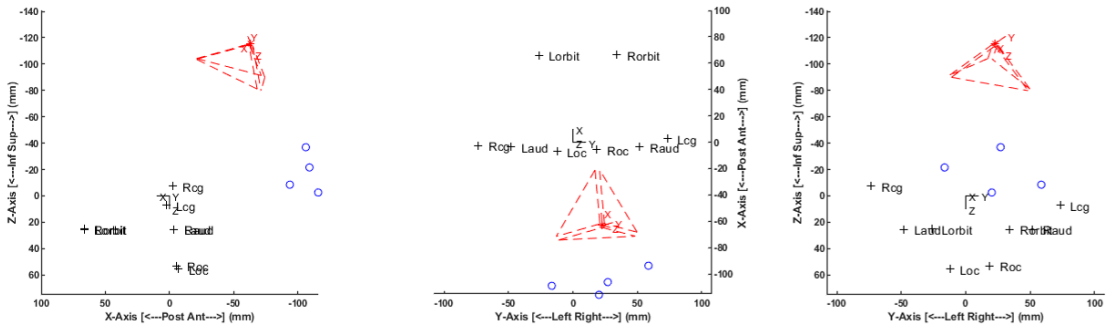

Figure 4.2.1.9.2.2.1-2: Local sensor orientations for t-NAP are shown in the head local coordinate system, along with head anatomic points

4.2.1.9.2.2.2. Spine and pelvis (6DOF)

The four points digitized on the sensor's stamped surface were combined with engineering drawings of the sensor to determine its local orientation (Figure 4.2.1.9.2.2.2-1). Points 1 and 2 were located on the edge of the sensor where the wires exited the housing, and Points 3 and 4 were located on the opposite edge. The naming sequence was such that Points 2, 3, and 4 were clockwise from the previous point when looking normal to the sensor's stamped surface.

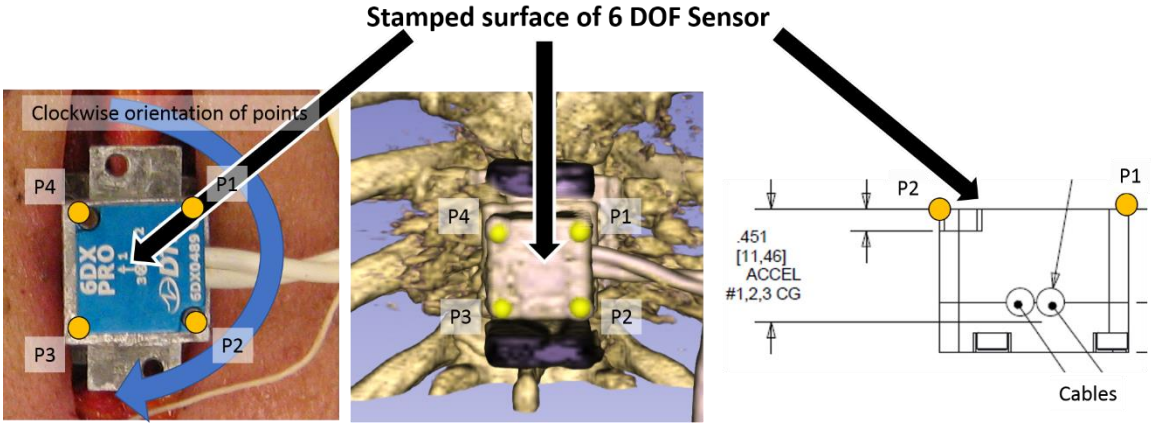

Figure 4.2.1.9.2.2.2-1: Left is a picture of the 6DOF sensor on a spine mount with the naming scheme of sensor orientation points 1-4. The middle is a CT scan of the vertebrae's sensor before the test shows the digitized points. Right is the 6DOF sensor drawing from the surface of the wires' exit point and the distance from the stamped surface to the accelerometer CG.

The local axes are labeled on the sensor's top surface as axes 1, 2, and 3 (Figure 4.2.1.9.2.2.2-2), hereafter referred to as the S1, S2, and S3 axes. The positive S1 axis is normal to and points in the opposite direction of the surface with the wires. The positive S3 is normal to the stamped surface and points towards the sensor base. The

positive S2 axis is perpendicular to the S1 and S3 axes and is determined by crossing the S3 axis into the S1 axis.

Figure 4.2.1.9.2.2.2-2: The stamped surface of the 6DOF sensor showing the S1, S2, and S3 axes

The S1, S2, and S3 axes were determined from the four CT points. First, two reference lines, R1 and R2, were calculated. R1 was defined by subtracting Point 1 from Point 2 and R2 by subtracting Point 3 from Point 2. The S3 axis was then determined by crossing R2 into R1. The S2 axis was calculated by crossing the S3 axis with the R2 axis, and the S1 axis was determined by crossing the S2 axis into the S3 axis. The calculated local sensor axes were then combined with the sensor polarity information from the DAS, as well as relabeling the S1, S2, and S3 axes X, Y, and Z depending on which local sensor axis most closely corresponded to the local anatomic axes (Figure 4.2.1.9.2.2.2-3).

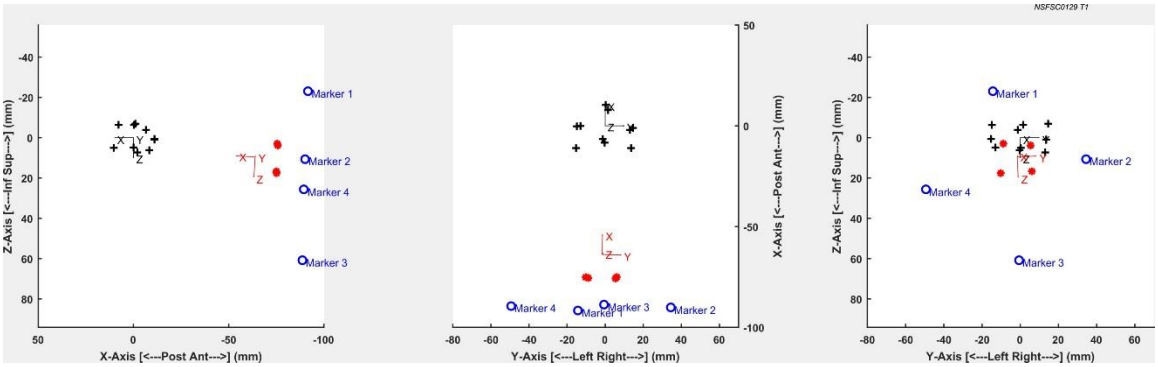

Figure 4.2.1.9.2.2.2-3: The four 6DOF sensor points and local sensor axes in red, the anatomic points and anatomic coordinate system in black, and the Vicon markers in blue

4.2.1.9.2.2.3. Restraint load cells (seat, knee, and foot)

The orientations of the load cells at the seat, knee, and foot relative to the ground were calculated by measuring the angular offset of the +x axis (backward to forwards) with respect to the horizontal (Figures 4.2.1.9.2.2.3-1 through 4.2.1.9.2.2.3-3). Note that the seat load cell angular offset was zero.

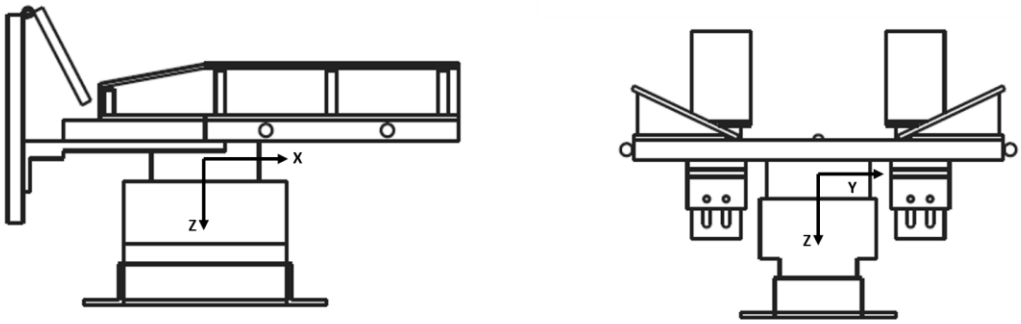

Figure 4.2.1.9.2.2.3-1: Seat bottom load cell axes with (left) side view and the (right) view from behind

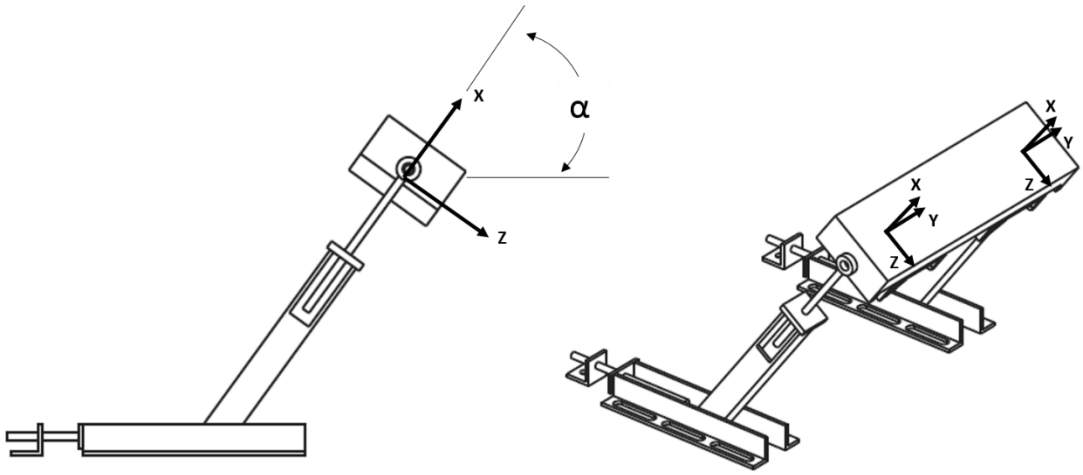

Figure 4.2.1.9.2.2.3-2: Tibia load cell axes with (Left) a side view and the angle α, which is the angle between the +x axis and the ground, and (Right) an oblique view of the orientation of the two load cells behind the solid bracket

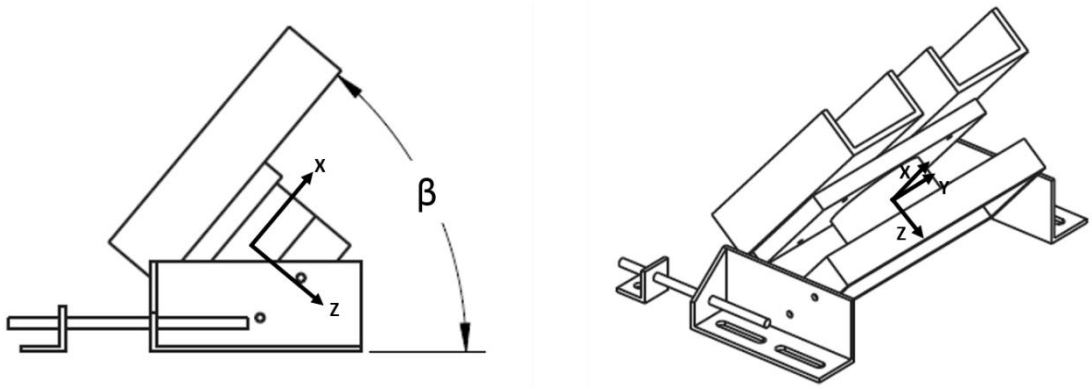

Figure 4.2.1.9.2.2.3-3: Foot load cell axes with (Left) a side view and the angle β, the angle between the +x axis and the ground, and (Right) an oblique view of the orientation of the load cell.

4.2.1.9.2.3. Motion-Capture Marker Local-Coordinate-System Calculation

Two sets of identical marker local coordinate systems were defined at each anatomic coordinate system. The first was calculated using the digitized coordinates of the marker centers from the pretest CT scan. The second was determined at each time

point from the measured three-dimensional marker trajectories. Figure 4.2.1.9.2.3-1 shows the marker labeling scheme.

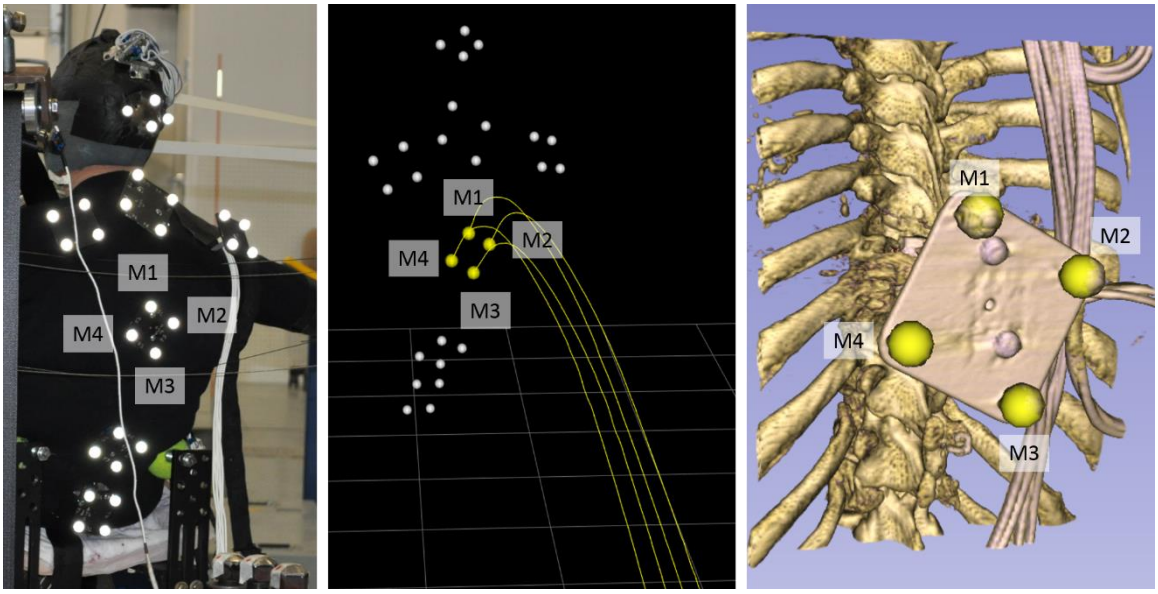

Figure 4.2.1.9.2.3-1: Left shows a pre-test photo of the dorsal side of the occupant and the labeling scheme for the T8 markers. The middle is the reconstructed T8 trajectories from the impact test and marker labels. Right is a 3-D volume of the CT scan showing the identical labeling scheme on the T8 marker plate.

The local marker coordinate system was determined by calculating two reference lines (R1 and R2). The first (R1) was found by subtracting M2 from M4 and the second (R2) by subtracting M3 from M4. The origin of the marker coordinate system was defined at M1, the R1 line was defined as the Z' axis, the cross product of R2 and R1 was determined the X' axis, and the Y' axis was computed by crossing the Z' axis with the X' axis. Figure 4.2.1.9.2.3-2 shows the CT scan calculation, and Figure 4.2.1.9.2.3-3 shows the same calculation for the motion-capture data at one point in time. Note that the local marker coordinate system is calculated for the motion-capture data at every time-step.

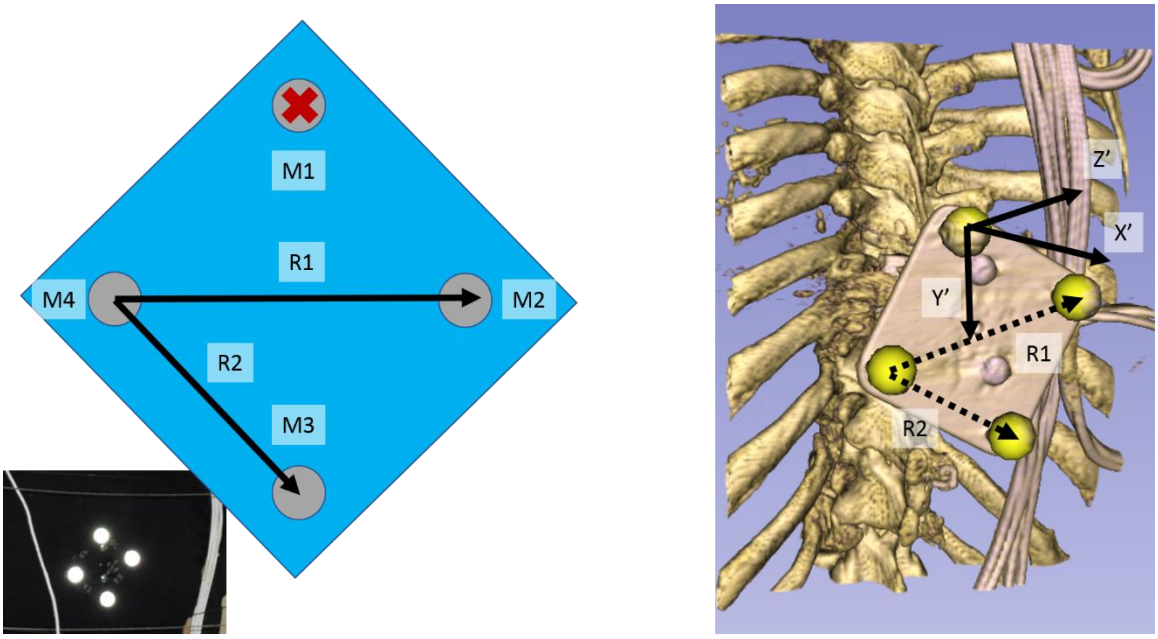

Figure 4.2.1.9.2.3-2: Left shows a diagram of the spine mounting plate with marker labeling scheme. The marker coordinate system's origin is Marker 1 (M1) (shown by red x). The first reference line (R1) is between Marker 2 (M2) and Marker 4 (M4). The second reference line (R2) is between M3 and M4. Right shows a reconstructed 3-d volume from a pre-test CT scan. The marker plate and markers are indicated with the two reference lines and the computed local marker coordinate system with the origin at Marker 1.

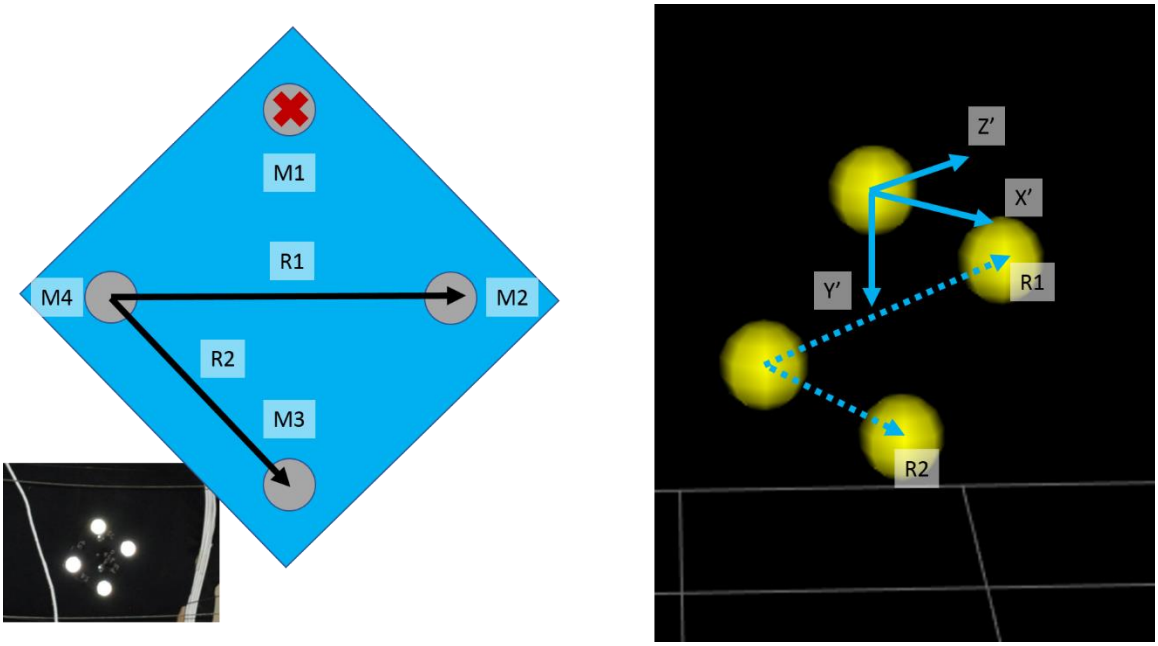

Figure 4.2.1.9.2.3-3: Left shows a diagram of the spine mounting plate with marker labeling scheme. The origin of the marker coordinate system is Marker 1 (M1, indicated by red x). The first reference line (R1) is between Marker 2 (M2) and Marker 4 (M4). The second reference line (R2) is between M3 and M4. Right shows the reconstructed markers from the motion-capture system before impact. The markers are shown with the two reference lines and the computed local marker coordinate system with the origin at Marker 1.

4.2.1.9.2.4. Sensor and Marker to Anatomic Transformation Matrix

Using the anatomic rotation matrix ($R_{Anat/CT}$) described in 4.2.1.9.2.1 and the sensor rotation matrix ($R_{Sensor/CT}$) described in 4.2.1.9.2.2, the transformation matrix relating the sensor to the anatomic coordinate system was calculated using Equation 4.2.1.9.2.4-1.

$$[R]_{Anat/Sensor} = [R]_{Anat/CT} * [R]_{CT/Sensor}$$ ***Equation 4.2.1.9.2.4-1***

where:

$$[R]_{CT/Sensor} = [R]_{Sensor/CT}{}^{-1}$$ ***Equation 4.2.1.9.2.4-2***

Similarly, the anatomic rotation and marker rotation matrix ($R_{Marker/CT}$) described in 4.2.1.9.2.3 were used to calculate the transformation matrix relating the marker to the anatomic coordinate system as shown in Equation 2.1.9.2.4-3.

$$[R]_{Anat/Marker} = [R]_{Anat/CT} * [R]_{CT/Marker}$$ ***Equation 4.2.1.9.2.4-3***

where:

$$[R]_{CT/Marker} = [R]_{Marker/CT}{}^{-1}$$ ***Equation 4.2.1.9.2.4-4***

Each rotation matrix is a 4 X 4 matrix and generically defined as:

$$[R]_{A/B} = \begin{bmatrix} i_a \cdot i_b & i_a \cdot j_b & i_a \cdot k_b & \mathrm{d_x} \\ j_a \cdot i_b & j_a \cdot j_b & j_a \cdot k_b & \mathrm{d_y} \\ k_a \cdot i_b & k_a \cdot j_b & k_a \cdot k_b & \mathrm{d_z} \\ 0 & 0 & 0 & 1 \end{bmatrix}$$ ***Equation 4.2.1.9.2.4-5***

where:

- i_a, j_b, and k_a are the unit vectors of XYZ system in A,
- i_b, j_b, and k_b are the unit vectors of XYZ system in B, and
- d_x, d_y, and d_z are the coordinates of the B origin in the A reference system.

4.2.1.9.3. PMHS-Sensor Local Anatomic Calculations

4.2.1.9.3.1. Head

The NAP used combinations of orthogonally mounted pairs of accelerometers [47] to calculate angular acceleration (Equations 4.2.1.9.3.1-1 through 4.2.1.9.3.1-3). A picture and schematic of the NAP are shown in Figure 4.2.1.9.3.1-1.

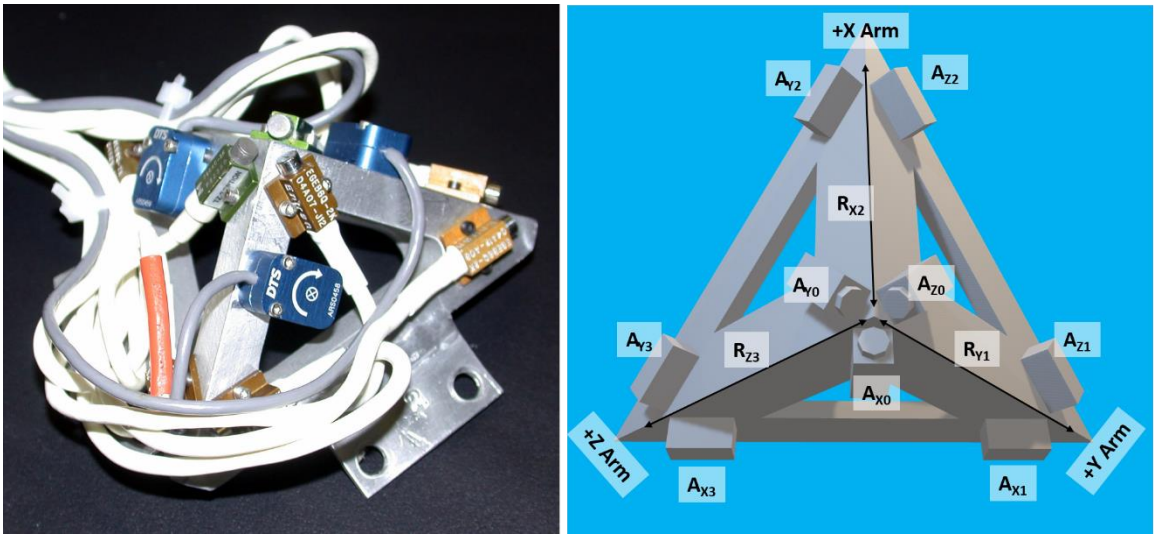

Figure 4.2.1.9.3.1-1: Left shows a picture of the t-NAP with 3 ARS. Right is a schematic of the accelerometer layout and arm lengths.

Equations 4.2.1.9.3.1-1 through 4.2.1.9.3.1-3 use the naming convention shown in Figure 4.2.1.9.3.1-1 (right).

$$\alpha_X = \frac{A_{Z1} - A_{Z0}}{2R_{Y1}} - \frac{A_{Y3} - A_{Y0}}{2R_{Z3}}$$

Equation 4.2.1.9.3.1-1

$$\alpha_Y = \frac{A_{X3} - A_{X0}}{2R_{Z3}} - \frac{A_{Z2} - A_{Z0}}{2R_{X2}}$$

Equation 4.2.1.9.3.1-2

$$\alpha_Z = \frac{A_{Y2} - A_{Y0}}{2R_{X2}} - \frac{A_{X1} - A_{X0}}{2R_{Y1}}$$ ***Equation 4.2.1.9.3.1-3***

Note that the angular accelerations calculated in the above equations are relative to the sensor coordinate system. The anatomic angular accelerations were determined by:

$$\{\propto\}_{Anat} = [R]_{Anat/Sensor}\,\{\propto\}_{Sensor}$$ ***Equation 4.2.1.9.3.1-4***

Similarly, the anatomic angular velocities were obtained from the triaxial angular rate sensors mounted to the t-NAP and calculated using Equation 4.2.1.9.3.1-5.

$$\{\omega\}_{Anat} = [R]_{Anat/Sensor}\,\{\omega\}_{Sensor}$$ ***Equation 4.2.1.9.3.1-5***

The head CG linear accelerations were determined by first aligning the triaxial accelerometer at the origin of the t-NAP (A_{X0}, A_{Y0}, A_{Z0}) with the anatomic coordinate system, as shown in Equation 4.2.1.9.3.1-6.

$$\{a_0\}_{Anat} = [R]_{Anat/Sensor}\,\{a_0\}_{Sensor}$$ ***Equation 4.2.1.9.3.1-6***

Using α_{anat}, ω_{anat}, $a0_{anat}$, and r_s, the head anatomic linear accelerations were determined using Equation 4.2.1.9.3.1-7.

$$\vec{a}_{anat} = \vec{a}_{0_{anat}} - [\vec{\alpha}_{anat} \times \vec{r}_s + \vec{\omega}_{anat} \times (\vec{\omega}_{anat} \times \vec{r}_s)]$$ ***Equation 4.2.1.9.3.1-7***

where r_s is the position of the sensor in the head coordinate system and corresponds to the first three rows of the fourth column of the $[R]_{Anat/sensor}$ rotation matrix

Equation 4.2.1.9.3.1-7 expands to:

$$a_{anat_x} = a_{0_{anat_x}} + r_{s_x}\left(\omega_{anat_y}^2 + \omega_{anat_z}^2\right) - r_{s_y}\left(\omega_{anat_x}\omega_{anat_y} - \alpha_{anat_z}\right) - r_{s_z}\left(\omega_{anat_x}\omega_{anat_z} + \alpha_{anat_y}\right)$$

Equation 4.2.1.9.3.1-8

$$a_{anat_y} = a_{0_{anat_y}} - r_{s_x}\left(\omega_{anat_x}\omega_{anat_y} + \alpha_{anat_z}\right) + r_{s_y}\left(\omega_{anat_x}^2 + \omega_{anat_z}^2\right) - r_{s_z}\left(\omega_{anat_y}\omega_{anat_z} - \alpha_{anat_x}\right)$$

Equation 4.2.1.9.3.1-9

$$a_{anat_z} = a_{0_{anat_z}} - r_{s_x}\left(\omega_{anat_x}\omega_{anat_z} - \alpha_{anat_y}\right) - r_{s_y}\left(\omega_{anat_y}\omega_{anat_z} + \alpha_{anat_x}\right) + r_{s_z}\left(\omega_{anat_x}^2 + \omega_{anat_y}^2\right)$$

Equation 4.2.1.9.3.1-10

4.2.1.9.3.2. Occipital Condyle (OC) loads

A free-body diagram of the head with no externally applied forces is shown in Figure 4.2.1.9.3.2-1.

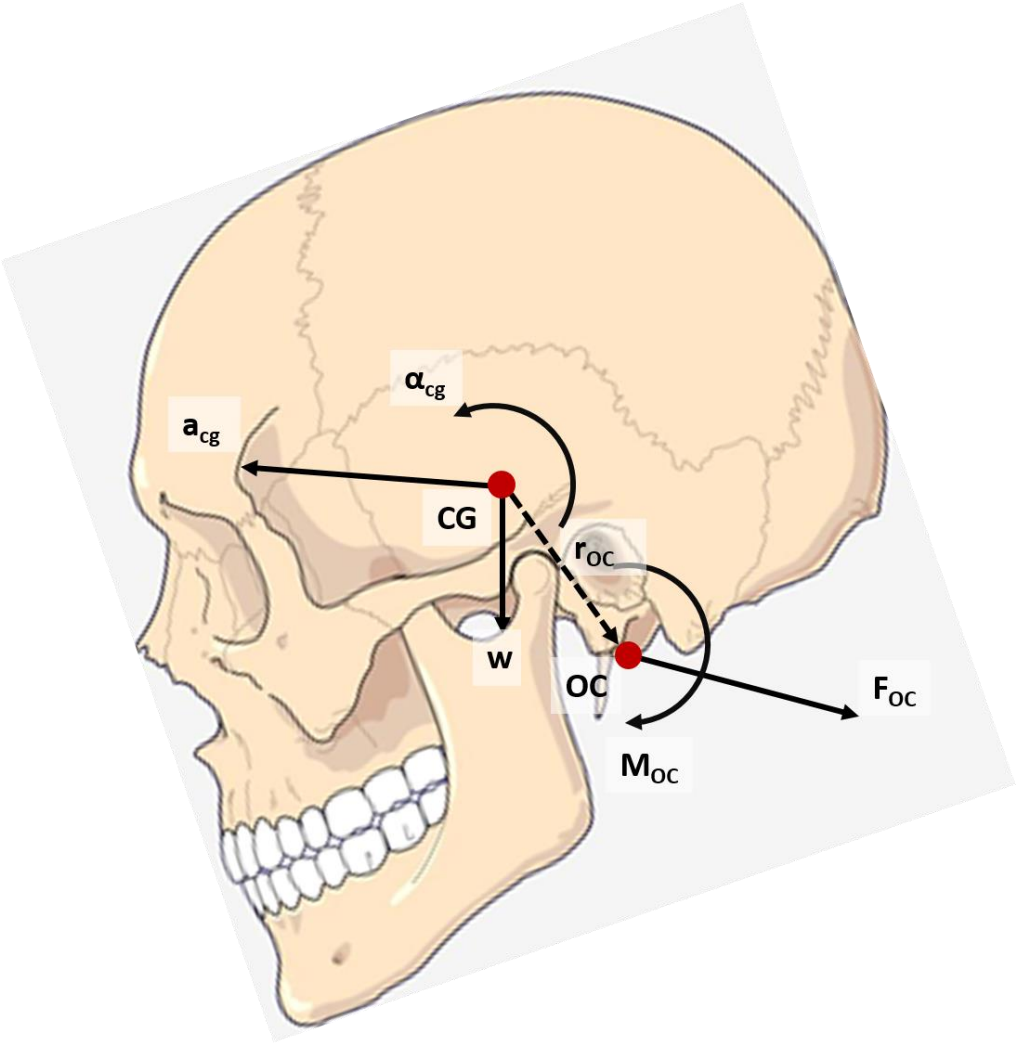

Figure 4.2.1.9.3.2-1: Free-body diagram of the head with linear and angular acceleration a_{cg} and α_{cg}. F_{OC} and M_{OC} are loads at the occipital condyles. W is the head's weight, and r_{OC} is the vector from the head center of gravity to the occipital condyles.

The sum of all the forces acting on the head is equal to the rate of change in its momentum, and, similarly, the sum of all the torques acting on the head is equal to its rate of change in angular moment. Neglecting the weight vector, the force at the occipital condyles is determined by:

$$\vec{F}_{OC} = m_{Head}\ \vec{a}_{cg} \qquad \textit{Equation 4.2.1.9.3.2-1}$$

where m_{head} is the mass of the head.

The moment at the occipital condyles is determined indirectly by calculating the moments about the head center of gravity.

$$\frac{dH}{dt} = r_{OC} \times F_{OC} + M_{OC}$$ ***Equation 4.2.1.9.3.2-2***

$$I\alpha_{anat} + \omega_{anat} \times I\omega_{anat} = r_{OC} \times F_{OC} + M_{OC}$$ ***Equation 4.2.1.9.3.2-3***

$$M_{OC} = \alpha_{anat} + \omega_{anat} \times I\omega_{anat} - r_{OC} \times F_{OC}$$ ***Equation 4.2.1.9.3.2-4***

The mass, MOI, and center of gravity of the head were determined using previously described methods [3].

4.2.1.9.3.3. Spine and pelvis

For the spine and pelvis, a 4x4 orientation matrix of the 6DOF blocks was calculated relative to the local anatomy using the sensors' coordinates and anatomic fiducials. Angular accelerations were calculated from the 6DOF blocks by taking the derivative of the angular velocities. Next, the sensor time-history data were aligned with the local anatomic coordinate system using the first three rows and the orientation matrix's first three columns. Finally, the anatomic origin's linear accelerations were computed using Equation 4.2.1.9.3.3-1 (same as Equation 4.2.1.9.3.1-7).

$$\vec{a}_{anat} = \vec{a}_{0_{anat}} - [\vec{\alpha}_{anat} \times \vec{r}_s + \vec{\omega}_{anat} \times (\vec{\omega}_{anat} \times \vec{r}_s)]$$ ***Equation 4.2.1.9.3.3-1***

4.2.1.9.4. Buck Sensor-Data Reduction

Load cell forces at the foot and tibia restraints and the seat bottom were inertially compensated using triaxial accelerometers attached to the transducer mounting plate. The accelerometer data was multiplied by the mass of one half of the load cell plus the mass of any fixtures on the specimen side of the load cell and then subtracted from the raw load cell data (Equation 4.2.1.9.4-1).

$$F_c = F_{LC} - \left(0.5 * M_{LC} + M_{plate}\right) * a_{plate} \qquad \textbf{Equation 4.2.1.9.4-1}$$

4.2.1.9.5. Motion-Capture Local Anatomic Calculations

At each anatomic location, the markers' three-dimensional positions were related to the anatomic coordinate system using the methods described in Section 4.2.1.9.2.4. The two marker-based coordinate systems (motion capture in Section 4.2.1.9.2.1.8 and CT in Section 4.2.1.9.2.1.9) were used to compute the anatomical origin and orientation at each time-step in the motion-capture coordinate system.

A 4 x 4 rotation matrix (shown below) that relates the local (anatomic) coordinate system (LCS) to the motion-capture coordinate system (MCCS) was calculated for the head, T1, T8, L2, pelvis, sternum, left and right rib 4, left and right rib 7, and seat.

$$\begin{bmatrix} r_{11} & r_{12} & r_{13} & d_x \\ r_{21} & r_{22} & r_{23} & d_y \\ r_{31} & r_{32} & r_{33} & d_z \\ 0 & 0 & 0 & 1 \end{bmatrix} \qquad \textbf{Equation 4.2.1.9.5-1}$$

where:

- r_{11}, r_{12}, and r_{13} are the MCCS x unit vector in the LCS,
- r_{21}, r_{22}, and r_{23} are the MCCS y unit vector in the LCS,
- r_{31}, r_{32}, and r_{33} are the MCCS z unit vector in the LCS, and
- d_x, d_y, and d_z are the position of the local origin in the MCCS.

$$\begin{Bmatrix} X \\ Y \\ Z \end{Bmatrix}_{MCCS} = \begin{bmatrix} r_{11} & r_{12} & r_{13} \\ r_{21} & r_{22} & r_{23} \\ r_{31} & r_{32} & r_{33} \end{bmatrix} \begin{Bmatrix} x' \\ y' \\ z' \end{Bmatrix}_{LCS} + \begin{Bmatrix} d_x \\ d_y \\ d_z \end{Bmatrix} \qquad \textit{Equation 4.2.1.9.5-2}$$

4.2.1.10. Injury Assessment

Upon completion of the test, a set of x-ray and CT scans were made. A detailed autopsy was conducted, with special attention paid to the thoracic cage's skeletal and internal contents and abdominal and pelvic cavities. Rib fractures were documented and photographed.

4.2.1.11. Global Corridors Construction

Global corridors for the following sensor-derived data were constructed for:

- head linear and angular accelerations and angular velocities,
- spine and pelvis linear accelerations and angular velocities,
- OC forces and moments,
- occupant restraint forces and moments (seat, tibia plate, and foot plate), and
- input acceleration.

Corridors for the upper and lower shoulder belt and left and right lab belt forces were determined but were not referenced to the global coordinate system (loads were measured relative to the belt).

Global corridors for the three-dimensional position data were determined for the:

- head,
- spine, and
- pelvis.

The seat coordinate system (shown in Section 4.2.1.9.2.1.7) was the logical choice for the global reference. It was the only coordinate system identical in each test, and the seat is commonly used as a reference point in the automotive environment. The methods for calculating the sensor data in the anatomic coordinate system are detailed in Section 4.2.9.3 and the three-dimensional position data in Section 4.2.9.5.

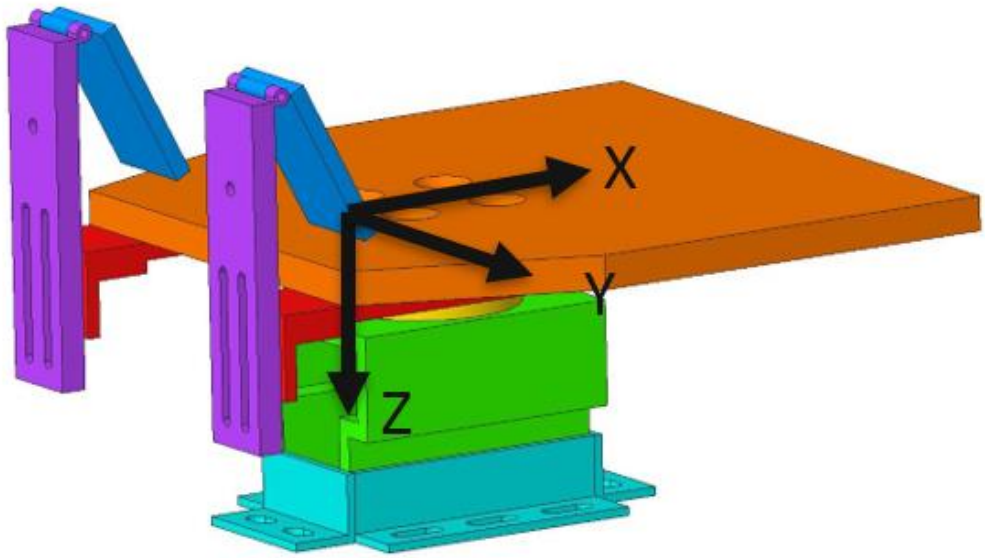

Figure 4.2.1.11-1: Global coordinate system where the x-axis is at the centerline of the seat (+ forward), the z-axis is perpendicular to the top surface (+ down), and the y-axis is perpendicular to the x-z plane (+ right). The origin coincides with the H-Point of the 50th-percentile male, at the top surface of the seat, and centered between the lateral edges.

4.2.1.11.1. Sensor-Derived-Data Global Corridors

4.2.1.11.1.1. Anatomic Sensor Data

At each time-step, the local anatomic sensor-derived data were determined using the methods described in Section 4.2.9.3. To align the anatomic time-history data to the global coordinate system, each local anatomic coordinate system's orientation had to be determined relative to the seat at each time-step. The three-dimensional position data from the head, spine, pelvis, and seat markers (sampled at 1 kHz) were oversampled using a cubic spline interpolation to match the sampling rate of the sensor data (20 kHz). The rotation matrix of each anatomic region relative to the seat (global coordinate) was

determined by multiplying the appropriate 4 x 4 matrices, as shown in Equation 4.2.1.11.1.1-1.

$$[R]_{GlobalCS/AnatCS} = [R]_{GlobalCS/MCCS} * [R]_{MCCS/AnatCS} \qquad \textbf{Equation 4.2.1.11.1.1-1}$$

where:

- **[R]$_{GlobalCS/AnatCS}$** is the rotation matrix of the local anatomic (head, spine, and pelvis) coordinate system in the global (seat) reference frame,
- **[R]$_{GlobalCS/MCCS}$** is the inverse of the **[R]$_{MCCS/GlobalCS}$** where **[R]$_{MCCS/GlobalCS}$** is rotation matrix of the global (seat) reference frame in the motion capture coordinate system, and
- **[R]$_{MCCS/AnatCS}$** is the transformation matrix of the local anatomic (head, spine, and pelvis) coordinate system in the motion capture coordinate system.

Note that the above matrices are calculated at each time step.

Next, the data were transformed to the global coordinate system by multiplying the first three rows and columns of the [R]$_{GlobalCS/AnatCS}$ by the anatomic sensor-derived data as shown in Equation 4.2.1.11.1.1-2.

$$\begin{Bmatrix} X \\ Y \\ Z \end{Bmatrix}_{GlobalCS} = [\mathrm{R}]_{GlobalCS/AnatCS} \begin{Bmatrix} x' \\ y' \\ z' \end{Bmatrix}_{AnatSensor} \qquad \textbf{Equation 4.2.1.11.1.1-2}$$

Two sets of corridors were then determined, one for the near-side high-speed tests and one for the far-side high-speed tests. The corridors were constructed by computing the average and standard deviation of the anatomic sensor-derived data referenced to the

global coordinate system at each time-step. The mean at each time-point represented the average response, and the plus and minus one standard deviation at each time-point represented the boundaries of the corridor.

4.2.1.11.1.2. Buck Sensor Data

The loads at the seat, knee, and foot restraints were transformed into the global coordinate system using the offset angles recorded as part of the pre-test occupant measurements. Note that the seat load cell was coincident with the global coordinate system. The knee and foot restraint loads were aligned by rotating about the sensor y-axis by the offset angles. The acceleration of the seat in global coordinates was determined by rotating the sled linear acceleration about the sled z-axis (+30 degrees for near-side impact or -30 degrees for far-side impact). The belt loads were not transformed into the global coordinate system.

Similar to the data in Section 4.2.1.11.1.1, the corridors were constructed for the restraint loads and seat linear acceleration by calculating the average and standard deviation of the global data at each time step. The mean at each time-point represented the average response, and the plus- and minus one standard deviation at each time-point represented the boundaries of the corridor. The belt load corridors were determined in the same manner but with the sensor data.

4.2.1.11.2. Motion Capture Global Corridors

Three-dimensional kinematic corridors of the head, spine, and pelvis were constructed by separately determining the mean position and orientation at each time-step in near-

and far-side high-speed impacts. The corridor boundaries were determined by calculating a standard deviation ellipsoid (SDE) at each time-step.

4.2.1.11.2.1. Mean position and orientation

To minimize specimen anthropometry and seating position variability, the average pre-test positions of the head, T1, T8, L2, and sacrum were calculated relative to the seat. This averaged anatomic offset was used as a common starting point for all specimens for the fore/aft and vertical trajectories. The lateral trajectories were assumed to start at zero, corresponding to the centerline of the seat. Data were aligned using the common t-zero signal from the sled, which represented the onset of sled acceleration. The average corridors for the near- and far-side tests were calculated separately by calculating the mean position at each anatomical time-step relative to the sled. The average orientation at each anatomic location was computed at every time step using Equation 4.2.1.11.2.1-1, and the methods are described elsewhere [73].

$$M = \sum_{i=1}^{n} q_i q_i^T$$

Equation 4.2.1.11.2.1-1

where q_i is the quaternion corresponding to i^{th} specimen's 3 x 3 rotation matrix at a given time step.

The average quaternion at that time step is found by determining the eigenvector corresponding to the M matrix's maximum eigenvalue. The average quaternion can then be transformed in a 3 X 3 rotation matrix to represent the average orientation at

that time step. An example of the average orientation technique is shown in Figure 4.2.1.11.2.1-1.

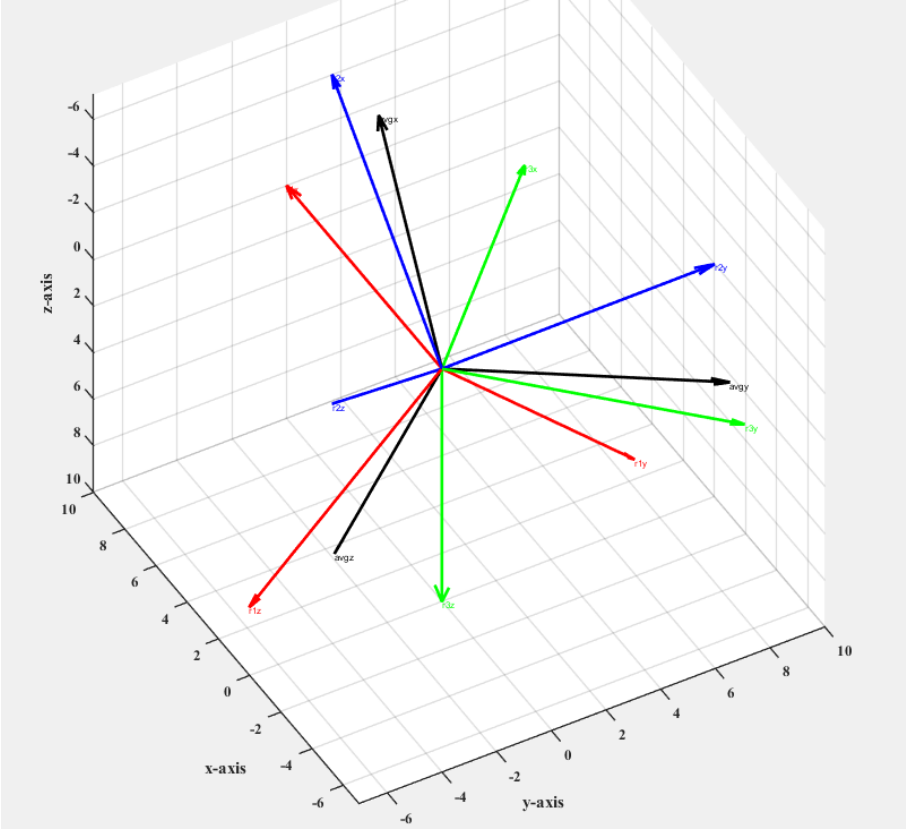

Figure 4.2.1.11.2.1-1: Average rotation matrix (black) determined from three orientation matrices. Red represents a 45-degree rotation about the x-axis, blue 45-degree rotation about the y-axis, and green 45-degree rotation about the z-axis.

4.2.1.11.2.2. Corridor Boundaries

The corridor's borders were determined by calculating the standard deviational ellipsoid (SDE) at each time-step for all anatomic locations. SDEs are used in geographic information system data to estimate data dispersion and orientation in three-dimensional space. It has been used to track the uncertainty of measurements on maps, dispersion of geographic features, and the distribution and trend in crimes.

Originally proposed for planar (2-dimensional) applications in 1926 [74], it was later extended into higher-dimensional Euclidean space [75]. The SDE is determined by a spectral decomposition of the anatomic position data's covariance matrix at each time-step. This process is summarized in Equation 4.2.1.11.2.2-1.

$$C = QDQ^T \qquad \textbf{Equation 4.2.1.11.2.2-1}$$

where C is the covariance matrix and D is the eigenvalues. The SDE is found by scaling a unit sphere by the covariance matrix's square root, which is shown in Equation 4.2.1.11.2.2-2.

$$SDE = QD^{1/2}Q^T T \qquad \textbf{Equation 4.2.1.11.2.2-2}$$

where T is a unit sphere, D is the square root of the covariance matrix and represent the lengths of semi-axes, and Q is the rotation matrix. Equation 4.2.1.11.2.2-2 is the inverse Mahalanobis transformation, where the unit sphere T is stretched by the square of the eigenvalues along each axis and then rotated by the orthogonal matrix Q. Figure 4.2.1.11.2.2-1 shows a set of theoretical data along with the calculated SDE and a rectangular cuboid, which represents the standard deviations in the x, y, and z axes. The theoretical data set consisted of 600 multivariate, normally distributed data points with a mean of (0,0,0) where the distribution was:

$$y = f(x, \mu, \Sigma) = \frac{1}{\sqrt{|\Sigma|(2\pi)^d}} e^{-\frac{1}{2}(x-\mu)\Sigma^{-1}\frac{1}{2}(x-\mu)} \qquad \textbf{Equation 4.2.1.11.2.2-3}$$

And the covariance matrix, Σ:

$$\Sigma = \begin{bmatrix} 4 & -2 & 1 \\ -2 & 10 & 2 \\ 1 & 2 & 5 \end{bmatrix}$$

Equation 4.2.1.11.2.2-4

The SDE in Figure 4.2.1.11.2.2-1 has a magnification factor of one, which can be thought of as +/- one standard deviation for the linear case. Unlike the single dimension, a magnification of one for a 3-dimensional SDE does not contain 68% of the samples but only 20%. The confidence interval for a 3rd-order SDE can be calculated using Equation 4.2.1.11.2.2-5 [75].

$$P_3(r) = \operatorname{erf}\left(\frac{r}{\sqrt{2}}\right) - \left(\frac{-r}{2}\right)\frac{e^{\frac{-r^2}{2}}}{\Gamma(1.5)}$$

Equation 4.2.1.11.2.2-5

where erf is the error function, r is the magnification factor, and Γ is the gamma function.

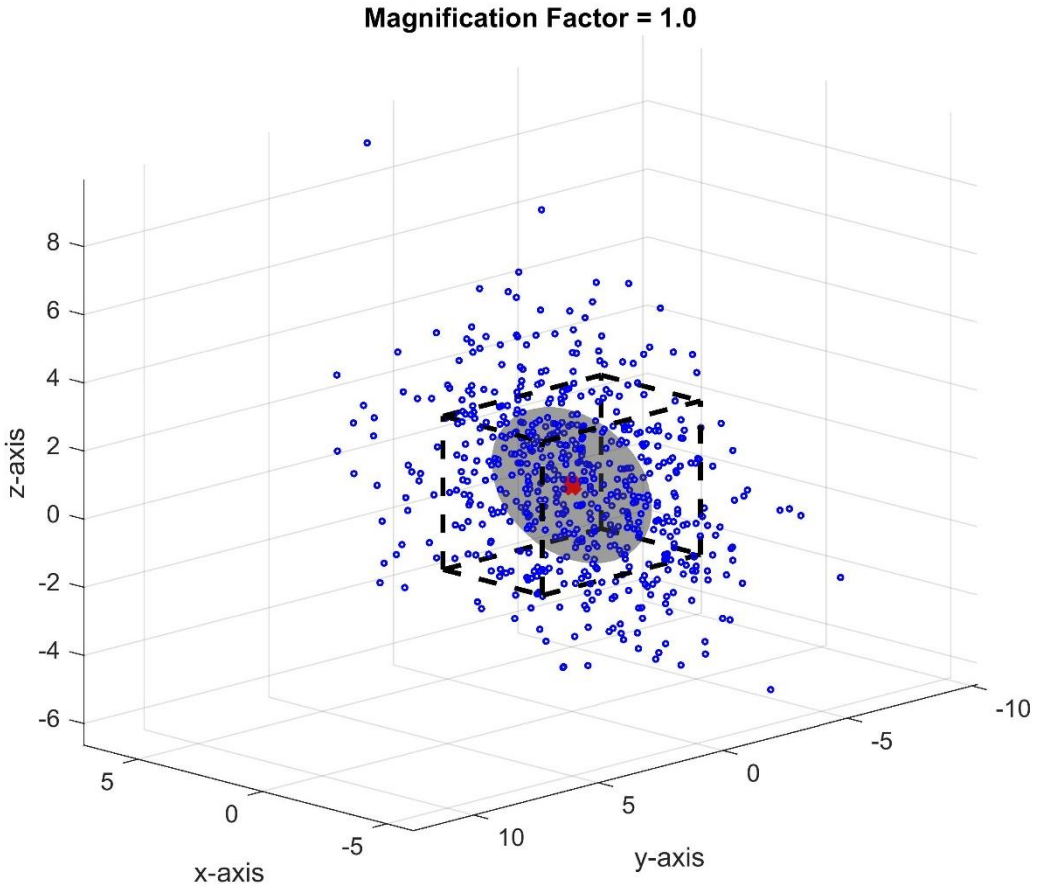

Figure 4.2.1.11.2.2-1: Theoretical set of data consisting of 600 multivariate normally distributed random numbers. The SDE with a magnification ratio of 1 is shown in gray, and the dashed black rectangular cuboid shows the bounds of the standard deviation in the x, y, and z axes.

Figure 4.2.1.11.2.2-2 shows the 3rd order SDE confidence interval as a function of the magnification factor. As shown, an SDE with a magnification factor of 1.878 contains 68% of the data, which is the one-dimensional equivalent of +/- one standard deviation.

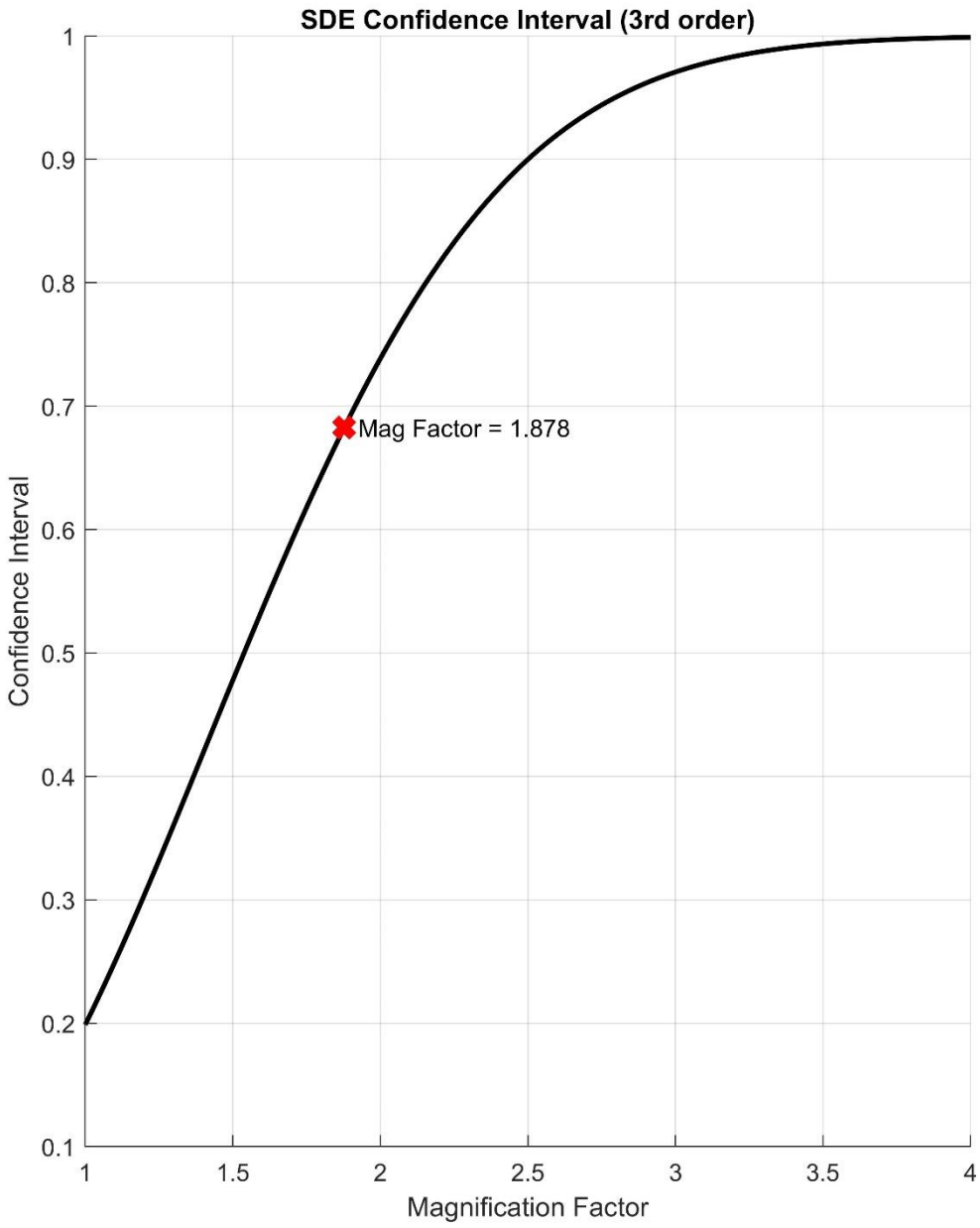

Figure 4.2.1.11.2.2-2: The 3rd-Order SDE confidence intervals as a function of the magnification factor. The red x shows that at a magnification factor of 1.878, the confidence interval is 0.682,7, equivalent to one standard deviation for one-dimensional data.

To properly scale the SDE, the magnification factor is multiplied by the eigenvalues in the $D^{1/2}$ matrix from Equation 4.2.1.11.2.2-2, where the eigenvalues were the lengths of the semi-axes of the ellipse. For the current study, the corridor boundaries will be determined at every time-step for all anatomic locations using a magnification factor of 1.878. The same set of theoretical data from Figure 4.2.1.11.2.2-1, with an SDE calculated using a magnification factor of 1.878, is shown in Figure 4.2.1.11.2.2-3.

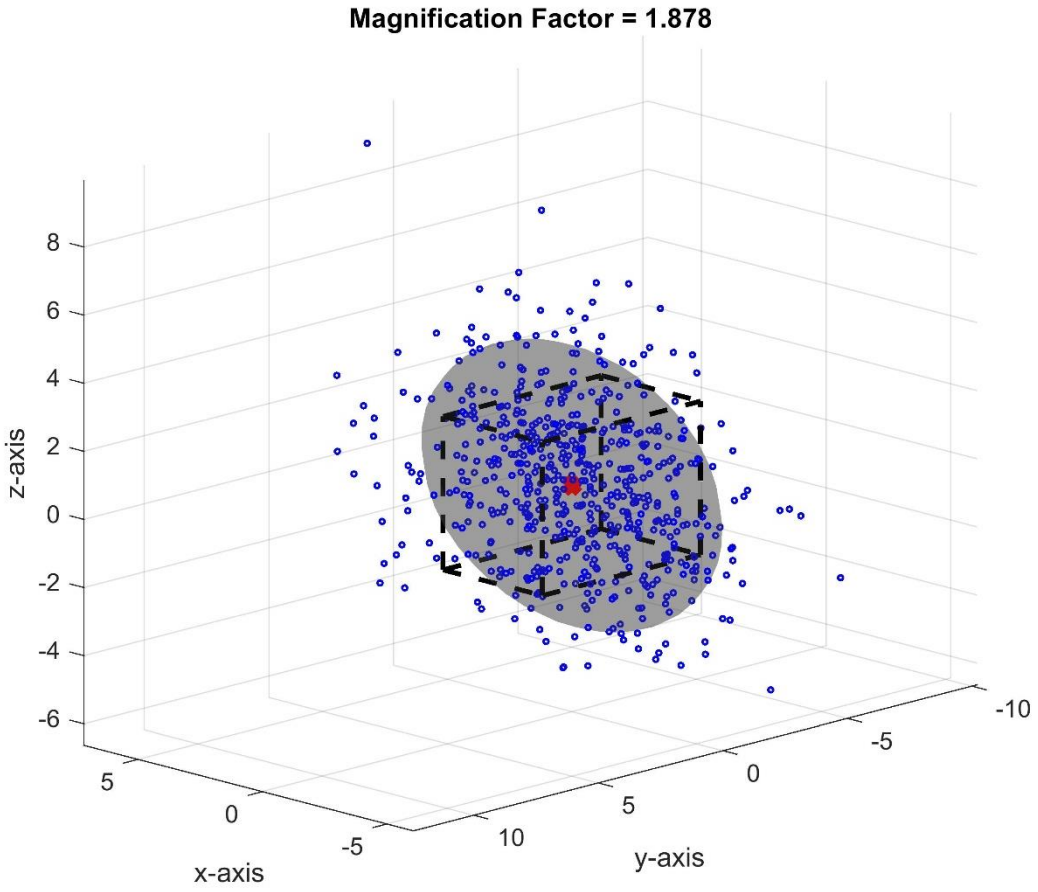

Figure 4.2.1.11.2.2-3: Theoretical set of data consisting of 600 multivariate normal distributed random numbers. The SDE with a magnification ratio of 1.878 is shown in gray, and the dashed black rectangular cuboid shows the bounds of the standard deviation in the x, y, and z axes.

4.2.2. Non-Planar Thorax Injury Risk Curve Development

4.2.2.1. Thorax Deflection Calculation

To calculate thorax deflection, the positions at left and right rib 4, left and right rib 7, and the sternum were transformed to the T8 coordinate system using Equation 4.2.2.1-1.

$$\begin{Bmatrix} X \\ Y \\ Z \end{Bmatrix}_{Thorax/T8} = [R]_{T8/MCCS} * [R]_{MCCS/Thorax} * \begin{Bmatrix} 0 \\ 0 \\ 0 \\ 1 \end{Bmatrix} \qquad \textit{Equation 4.2.2.1-1}$$

where:

- $[R]_{T8/MCCS}$ is the inverse of $[R]_{MCCS/T8}$ where $[R]_{MCCS/T8}$ is the rotation matrix of T8 in the MCCS coordinate system,
- $[R]_{MCCS/Thorax}$ is the rotation matrix of the thorax (ribs or sternum) in the MCCS coordinate system,
- $[0\ 0\ 0\ 1]^T$ is used to determine the origin point of the thorax (ribs or sternum), and
- $[X\ Y\ Z]_{Thorax\_T8}^T$ is the thorax origin's position (ribs or sternum) in the T8 coordinate system.

Next, the deflections were calculated as the change-in-position of the thorax origin (ribs or sternum) in the T8 coordinate system. Four separate deflection calculations were made:

1. A/P (x),
2. transverse plane (x-y),
3. sagittal plane (x-z), and
4. multiplanar (x-y-z) type.

Equations for the four deflections are given below:

$$\Delta_X = \sqrt{(Th_{xt} - Th_{x0})^2} \qquad \textit{Equation 4.2.2.1-2}$$

$$\Delta_{XY} = \sqrt{(Th_{xt} - Th_{x0})^2 + \left(Th_{yt} - Th_{y0}\right)^2} \qquad \textit{Equation 4.2.2.1-3}$$

$$\Delta_{XZ} = \sqrt{(Th_{xt} - Th_{x0})^2 + (Th_{zt} - Th_{z0})^2} \qquad \textit{Equation 4.2.2.1-4}$$

$$\Delta_{XYZ} = \sqrt{(Th_{xt} - Th_{x0})^2 + \left(Th_{yt} - Th_{y0}\right)^2 + (Th_{zt} - Th_{z0})^2} \qquad \textit{Equation 4.2.2.1-5}$$

4.2.2.2. Survival Analysis

AIS 2+ Injury Risk Curves (IRCs) were developed for sternum deflection by calculating the deflections for the near- and far-side impacts for the high- and low-speed tests. For the statistical analysis, peak x, x-y, x-z, and x-y-z deflections were selected as the primary response variables. Injury outcomes were categorized into two groups: AIS 2 or greater were considered injured, while injuries at AIS less than or equal to 1 were considered non-injured. All injury data was considered left censored while the non-injured was right censored. Data from near- and far-side impacts were grouped together.

Parametric Statistical Survival Modeling (PSSM) was performed on R-software using updated techniques from the ISO/TC22/SC12/WG6 working group of the International Standards Organization (ISO) recommendations [76, 77]. The ISO recommend approach is to (a) collect data, (b) assign censor status, (c) check for multiple injury mechanisms, (d) separate samples by injury mechanism, (e) estimate distribution parameters, (f) identify overly influential observations, (g) choose the distribution, (h) check the validity of predictions against existing results, (i) calculate 95% confidence intervals, (j) assess the quality index, and (k) recommend one curve per body region.

PSSM requires an assumption of the data distribution, and Weibull, log-normal, and log-logistic are the most commonly used in survival analysis. The Weibull distribution's cumulative density function is given in Equation 4.2.2.2-1, log-logistic in 4.2.2.2-2, and lognormal in 4.2.2.2-3 – 4.2.2.2-4.

$$\mathrm{F(x)} = 1 - \mathrm{e}^{-\left(\frac{t}{\lambda}\right)^{\gamma}} \qquad \textit{Equation 4.2.2.2-1}$$

$$\mathrm{f(x)} = \frac{1}{1 + \left(t/\lambda\right)^{-\gamma}} \qquad \textit{Equation 4.2.2.2-2}$$

$$\mathrm{f(x)} = \Phi(\gamma \log \lambda t) \qquad \textit{Equation 4.2.2.2-3}$$

$$\Phi(t) = \int_{-\infty}^{t} \frac{1}{\sqrt{2\pi}} \mathrm{e}^{-\frac{y^2}{2}}\, dy \qquad \textit{Equation 4.2.2.2-4}$$

where γ is the shape parameter and λ is the scale parameter, which are estimated by the maximum likelihood approach. The optimal distribution was selected based on the lowest Akaike Information Criterion (AIC), and the Brier Score Metric (BSM) was calculated for each response variable [78, 79]. The response variable that produced the lowest BSM was considered the best metric describing the sternum deflection response to oblique frontal impacts. The plus-minus 95% confidence interval bounds were computed based on the delta method [80]. The NCIS—defined as the ratio of the confidence interval width to the magnitude of the metric (Equation 4.2.2.2-5)—was determined at a specific probability of injury.

$$NCIS = \frac{UL_p - LL_p}{M_p} \qquad \textit{Equation 4.2.2.2-5}$$

where p is the probability of injury, M_p is the mean value of the metric, and UL_p and LL_p are the upper and lower limits of the confidence intervals at that probability.

The following rating scale was used to assess the NCIS values [81]:

Table 4.2.2.2-1: NCIS Rating

Range	Rating
< 0.5	Good
0.5 – 1	Fair
1 – 1.5	Marginal
> 1.5	Unacceptable

4.3. RESULTS

4.3.1. PMHS Demographics

4.3.1.1. High-Speed Tests

Table 4.3.1.1-1: High-Speed Specimen Demographics

	Test ID	HS number	Age (years)	Stature (cm)	Mass (kg)	QCT BMD (mg/cc)
Near	NSFSC0122	794	62	154.9	48.1	121.8
	NSFSC0123	802	57	160.0	44.4	102.0
	NSFSC0124	921	69	161.8	42.6	82.2
	NSFSC0127	923	89†	157.4	40.8	117.4
	NSFSC0128	959	75	167.6†	60.3†	102.5
Far	NSFSC0120	790	59	155.0	53.4	161.0
	NSFSC0121	905	78	152.4	54.5	140.7
	NSFSC0125	913	83	154.9	46.7	118.4
	NSFSC0126	947	65	149.9	39.5	166.2
	NSFSC0129	957	79	149.9	43.1	99.4
Stats	Avg near	n/a	70.4	160.3	47.2	105.2
	Std near	n/a	12.4	4.8	7.8	15.6
	Avg far	n/a	72.8	152.4	47.4	137.1
	Std far	n/a	10.3	2.5	6.5	28.3
	Avg all	n/a	71.6	156.4	47.3	121.2
	Std all	n/a	10.8	5.5	6.8	27.3

† parameter outside inclusion criteria

4.3.1.2. Low-Speed Tests

Table 4.3.1.2-1: Low-Speed Specimen Demographics

	Test ID	HS number	Age (years)	Stature (cm)	Mass (kg)	QCT BMD (mg/cc)
Near	NSFSC0130	HS970	92†	162.6†	47.7	82.5
	NSFSC0132	HS979	70	147.3	46.4	124.4
	NSFSC0134	HS1001	83	157	37.3	207.1
Far	NSFSC0136	HS958	85	154.9	57.2†	113.9
	NSFSC0138	HS1009	86†	162.1†	49.4	89.2
	NSFSC0140	HS1011	58	160.5	37.7	150.7
Stats	Avg near		82	155.6	43.8	138.0
	Std near		11	7.7	5.7	63.4
	Avg far		76	159.2	48.1	117.9
	Std far		16	3.8	9.8	30.9
	Avg all		79	157.4	46.0	128.0
	Std all		13	5.8	7.5	46.0

† parameter outside inclusion criteria

4.3.1.3. Global Sensor Corridors

Figures 4.3.1.3-1 – 4.3.1.3-10 show the Global Sensor Corridor linear accelerations and the angular velocities for near- and far-side impacts for the head, spine, and pelvis. The corridor is expressed as +/- one standard deviation from the mean. The mean response for the far-side head linear acceleration is smaller in the x and y axes than the near-side, while the z-axis curves are comparable. This is due to the interaction of the occupant with the seat belt. The three-point restraint is not as effective in far-side impacts, and the occupant motion is less controlled than the near-side. For the head angular velocity response, the x and z responses are higher in near-side impacts as the head rotates around the shoulder belt restraint, while in far-side impacts, there is less interaction with the belt. Despite the inherent variability of PMHS and the data reduction process,

the width of corridor boundaries is relatively low, suggesting that the method for developing Global Corridor for sensor data can be effectively applied to carefully designed experiments.

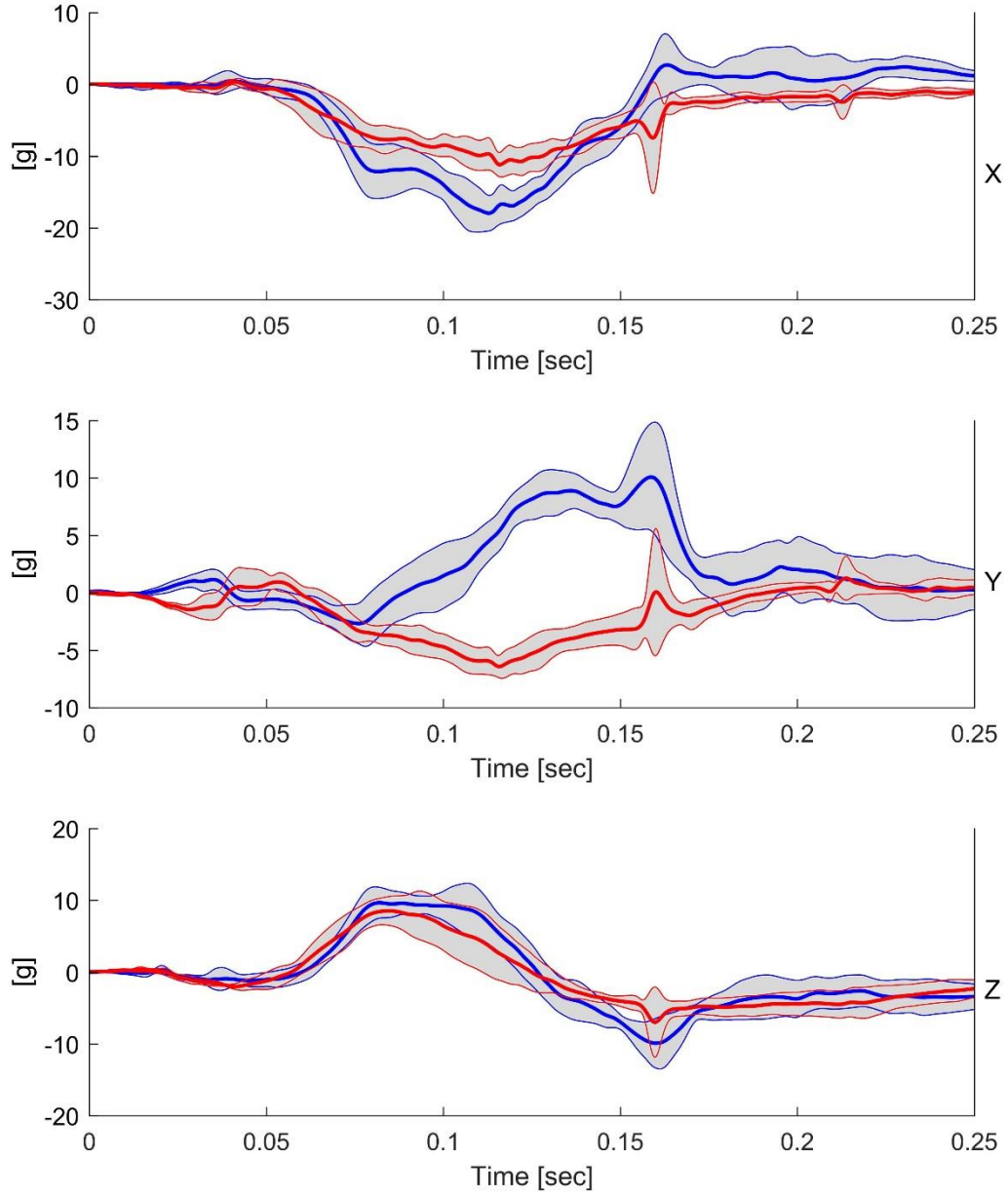

Figure 4.3.1.3-1: Global corridors for head linear accelerations in x (top), y (middle), and z (lower) directions for near- (blue) and far-(red) side impacts. The mean response is shown by the thick lines, while the boundaries of the corridor (± one standard deviation from the mean) are shown by the thin lines. The corridors are shaded between the upper and lower boundaries.

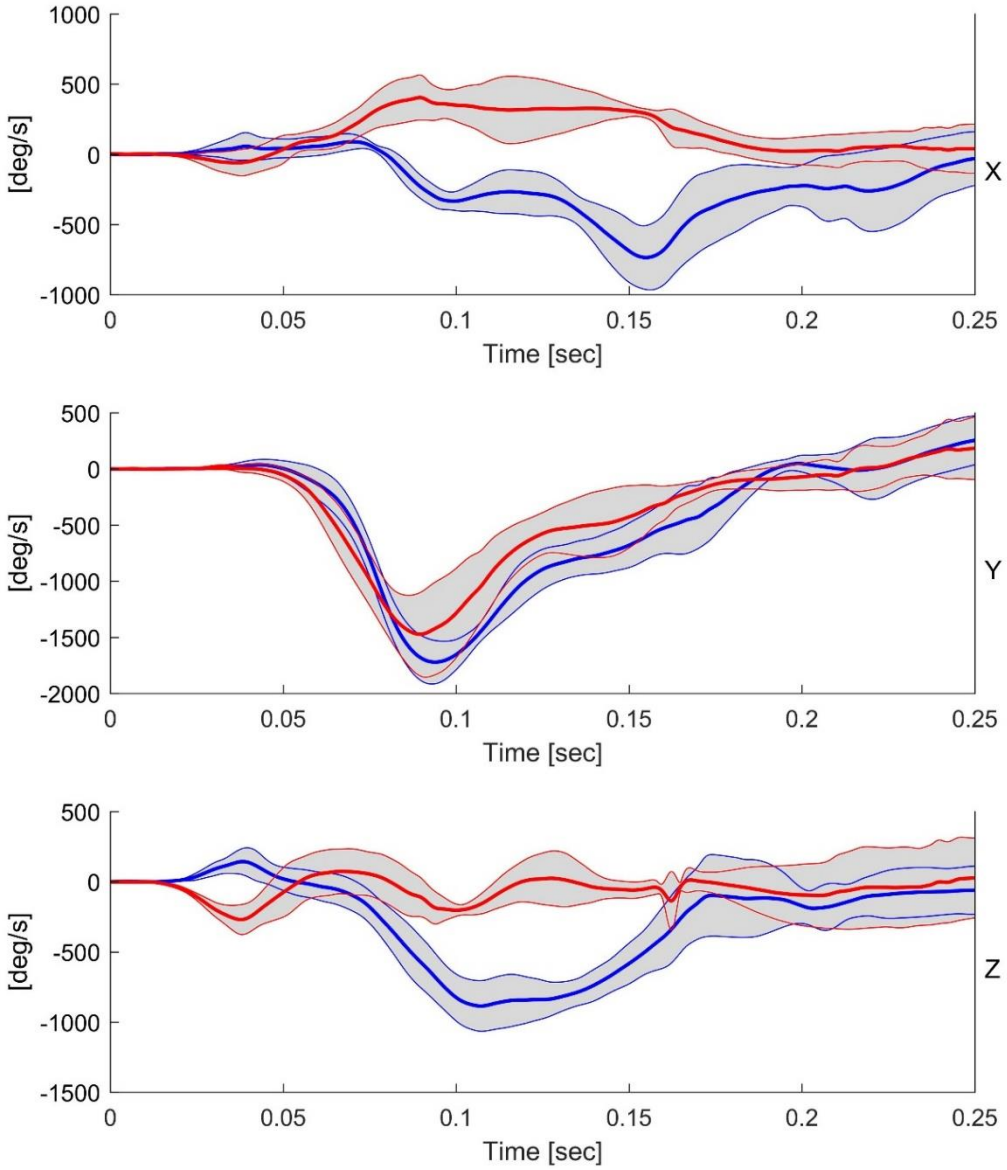

Figure 4.3.1.3-2: Global corridors for head angular velocities in x (top), y (middle), and z (lower) directions for near- (blue) and far-(red) side impacts. The mean response is shown by the thick lines, while the boundaries of the corridor (± one standard deviation from the mean) are shown by the thin lines. The corridors are shaded between the upper and lower boundaries.

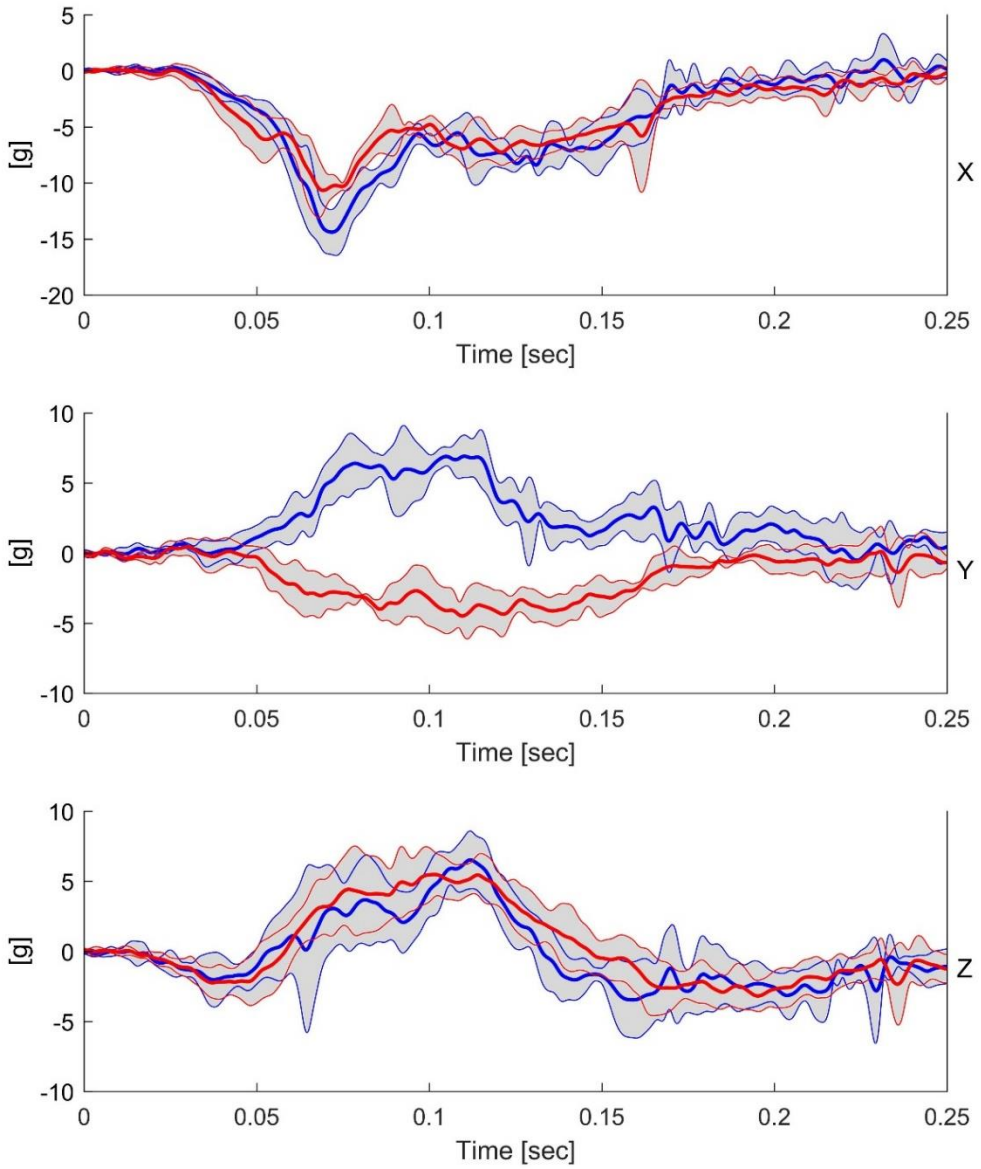

Figure 4.3.1.3-3: Global corridors for T1 linear accelerations in x (top), y (middle), and z (lower) directions for near- (blue) and far-(red) side impacts. The mean response is shown by the thick lines, while the boundaries of the corridor (± one standard deviation from the mean) are shown by the thin lines. The corridors are shaded between the upper and lower boundaries.

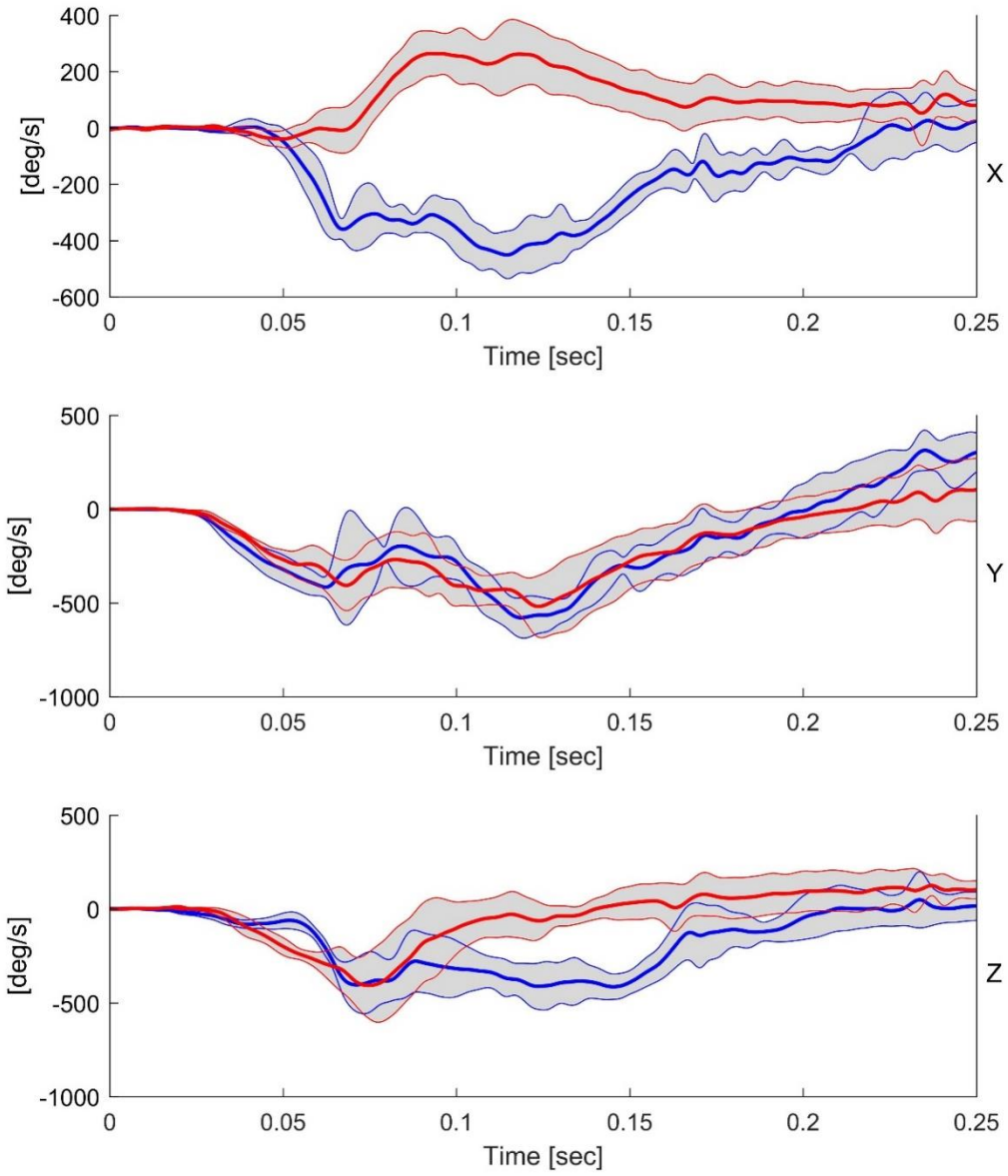

Figure 4.3.1.3-4: Global corridors for T1 angular velocities in x (top), y (middle), and z (lower) directions for near- (blue) and far-(red) side impacts. The mean response is shown by the thick lines, while the boundaries of the corridor (± one standard deviation from the mean) are shown by the thin lines. The corridors are shaded between the upper and lower boundaries.

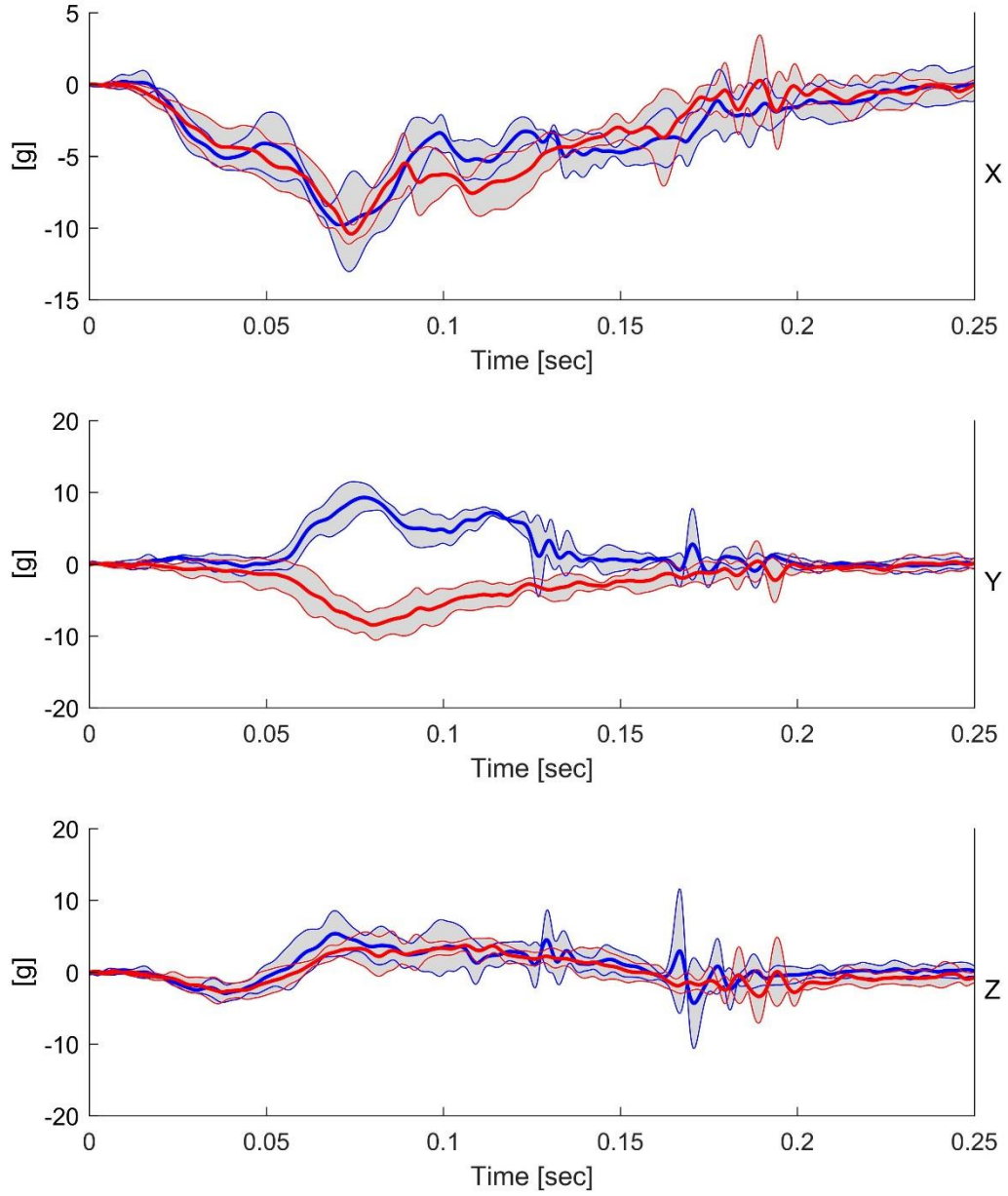

Figure 4.3.1.3-5: Global corridors for T8 linear accelerations in x (top), y (middle), and z (lower) directions for near- (blue) and far-side (red) impacts. The mean response is shown by the thick lines, while the boundaries of the corridor (± one standard deviation from the mean) are shown by the thin lines. The corridors are shaded between the upper and lower boundaries.

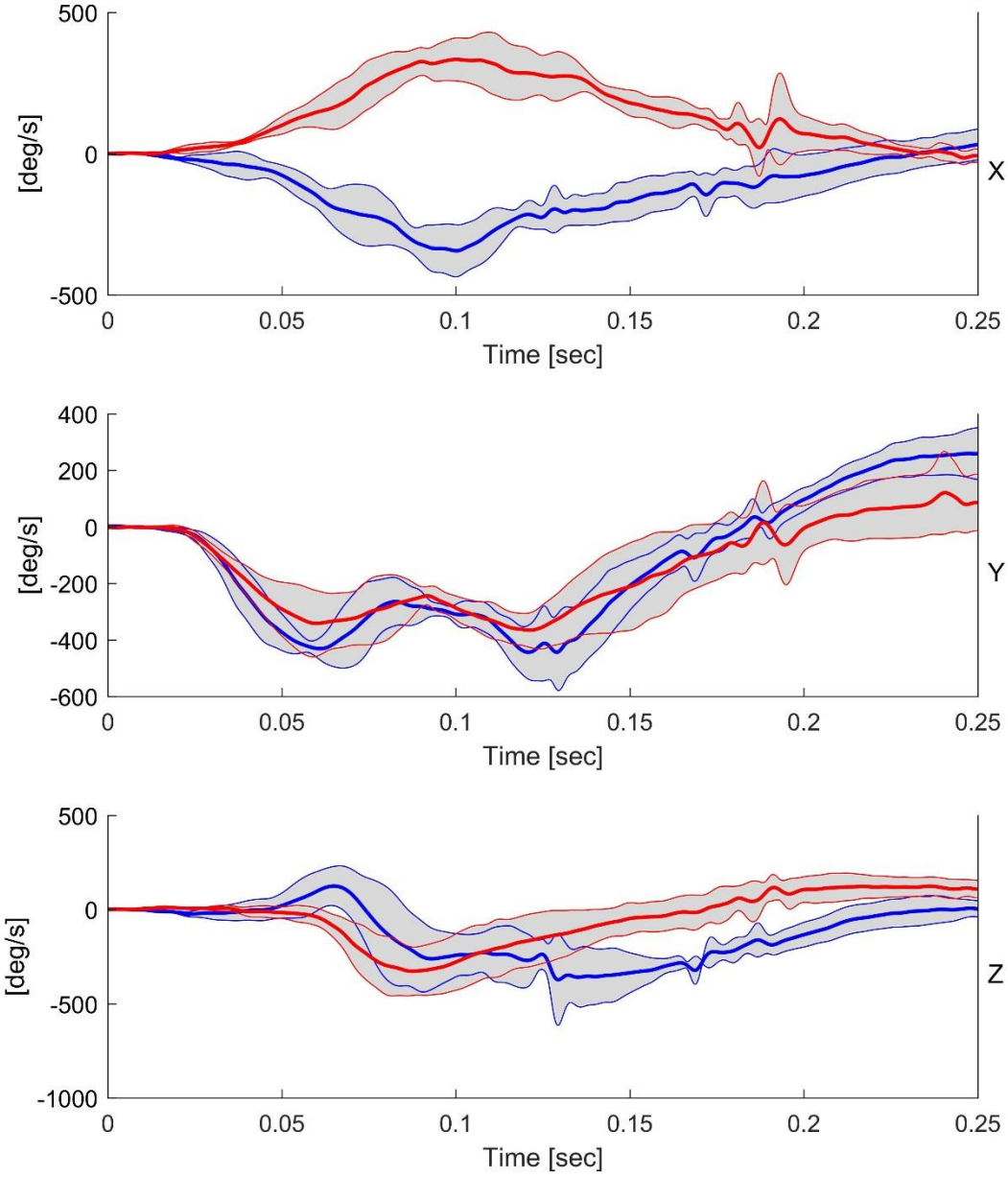

Figure 4.3.1.3-6: Global corridors for T8 angular velocities in x (top), y (middle), and z (lower) directions for near- (blue) and far-side (red) impacts. The mean response is shown by the thick lines, while the boundaries of the corridor (± one standard deviation from the mean) are shown by the thin lines. The corridors are shaded between the upper and lower boundaries.

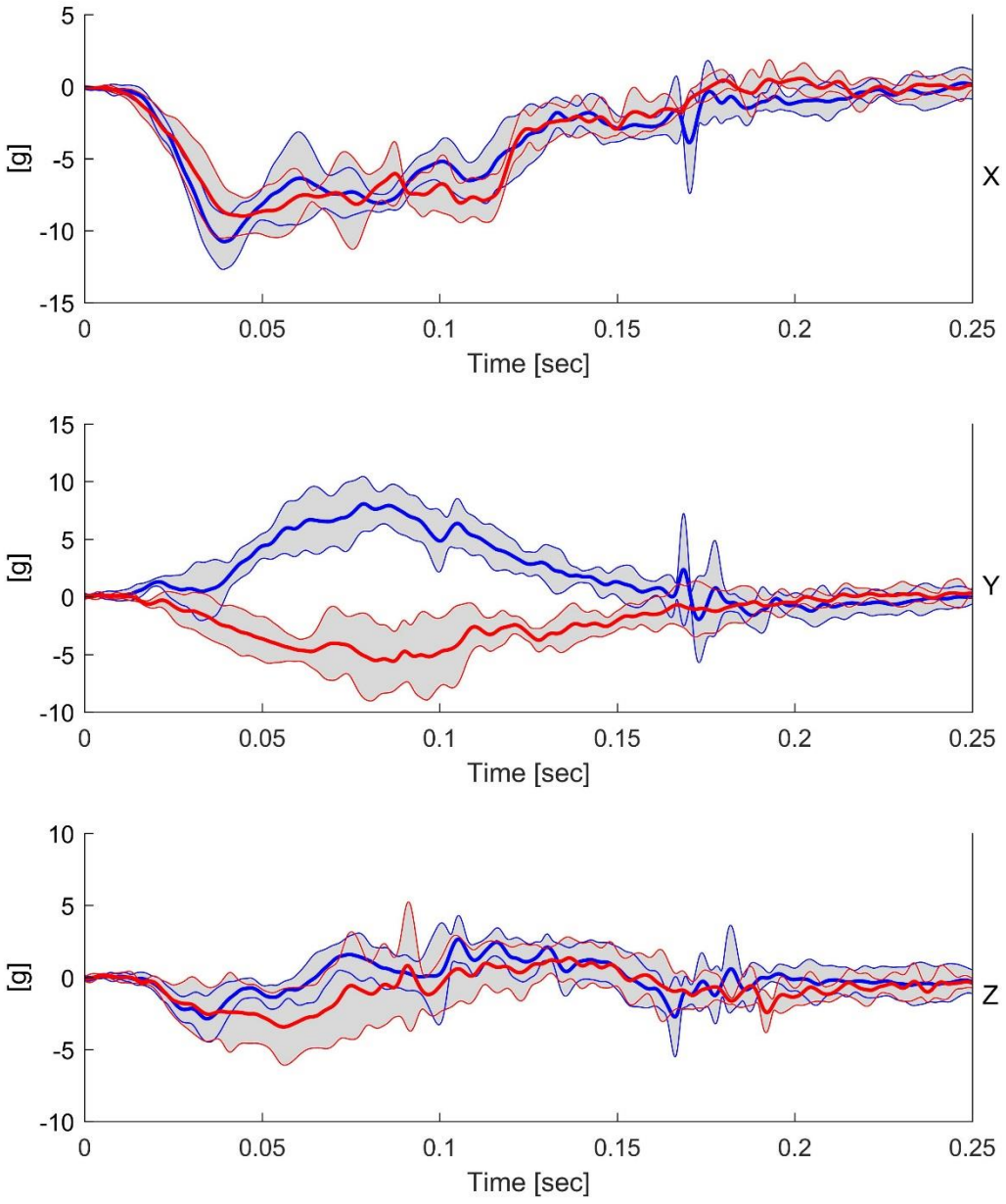

Figure 4.3.1.3-7: Global corridors for L2 linear accelerations in x (top), y (middle), and z (lower) directions for near- (blue) and far-side (red) impacts. The mean response is shown by the thick lines, while the boundaries of the corridor (± one standard deviation from the mean) are shown by the thin lines. The corridors are shaded between the upper and lower boundaries.

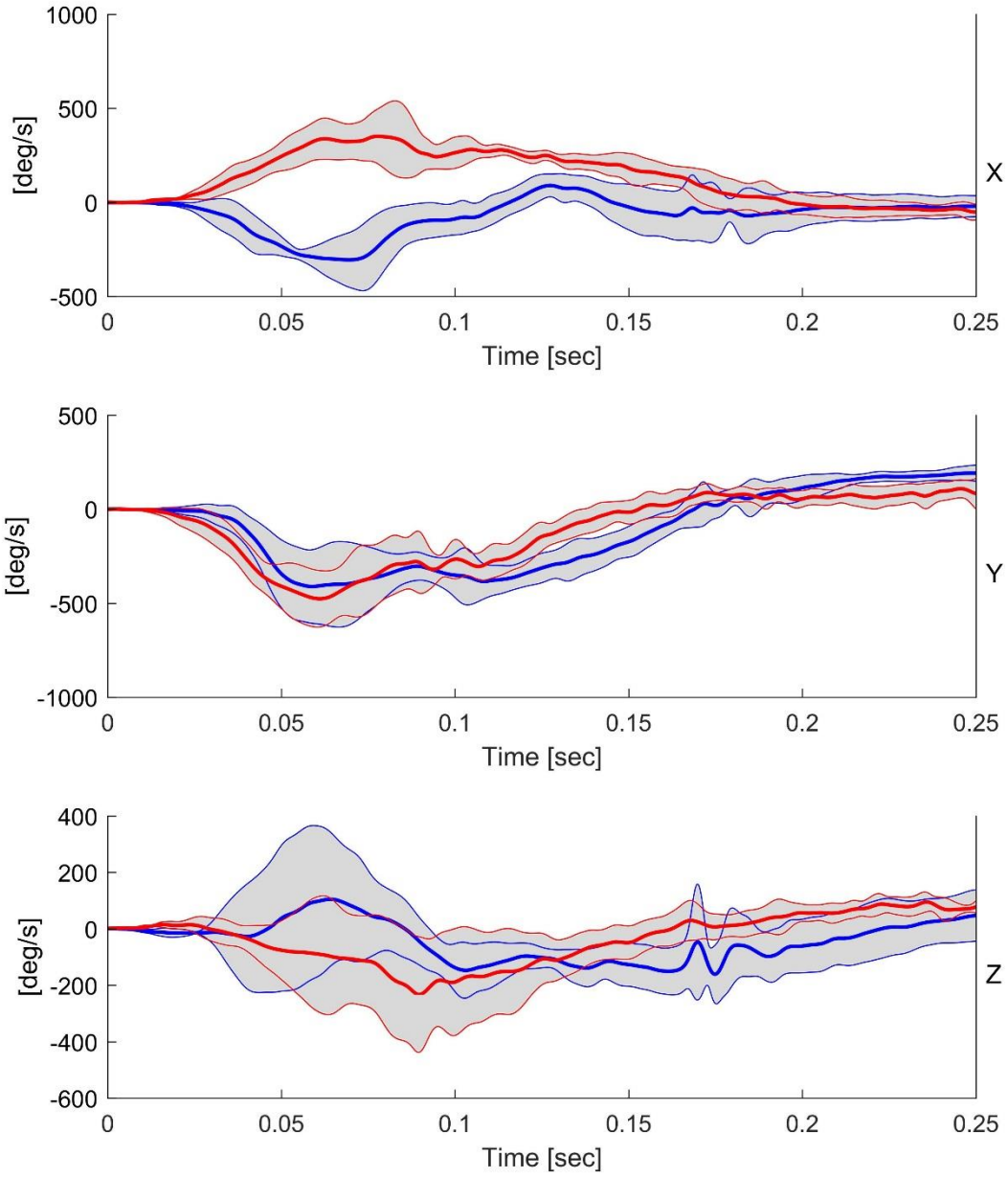

Figure 4.3.1.3-8: Global corridors for L2 angular velocities in x (top), y (middle), and z (lower) directions for near- (blue) and far-side (red) impacts. The mean response is shown by the thick lines, while the boundaries of the corridor (± one standard deviation from the mean) are shown by the thin lines. The corridors are shaded between the upper and lower boundaries.

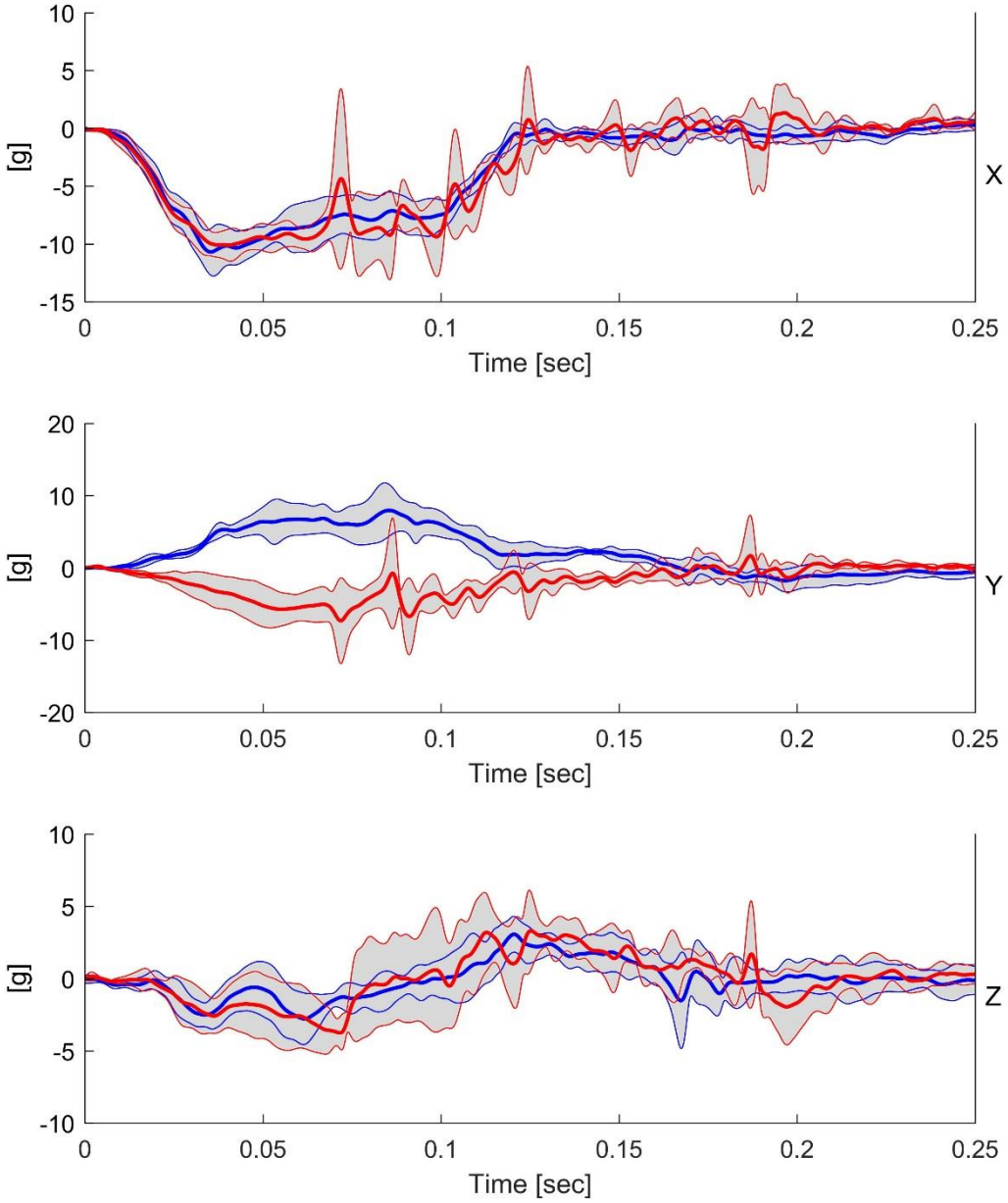

Figure 4.3.1.3-9: Global corridors for sacral linear accelerations in x (top), y (middle), and z (lower) directions for near- (blue) and far-side (red) impacts. The mean response is shown by the thick lines, while the boundaries of the corridor (± one standard deviation from the mean) are shown by the thin lines. The corridors are shaded between the upper and lower boundaries.

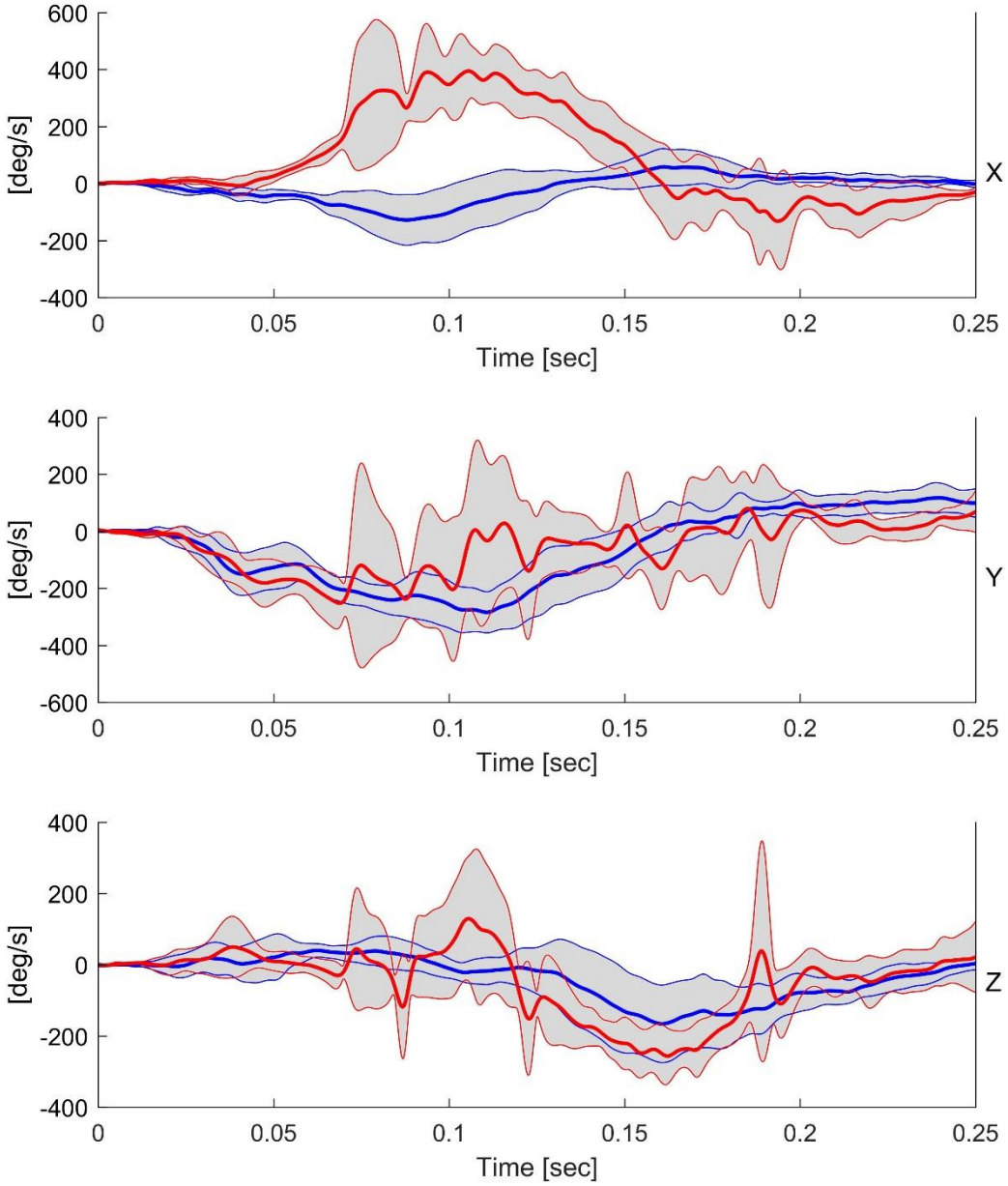

Figure 4.3.1.3-10: Global corridors for sacral angular velocities in x (top), y (middle), and z (lower) directions for near- (blue) and far-side (red) impacts. The mean response is shown by the thick lines, while the boundaries of the corridor (± one standard deviation from the mean) are shown by the thin lines. The corridors are shaded between the upper and lower boundaries.

4.3.1.4. Global Kinematic Corridors

The following three figures represent the far-side mean trajectory and orientation relative to the seat for the head, T1, T8, L2, and sacrum. While the average orientation has been calculated at every-time step, the unit vectors of the local anatomic orientation are shown at every 50 ms time-step for clarity. The head demonstrates the largest excursion, and the overall motion at the anatomic regions decreases from superior to inferior. This is due to the test's boundary conditions where the pelvis was restrained by the lap belt and rigid knee and foot restraint. The interaction with the shoulder belt controlled the head and spine kinematics. Similarly, the head and T1 show the largest change in orientation with minimal change observed at the pelvis.

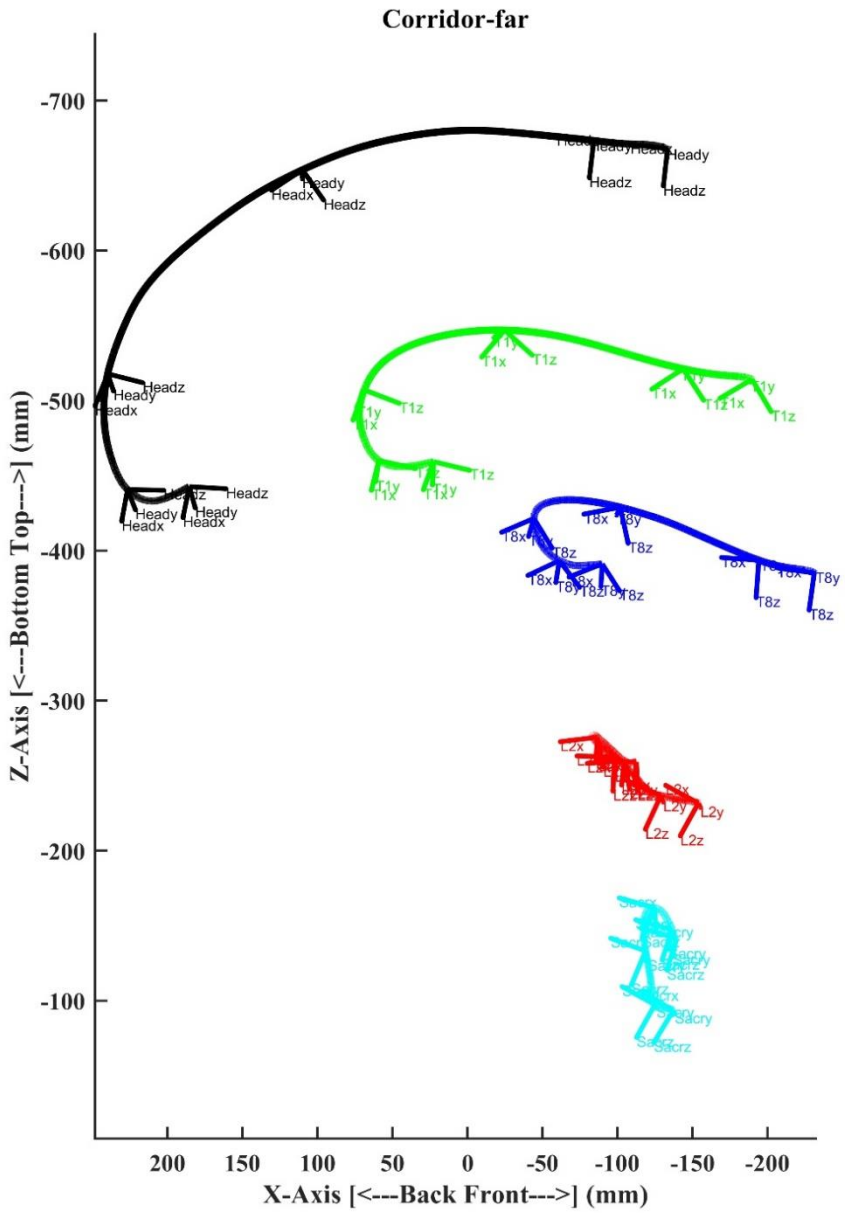

Figure 4.3.1.4-1: Lateral view of mean response of the head (black), T1 (green), T8 (blue), L2 (red), and pelvis (cyan) in far-side impacts. Average linear displacements are shown with the solid black curves. Average orientation is shown at discrete time intervals with orthogonal unit vectors at each body region.

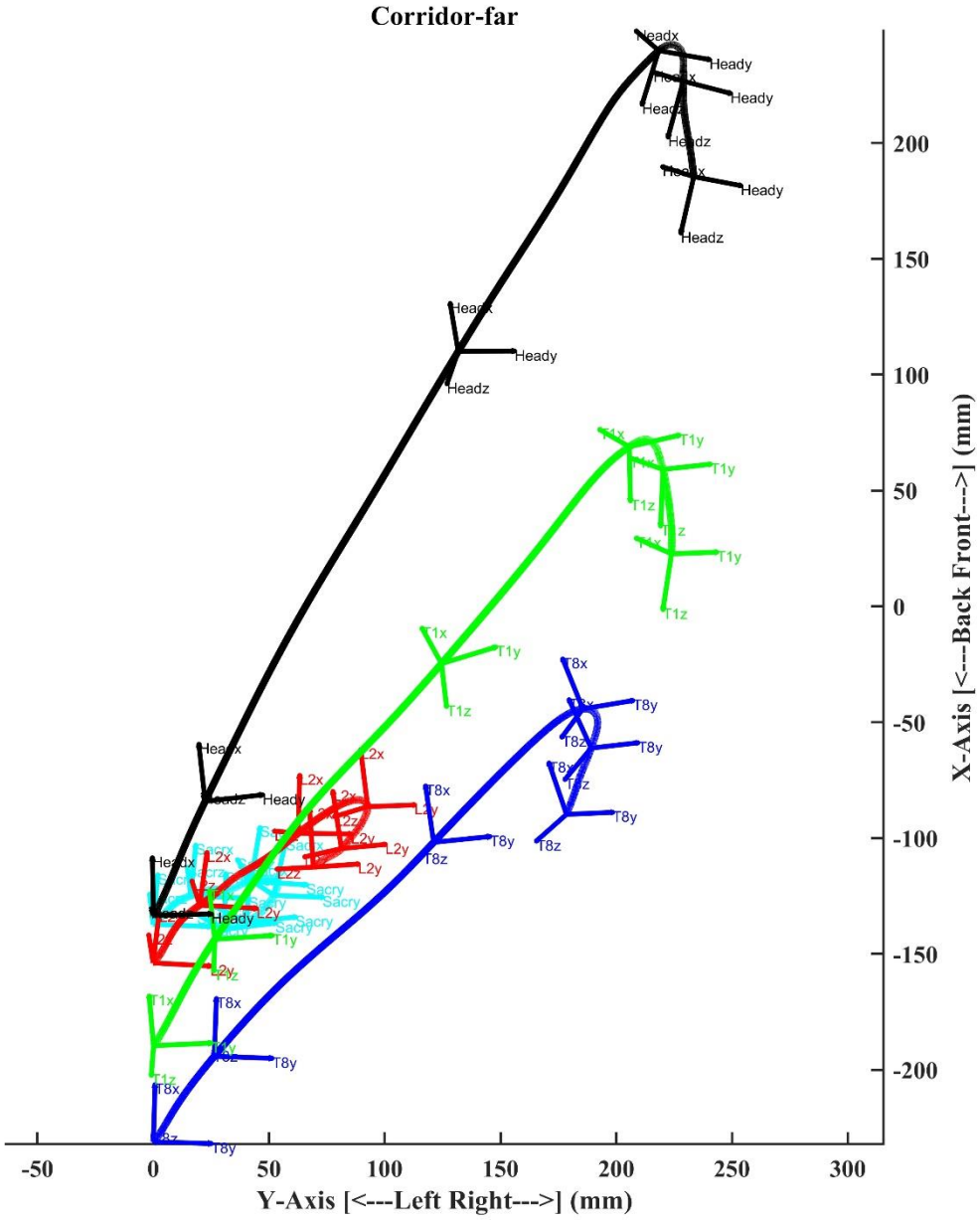

Figure 4.3.1.4-2: Overhead view of mean response of the head (black), T1 (green), T8 (blue), L2 (red), and pelvis (cyan) in far-side impacts. Average linear displacements are shown with the solid black curves. Average orientation is shown at discrete time intervals with orthogonal unit vectors at each body region.

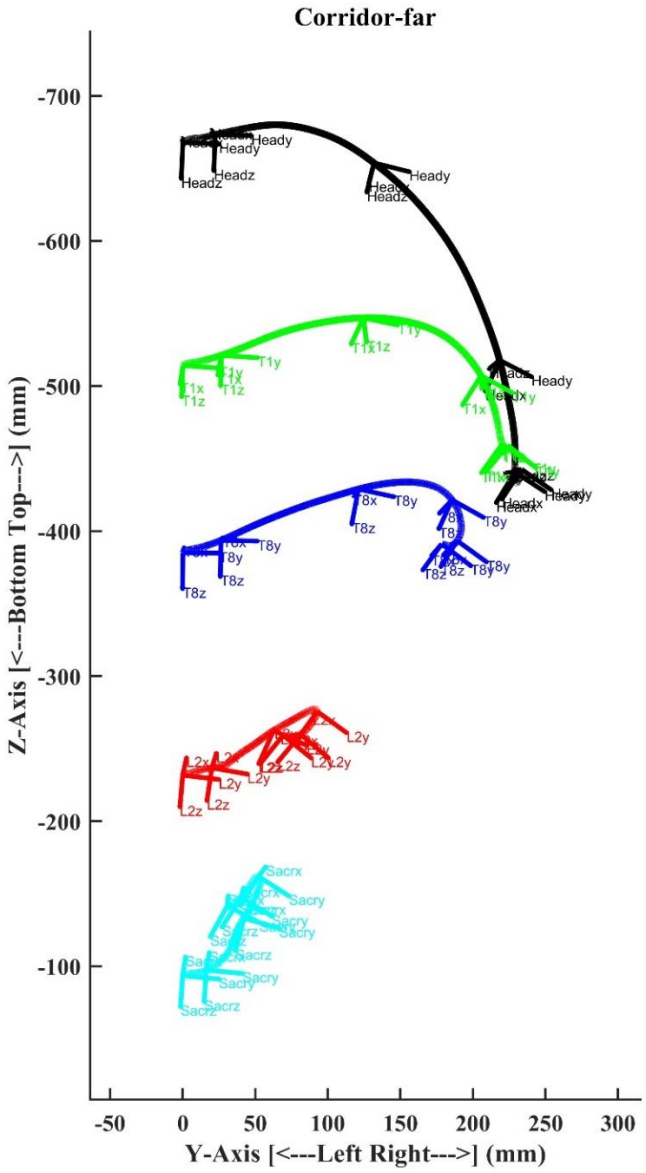

Figure 4.3.1.4-3: Rear view of mean response of the head (black), T1 (green), T8 (blue), L2 (red), and pelvis (cyan) in far-side impacts. Average linear displacements are shown with the solid black curves. Average orientation is shown in at discrete time intervals with orthogonal unit vectors at each body region.

The boundaries of the Global Kinematic head corridors with respect to the seat were calculated as 3-d error ellipsoids at every point in time (total of 4,001 ellipses for the event). The error ellipsoids were centered at the mean point at every time-step. Thus, the corridor's boundaries are the outer surface of the ellipsoid, which are determined by the semi-major lengths and three-dimensional orientation of the ellipsoid. Figures 4.3.1.4-4 through 4.3.1.4-6 show sample ellipsoids plotted in the three planes at discrete time intervals to demonstrate how the shape and size changes during the event. Larger ellipsoids indicate a greater spread in the data.

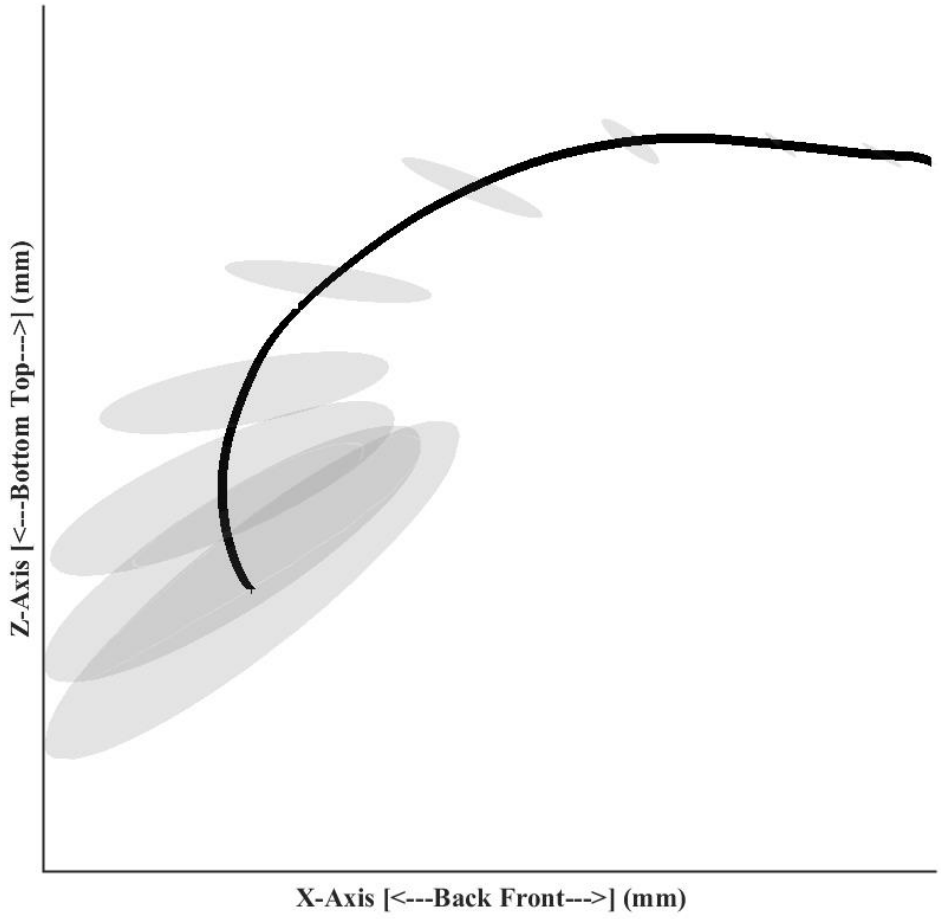

Figure 4.3.1.4-4: Schematic lateral view of mean response (solid black curve) of the head with the shaded corridor composed of 3-d error ellipsoids plotted at every 20 ms (400th point). Note how the 3-d ellipsoid enlarges as the head moves forward; this indicates an increase in the data spread. Also, the darker shading represents volumes where the ellipsoids overlap.

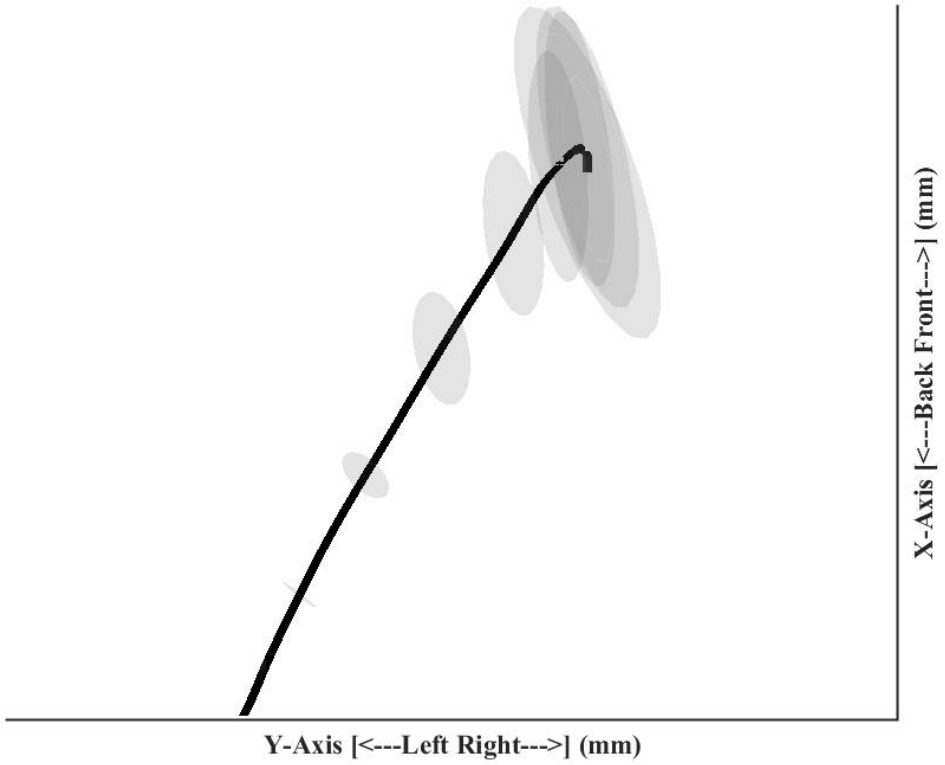

Figure 4.3.1.4-5: Schematic overhead view of mean response (solid black curve) of the head with the shaded corridor composed of 3-d error ellipsoids plotted at every 20 ms (400th point). Note how the 3-d ellipsoid enlarges as the head moves forward, which indicates an increase in the spread of the data. Also, the darker shading represents volumes where the ellipsoids overlap.

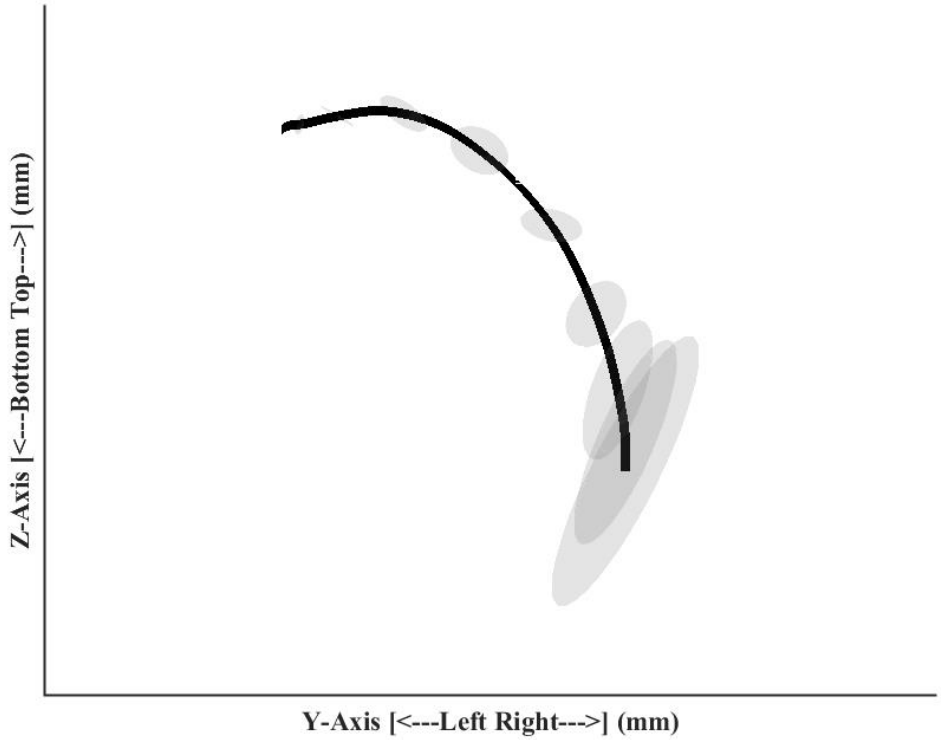

Figure 4.3.1.4-6: Schematic rear view of mean response (solid black curve) of the head with the shaded corridor composed of 3-d error ellipsoids plotted at every 20 ms (400th point). Note how the 3-d ellipsoid enlarges as the head moves forward, which indicates an increase in the spread of the data. Also, the darker shading represents volumes where the ellipsoids overlap.

The following set of three figures show the Global Kinematic far-side head corridors. The black curves are the mean response, and the three-dimensional ellipsoids determine the boundaries. While the ellipsoids were calculated at every time-step, for clarity, the figures depict the ellipsoids at every 10th time-step (every 0.5 ms). As stated above, the darker shading represents an overlap of the ellipsoids as the semi-major axes

change in length and orientation. The corridors are the outer boundaries of the ellipsoids.

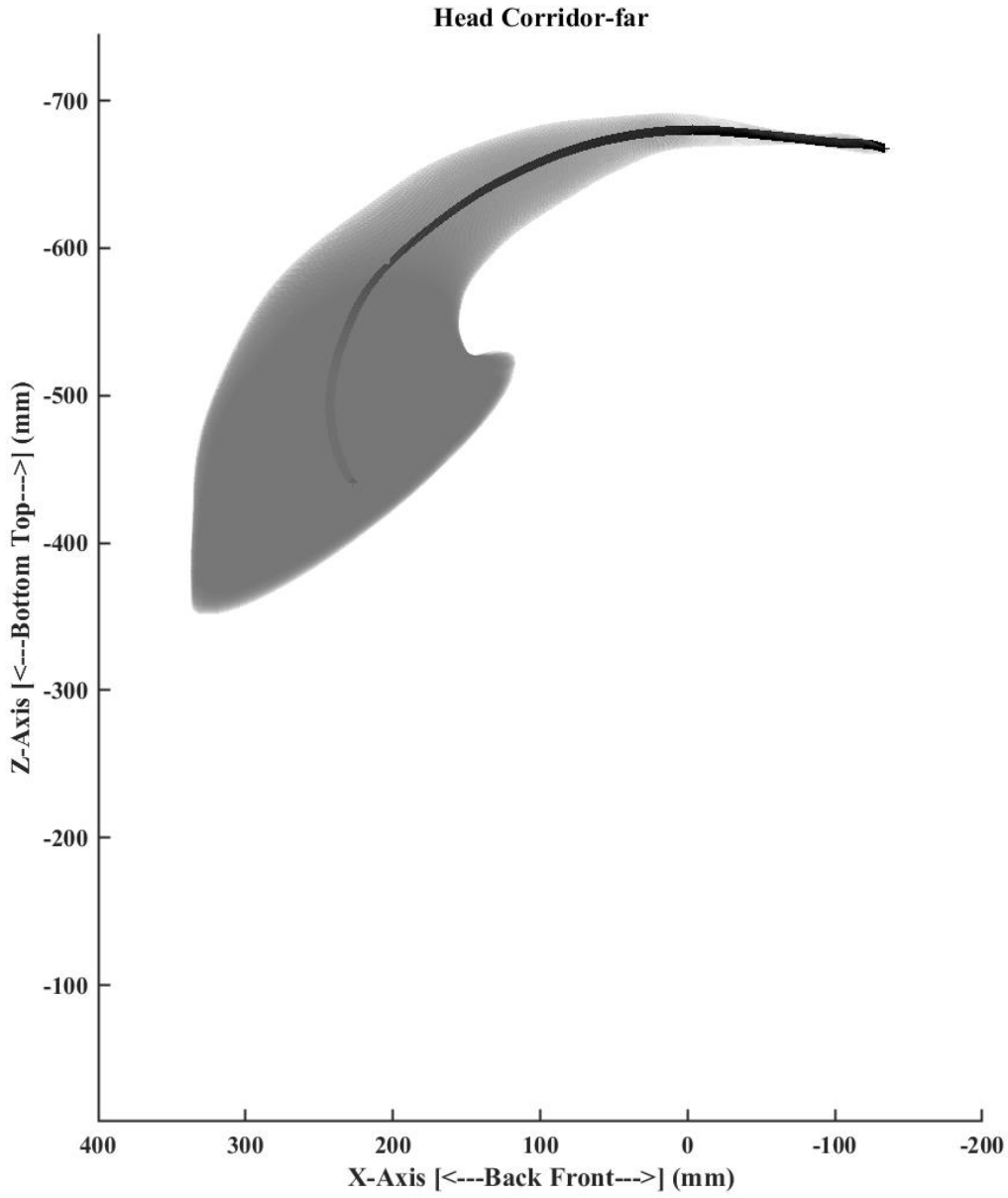

Figure 4.3.1.4-7: Lateral view of far-side mean response (solid black curve) of the head with shaded corridor composed of 3-d error ellipsoids plotted at every 10th-time step

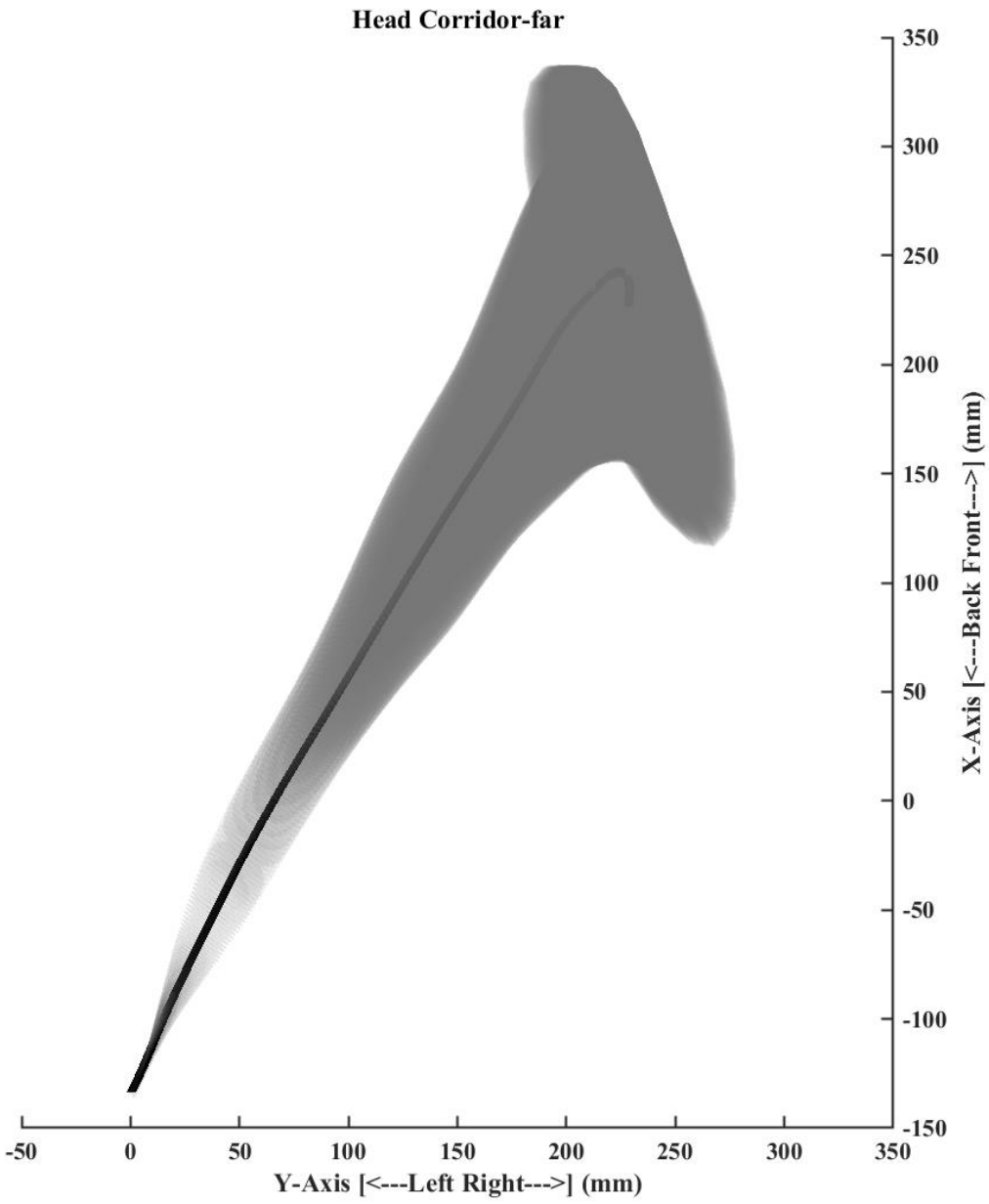

Figure 4.3.1.4-8: Overhead view of far-side mean response (solid black curve) of the head with shaded corridor composed of 3-d error ellipsoids plotted at every 10th-time step

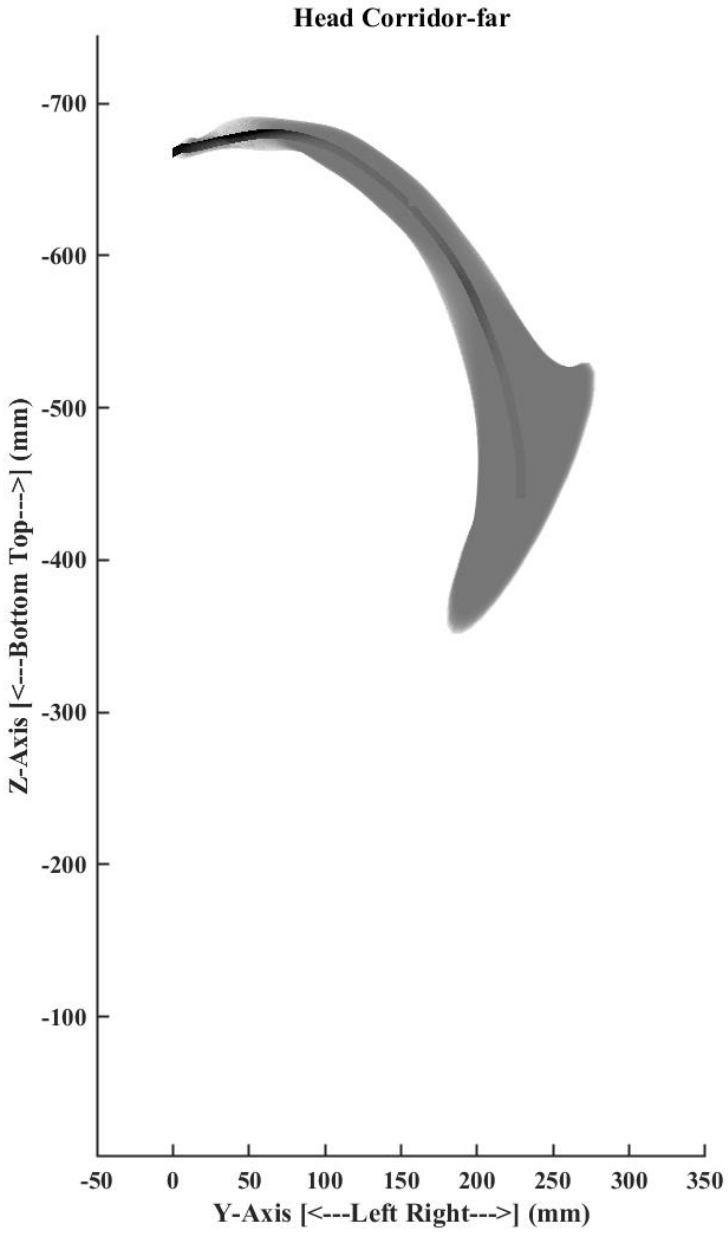

Figure 4.3.1.4-9: Rear view of far-side mean response (solid black curve) of the head with shaded corridor composed of 3-d error ellipsoids plotted at every 10th-time step

The following three figures represent the near-side mean trajectory and orientation relative to the seat for the head, T1, T8, L2, and sacrum. While the average orientation has been calculated at every-time step, for clarity, the unit vectors of the local anatomic orientation is shown at every 50 msec. The head demonstrates the largest excursion, and the overall motion at the anatomic regions decreases from superior to inferior. This is due to the test's boundary conditions where the pelvis was restrained by the lap belt and rigid knee and foot restraint. The interaction with the shoulder belt controlled the head and spine kinematics. Similarly, the head and T1 show the largest change in orientation with minimal change observed at the pelvis.

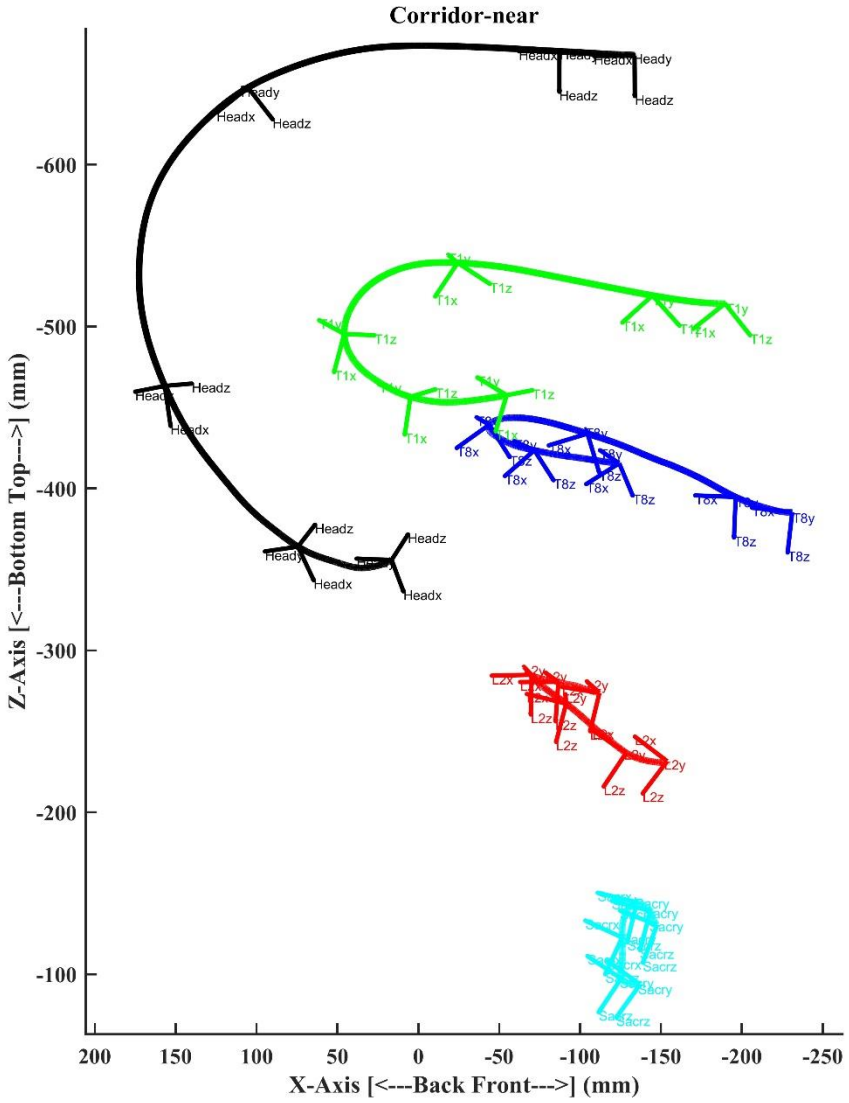

Figure 4.3.1.4-10: Lateral view of mean response of the head (black), T1 (green), T8 (blue), L2 (red), and pelvis (cyan) in near-side impacts. Average linear displacements are shown with the solid curves. Average orientation is shown in at discrete time intervals with orthogonal unit vectors at each body region.

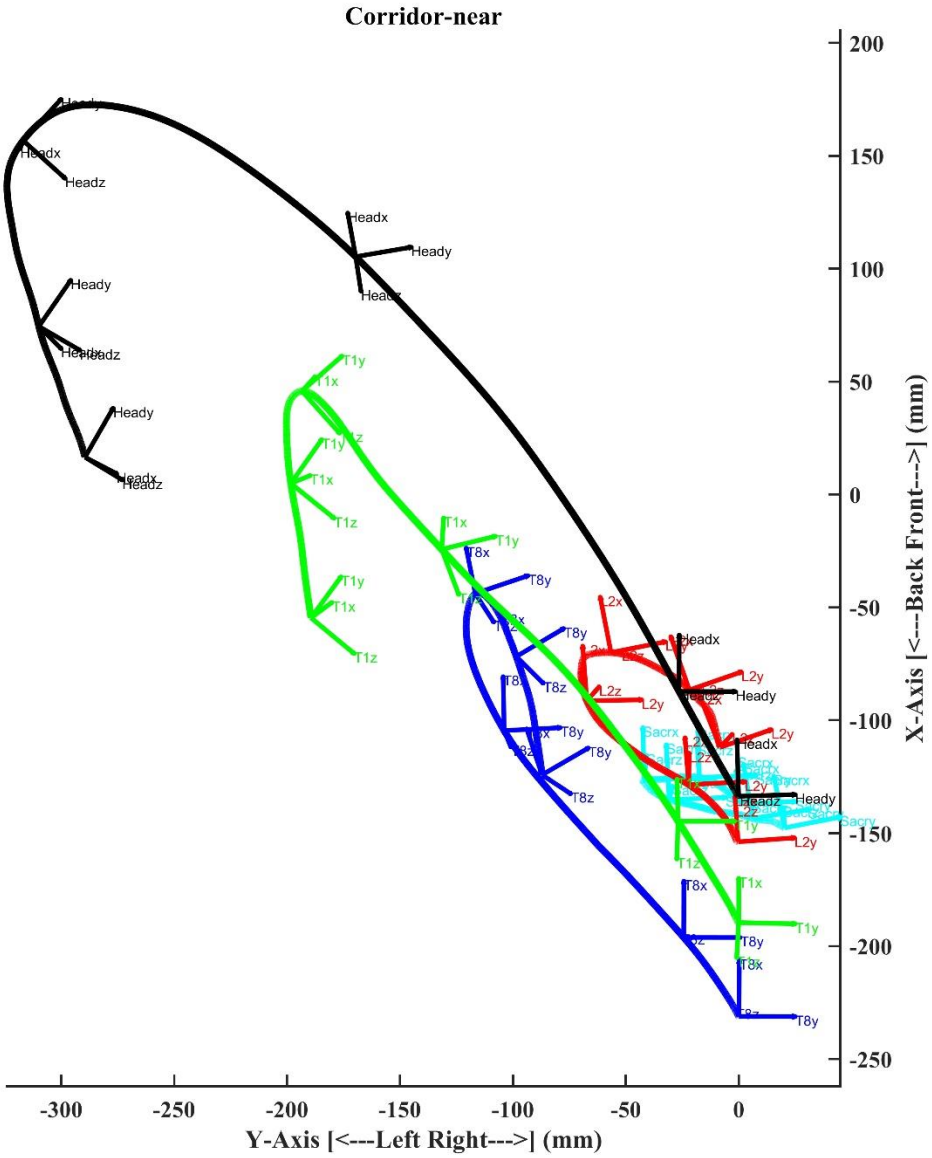

Figure 4.3.1.4-11: Overhead view of mean response of the head (black), T1 (green), T8 (blue), L2 (red), and pelvis (cyan) in near-side impacts. Average linear displacements are shown with the solid curves. Average orientation is shown in at discrete time intervals with orthogonal unit vectors at each body region.

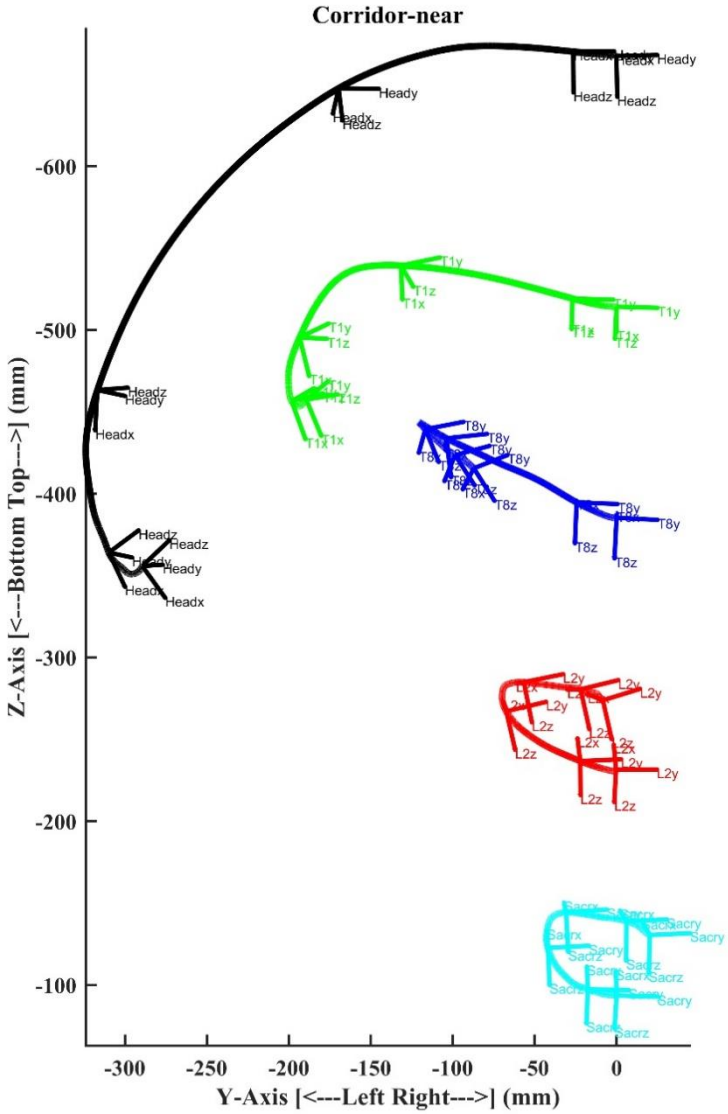

Figure 4.3.1.4-12: Rear view of mean response of the head (black), T1 (green), T8 (blue), L2 (red), and pelvis (cyan)in near-side impacts. Average linear displacements are shown with the solid curves. Average orientation is shown in at discrete time intervals with orthogonal unit vectors at each body region.

The following set of three figures show the Global Kinematic near-side head corridors. The black curves are the mean response, and the boundaries are determined by the three-dimensional ellipsoids. While the ellipsoids were calculated at every time-step, for clarity, the figures depict the ellipsoids at every 10^{th} time-step (every 0.5 ms). As stated above, the darker shading represents an overlap of the ellipsoids as the semi-major axes change in length and orientation. The corridors are the outer boundaries of the ellipsoids.

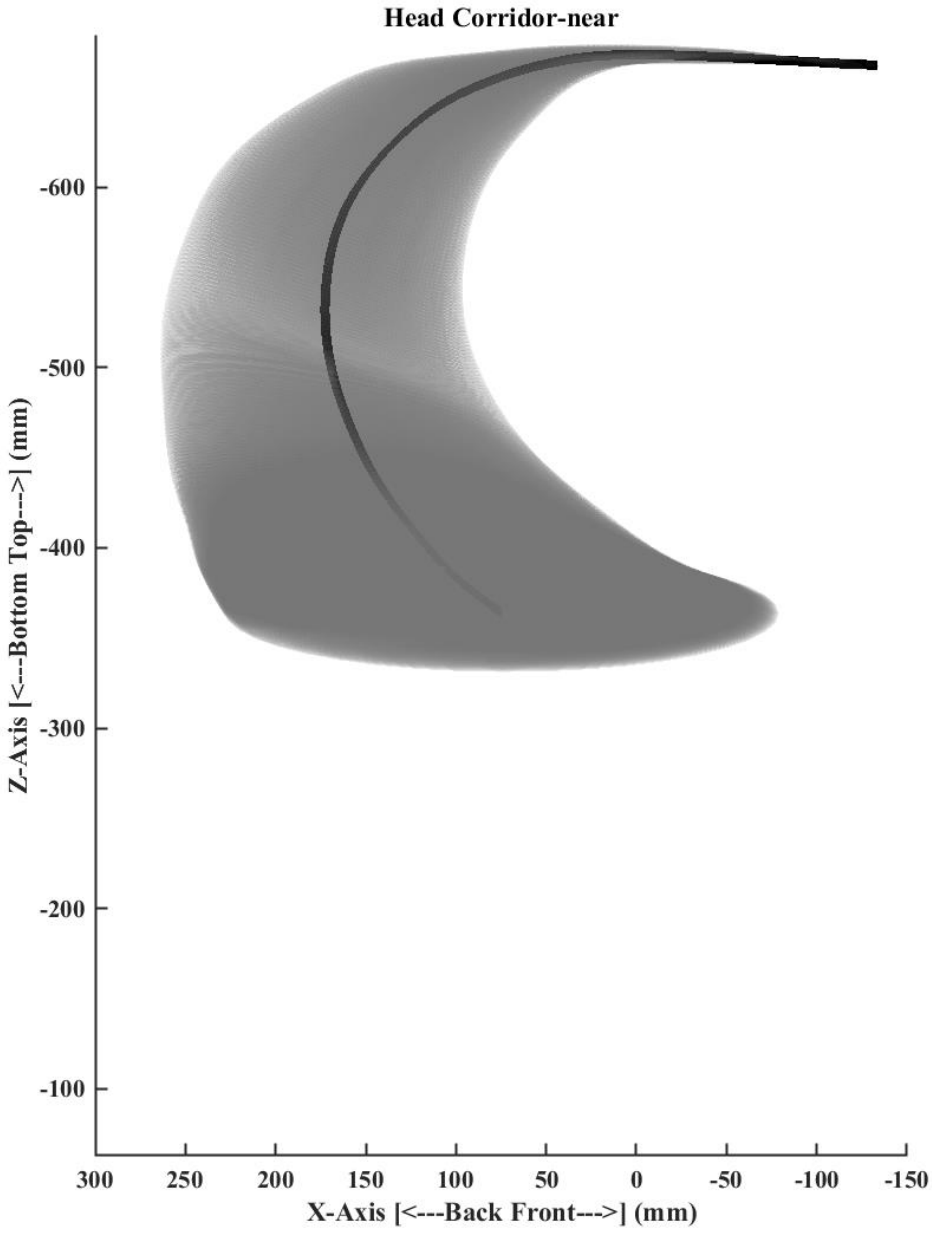

Figure 4.3.1.4-13: Lateral view of near-side mean response (solid black curve) of the head with shaded corridor composed of 3-d error ellipsoids plotted at every 10th-time step

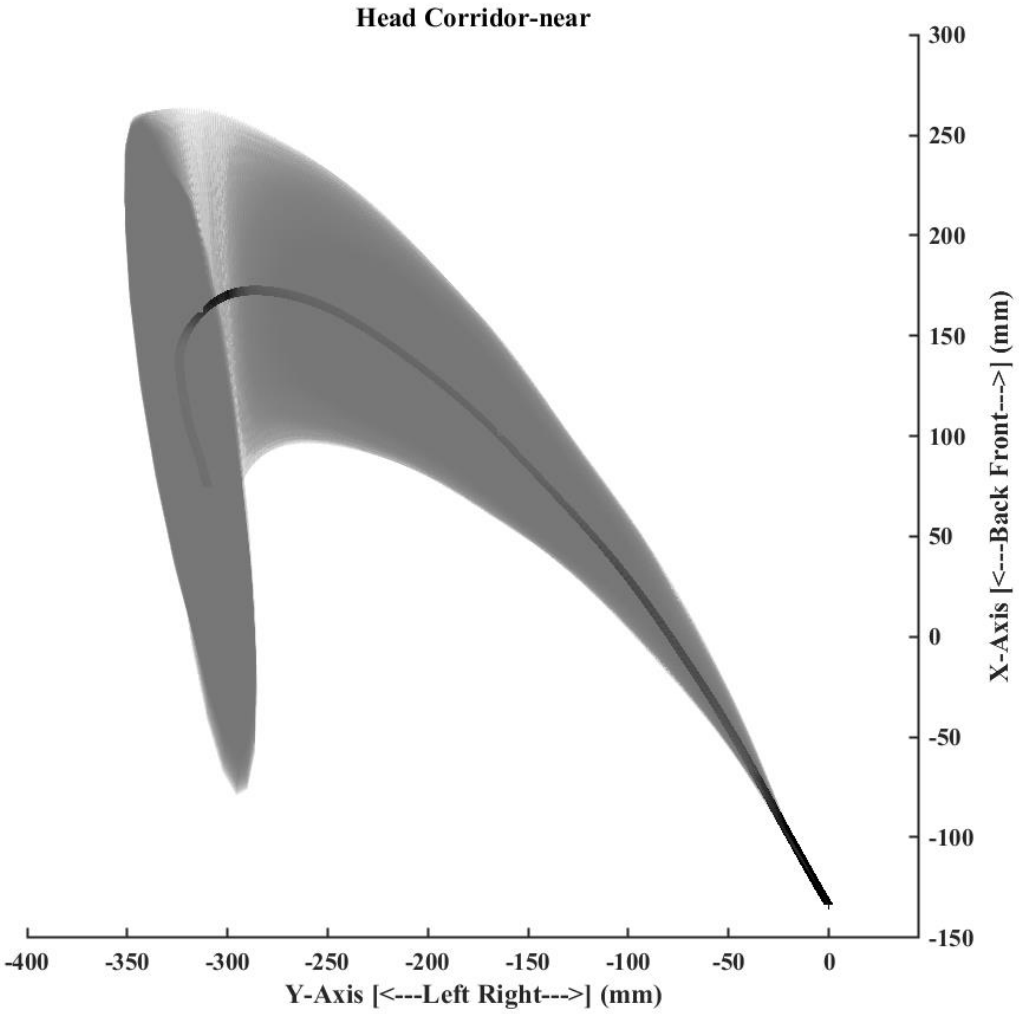

Figure 4.3.1.4-14: Overhead view of near-side mean response (solid black curve) of the head with shaded corridor composed of 3-d error ellipsoids plotted at every 10th-time step

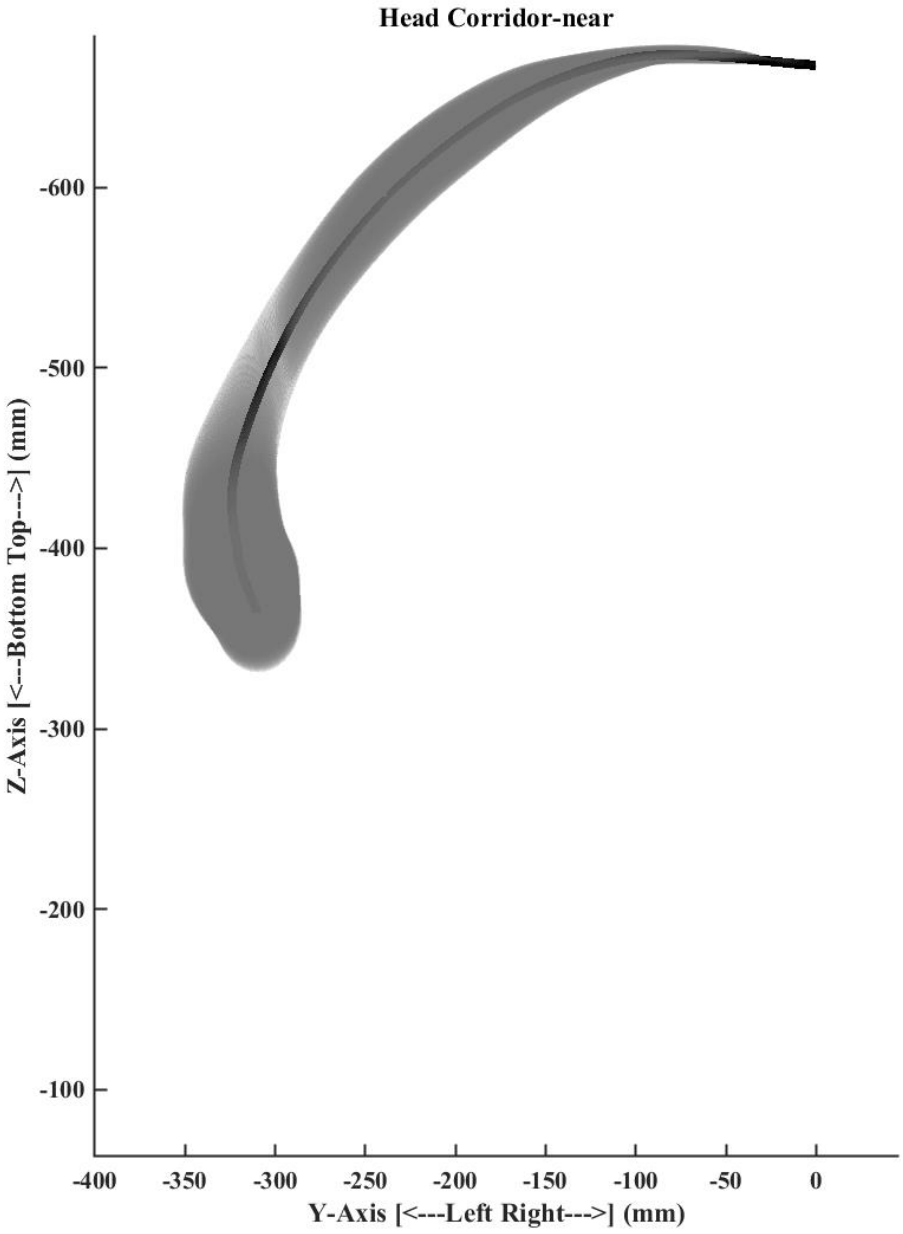

Figure 4.3.1.4-15: Rear view of near-side mean response (solid black curve) of the head with shaded corridor composed of 3-d error ellipsoids plotted at every 10th-time step

4.3.1.5. Non-Planar Thorax Injury Risk Curve

The tables below show the peak sternum deflections values for the A/P, sagittal, transverse, and multiplane metrics for the high- and low-speed tests in near- and far-side impacts. On a specimen-by-specimen basis, the multiplanar deflection was the largest, while the A/P deflection was the lowest.

Table 4.3.1.5-1: Far-side sternum deflections (mm) and injury outcomes

Test ID	Velocity	Injury	A/P	Transverse	Sagittal	Multiplanar
NSFSC0120	High	No	40.9	41.8	41.8	42.7
NSFSC0121	High	No	34.1	35.5	34.6	36.1
NSFSC0125	High	Yes	27.0	28.4	28.8	30.2
NSFSC0126	High	Yes	31.0	31.2	32.9	33.1
NSFSC0129	High	Yes	46.0	46.1	46.8	46.8
NSFSC0136	Low	Yes	30.4	34.8	30.5	34.8
NSFSC0138	Low	No	28.2	28.3	28.4	28.6
NSFSC0140	Low	No	10.7	12.9	10.8	13.0

Table 4.3.1.5-2: Near-side sternum deflections (mm) and injury outcomes

Test ID	Velocity	Injury	A/P	Transverse	Sagittal	Multiplanar
NSFSC0122	High	Yes	62.0	62.2	64.5	64.6
NSFSC0123	High	Yes	62.3	74.9	70.1	81.1
NSFSC0127	High	Yes	57.4	57.5	57.4	57.5
NSFSC0124	High	No	27.5	28.3	33.2	33.9
NSFSC0128	High	No	33.9	39.5	34.5	40.0
NSFSC0130	Low	No	26.4	26.6	27.7	27.9
NSFSC0132	Low	No	43.8	43.9	46.0	46.0
NSFSC0134	Low	No	18.8	19.0	18.8	19.0

The following table and plot show the summary of results from the survival analysis and the injury risk curves for A/P sternum deflection.

Table 4.3.1.5-3: Summary of survival analysis results for A/P sternum deflection

Risk Level	95% Confidence intervals		Deflection (mm)	Upper 95% CI	Quality index
	Lower bound	Upper bound			
0.05	18	40	27	0.82	Fair
0.10	23	44	32	0.66	Fair
0.25	32	51	40	0.46	Good
0.50	41	59	49	0.35	Good
0.75	58	69	58	0.35	Good
0.90	53	79	65	0.40	Good
0.95	69	86	69	0.44	Good

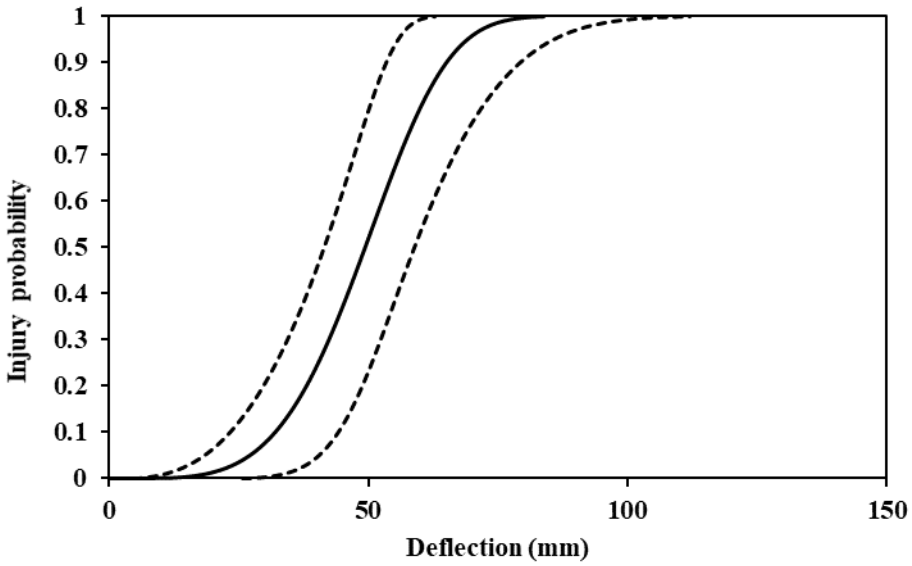

Figure 4.3.1.4-16: Injury risk curve for A/P sternum deflection. The solid black line represents AIS2+ injury risk as a function of A/P deflection. The dotted black curves are the boundaries of the 95% confidence intervals.

The following table and plot show the summary of results from the survival analysis and the injury risk curves for transverse sternum deflection.

Table 4.3.1.5-4: Summary of survival analysis results for transverse sternum deflection

Risk Level	95% Confidence intervals		Deflection (mm)	Upper 95% CI	Quality index
	Lower bound	Upper bound			
0.05	18	41	27	0.88	Fair
0.10	23	46	33	0.71	Fair
0.25	33	54	42	0.50	Fair
0.50	43	64	53	0.39	Good
0.75	63	76	63	0.39	Good
0.90	58	89	71	0.43	Good
0.95	76	96	76	0.47	Good

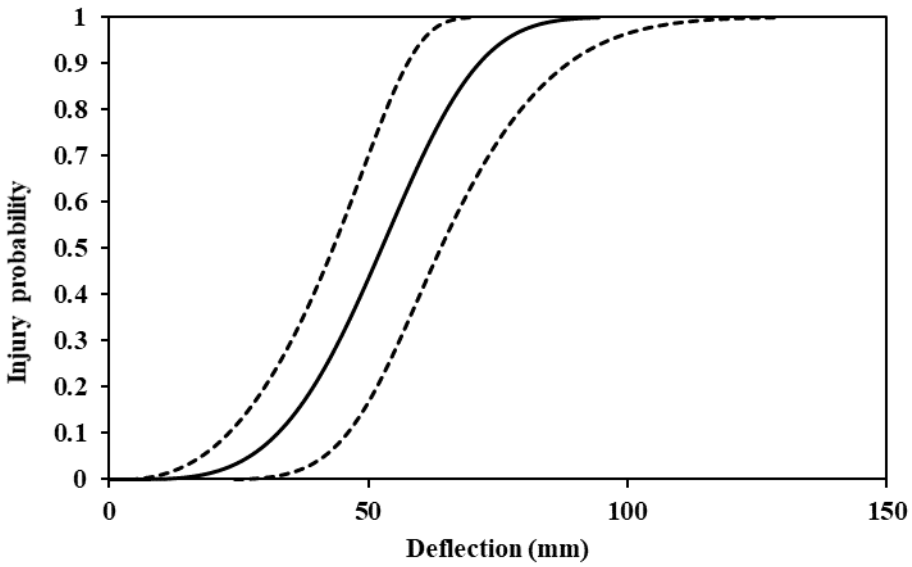

Figure 4.3.1.4-17: Injury risk curve for transverse sternum deflection. The solid black line represents AIS2+ injury risk as a function of transverse deflection. The dotted black curves are the boundaries of the 95% confidence intervals.

The following table and plot show the summary of results from the survival analysis and the injury risk curves for sagittal sternum deflection.

Table 4.3.1.5-5: Summary of survival analysis results for sagittal sternum deflection

Risk Level	95% Confidence intervals		Deflection (mm)	Upper 95% CI	Quality index
	Lower bound	Upper bound			
0.05	18	42	27	0.85	Fair
0.10	23	46	33	0.69	Fair
0.25	33	53	42	0.48	Good
0.50	43	63	52	0.38	Good
0.75	62	74	62	0.37	Good
0.90	57	86	70	0.42	Good
0.95	74	93	74	0.46	Good

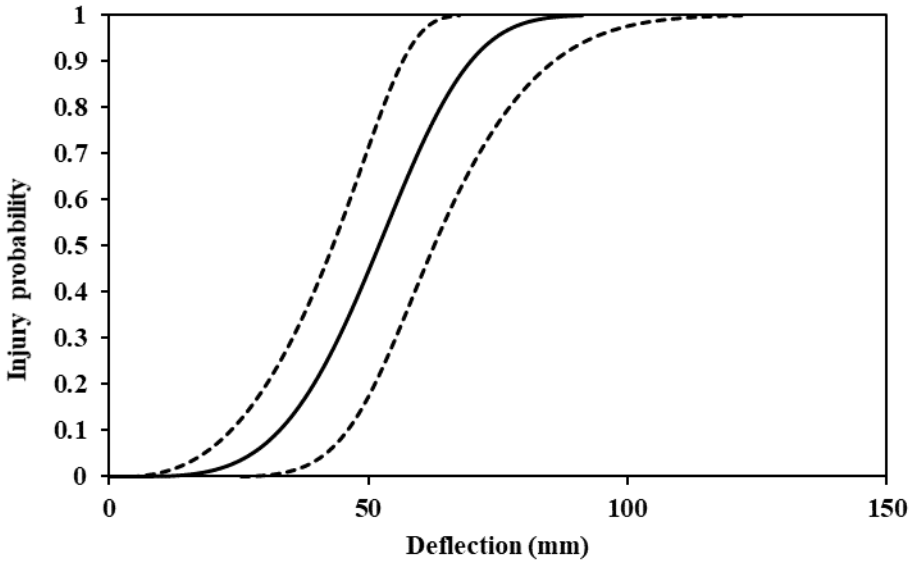

Figure 4.3.1.4-18: Injury risk curve for sagittal sternum deflection. The solid black line represents AIS2+ injury risk as a function of sagittal deflection. The dotted black curves are the boundaries of the 95% confidence intervals.

The following table and plot show the summary of results from the survival analysis and the injury risk curves for multiplanar sternum deflection.

Table 4.3.1.5-6: Summary of survival analysis results for multiplanar sternum deflection

Risk Level	95% Confidence intervals		Deflection (mm)	Upper 95% CI	Quality index
	Lower bound	Upper bound			
0.05	17	42	27	0.91	Fair
0.10	23	47	33	0.74	Fair
0.25	33	56	43	0.53	Fair
0.50	45	67	55	0.42	Good
0.75	66	81	66	0.41	Good
0.90	61	95	76	0.45	Good
0.95	81	104	81	0.49	Good

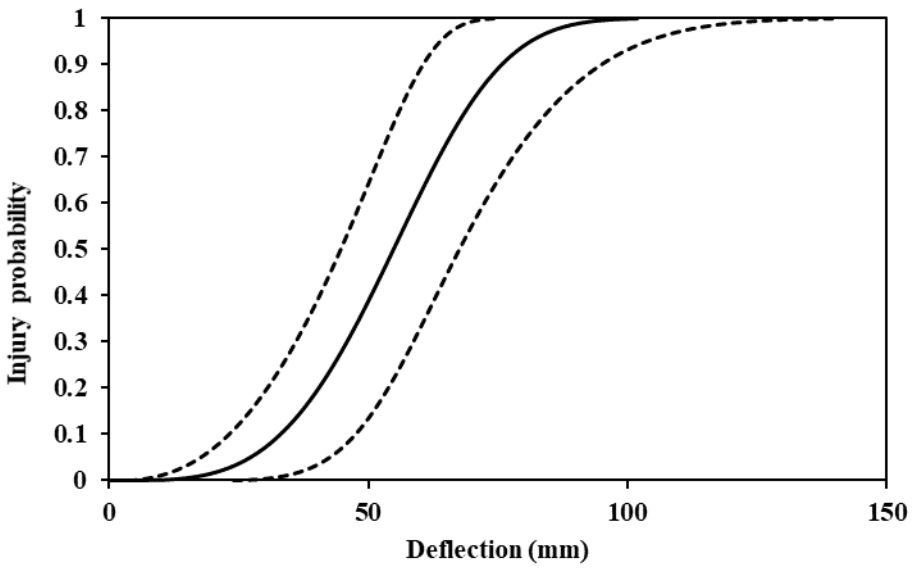

Figure 4.3.1.4-19: Injury risk curve for multiplanar sternum deflection. The solid black line represents AIS2+ injury risk as a function of multiplanar deflection. The dotted black curves are the boundaries of the 95% confidence intervals.

The Brier Metric Scores for the four sternum deflection metrics were 5.40, 5.18, 5.29, and 5.17 for the A/P, transverse, sagittal, and multiplanar deflections, respectively.

Therefore, the multiplanar sternum deflection was considered the injury risk curve to best represent the injuries to small females in near- and far-side impacts.

4.4. DISCUSSION

Ten healthy small female PMHS were tested in near- and far-side high-speed oblique frontal impacts (5 PMHS in each condition). Global linear acceleration and angular velocity response corridors were calculated. The proximal anatomic regions showed similar responses in magnitude and curve morphology for the two Global Corridors, except the y-linear accelerations and x angular velocities were opposite. Distal segments (head and T1) demonstrated less agreement in the x- and y-axes for linear acceleration and x- and z-axes for angular velocity. These two trends were attributed to the boundary conditions of the test. The occupant's feet and legs were fixed to rigid supports, and the pelvis had rigid lateral constraints and was restrained by the lap belt. As such, the lower extremities and pelvis were well coupled to the base of the sled for both near- and far-side impacts and yielded a similar response. The distal segments were restrained by a driver's side (left shoulder to right hip) shoulder belt, and the interaction of the occupant with the belt was different in near- and far-side impacts. The occupant is less restrained by the 3-point belt in far-side impacts and is, therefore, less coupled to the sled. The superior segments' response in far-side impacts generally have a longer width and are lower in magnitude than the near-side response.

One of the challenges of using experimental data to compare the outputs from the human body computer models is understanding how those data were gathered and processed. Fundamentally, modelers need to know the coordinate system(s) and

origin(s) of the PMHS data, instrumentation issues (such as placement location), and how these factors are accurately duplicated in the finite-element simulations. Any inaccuracies in incorporating these variables can lead to unknown sources of error in the model validation process, and the ensuing inferences gleaned from simulations. Due to academia's constraints and journal publication practices, modelers may not have access to sufficient information to transform experimental data from published reports accurately. For example, the set of Global Corridors presented in the current study is referenced to a global axis system for clarity and portability to whole-human-body computer models. In order to align the PMHS local linear accelerations and angular velocities to a global time-history format, the three-dimensional orientations of the local axes must be determined at each time-step. This is best calculated using the local marker trajectory data collected from a motion-capture system. The positions of the markers relative to the local anatomic and sensor axes must be known to reorient the data to a global axis system accurately. Expressing corridors in a global format reduces errors in data translation for input and comparison with human body computational models. These important factors were the impetus for the development of the Global Sensor Corridors.

The second objective of creating Global Corridors was the development of female-specific three-dimensional kinematic biofidelity corridors in oblique near- and far-side frontal impacts for the head, spine, and pelvis. One advantage of this data is that the corridors were constructed from female-only PMHS tests and are thus directly applicable to the development and validation of physical and computational female

surrogates. There are differences between men and women in terms of spine hard- and soft-tissue component geometries, column curvatures, and structural properties (Yoganandan et al., 2017). Others have shown that the segmental spinal motions in females are significantly less than males (Stemper et al., 2003), which may be attributed to known differences in spinal geometry (Liguoro et al., 1994; Parenteau et al., 2014) and spinal joint facet anatomy (Yoganandan et al., 2003). It is also well known that the lumbar spine's bone mineral density is sex and age-specific (Bruno et al., 2014; Mosekilde and Mosekilde, 1990). These factors suggest that it may not be appropriate to include male PMHS response data for these purposes. Variations in the above characteristics may result in differences in the three-dimensional spine kinematics between male and female subjects, especially considering that the current study's occupant response occurs in all three anatomic planes (flexion, lateral bending, and axial rotation).

To minimize the biological variability between PMHS, care was taken to pre-screen specimens for mass, stature, and QCT BMD of the lumbar spine. This inclusion criterion was designed to represent a small and 'healthy' female population (ACR, 2013). As indicated earlier, many types of normalization and scaling (Yoganandan et al., 2014) techniques have been used to construct biofidelity response corridors. For whole-body responses, an equal-stress equal-velocity (Eppinger R. et al., 1984) approach has been used to develop injury corridors for the ES-2re (Kuppa et al., 2003). This technique assumes a linear relationship between length, mass, and time units to scale PMHS response using a factor proportional to total body mass. Its straightforward approach is

useful for large sets of PMHS data with large deviations in occupant mass. The mass scaling approach was not used to develop the corridors for the following reasons: factors such as local flexibility of the spine in sagittal and coronal bending and stiffness of the rib cage affect the three-dimensional kinematics of the occupant in this oblique mode, factors which the overall mass scaling does not accommodate. Moreover, given the test's boundary conditions, the total mass of the specimen is likely not representative of the occupants' response.; lower extremities were fixed against rigid restraints distal to the knees and inferior to the feet, and pelvis excursion was limited by the lap belt and lateral wedges on the seat. It may be appropriate to scale based on the mass superior to the pelvis from a mechanics perspective. Anthropometry studies of females have shown this to be approximately 37% of the total body mass (Young et al., 1983). Given the relatively low variability (coefficient of variation less than 12%) in specimen mass for each condition and the above factors, the responses of the PMHS were not normalized/scaled to develop the current set of biofidelity corridors for near- and far-side for head, spine, and pelvis responses to oblique frontal impacts.

Occupant three-dimensional kinematics have been reported from previous near-side frontal oblique tests from three PMHS approximating a 50th-percentile male. (Acosta et al., 2016). In these experiments, the PMHS were seated on a buck replicated by the current study at a 30-degree angle (near-side) from the acceleration vector. The specimen seating procedure (lower extremities, pelvis, torso, and head), restraints, acceleration pulse, and local coordinate systems were similar. The only notable difference was that the male PMHS limited the load on the D-Ring side of the shoulder

belt to 3 kN, while the current was 2 kN. As a preliminary evaluation of the male versus female response, the female near-side peak mean displacements agree with the male data in all body regions in the forward direction. There is a similar agreement in the lateral direction for all body regions except the head, which showed more displacement in the female experiments. This difference was attributed to a large variation in one specimen (4^{th} specimen), the oldest specimen. Cervical spine motion affects head kinematics, and perhaps in this specimen, the effect was greater than in other specimens. Given that the male subjects were on average 18 cm taller in stature, from a purely geometric standpoint, it would be reasonable to expect larger peak excursions in the male tests than the female tests for the same belt load limit condition. However, the present study (female tests) used a 2 kN load limiter—in contrast to the 3 kN limiter used in the male tests. Thus, while the male subjects were taller, this difference in excursion was reduced due to the load limiter differences between the male and female test series. This observation highlights the role of shoulder belt load-limiting devices on occupant kinematics.

When comparing the Global kinematic corridors, higher peak mean excursions were observed in the fore/aft and lateral directions for the far-side tests for all anatomical structures except the head in the lateral direction. The excursions were generally greater at the head, spine, and pelvis in the far-side, likely due to the interaction with the shoulder belt. As noted above, the higher lateral excursion at the head in the near-side test condition was attributed to the oldest specimen's response. Given the usage of three-point restraints in automobile front and rear seating positions,

as well as differences in kinematics observed between near- and far-side tests, physical and computational surrogates need to be validated in both configurations.

The second objective was to determine the sternum deflection using four different metrics (A/P, transverse, sagittal, and multiplanar). Sternum deflection was selected as the injury metric as it reliably characterizes chest injuries in frontal and oblique impacts and is measurable with dummies. Also, the sternum was directly loaded by the belt in both near- and far-side impacts, and thus data from both impacts were combined for survival analysis. These deflections apply to the driver occupant kinematics, as the specimens were seated in a standard driving position. From a statistical perspective, the multiplanar deflection IRC was equivalent to the transverse-plane deflection. More notably, it is anticipated that occupant seating postures will change (e.g., reclined postures and/or obliquely mounted seats) as the industry progresses to higher vehicular automation levels. Because of the small sample size, the IRCs should be considered as preliminary tolerance data for females. Additional tests are needed to increase the IRC's robustness and examine factors such as age and body mass index on injuries. Uncertainties in the motion-capture data are a source of error and are approximately 1–2 mm for this rate of loading and capture volume. The current results indicate that the peak sternum x-y-z (multiplanar) deflection is the optimal metric that best describes the underlying response to chest injuries at the AIS 2+ level to small females from oblique frontal impacts.

As the automotive fleet moves towards highly automated vehicles, human body computer models and ATDs will need to be validated in combined loading directions. It

is anticipated that occupants will experience off-axis loads in pure frontal impacts due to alternative seating positions, as alternative seating positions change the occupant's sagittal plane's orientation to the centerline of the vehicle. This may change occupant kinematics and injury patterns that need further research. The presently developed novel methodologies can be effectively used to assess these surrogates and advance human safety.

4.5. SUMMARY

- Whole-body sled tests were conducted in near- and far-side frontal impacts simulating a driver occupant in an automotive environment.
- Global sensor corridors were developed for the linear accelerations and angular velocities for different body regions—head, spine (T1, T8, and L2), and pelvis.
- Global kinematic corridors were developed for the head, spine (T1, T8, and L2), and pelvis. The corridors showed the mean linear and orientation in three dimensions.
- Error ellipsoids for the global head kinematics were shown to define the boundaries of the corridor. The corridor boundaries increased in size throughout the event, which indicated the spread of the data.
- Sternum deflection was calculated using four different metrics: (1) A/P, (2) transverse, (3) sagittal, and (4) mulitplanar.
- AIS 2+ injury risk curves were developed for each metric using the peak sternum deflection and the injury information from the high and low-speed tests. Brier Score Metrics were also calculated.
- The optimal injury risk curve was associated with the multiplanar deflection metric.
- These methodologies are relevant as developments in autonomous technologies lead to non-standard seating postures in newer vehicles. Occupant loading in vehicle crashes is likely to result in multiplanar response and injury mechanisms.

- Work is being conducted in our laboratory using these methods for calculated the global sensor and kinematic corridors and injury risk curves to assess the THOR-05F ATD for the National Highway Traffic Safety Administration (NHTSA).

CHAPTER 5. DESIGN OF AN EXPERIMENT TO APPLY COMPLEX LOADING TO THE CERVICAL SPINE

5.1. INTRODUCTION

5.1.1. Background

Human tolerance and injury criteria have been developed using Post Mortem Human Surrogate (PMHS) tests under the primary modes: flexion-extension representing the sagittal bending behavior for frontal impacts left to right bending response representing the lateral bending behavior for side impacts, compressive response representing the axial behavior for rollover-type impacts, and inertial extension-flexion response for rear impacts [82]. Dummies (Hybrid III, ES2-re, WorldSID, BioRID) have been developed using the PMHS responses. Human tolerance in the form of injury criteria ($N_{ij,}$ for example) has been promulgated by regulatory agencies in the US and Europe [83]. Computational finite-element models have been used to understand the intrinsic responses better. For example, the University of Strasbourg has developed a sophisticated model that has been validated under some of the above 'simple' loading modes and for which segmental forces and moments have been determined [84-87].

While these efforts have proven effective in improving safety, posture effects have essentially been limited to controlled single plane/axis. Modern automotive environments involve increasing attention to advancing vehicle automation, which includes developing different seating systems. These different seating systems may expose the vehicle occupant to alternate and complex postures. It is well known that the human spine tolerance to inertial- or contact-induced external mechanical impact

depends on the initial posture or orientation [88]. For example, the stiffness of the spine is different in flexion, extension, and lateral bending. It is also known that the segmental rotations of the neck are different between cervical spinal levels due to the characteristic anatomy of the human vertebral column—e.g., (a) uncovertebral joints in the subaxial (C2-C7) spine, (b) intervertebral disc-less joints in the upper cervical spine (occiput to C2), and (c) anatomy of the facet joints [89-91]. To determine the complex biomechanical behavior of the neck under external mechanical loading, focused studies are needed.

5.1.2. Objectives

The objectives of this research are to develop an experimental protocol for conducting tests using PMHS cervical spines that will record forces and moments using load cells, record motions of retroreflective targets at different spinal levels, and process synchronized load cell and kinematic data for use in computational models, thus describing the biomechanical responses of the PMHS cervical spines under complex loading.

5.2. METHODS

5.2.1. Specimen Preparation

PMHS cervical spine was isolated from Head to T1. Before preparation, a set of CT scans were obtained and evaluated by a clinician. The specimen's inferior end was potted in polymethyl-methacrylate (PMMA) such that the T1/C7 disc is unconstrained. The distal cranium was removed and potted such that the OC-C1 joint was unconstrained. Figure 5.2.1-1 shows the details of the cranium isolation.

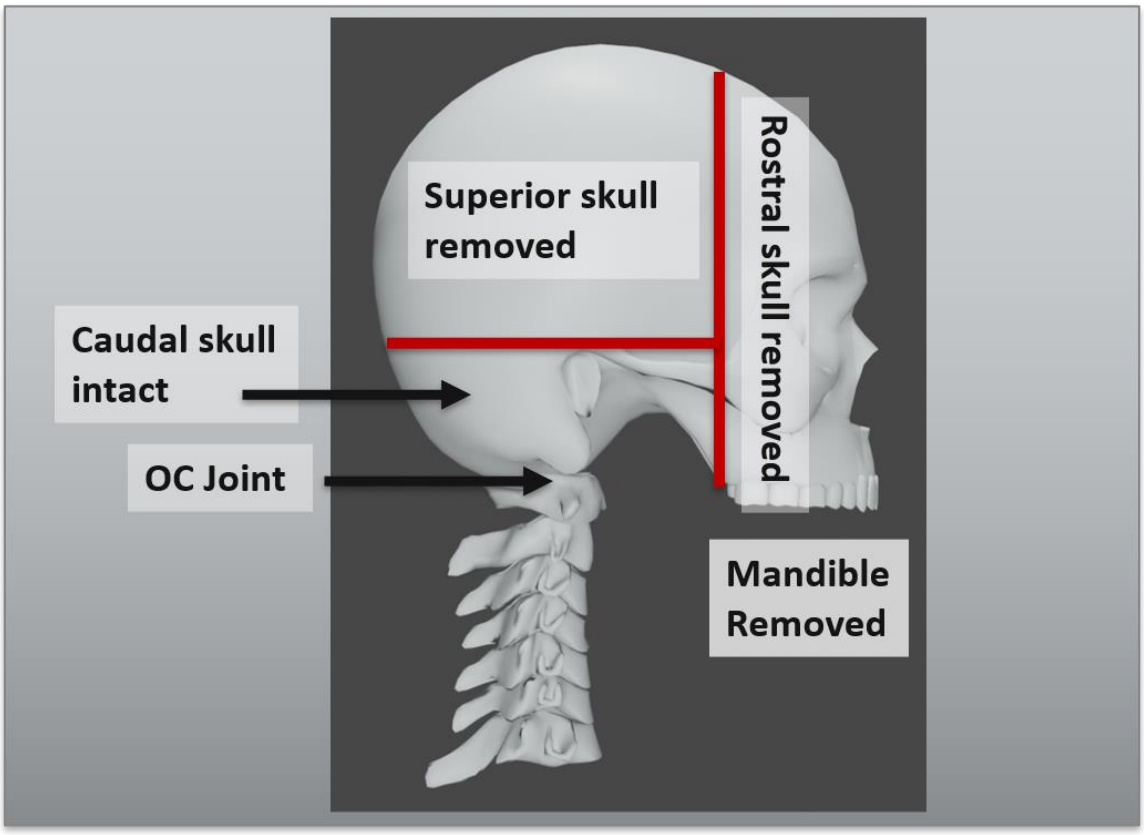

Figure 5.2.1-1: Details of cranium isolation

Six-axis load cells were mounted distal to the superior PMMA and proximal to the inferior PMMA. Sets of three non-collinear retroreflective targets were attached to the anterior vertebral body at alternating levels, C3-C7. Additionally, three targets were mounted on the anterior surface of the inferior and superior PMMA. Prior to testing, a set of instrumented CT scans were obtained. Figure 5.2.1-2 shows the pre-test CT scans.

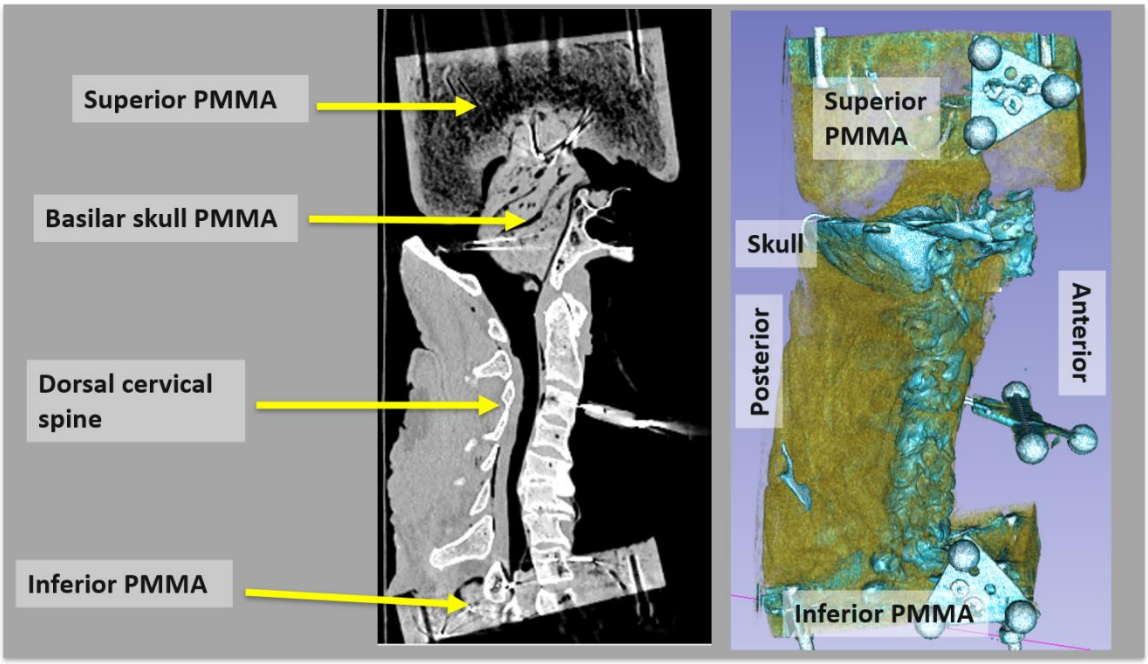

Figure 5.2.1-2: Mid-sagittal planar CT scan on the left and reconstructed 3-d CT scan on the right. Superior, basilar skull, and inferior PMMA are shown, along with retroreflective targets at the superior PMMA (head), cervical spine, and inferior PMMA (T1).

5.2.2. Test Device

Testing was conducted using an electro-hydraulic piston, which applied a rate-controlled linear displacement. A new device was fabricated, termed Dynamic Moment System (DMS), to transfer the piston's linear motion to a torque (Figure 5.2.2-1). In the DMS, the piston is connected to a rotary disc via a slider-crank mechanism so that the vertical motion of the piston changes the angular position of the disk. A transmission shaft connects the disc to the isolated neck using an adjustable loading arm and interface plate. The interface plate connects the loading arm to the superior PMMA. The loading arm has an adjustable slot to align the transmission shaft's center at the occipital condyle joint. Figure 5.2.2-2 shows a schematic of how the piston's linear motion induces rotation about the occipital condyle joint.

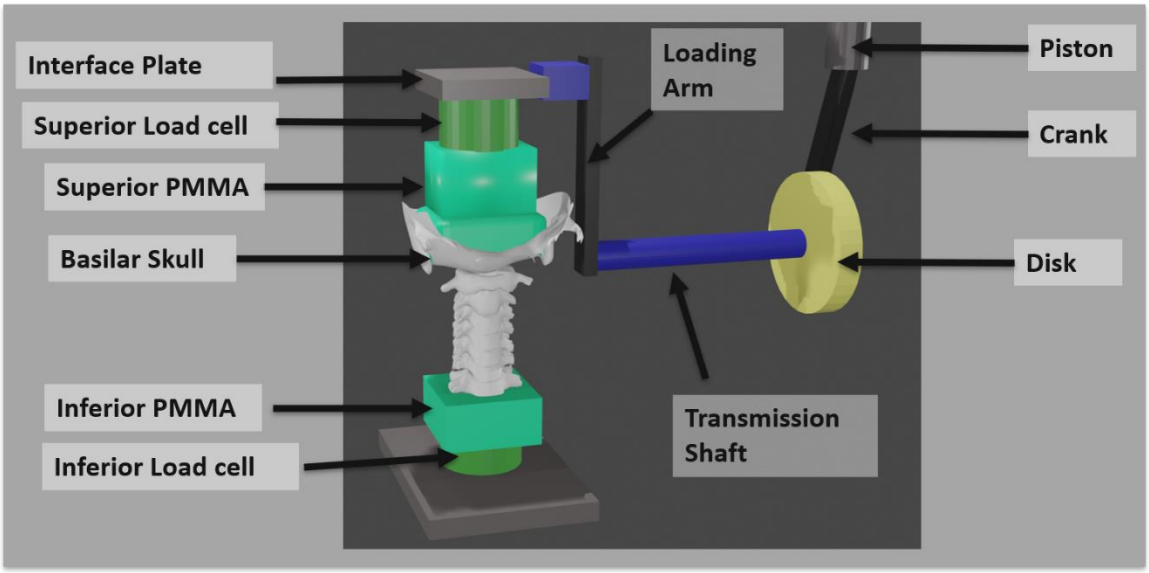

Figure 5.2.2-1: Schematic of Dynamic Moment System (DMS) including piston, crank, disk, transmission shaft, loading arm, and interface plate. The image's left side contains the isolated specimen in oblique coronal view with PMMA and load cells. Note the Transmission Shaft is aligned with the center of the occipital condyle joint.

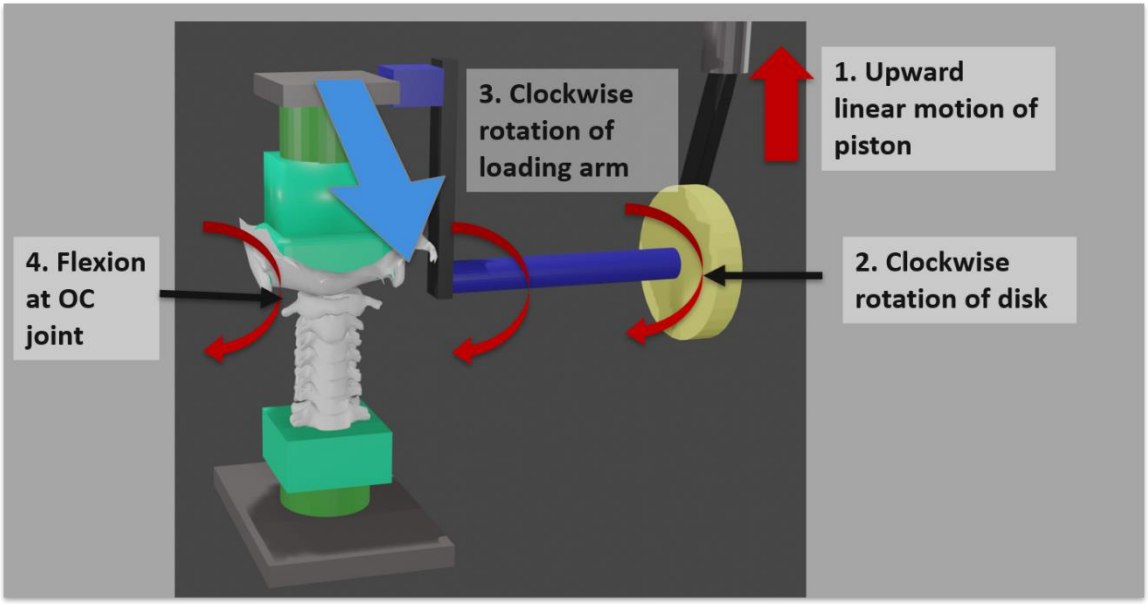

Figure 5.2.2-2: Schematic of DMS operation. The upward motion of the linear piston causes a clockwise rotation of the disk and transmission shaft. This causes clockwise rotation of the loading arm resulting in a flexion motion at the OC joint.

5.2.3. Test Setup and Analysis

The specimen was placed on the spinal positioning device described in Chapter 4 to align the isolated specimen such that T1 was angled 25 degrees from the horizontal to mimic the seated posture of an automobile occupant. The head was placed with the Frankfurt plane oriented horizontally. The superior PMMA was connected to the loading arm of the DMS via an interface plate. The plate allowed rotation of the head in the transverse plane while maintaining the neck's sagittal alignment (rotation at OC joint). The head was rotated 20 degrees clockwise (eyes to the right). The spine's height was adjusted using the vertical lift platform to align the OC joint with the center of the transmission shaft. The loading arm was adjusted to minimize axial preload. Figure 5.2.3-1 shows a schematic of the pre-test posture of the specimen and the device.

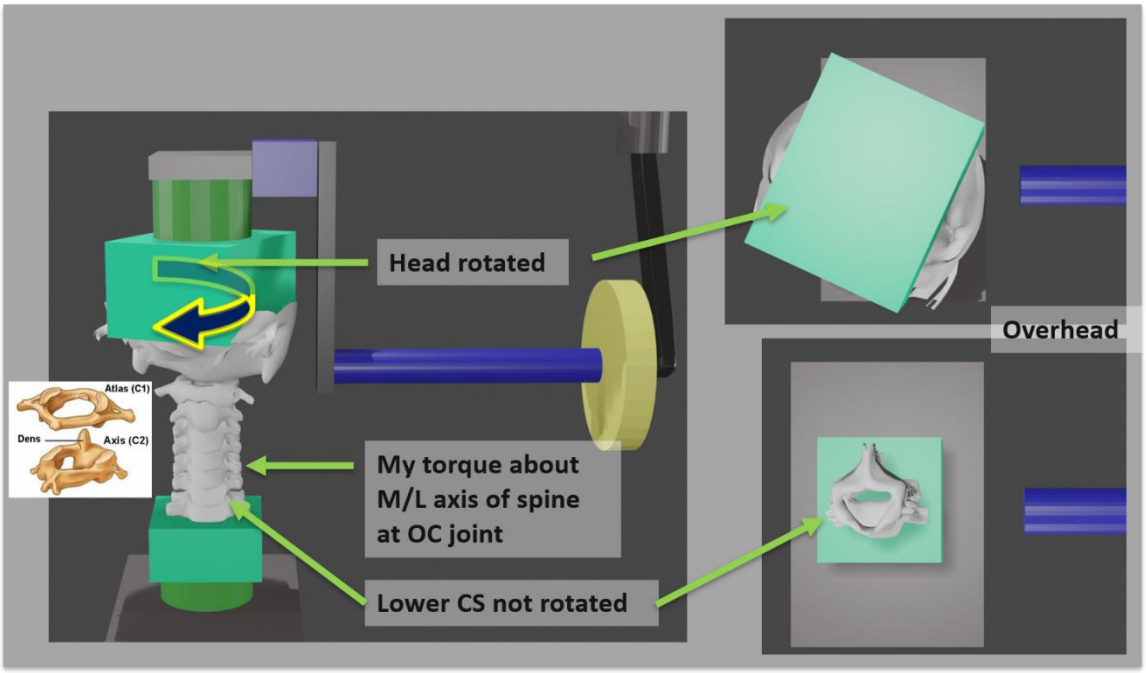

Figure 5.2.3-1: Left shows a coronal plane schematic of the specimen's pre-test posture in the DMS. The upper right shows an overhead view of the superior PMMA rotated to the right. The lower right shows the cervical spine with the sagittal alignment maintained.

The piston velocity was such that peak loading to the specimen was 1,000 rad/s at the superior PMMA. Load cell data was collected at 20 kHz. Three-dimensional kinematics were collected using a six-camera motion-capture system a 1 kHz. Occipital condyle loads were calculated using the superior load cell data and three-dimensional anatomic kinematics.

5.3. RESULTS

The oblique 20-degree tests produced minimal shear forces (Fx and Fy) and approximately 100 N of axial force. Peak bending moments were 45 Nm in the coronal (Mx) and sagittal (My) planes at about the same time. This shows the oblique loading from the uniaxial piston-induced complex loading (loading that was not directly aligned to the joint's mediolateral axis) to the spine. Figures 5.3-1 through 5.3-3 show the occipital condyle forces, and Figures 5.3-4 through 5.3-6 the occipital moments from the 20-degree oblique test.

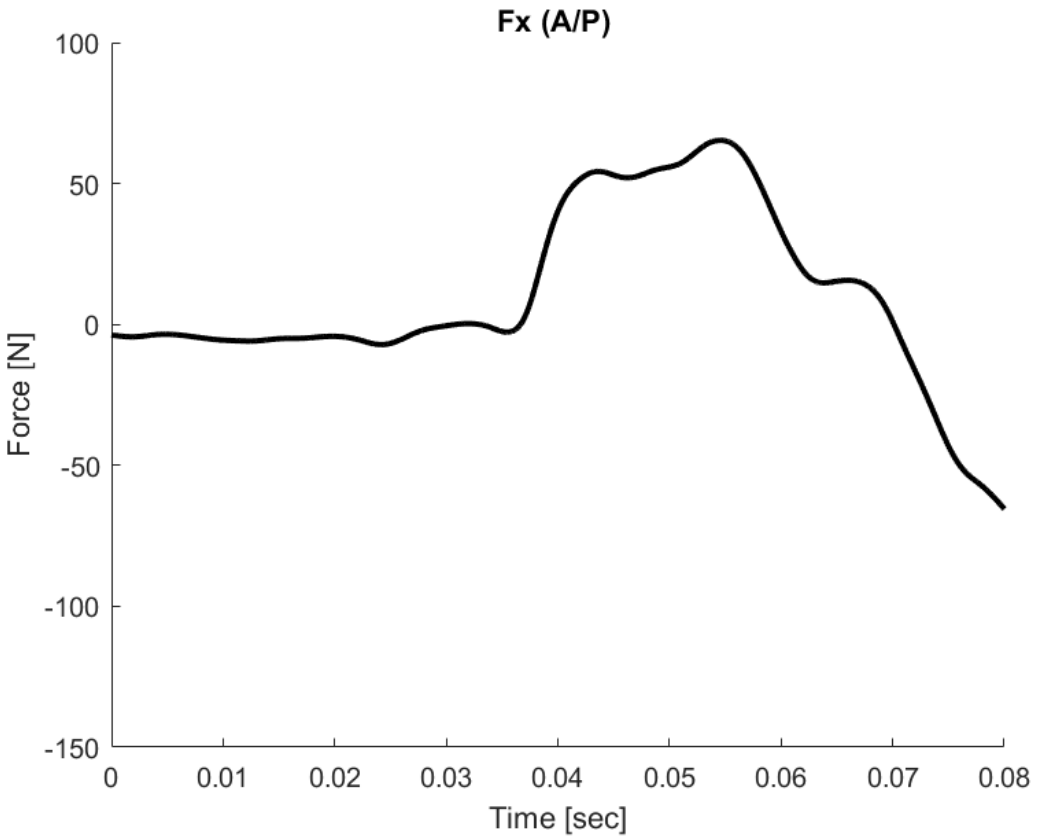

Figure 5.3-1: Fx (Anteroposterior) occipital condyle force from 20-degree oblique isolated PMHS test

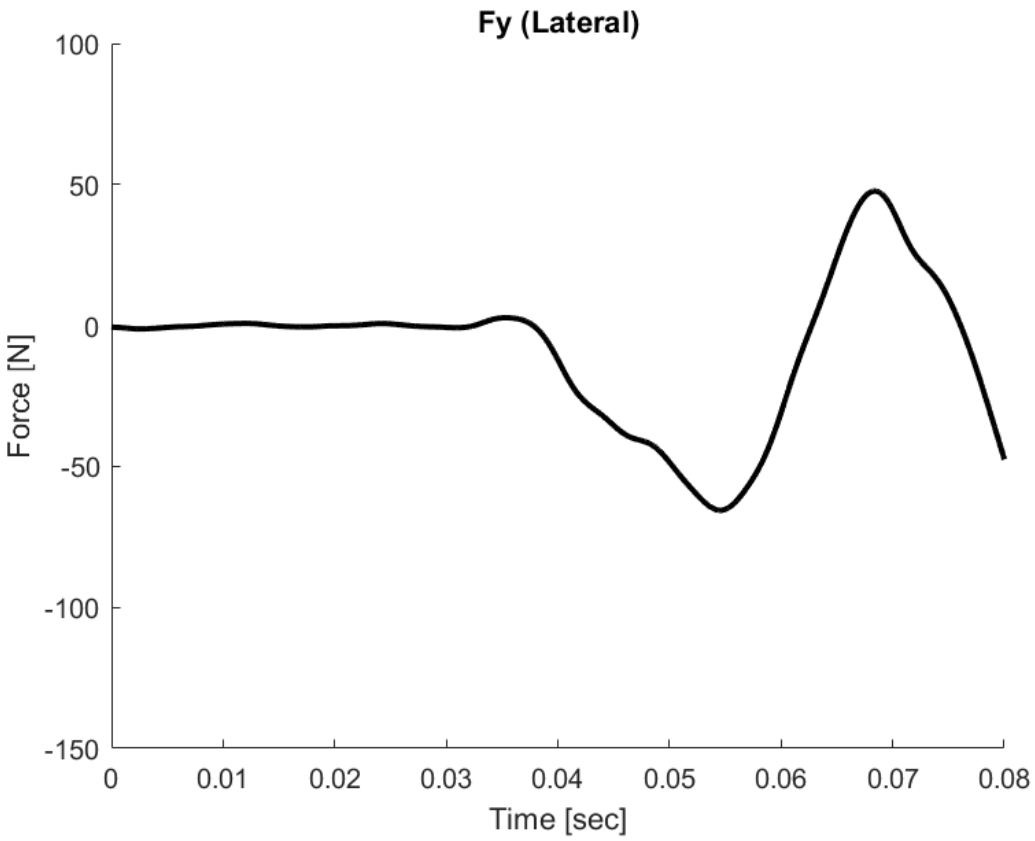

Figure 5.3-2: Fy (Lateral) occipital condyle force from 20-degree oblique isolated PMHS test

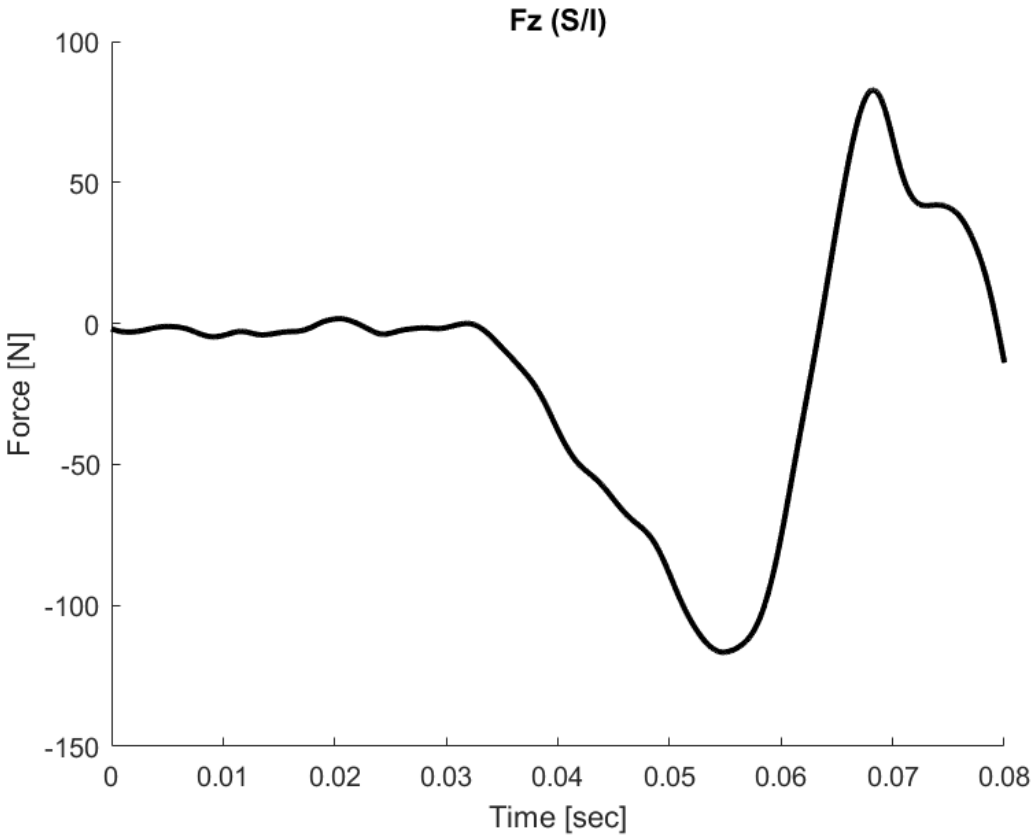

Figure 5.3-3: Fz (superior-inferior) occipital condyle force from 20-degree oblique isolated PMHS test

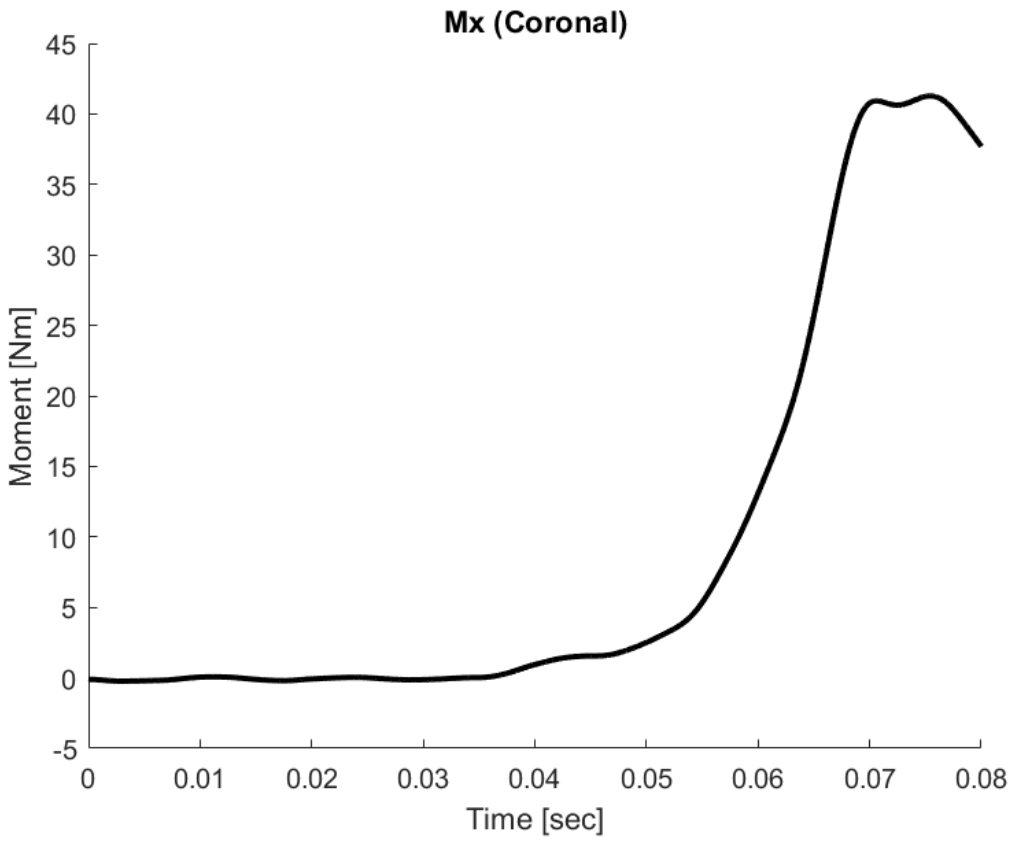

Figure 5.3-4: Mx (Coronal) occipital condyle moment from 20-degree oblique isolated PMHS test

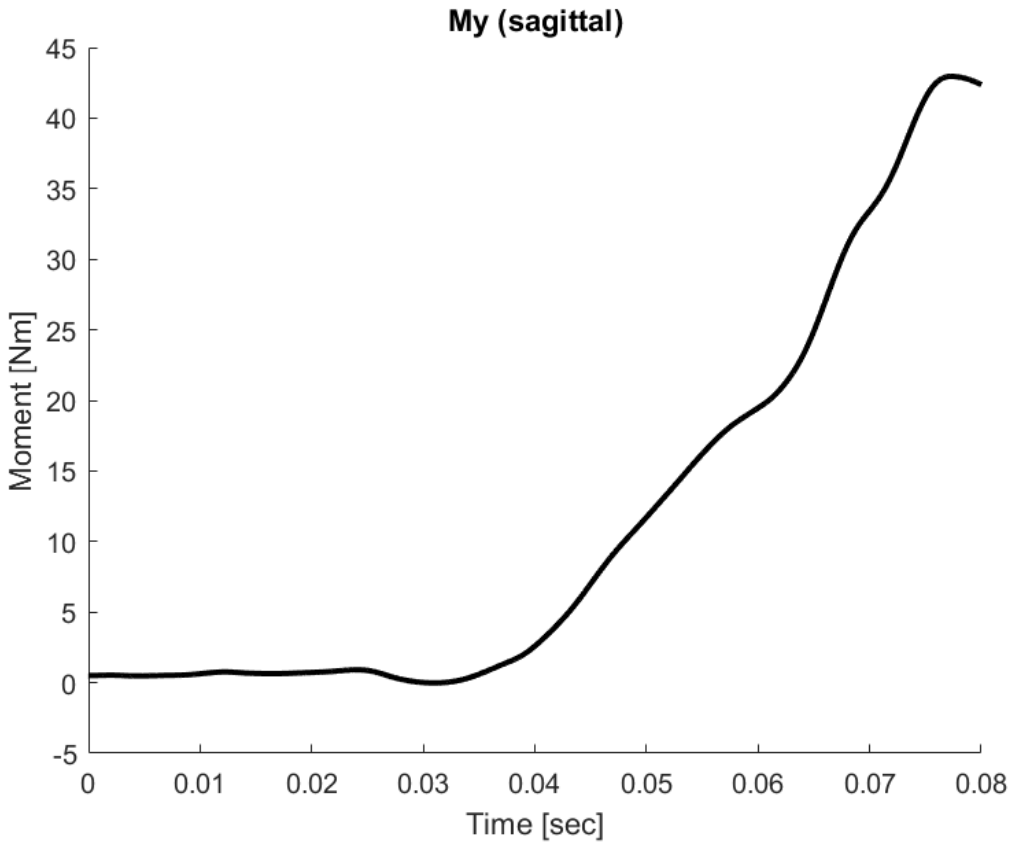

Figure 5.3-5: My (Sagittal) occipital condyle moment from 20-degree oblique isolated PMHS test

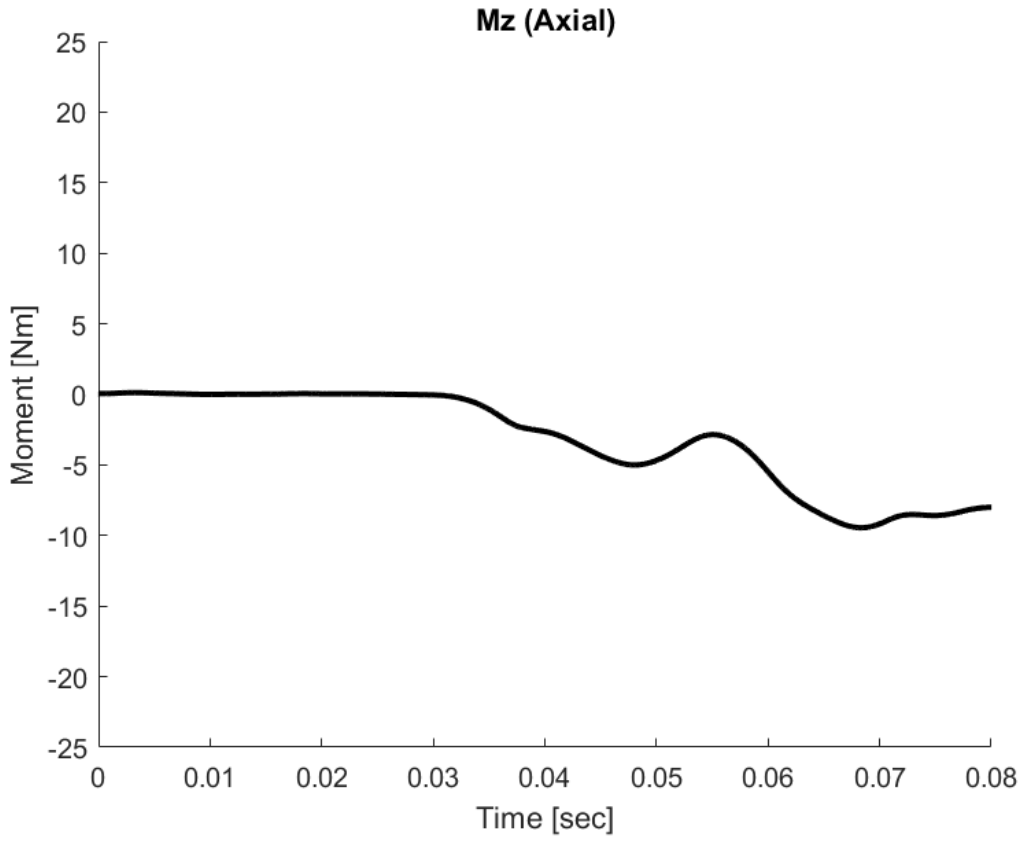

Figure 5.3-6: Mz (Axial) occipital condyle moment from 20-degree oblique isolated PMHS test

5.4. DISCUSSION

The present experimental model describes a new device and test methodology for applying complex loads to the occipital condyle joint in the form of a non-planar moment (bending about an axis not aligned with the mediolateral axis of the occipital condyle joint). One of DMS's first design challenges was translating the piston's linear translation to an angular motion. This was achieved by connecting the piston to a slider-crank mechanism that consisted of the crank arm and disk. The next step was to align the applied moment from the rotating disk to the anatomic level of the center of

the occipital condyle joint in the isolated PMHS. This was accomplished through three elements of the test device. The first was the transmission shaft, which was connected to the disk and acted as the moment's alignment axis. The second was the adjustable loading arm, which transferred the torque from the transmission shaft such that the load was applied to the top of the superior PMMA while keeping the center of rotation about the axis of the transmission shaft. The third element was the spinal position device's vertical lift table, which positioned the center of the occipital condyle joint coincident with the transmission shaft while minimizing axial preload. These experimental design features minimized parasitic loads present in simpler designs that directly connect the piston to a rigid moment arm. The final component on the specimen's cranial end was the adjustable plate, which permitted axial rotation of the basilar skull relative to the spine. This feature was necessary to achieve loading along an axis not coincident with the mediolateral axis of the occipital condyle joint, facilitating the induction of a complex load to the specimen. Finally, on the caudal end, the rotational plates and x-y table of the previously described spinal positioning device was used to achieve a standard seated posture of the cervical thoracic joint (25 degrees with respect to the horizontal).

This experimental model also had the flexibility to introduce retroreflective targets at multiple cervical spine levels to record three-dimensional anatomic kinematics. This allowed a full kinetic analysis of complex loading to the occipital condyle joint as demonstrated by an isolated PMHS test, wherein the head was rotated 20 degrees axially with respect to the cervical spine and a complex was load was applied

using a linear piston as the load-delivering device. The force and moment time-history plots from this experimental design demonstrate the ability to induce the complex loading to the occipital condyle joint and record the biomechanical data. Thus, this experimental model successfully reproduced the goals of applying complex loads to a head-neck specimen. Tests are currently being conducted in our laboratory to develop injury risk curves for military and automotive environments.

5.5. SUMMARY

- Application of complex loading to an isolated PMHS using a linear piston as input requires a sophisticated experimental design to minimize parasitic loads to the spine, e.g., more than a rigid moment arm.
- A novel experimental device was designed to deliver a moment at the occipital condyle level through an axis that was not coincident with the mediolateral axis of the joint.
- An isolated PMHS test was conducted to demonstrate the effectiveness of the device.
- In this experiment, the specimen was positioned such that the basilar skull was rotated 20 degrees axially to the right relative to the cervical spine.
- Loading was delivered at the occipital condyle joint via the dynamic moment system at a rate of 1,000 rad/s.
- Force, moment, and three-dimensional kinematics were collected.
- Data from the superior load cell and anatomic information obtained from pre-test CTs were used to calculate the occipital condyle loads.
- The experiment results demonstrate complex loading (moments in the coronal and sagittal planes) at the occipital condyle joint with minimal shear forces.
- An isolated PMHS sled test experimental design was pursued that replicated an obliquely seated occupant in an aircraft environment in terms of seat geometry, belt restraint, and acceleration pulse.

- Work is being conducted in our laboratory using this experimental design to determine injury risk curves

CHAPTER 6. SUMMARY OF CONTRIBUTIONS

6.1. IMPACT ON CURRENT PRACTICE

- The novel experimental design for evaluating wearable sensors established a new technique for accurately placing a reference sensor near the head center of gravity of a PMHS. This new method requires a CT scan using a reference plate attached to the head prior to instrumentation. Measurements from the CT scan are used to align the head relative to the single-axis drill to accurately place the sensor. The techniques described in this chapter have changed how PMHS is instrumented when the head sensor is not attached to the exterior cranium. The experimental protocol used pneumatic cylinders to support the head that retracted prior to impact. Controlling the head position such that the specimen achieved a similar pre-test posture for each impact was difficult, especially with the helmet's added mass. The pneumatic cylinders supported the head at three separate locations and helped achieve a repeatable posture while not affecting the impact response of the PMHS. This new practice of supporting the head for isolated head-neck tests is currently being used in our laboratory test protocol.
- The design of an experiment to induce non-planar loading to the lumbar spine used the results of whole-body experiments to define the isolated PMHS test conditions (loading rate and posture). The failure loads were measured using a load cell fixed to the inferior end of the isolated lumbar spine, and anatomic loads were calculated using offset measurements from instrumented CT scans. To replicate the injuries observed in the whole-body test, the isolated specimen

was placed in a posture similar to the whole-body test at the time of failure. To quantify the posture-induced pre-loads on the isolated tests, the static loads were measured prior to each test, and the offsets were maintained in the anatomic load calculations. The experimental practice of using whole-body PMHS failure conditions to define the test parameters of an isolated test and build a device that replicated this posture was developed in this experimental design.

- The novel methods to analyze three-dimensional kinematics used the results of frontal oblique PMHS experiments to determine response corridors of the head, spine, and pelvis. Typically, PMHS response corridor boundaries are defined in the x, y, and z axes independently using the mean and +/- a standard deviation scale. The current study employs a new technique to define these corridors using standard deviational ellipses, which use the PMHS response variability in all three axes simultaneously. This new method is more appropriate for non-planar loading. The analysis methods also demonstrated a technique for assessing the deflection metric, which statistically best~~s~~ represented injury in this loading scenario. With the use of the hierarchical or ranking of metrics coupled with survival analysis and interrelated three-dimensional kinematics, these processes have opened new avenues for advancing vehicles' crashworthiness and human safety in multiple environments.
- The design of an experiment to examine non-planar loading to the cervical spine used a novel device to translate the linear motion of a single axis piston into a

rotational motion at the occipital condyle joint about an axis that was not orthogonal to the sagittal plane. This study designed a new experimental practice for applying dynamic moments in more than one plane (coronal and sagittal). As in the case of the previous topic regarding injury measures, this topic is focused on including the off-axis or off-nominal postures, and the only common posture adopted hitherto for human safety. As off-axis postures are no longer perceived as special 'out-of-position' postures in the future vehicle and other environments, the present methodology has opened another novel avenue to pursue these issues for injury criteria and safety.

6.2. IMPACT ON STANDARDS

- The design of an experimental technique to assess wearable sensors for head exposure established a new standard for quantifying these sensors' accuracy. Many studies to evaluate sensor accuracy have relied on ATD experiments, which lack important biofidelity boundary conditions. The current study techniques describe how to place a reference sensor at the PMHS head center-of-gravity accurately. The reference sensor's output can be directly compared to wearable sensor calculations and serves as a quantifiable metric to assess accuracy.
- Results from the whole-body oblique impact experiments were used to help define a preliminary axial force injury criterion for occupants in obliquely oriented seats in the aircraft environment. Additional tests using the isolated lumbar spine experimental model can be used to define injury tolerance in an oblique loading scenario.

- The kinematic biofidelity corridors of the head, spine, and pelvis determined in the current study represent a new method for defining the corridors' boundaries using variation about all three axes simultaneously. Additionally, the mean orientation at each timestep was also determined. These techniques can be incorporated into new standards that evaluate ATD and human body model surrogates. The current techniques apply to non-planar loading, which may be more relevant as the automotive industry moves to non-standard seating positions and occupant postures.
- Data from the non-planar loading to the cervical spine is currently being used to determine a standard set of combined loading data to validate the head/neck's finite element models. This experimental design is also currently being used to assess the biofidelity of the THOR-05F ATD neck.

6.3. PEER-REVIEWED PUBLICATIONS

1. Humm, J. and N. Yoganandan (2020). "Development of chest deflection injury risk curve in oblique frontal small female PMHS sled tests." Traffic Inj Prev: 1-2.
2. Humm, J.R., et al., Responses and Injuries to PMHS in Side-Facing and Oblique Seats in Horizontal Longitudinal Sled Tests per FAA Emergency Landing Conditions. Stapp Car Crash J, 2016. 60: p. 135-163.
3. Humm, J., et al. (2015). "Injuries to Post Mortem Human Surrogates in Oblique Aircraft Seat Environment." Biomed Sci Instrum 51: 431-438.
4. Humm, J.R., et al., Three-dimensional kinematic corridors of the head, spine, and pelvis for small female driver seat occupants in near- and far-side oblique frontal impacts. Traffic Inj Prev, 2018. 19(sup2): p. S64-S69.

5. Humm JR, et. al., Novel experimental techniques using PMHS and CT scans to assess the performance of wearable sensors for mild traumatic brain injury applications for different populations, IRCOBI Conference, 2018 Athens, Greece

6.4. GRANT AWARDS FROM CURRENT STUDY

Role: Principal Investigator
Funding Agency: Department of Transportation
Title: THOR-50M Gold Standard Sled Testing

Role: Principal Investigator
Funding Agency: Association for the Advancement of Automotive Medicine
Title: Chest Deflection Injury Criteria for Automated Vehicle Environments

Role: Principal Investigator
Funding Agency: Department of Transportation
Title: THOR- 5th Neck Testing for Injury Risk Function Development

Role: Co-PI (PI:Yoganandan)
Funding Agency: Department of Transportation
Title: Small Female/Older Occupant Thoracic Biofidelity

BIBLIOGRAPHY

1. Yoganandan, N., et al., *Oblique Loading in Post Mortem Human Surrogates from Vehicle Lateral Impact Tests using Chestbands.* Stapp Car Crash J, 2015. **59**: p. 1-22.
2. Yoganandan, N., et al., *Injuries in Full-Scale Vehicle Side Impact Moving Deformable Barrier and Pole Tests Using Postmortem Human Subjects.* Traffic Inj Prev, 2015. **16 Suppl 2**: p. S224-30.
3. Pintar, F.A., N. Yoganandan, and J. Baisden, *Characterizing occipital condyle loads under high-speed head rotation.* Stapp Car Crash J, 2005. **49**: p. 33-47.
4. Pintar, F.A., N. Yoganandan, and D.J. Maiman, *Lower cervical spine loading in frontal sled tests using inverse dynamics: potential applications for lower neck injury criteria.* Stapp Car Crash J, 2010. **54**: p. 133-66.
5. Maiman, D.J., et al., *Effects of anterior vertebral grafting on the traumatized lumbar spine after pedicle screw-plate fixation.* Spine (Phila Pa 1976), 1993. **18**(16): p. 2423-30.
6. Yoganandan, N., et al., *Thoracic Biomechanics with Air Bag Restraint.* Stapp Car Crash J, 1993. **37**: p. 11.
7. Yoganandan, N., et al., *Thoracic Deformation Contours in a Frontal Impact.* Stapp Car Crash J, 1991. **35**: p. 16.
8. Yoganandan, N., et al., *Injury biomechanics of the human cervical column.* Spine (Phila Pa 1976), 1990. **15**(10): p. 1031-9.
9. Pintar, F.A., et al., *The biomechanics of lumbar facetectomy under compression-flexion.* Spine (Phila Pa 1976), 1992. **17**(7): p. 804-10.
10. Yoganandan, N., et al., *Strength and kinematic response of dynamic cervical spine injuries.* Spine (Phila Pa 1976), 1991. **16**(10 Suppl): p. S511-7.
11. Schmidt, G., et al., *Results of 49 Cadaver Tests Simulating Frontal Collision of Front Seat Passenger.* Stapp Car Crash J, 1974: p. 8.
12. Harris, G.F., et al., *A biomechanical impact test system for head and facial injury assessment and model development.* J Biomed Eng, 1993. **15**(1): p. 67-73.
13. Maltese, M.R., et al., *Response corridors of human surrogates in lateral impacts.* Stapp Car Crash J, 2002. **46**: p. 321-51.
14. Pintar, F., et al., *Instrumentation of Human Surrogates for Side Impact.* Stapp Car Crash J, 1996. **40**: p. 13.
15. Stemper, B.D. and F.A. Pintar, *Biomechanics of concussion.* Prog Neurol Surg, 2014. **28**: p. 14-27.
16. McCrea, M.A., B. Asken, and L.D. Nelson, *Neuropsychological Screening of Sport-Related Concussion.* Neurol Clin, 2017. **35**(3): p. 487-500.
17. McCrea, M., et al., *Immediate neurocognitive effects of concussion.* Neurosurgery, 2002. **50**(5): p. 1032-40; discussion 1040-2.
18. Stemper, B.D., et al., *Repetitive Head Impact Exposure in College Football Following an NCAA Rule Change to Eliminate Two-A-Day Preseason Practices: A Study from the NCAA-DoD CARE Consortium.* Ann Biomed Eng, 2019.

19. McCrea, M., et al., *Return to play and risk of repeat concussion in collegiate football players: comparative analysis from the NCAA Concussion Study (1999-2001) and CARE Consortium (2014-2017).* Br J Sports Med, 2019.
20. Humm, J.R., et al., *Responses and Injuries to PMHS in Side-Facing and Oblique Seats in Horizontal Longitudinal Sled Tests per FAA Emergency Landing Conditions.* Stapp Car Crash J, 2016. **60**: p. 135-163.
21. Mertz, H. and L. Patrick, *Strength and Response of the Human Neck.* Stapp Car Crash J, 1971. **15**: p. 26.
22. Nightingale, R.W., et al., *Flexion and extension structural properties and strengths for male cervical spine segments.* J Biomech, 2007. **40**(3): p. 535-42.
23. Nightingale, R.W., et al., *Comparative strengths and structural properties of the upper and lower cervical spine in flexion and extension.* J Biomech, 2002. **35**(6): p. 725-32.
24. Panjabi, M.M., et al., *Experimental study of atlas injuries. I. Biomechanical analysis of their mechanisms and fracture patterns.* Spine (Phila Pa 1976), 1991. **16**(10 Suppl): p. S460-5.
25. Humm, J.R., et al., *Three-dimensional kinematic corridors of the head, spine, and pelvis for small female driver seat occupants in near- and far-side oblique frontal impacts.* Traffic Inj Prev, 2018. **19**(sup2): p. S64-S69.
26. (CDC), C.f.D.C.a.P., *Sport-related recurrent brain injuries - United States*, in *MMWR Morb Mortal Wkly Rep*. 1997.
27. Langlois, J.A., W. Rutland-Brown, and M.M. Wald, *The epidemiology andimpact of traumatic brain injury: A brief overview.* Journal Head Trauma Rehail, 2006. **21**(5): p. 375-278.
28. McCrory, P., W.H. Meeuwisse, and M. Aubry, *Consensus statement on concussion in sport: the 4th International Conference on Concussion in Sport held in Zurich, November 2012.* British Journal of Sports Medicine, 2013. **47**: p. 250-58.
29. Gennarelli, T. and D. Graham, *Neuropahtology of the Head Injuries.* Seminars in Clinical Neuropsychiatry, 1998. **3**(3): p. 160-175.
30. Gennarelli, T., *Head injury mechanisms and cerebral concussion and diffuse brain injuries*, in *Athletic injuries to the head, neck, and face*. 1991, Mosby: St. Louis. p. 270-228.
31. Clark, M. and K. Guskiewicz, *Sport related traumatic brain injury*, in *Translation research in traumatic brain injury*. 2016, CRC Press/Taylor and Francis Group: Boca Raton.
32. Lissner, H.R., M. Lebow, and F.G. Evans, *Experimental studies on the relation between acceleration and intracranial pressure changes in man.* Surgery Gynecology and Obstetrics, 1960: p. 328-338.
33. Gadd, C.W., *Use of a weighted-impulse criterion for estimating injury hazard.* Stapp Car Crash Conference, 1966. **10**.
34. Versace, J., *A review of the severity index.* Stapp Car Crash Conference, 1971. **15th**.

35. Gennarelli, T.A., A.K. Ommaya, and L.E. Thibault, *Comparison of translational and rotational head motions in experimental cerebral concussion.* Fifteenth Stapp Car Crash Conference, 1971.
36. Gennarelli, T.A., L.E. Thibault, and A.K. Ommaya, *Pathophysiologic responses to rotational and translational accelerations of the head.* Society of Automotive Engineers, 1972.
37. Takhounts, E.G., et al., *Development of Brain Injury Crtieria (BrIC).* Stapp Car Crash Conference, 2013. **57**: p. 243-266.
38. McCrea, M., *Unreported concussin in high school football players: implicatinos for prevention.* Clinical Journal of Rehabil., 2006. **21**(5): p. 375-378.
39. Guskiewicz, K.M., et al., *Epidemiology of concussion in collegiate and high school football players.* The American Journal of Sports Medicine, 2000. **28**(5): p. 643-650.
40. Pellman, E.J., *Concussion in professional football: Epidemiological features of game injuires and review of the literature.* Neurosurgery, 2004. **54**(1): p. 81-94.
41. Nevins, D., L. Smith, and J. Kensrud, *Laboratory Evaluation of Wireless Head Impact Sensor.* Procedia Engineering, 2015. **112**: p. 175-179.
42. GP, S., et al., *alidation of a skin-mounted sensor for measuring in-vivo head impacts*, in *IRCOBI*. 2015: Lyons, France.
43. Allison, M.A., et al., *Validation of a Helmet-Based System to Measure Head Impact Biomechanics in Ice Hockey.* Medicine & Science in Sports & Exercise, 2014. **46**(1): p. 115-123.
44. Yoganandan, N., et al., *Physical properties of the human head: mass, center of gravity and moment of inertia.* J Biomech, 2009. **42**(9): p. 1177-92.
45. Yoganandan, N., et al., *Head motions using nine accelerometer package and angular rate sensors.* Biomed Sci Instrum, 2008. **44**: p. 256-61.
46. Kang, Y.S., K. Moorhouse, and J.H. Bolte, *Measurement of six degrees of freedom head kinematics in impact conditions employing six accelerometers and three angular rate sensors (6aomega configuration).* J Biomech Eng, 2011. **133**(11): p. 111007.
47. Padgaonkar, A.J., K.W. Krieger, and A.I. King, *Measurement of Angular Acceleration of a Rigid Body Using Linear Accelerometers.* Journal of Applied Mechanics, 1975. **42**(3): p. 552-556.
48. Shah, A.S., et al., *Methodology to Study Attenuation of a Blast Wave Through the Cranium.* 2011(54884): p. 17-24.
49. Yoganandan, N. and A. Banerjee, *Survival Analysis-Based Human Head Injury Risk Curves: Focus on Skull Fracture.* J Neurotrauma, 2018. **35**(11): p. 1272-1279.
50. Kimpara, H. and M. Iwamoto, *Mild traumatic brain injury predictors based on angular accelerations during impacts.* Ann Biomed Eng, 2012. **40**(1): p. 114-26.
51. CFR, U., *U.S. Code of Federal Regulations, Title 14, Parts 25.561, 23.785, 25.562, 25.785, 121.291 Washington, DC: U.S. GPO.*
52. NTSB, *National Transportation Safety Board, "Survivability of Accidents Involving Part 121 U.S. Air Carrier Operations, 1983 Through 2000", Safety Report NTSB/SR-01/01, Washington DC.* 2001.

53. Yoganandan, N., et al., *Upper neck forces and moments and cranial angular accelerations in lateral impact.* Ann Biomed Eng, 2008. **36**(3): p. 406-14.
54. Philippens, M., et al., *ES2 neck injury assessment reference values for lateral loading in side facing seats.* Stapp Car Crash J, 2009. **53**: p. 421-41.
55. Humm, J., et al., *Injuries to Post Mortem Human Surrogates in Oblique Aircraft Seat Environment.* Biomed Sci Instrum, 2015. **51**: p. 431-8.
56. Dewesse, R.W., D.M. Moorcraft, and J.A. Pellettiere, *Civil Aviation Crash Injury Protection*, in *Accidental Injury: Biomechanics and Prevention*, N. Yoganandan, A. Nahum, and J. Melvin, Editors. 2015, Springer, : NY. p. 811-827.
57. Cavanaugh, J., et al., *Biomechanical response and injury tolerance of the pelvis in twelve sled side impacts. Proceedings of the 34th STAPP Car Crash Conference, SAE 902305, pp. 1–12.* 1990.
58. Cavanaugh, J., et al., *Injury and response of the thorax in side impact cadaveric tests, Proceedings of the 37th STAPP Car Crash Conference.* 1993.
59. Pintar, F.A., et al., *Worldsid assessment of far side impact countermeasures.* Annu Proc Assoc Adv Automot Med, 2006. **50**: p. 199-219.
60. Pintar, F.A., et al., *Comparison of PMHS, WorldSID, and THOR-NT responses in simulated far side impact.* Stapp Car Crash J, 2007. **51**: p. 313-60.
61. Yoganandan, N., et al., *Biomechanics of side impact: injury criteria, aging occupants, and airbag technology.* J Biomech, 2007. **40**(2): p. 227-43.
62. Yoganandan, N., et al., *Thoraco-abdominal deflection responses of post mortem human surrogates in side impacts.* Stapp Car Crash J, 2012. **56**: p. 49-64.
63. Yoganandan, N., et al., *Oblique lateral impact biofidelity deflection corridors from Post Mortem Human Surrogates.* Stapp Car Crash J, 2013. **57**: p. 427-40.
64. Viano, D.C., *Biomechanical response and injuries in blunt lateral impact, STAPP Conference Proceedings, 113–142.* 1989.
65. Yoganandan, N., et al., *Bone mineral density of human female cervical and lumbar spines from quantitative computed tomography.* Spine (Phila Pa 1976), 2006. **31**(1): p. 73-6.
66. Yoganandan, N., et al., *Trabecular bone density of male human cervical and lumbar vertebrae.* Bone, 2006. **39**(2): p. 336-44.
67. SAE, *Instrumentation for impact test, J211-1, Warrendale, PA.* 2003.
68. FMVSS-214, *49Code of Federal Regulations: 571.214*, in *49 CFR; Parts 571. Side Impact Protection*. 2008, US Government Printing Office: Washington, DC.
69. Kuppa, S., et al., *Development of Side Impact Thoracic Injury Criteria and Their Application to the Modified ES-2 Dummy with Rib Extensions (ES-2re).* Stapp Car Crash J, 2003. **47**: p. 189-210.
70. Cavanaugh, J. and N. Yoganandan, *Thoracic Injury Bomechanics*, in *Accidental Injury: Biomechanics and Prevention*, N. Yoganandan, A. Nahum, and J. Melvin, Editors. 2015, Springer, : NY. p. 331-372.
71. Hardy, W.N., et al., *Impact and Injury Response of the Abdomen*, in *Accidental Injury: Biomechanics and Prevention*, N. Yoganandan, A. Nahum, and J. Melvin, Editors. 2015, Springer, : NY. p. 373-434.

72. Shaw, G., et al., *Impact response of restrained PMHS in frontal sled tests: skeletal deformation patterns under seat belt loading.* Stapp Car Crash J, 2009. **53**: p. 1-48.
73. Markley, F.L., et al., *Averaging Quaternions.* Journal of Guidance, Control, and Dynamics, 2007. **30**(4): p. 1193-1197.
74. Lefever, D.W., *Measuring Geographic Concentration by Means of the Standard Deviational Ellipse.* American Journal of Sociology, 1926. **32**(1): p. 88-94.
75. Wang, B., W. Shi, and Z. Miao, *Confidence Analysis of Standard Deviational Ellipse and Its Extension into Higher Dimensional Euclidean Space.* PLoS ONE, 2015. **10**(3): p. e0118537.
76. Yoganandan, N., et al., *Deriving injury risk curves using survival analysis from biomechanical experiments.* J Biomech, 2016. **49**(14): p. 3260-3267.
77. Yoganandan, N., et al., *Foot-Ankle Fractures and Injury Probability Curves from Post-mortem Human Surrogate Tests.* Ann Biomed Eng, 2016. **44**(10): p. 2937-2947.
78. Akaike, A., *A new look at the statistical model identification.* IEEE Transactions on Automatic Control, 1974. **19**: p. 716-723.
79. Brier, G.W., *Verification of forecasts expressed in terms of probability.* Monthly Weather Review. , 1950. **78**(8): p. 1-3.
80. Parr, W.C., *A note on the jackknife, the bootstrap and the delta method estimators of bias and variance. .* Biometrika 1983. 70(3): p. 719-722., 1983. **70**(3): p. 719-722.
81. Petitjean, A., et al., *Normalization and scaling for human response corridors and development of risk curves* in *Accidental Injury: Biomechanics and Prevention*, N. Yoganandan, A.M. Nahum, and J.W. Melvin, Editors. 2015, Springer,: NY. p. 769-792.
82. Yoganandan, N., A.M. Nahum, and J.W. Melvin, eds. *Accidental Injury: Biomechanics and Prevention, 851 pp.* Third ed. 2015, Springer,: NY. 851.
83. FMVSS-208, *FMVSS 208: 49Code of Federal Regulations: 571.208*. 2001, US Government Printing Office: Washington, DC.
84. Meyer, F., et al., *Human Neck Finite Element Model Development and Validation against Original Experimental Data.* Stapp Car Crash J, 2004. **48**: p. 177-206.
85. Meyer, F., et al., *Development and validation of a coupled headneck FEM – application to whiplash injury criteria investigation.* International Journal of Crashworthiness, 2012.
86. Meyer, F. and R. Willinger, *Modelling of car seat and human body interaction under rear impact.* International Journal of Crashworthiness, 2006.
87. Meyer, F. and R. Willinger, *Protection from motorcycle neck-barces using FE modelling.* SPorts Engineering, 2018. **23**: p. 307-316.
88. Maiman, D.J., N. Yoganandan, and F.A. Pintar, *Preinjury cervical alignment affecting spinal trauma.* J Neurosurg, 2002. **97**(1 Suppl): p. 57-62.
89. Yoganandan, N., et al., *Anatomic study of the morphology of human cervical facet joint.* Spine (Phila Pa 1976), 2003. **28**(20): p. 2317-23.

90. Clark, C.R. and E.C. Benzel, *The Cervical Spine.* 2005, Lippincott Williams & Wilkins, MD. 1250.
91. Hall, M.C., *Luschka's Joint*. 1965: Springfield, Thomas.